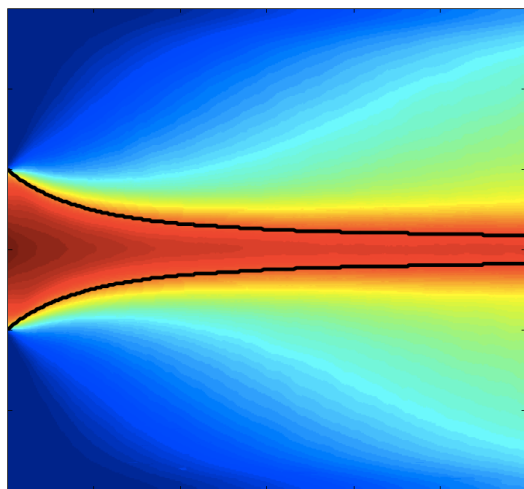THESIS FOR THE DEGREE OF DOCTOR OF PHILOSOPHY IN
THERMO AND FLUID DYNAMICS

The One-Dimensional Turbulence Model
Applied to Spray Atomization

AMIRREZA MOVAGHAR

Department of Mechanics and Maritime Sciences
CHALMERS UNIVERSITY OF TECHNOLOGY
Gothenburg, Sweden, 2018

The One-Dimensional Turbulence (ODT) Model Applied to Spray Atomization

ABSTRACT

Numerical simulation of the spray behavior is an important part of engine research and is critical for combustion optimization. Successful implementation of the advanced modeling tools for sprays is strongly dependent on our current understanding of the physical processes involved. One of the main processes occurring close to the nozzle is primary atomization. It governs the initial size and velocity distribution of droplets formed at the liquid jet surface. This process is not yet fully understood due to challenges in experimental observation of the region close to the nozzle. This has kept the primary atomization as one of the least developed model components in spray simulation and in need of improvement.

In this dissertation, a new primary atomization model is proposed based on the One-Dimensional Turbulence (ODT) model framework. ODT is a stochastic turbulence model simulating turbulent flow evolution along a notional 1D line of sight by applying instantaneous maps to represent the effect of individual turbulent eddies on property profiles. This approach provides affordable high resolution at the liquid/gas interface, which is essential for capturing the local behavior of the breakup process.

This new approach is assessed under different operating conditions parameterized by the liquid jet Reynolds and Weber numbers. ODT primary atomization results have been provided as an input to a spray model in conventional form to evaluate its predictive capability. These efforts are reported in several manuscripts attached to this dissertation.

Furthermore, to better understand the physics behind primary atomization, a canonical simulation configuration is developed that isolates the interaction between surface tension and surrounding turbulence. The ability of the model to capture the breakup is assessed with the available Detailed Numerical Simulation (DNS) data for further improvements.

Lastly, a new strategy is proposed to use ODT as a subgrid resolution model in LES/VOF simulations to describe/model unresolved subgrid interface dynamics.

Keywords: Turbulence, Primary breakup, One Dimensional Turbulence(ODT)

List of Publications

This thesis consists of an extended summary and the following appended publications, referred to in the text by their Roman numerals:

I. H. Grosshans, **A. Movaghar**, L. Cao, M. Oevermann, R-Z. Szasz, L. Fuchs, "Sensitivity of VOF Simulations of the Liquid Jet Breakup to Physical and Numerical Parameters" in *Computers & Fluids*, Vol 136 (2016): 312-323l.

II. **A. Movaghar**, M. Linne, M. Oevermann, F. Meiselbach, H. Schmidt, Alan R. Kerstein, "Numerical Investigation of Turbulent-jet Primary Breakup Using One-Dimensional Turbulence," in *International Journal of Multiphase Flow*, Vol 89 (2017): 241-254.

III. Alan R. Kerstein, **A. Movaghar**, M. Oevermann, "Parameter Dependences of the Onset of Turbulent Liquid-jet Breakup," in *Journal of Fluid Mechanics*, Vol 811 (2017).

IV. **A. Movaghar**, M. Linne, M. Herrmann, A. R. Kerstein, M. Oevermann, "Modeling and Numerical Study of Primary Breakup Under Diesel Conditions," in *International Journal of Multiphase Flow*, Vol 98 (2018): 110-119.

V. **A. Movaghar**, R. Chiodi, M. Oevermann, O. Desjardins, A. R. Kerstein, "Assessment of an Atomization Model Based on One-Dimensional Turbulence using Direct Numerical Simulation of a Decaying Turbulent Interfacial Flow," in *Physics of Fluids*, Under review.

VI. **A. Movaghar**, R. Chiodi, M. Oevermann, O. Desjardins, A. R. Kerstein, "A Subgrid-Scale Model for Large-Eddy Simulation of Liquid/Gas Interfaces Based on One-Dimensional Turbulence," in *Ercoftac Colloquium 589, Turbulent Cascades II*, (2017), Springer, in print.

Other Relevant Publications

▷ **A. Movaghar**, M. Linne, M. Oevermann, F. Meiselbach, H. Schmidt, A. R. Kerstein, "Numerical investigation of turbulent-jet primary breakup using one-dimensional turbulence," in *Annual Conference on Liquid Atomization and Spray Systems, ILASS Europe*, Bremen, Germany, 2014.

▷ **A. Movaghar**, M. Linne, M. Oevermann, A. R. Kerstein, "Numerical study of the interaction between turbulence and surface tension using One-Dimensional Turbulence," in *Annual Conference on Liquid Atomization and Spray Systems, ILASS America*, Raleigh, NC, USA, 2015.

▷ **A. Movaghar**, M. Linne, M. Oevermann, Alan R. Kerstein, "Numerical and experimental study of liquid breakup at the surface of turbulent jets," in *International Conference on Liquid Atomization and Spray Systems, ICLASS* , Tainan, Taiwan, 2015.

▷ **Movaghar, A.**, M. Linne, L. Bravo, M. Oevermann, A. R. Kerstein, "Numerical study of droplet statistics resulting from turbulent jet primary breakup," in *9th International Conference on Multiphase Flow (ICMF)*, Firenze, Italy, 2016

▷ **A. Movaghar**, M. Linne, M. Herrmann, A. R. Kerstein, M. Oevermann, "Modeling and numerical study of primary breakup under diesel conditions," in *Annual Conference on Liquid Atomization and Spray Systems, ILASS America* , Atlanta, GA, USA, 2017.

▷ **A. Movaghar**, A. R. Kerstein, M. Oevermann, "The One-Dimensional Turbulence (ODT) model applied to spray atomization," in *70th Annual Meeting of the APS Division of Fluid Dynamics* , Denver, CO, USA, 2017.

Acknowledgments

As well-noted by Dr. Ragnar Larusson [121], being a doctoral student is not just writing a couple of papers, is a great journey of personal development shaped by people around you (for example a president with his spontaneous decision-making style).

Spoiled is not the word. Few students are fortunate enough to have three well-known advisors. I would first like to thank my supervisor, Michael Oevermann who gave me the opportunity to work at this project. I appreciate his guidance and open door policy. I have been further privileged to work with Alan Kerstein. The father of ODT, who has limitness power of generating ideas. Alan, I do not call you just an esteemed mentor, I am proud to call you a colleague and a friend. A ton of thanks goes out to Mark linne, for all his insights and motivations during this project.

Special thanks go to Falko Meiselbach for teaching me ODT, I was lucky to have you by my side through thick and thin. During my studies, I got a chance to spend a couple of months at Cornell University, I truly thank Olivier Desjardins and Robert Chiodi for all their hospitality and collaboration.

To all my colleagues at Chalmers, thank you for all good times we had together! The trips to Munich and India were the special ones. Even playing football at the cost of missing Swedish summer !

To all my friends in Sweden, who remained or who choosed other endeavours, who made my life more enjoyable and charming, Thank you !

The European Erasmus Program is also acknowledged for improving what I call the European mixing process.

Ulla, Elenor, Ingmar thank you for all your help. There were no problems that could not be solved.

Last but not the least, I would like to thank my family for the love and the support they gave me all these years. Of course Dad, Tyres ROCK !

Contents

Part I

Extended Summary

1

Introduction

1.1 Motivation and context

In the context of current energy and environmental warnings, the design objectives for combustion systems are being redefined to put a stronger emphasis on reducing pollutant emissions and improving efficiency in order to reduce fuel consumption [1]. One of the main processes in combustion systems is fuel injection. As Figure 1.1 shows, when the fuel leaves the nozzle, turbulence inside the liquid jet and aerodynamic interaction between the liquid and gas phase make the liquid surface unstable and leading to formation of ligaments and droplets. This process which occurs close to the nozzle is usually referred to as primary breakup. The droplets formed during primary breakup separate into smaller ones, evaporate and create the dilute spray. These processes significantly affect the ignition behaviour, heat release, fuel consumption and exhaust emissions of the combustion reaction. The importance of primary atomization has led researchers to investigate the near nozzle regions experimentally for a long time. Experimental observation of the regions close to the nozzle has

proven challenging though. Often results are blurred due to multi scattering effects caused by the large number of droplets. Recently, advanced experimental techniques like ballistic imaging [2–4] or X-ray diagnostics [5–7] have enabled detailed inevestigation of phenomena in the optically dense region of the liquid core of a jet. Nevertheless, the data extracted from such experiments is currently very limited and may not lead to a detailed understanding of relevant physical processes involved in the primary breakup.

Computational fuid dynamics (CFD) offers a viable platform to investigate such flows, providing a wealth of data from which much information can be extracted. The spray and atomizing processes can be described as a multiphase phenomena, involving liquid phase in the form of droplets and the gas phase as a continuum. In industrial applications, a common approach to describe primary atomization numerically is the Eulerian Lagrangian method. In this approach, the gas phase is treated as a continuous field and the liquid jet is approximated by injecting droplets on the order of the nozzle diameter. The breakup process in these Eulerian Lagrangian simulations can be modeled using standard deterministic breakup models based on Taylor analogy breakup (TAB) [8, 9] or wave models [10]. Although such models are used frequently in engineering simulations, they do not resemble the real physics of primary breakup. Parameter tuning is usually necessary to match experimental data and should be done every time the flow conditions are changed.

Spray breakup models may be improved by using high resolution numerical simulations, for example, Detailed Numerical Simulation (DNS) and Large Eddy Simulation (LES). LES can provide a tradeoff between accuracy and computational cost by applying subgrid models to treat the unresolved flow-field. Direct Numerical Simulation (DNS) is aimed at removing turbulence uncertainty and resolving all of the flow length scales. However, routine use of DNS for industrial ranges of Reynolds numbers is still beyond the capacity of current computers.

Despite the advantages that both approaches have in solving the single phase Navier Stokes equations, complexity arises at the interface, where the singular nature of the surface tension force leads to discontinuities in fluid properties and pressure. These discontinuities require specialized methods to account for the jump in fluid properties at the interface and its advection.

Another challenge for simulating interfacial flows is obtaining an adequate resolution, due to the large range of length and time scales that exist in turbulent

interfacial flows. On the other hand, the criteria for resolution convergence is still being studied and has remained as a widely debated subject.
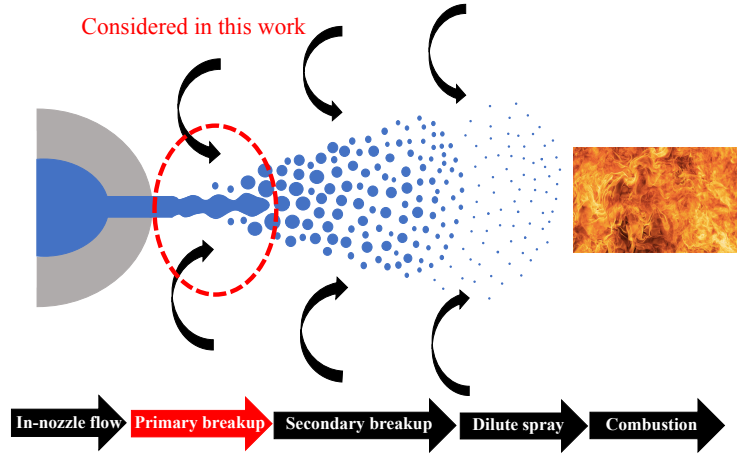
Figure 1.1: Diagram of spray formation

To fill in the resolution gap between LES and DNS, new models need to be proposed. One of these new models which is a primary focus of this thesis, is called One Dimensional Turbulence (ODT). ODT is a stochastic model that simulates the turbulent flow evolving along a notional one-dimensional line of sight by applying instantaneous maps to represent the effect of turbulent eddies on property profiles resolving all time and length scales. Since ODT can simulate all relevant scales, can be used for fundamental simulations of turbulence or as a subgrid model for LES simulations.

In this study, the ODT model is applied to simulate primary atomization. Accordingly, the ODT line is oriented in the direction of the most significant fluid properties gradient (normal to the interface). This configuration provides the sufficient resolution at the interface and overcomes the limitation of DNS to moderate Reynolds and Weber numbers due to computational resources. This new approach is assessed under different operating conditions. Later, the ODT primary atomization results are provided as an input to a conventional spray model to evaluate its predictive capability.

To better understand the underlying physics behind primary atomization, a

canonical simulation configuration is developed that isolates the interaction between surface tension and surrounding turbulence. The ability of the model to capture the breakup is assessed against the available Direct Numerical Simulation (DNS) data to guide further improvements.

Lastly, a new strategy is proposed to use ODT as a subgrid resolution model in LES/VOF simulations to describe/model unresolved subgrid interface dynamics. The ODT formulation and its assessment will be discussed in detail in the next chapters.

1.2 Dissertation organization

The remainder of this dissertation is divided into eighth chapters. Chapter 2 summerizes the fundamentals behind spray formation and atomization. Chapters 3 and 4 briefly discuss the One-Dimensional Turbulence (ODT) model and its extensions to gas liquid multiphase flow. Chapter 5 summarizes the assessment of ODT as a primary breakup model in different operating conditions. Chapter 6 is a short summary of the manuscript that is in preparation for submission to the journal Physics of Fluids. Chapter 7 discusses the new strategy proposed to to use ODT as a subgrid resolution model in LES/VOF simulations. Chapter 8 provides a summary of the appended papers. Finally key conclusions of this work are summarized in Chapter 9.

2

Fundamentals

2.1 Liquid jets and sprays

In engine applications the fuel spray characteristics are critical to determine the engine performance such as fuel consumption rate or exhaust gas emissions. In internal combustion engines sprays are used in order to mix liquid fuel with air and to increase its surface area for rapid evaporation and combustion.

Figure 2.1 shows a sketch of a typical flow originating from a pressure atomizer. The flow can be divided into different regimes. Directly at the nozzle orifice an intact core of the liquid phase exist. It rapidly disintegrates into ligaments and droplets from the liquid core surface, this part is called the primary breakup of the jet. When the core is broken up, the droplets and ligaments occupy still a considerable fraction of the volume compared to the encountered gas flow whithin a certain region. This spray region is generally called the dense spray.

The liquid structures breakup into smaller droplets further downstream and due to turbulent dispersion and droplet evaporation the average spacing between
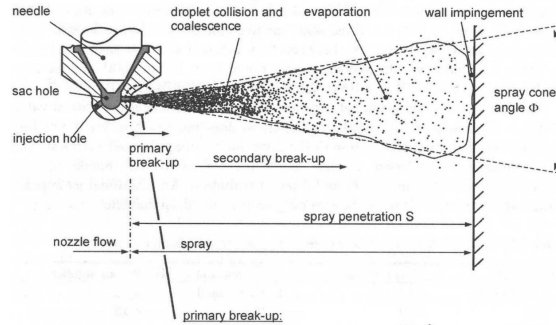
Figure 2.1: Full cone spray; including definition of spray angle, spray length and appearance of different regimes

droplets expands further downstream of the nozzle leading to a decreasing liquid volume fraction. When at some point the liquid volume fraction is small compared to the gaseous volume fraction, the spray regime is called a dilute spray.

Later the produced vapor mixes with oxidizer forming a combustible mixture which ignites due to the presence of the additional energy supply or due to autoignition by increasing pressure and temperature.

The droplet-droplet interactions in each of the discussed areas are different. In the dense spray it is often assumed that the droplet spacing is equal to the droplet diameter and liquid structures are non spherical and they frequently collide. In contrast in the dilute spray section the mean distance between droplets can be as much as $10 - 15$ droplet diameters, which implies that the volume fraction is of the order of 0.1%. As a result, the influence of droplets on each other is limited and collisions are rare.

2.2 Breakup of a liquid jet

The breakup of the liquid jet is caused by instabilities from aerodynamic forces acting on the jet surface, turbulent motions inside the liquid or cavitation.

For a systematic investigation of sprays it is common to introduce the following non dimension numbers:

Reynolds number $\qquad Re_{jet} = U_{inj}d_{nozzle}\rho_f/\mu_l,$ (2.1)

Weber number $\qquad We_{jet} = U_{inj}^2\rho_f d_{noz}/\sigma,$ (2.2)

Ohnesorge number $\qquad Oh_{jet} = \mu_l/\rho_f d_{noz}\sigma,$ (2.3)

where the indices l and g denotes the properties of the liquid and the gas phase, U_{inj} is the injection velocity, d_{nozzle} is the nozzle diameter and σ is the surface tension energy.

As Figure 2.2 shows, for primary breakup four different jet breakup regimes
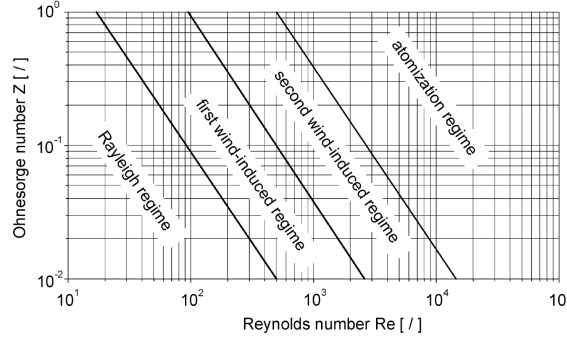
Figure 2.2: Spray regimes as function of Reynolds and Ohnesorge numbers [11]

are usually defined: I. the Rayleigh, II. the first wind induced, III. the second wind induced and IV. the atomization regime.

The Rayleigh breakup regime is controlled mainly by liquid inertia forces and surface tension. Breakup in this regime can be described by the growth of the axisymmetric surface perturbations. Drops are pinched off the jet when the perturbation amplitude equals the radius of the jet. In this regime the produced droplets are larger than the nozzle diameter.

If the injection velocity is increased, the jet will break up in the first wind induced regime. In this regime the velocities are high enough and aerodynamic stresses in result of liquid/gas interactions have significant influence on the primary breakup. The aerodynamic stresses add large wavelength disturbances to the jet which leads to a Rayleigh-Taylor instability. The droplets formed in this

regime are in the size of the nozzle diameter and the breakup length is larger than the nozzle diameter.

If the injection velocity is further increased the jet will break up in the second wind induced regime. Here the difference between the gas and the liquid velocity increases which leads to Kelvin Helmholtz instabilities. Due to the characteristic length scales of turbulence the perturbation covers a wide range of the spectrum and the breakup length and droplet sizes are small compared to the first wind induced regime.

When the injection velocity is large enough, the jet breaks up in the atomization regime. This is the most relevant regime for breakup of liquid fuels in engines. In this regime the droplets are much smaller than the nozzle diameter and they are produced immediately after the injector exit. The jet breakup in the atomization regime is mainly controlled by the turbulence level inside the jet and the aerodynamic stresses which both destabilize the liquid/gas interface. Former studies [2, 12, 13] showed that the surface instability on the liquid jet core has a critical role in the primary jet breakup process. These instabilities are investigated mainly by using linear stability analysis [14, 15], but recent studies [16] show that such a formulation is not sufficient for describing atomizing liquids under engine conditions or at high Reynolds numbers. Therefore there is a need to understand and model the interactions between two immiscible fluids in a turbulent environment.

3

One-Dimensional Turbulence

The goal of this chapter is to describe the variable density one-dimensional turbulence formulation used in this study. The formulation is not new per se but rather is a combination of previous formulations [17–20] and extensions to gas liquid multiphase flow.

The motivation for developing and adopting one-dimensional turbulence to simulate primary atomization can be explained by two main reasons. First, a one dimensional formulation enables affordable simulation of high Reynolds number turbulence over the full range of dynamically relevant time and length scales. Second, this approach reproduces diverse flow behaviors and permits high resolution of property gradients, which is needed to capture details of primary jet breakup.

The One-Dimensional Turbulence (ODT) simulation basically consists of these different mechanisms: I. Time advancement of mass, momentum, and energy along a 1D line of sight via standard transport equations, II. Turbulent advection via conservative mapping called eddy events, III. Eddy selection from an event rate distribution. These mechanisms will be discussed in following sections.

3.1   Time advancement in ODT

In this section, the equations governing temporal evolution of mass, momentum and energy on a $1D$ domain will be discussed. For a constant density flow in the absence of mean advection the momentum transport equation reduces to the diffusion equation. If the flow is incompressible, the diffusion equation can be written as,

$$\partial u_i(y,t)/\partial t = \partial \tau_{ij}/\partial x_j \tag{3.1}$$

where τ_{ij} denotes the Newtonian viscous stress tensor and is defined by

$$\tau_{ij} = -\nu(\partial_j u_i + \partial_i u_j). \tag{3.2}$$

In the current ODT implementations, the time derivative term is discretized using the Euler implicit first order time scheme based on the Thomas algorithm and the spatial discretization is based on the second order central difference scheme.

3.2   Eddy events

The one dimensional " eddy event " is the main mechanism in ODT to represent the advective term and eddy motion in turbulent flows. An eddy event includes a $1D$ mapping and a subsequent kernel transformations designed to mimic $3D$ physical processes and to preserve mass, momentum and energy on the $1D$ domain. The variable density formulation, which is the case in this study, needs additional kernel transformations to conserve momentum. These transformations will be discussed in next section.

The triplet map, maps a field $u(y,t)$ to $u(f(y;y_0,l)$ where

$$f(y) = y_0 + \begin{cases} 3(y - y_0), & \text{if } y_0 \leq y \leq y_0 + (l/3), \\ 2l - 3(y - y_0), & \text{if } y_0 + (l/3) \leq y \leq y_0 + (2l/3), \\ 3(y - y_0) - 2l, & \text{if } y_0 + (2l/3) \leq y \leq y_0 + l, \\ y - y_0, & \text{otherwise .} \end{cases} \tag{3.3}$$

as Figure 3.1 shows, the map parametrized by y_0 and l representing the position
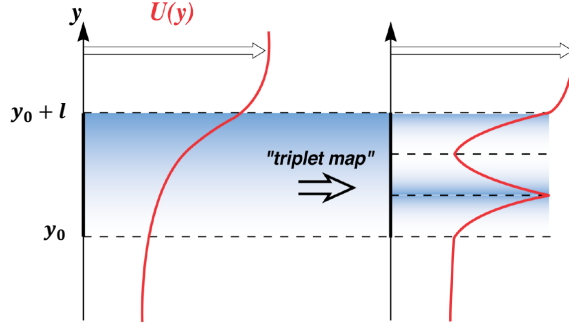
Figure 3.1: Triplet mapping mechanism

and length of an eddy acting on a $1D$ field. The triplet map mimics the characteristics of stretching and folding that are distinct processes governing turbulent flow. It induces a local reduction of length scales and the local strain increase geometrically.

Conceptually, the mapping takes the field on the interval $[y_0, y_0 + l]$ and compresses it to one-third of its original size. Three copies of the compressed field are used to replace the original field. Finally, the middle copy is inverted to preserve continuity. Outside the eddy range the profiles are unaffected by the eddy process. The triplet map is the the only possible re-arrangement of data to represent turbulent advection on a 1D line. However, due to its simplicity and its desired properties it is used in almost all ODT implementations.

The new formed vector $\hat{u}_i$ and scalar profiles $\hat{\phi}_i$ after the mapping event can be written as

$$\hat{u}_i(y,t) = u_i(f(y),t). \tag{3.4}$$

$$\hat{\phi}_i(y,t) = \phi_i(f(y),t). \tag{3.5}$$

3.2.1 Kernel transformations

The triplet map is measure preserving, which means that all integral properties (e.g. mass, momentum and energy) are the same before and after applying the map. There are features in fluid motion that influence kinetic energy in different

components and can not be captured directly by triplet mapping, equation (3.4). One of these mechanisms is pressure-velocity correlation which can not be seen explicitly by ODT and its effect should be modeled during the eddy events . One of the main effects of the pressure-velocity correlation in the turbulent flow is pressure strain or pressure scrambling term. The physical meaning of this term is how the energy is resdistributed among the velocity components or normal stresses. On the other word, the energy exchanged between velocity components must sum to zero, $\sum \Delta E_i = 0$. In ODT, this is modeled by exchanging energy between the three velocity components in a manner that emulates the pressure-velocity fluctuation interactions. To do so, instead of the simple map provided in equation (3.4) the velocity components are mapped as follows

$$\hat{u}_i(y,t) = u_i(f(y),t) + c_i K(y). \tag{3.6}$$

Here, the kernel $K(y) = y - f(y)$ is defined as the displacement of the fluid parcels due to the mapping process. The kernel is nonzero within the eddy range and integrates to zero so that it doesn't influence momentum conservation. To determine values for the kernel amplitudes we write down the kernel energy change for a given component due to mapping and kernel transformation,

$$
\begin{aligned}
\Delta E_{kin,i} &= \frac{1}{2}\rho_0 \int_{y_0}^{y_0+l} [(u_i(f(y),t) + c_i K(y))^2 - u_i(y,t)^2] dy \\
&= \rho_0 c_i \int_{y_0}^{y_0+l} u_i(f(y),t) K(y) dy - \frac{1}{2}\rho_0 c_i^2 \int_{y_0}^{y_0+l} K(y)^2 dy.
\end{aligned}
\tag{3.7}
$$

By introducing $u_{i,k} = \int_{y_0}^{y_0+l} u_i(f(y),t) K(y) dy$ and replacing $\int_{y_0}^{y_0+l} K(y)^2 dy$ with $\frac{4}{27} l^3$ as Ashurst et al. [17], the equation (3.7) summarizes to

$$\Delta E_{kin,i} = \rho_0 c_i l^2 u_{i,k} + \frac{2}{27}\rho_0 c_i^2 l^3. \tag{3.8}$$

The kernel amplitude, c_i is then determined from the solution of the quadratic equation (3.8),

$$c_i = \frac{27}{4l}\left(-u_{i,k} + \operatorname{sgn}(u_{i,k})\sqrt{u_{i,k}^2 + \frac{8}{27}\frac{\Delta E_{kin,i}}{\rho_0 l}}\ \right). \tag{3.9}$$

If no pressure scrambling is desired (i.e., $\Delta E_{kin,i} = 0$) we should have $c_i = 0$ and we recover the ODT triplet mapping formulation without kernel transformations, equation (3.4).

Pressure scrambling requires that the energy exchanged among components must sum to zero, $\sum_i \Delta E_{kin,i} = 0$. This requires finding the limited amount of energy that can be extracted from a given component. The maximum amount of energy that can be extracted from component i is obtained by differentiating equation (3.8) with respect to c_i and is given by

$$Q_i = -\Delta E_{kin,i}|_{max} = \frac{27}{8}\rho_0 l u_{i,k}^2. \tag{3.10}$$

If the constraint, $\sum_i \Delta E_{kin,i} = 0$ applies then the energy change for component i is given by a symmetric transformation of Q_i. That is, $\Delta E_{kin,i} = \alpha T_{ij} Q_j$. Here, T_{ij} is symmetric matrix and defined by

$$T_{ij} = \begin{cases} -1, & \text{if } i = j, \\ 0.5, & \text{if } i \neq j. \end{cases} \tag{3.11}$$

The parameter α determines the amount of kinetic energy that is redistributed to the velocity components. $\alpha = 0$ gives no and $\alpha = 2/3$ gives uniform redistribution. Inserting $\Delta E_{kin,i} = \alpha T_{ij} Q_j$ into equation (3.33) yields to a new formulation for the kernel amplitude, c_i,

$$c_i = \frac{27}{4l}\left(-u_{i,k} + \text{sgn}(u_{i,k})\sqrt{u_{i,k}^2 + \alpha T_{ij} u_{j,k}^2}\right). \tag{3.12}$$

On this basis, Figure 3.2 is an example to show how the kinetic energy is re-
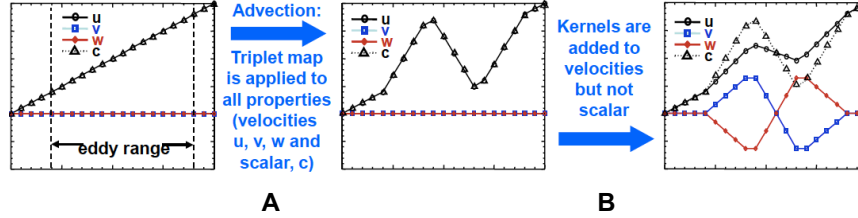

Figure 3.2: Triplet map and kernel mechanisms

distributed among velocity components by kernel mechanism. As seen in this plot, two different operations are shown by A and B; the operation A illustrates the affect of tripletmapping on the vector and scalar fields and the operation B shows the affect of kernel transformations on the velocity fields to achieve the

pressure scrambling criteria, $\sum_i \Delta E_{kin,i} = 0$.

Another example that deserves to discuss here is a buoyant flow where the potential energy has to be provided by reducing the kinetic energy of the velocity components. This requires that the energy change $\Delta E_{total} = \sum_i \Delta E_{kin,i} + \Delta E_{pot}$ be zero after each eddy event. Here, $\Delta E_{kin,i}$ is defined by equation (3.8) and ΔE_{pot} is the sum of all potential energy changes and is given by

$$\Delta E_{pot,g} = -g \int_{y_0}^{y_0+l} [\rho(f(y)) - \rho(y)]y\,dy = -g \int_{y_0}^{y_0+l} \rho(f(y))K(y)dy. \tag{3.13}$$

Good to mention, the Boussinessq approximation is adopted here and the variable density is counted only for gravitational term. We then define

$$\rho_K = \frac{1}{l^2} \int_{y_0}^{y_0+l} \rho(f(y))K(y)dy. \tag{3.14}$$

Now the total energy change of component i is written as

$$\Delta E_{tot,i} = \rho_0 c_i l^2 u_{i,k} + \frac{2}{27}\rho_0 c_i^2 l^3 - \beta_i g l^2 \rho_K. \tag{3.15}$$

where β_i is the potential energy partitioning coefficient and sum to unity. If the gravitational potential is partitioned with same portions among all components, we have $\beta_i = [\frac{1}{3}\ \frac{1}{3}\ \frac{1}{3}]^T$. The energy conservation implies $\sum_i \Delta E_{tot,i} = 0$. With accounting the availability of kinetic energy to exchange among components, $\Delta E_{total,i} = \alpha T_{ij}Q_j$; the kernel amplitude which conserves total energy can be computed by

$$c_i = \frac{27}{4l}(-u_{i,k} + \mathrm{sgn}(u_{i,k})\sqrt{u_{i,k}^2 + \alpha T_{ij}Q_j - \beta_i \frac{8}{27}\frac{lg\rho_K}{\rho_0}}). \tag{3.16}$$

In this work, we simulate multiphase flow where an eddy hits the phase boundary with different densities and the Boussinesq approximation not applies. Creating new faces by triplet mapping results in reducing the kinetic energy of the velocity components and increasing the surface tension energy respectively. This energy conversion should be counted for the momentum and energy conservation. As described above, conservation of energy implies

$$\sum_i \Delta E_{kin,i} + \Delta E_g + \Delta E_\sigma = \sum_i \Delta E_{tot,i} = 0 \tag{3.17}$$

ΔE_σ is the changes due to surface tension energy. This term will be discussed in detail in section 3.1.

For the variable density case Ashurst [17] proposed a new mechanism in ODT to conserve momentum and energy. The mapping transformation (equation (3.6)) now includes an additional Kernel transformation

$$\hat{u}_i(y,t) = u_i(f(y),t) + c_i K(y) + b_i J(y), \tag{3.18}$$

where

$$J(y) \equiv |K(y)| = |y - f(y)|. \tag{3.19}$$

To find a relation between the kernel amplitudes, c_i and b_i, we can write down the momentum conservation as,

$$\int_{y_0}^{y_0+l} \rho(f(y))[u_i(f(y),t) + c_i K(y) + b_i J(y)]dy$$
$$- \int_{y_0}^{y_0+l} \rho(y)u_i(y,t)dy = 0. \tag{3.20}$$

After some derivations we find that momentum conservation is obtained if the kernel constants are related by

$$b_i = (\rho_K/\rho_J)c_i = Ac_i, \tag{3.21}$$

where

$$\rho_K = l^{-2} \int \rho(f(y))K(y)dy \tag{3.22}$$

and

$$\rho_J = l^{-2} \int \rho(f(y))J(y)dy. \tag{3.23}$$

Then constant c_i is calculated by setting the kinetic energy change $\Delta E_{kin,i}$ to zero.

$$\Delta E_{kin,i} = \frac{1}{2} \int_{y_0}^{y_0+l} \rho(f(y))[u_i(f(y),t) + c_i K(y) + b_i J(y)]^2 dy$$
$$- \frac{1}{2} \int_{y_0}^{y_0+l} \rho(y)[u_i(y,t)]^2 dy. \tag{3.24}$$

After some manipulations we reach to,

$$\Delta E_{kin,i} = P_i c_i + S c_i^2, \tag{3.25}$$

Where we need following definitions:

$$P_i = l^2(u_{i,\rho K} - A u_{i,\rho J}), \tag{3.26}$$

$$S = l^3(\frac{1}{2}(A^2+1)\rho_{KK} - A\rho_{JK}), \tag{3.27}$$

$$u_{i,\rho K} \equiv l^{-2} \int_{y_0}^{y_0+l} \rho(f(y))u_i(f(y),t)K(y)dy, \tag{3.28}$$

$$u_{i,\rho J} \equiv l^{-2} \int_{y_0}^{y_0+l} \rho(f(y))u_i(f(y),t)J(y)dy, \tag{3.29}$$

$$\rho_{KK} \equiv l^{-3} \int_{y_0}^{y_0+l} \rho(f(y))K(y)^2 dy, \tag{3.30}$$

$$\rho_{KK} \equiv l^{-3} \int_{y_0}^{y_0+l} \rho(f(y))K(y)^2 dy, \tag{3.31}$$

$$\rho_{JK} \equiv l^{-3} \int_{y_0}^{y_0+l} \rho(f(y))J(y)K(y)dy. \tag{3.32}$$

The kernel amplitude c_i can be calculated by solving equation (3.17) which results in

$$c_i = 1/2S(-P_i + \text{sgn}(P_i)\sqrt{P_i^2 + \alpha \sum T_{ij}P_j^2 - 4\beta_i Sl^2 g\rho_K - 4\gamma_i S\Delta E_\sigma}) \tag{3.33}$$

Here $\text{sgn}(P_i)$ is the sign function, which ensures that c_i approaches zero for $\Delta E_{tot,i}$ approaching zero. The parameter α determines the amount of kinetic energy that is redistributed to the velocity components. $\alpha = 0$ gives no and $\alpha = 2/3$ gives uniform redistribution. The maximum amount of energy that can be extracted from component i is readily obtained by differentiating equation (3.25) with respect to c_i and is given by

$$Q_i = -\Delta E_{kin,i}|_{max} = P_i^2/4S. \tag{3.34}$$

β_i and γ_i are the potential energy and surface tension energy partitioning coefficients respectively. In this thesis, $\alpha = 2/3$ and γ_i is equal to $[\frac{1}{3}\frac{1}{3}\frac{1}{3}]^T$ because of equipartitioning of surface tension energy among all components.

3.3   The event rate distribution

We now discuss how to decide when and where an eddy event will occur and how big the eddy will be. ODT samples eddy events from an instantaneous distribution that evolves with the flow. The eddy event rate density (number of eddies per second per unit length) is assumed to be proportional to the inverse of an eddy time scale. Eddies of different sizes and locations have different turnover times and hence different event rates. The event rate density is defined to be

$$\lambda(t; y_0, l) = C/(l^2 \tau(y; y_0, l)).$$ (3.35)

It can be dimensionally described as $events/(location \times size \times time)$. The adjustable parameter C scales the overall eddy frequency and τ is the eddy time scale.

Therefore, the number of events per second for eddies located between y_0 and $y_0 + dy_0$ in the size range l to $l + dl$ becomes $\lambda(t; y_0, l)dy_0dl$.

The total eddy event rate on ODT line of length L is written as

$$\Lambda(t) = \int_0^L \int_{l_{min}}^l \lambda(t; l, y_0)dldy_0.$$ (3.36)

In continue, the eddy event probability density function (PDF) is defined by

$$P(t; l, y_0) = \lambda(t; l, y_0)/\Lambda.$$ (3.37)

Eddy occurrences are deemed to be a Poisson process in time with rate Λ. In principle, eddy occurrences can be sampled based on Poisson statistics, and the values (l, y_0) for each eddy can be sampled from the joint PDF, $P(l, y_0)$. In practice it would be computationally unaffordable to reconstruct the distribution every time an eddy event takes place and sample from it by numerical inversion.

To avoid the unacceptable cost of this procedure, a thinning method [21] is used. Therefore the next eddy event time is sampled from a Poisson process with the prescibed sampling rate, $\Lambda^* = 1/\Delta t_s \gg \Lambda$ where Δt_s is a given value. Then the trial eddies with different sizes and locations are sampled on the ODT line from a known distribution functions, $f(l)$ and $g(y_0)$. These distributions were discussed by McDermott [22] in detail. To accept or reject these trials a Monte-Carlo type method called "acceptance-rejection method" is used. In this method we accept the trial eddies with a probability proportional to the

difference between the two distribution functions. This probability is defined by

$$P = \frac{\lambda(l, y_0)}{\Lambda^* f(l) g(y_0)} = \frac{\lambda \Delta t_s}{f(l) g(y_0)} = \frac{C \Delta t_s}{l^2 \tau f(l) g(y_0)}.$$ (3.38)

We should always ensure that $\Lambda^* = 1/\Delta t_s \gg \Lambda$. This is enforced within ODT by oversampling that is adjusted using a target mean acceptance probability $\bar{P}$.

Finding λ by equation (3.35) needs determination of the eddy time scale. This can be done by constructing the eddy energy definition dimensionally from the characteristic length and time scales,

$$E \simeq 1/2 \rho_0 l (l/\tau)^2,$$ (3.39)

where l is the eddy size and τ is the eddy time scale.

As we will be using the time scale in equation (3.35) it is convenient to rearrange equation (3.39) to

$$1/\tau = C \sqrt{2E/\rho l^3}.$$ (3.40)

E shows the eddy energy balance, this means that an eddy contains different energetic budgets and they can be written as

$$E = E_{kin} + E_{model} - E_{viscous}.$$ (3.41)

On the right hand side, the first term is the final value of all the available kinetic energy, and the second term shows all the modeled energy terms, e.g. surface tension energy, buoyancy potential energy, and the last term denotes the viscous cutoff which suppresses unphysically small eddies.

3.3.1 The viscous cutoff

In the case of full variable density, it is convenient to use ρ_{KK} for the eddy density to find E_{visc}, equation (3.30). Then, we can construct a viscous energy scale as

$$E_{visc} \sim 1/2 \rho_{KK} l (l/\tau_v)^2.$$ (3.42)

The viscous time scale τ_v is calculated by

$$\tau_v = l^2/\nu,$$ (3.43)

where ν is the kinematic viscosity. In the variable density formulation we choose to use $\nu = \bar{\mu}/\rho_{variable}$ for the viscosity where

$$\bar{\mu} = (1/l \int_{y_0}^{y_0+l} 1/\mu(y)dy)^{-1}.$$

(3.44)

Finally we obtain the viscous cutoff term

$$E_{visc} = Z^2 \bar{\mu}/(2\rho_{variable}l).$$

(3.45)

where Z is another ODT tuning parameter.

3.4   Coupling sampling and transport mechanisms

One of the more confusing aspects of ODT to new users is how the eddy event sampling procedure is to be coupled with the temporal integration of the transport equation. Here we will present a simple algorithm for constant density transport of the scalar u with transport coefficient ν. This algorithm is shown in Figure 3.3. There, $N_{realization}$, N_{stat}, N_{tseg} represent the number of realizations, the number of averaging periods and the number of snapshots within each period, respectively. The time step for the next eddy sampling is sampled from a Poisson distribution P with mean time step $1/\Delta t_s$.

Inititizalization

for $N_{realization}$

    Inititizalize realization

      for N_{stat}

        for N_{tseg}

          $t_{Mark} = t_{Mark} + t_{End}/(N_{stat}N_{tseg})$

            while $(t < t_{Mark})$

              if $(t - t_0) \geq dt_{CU}$

                  Diffusion *step for* $\Delta t = t - t_0$

                  $t = t_0$

              else

              Sample the next eddy

              if *(eddy is accepted)*

                  Implementation of the eddy

                  Diffusion *step for* $\Delta t = t - t_0$

                  Adjust Δt_s *if needed to match the oversampling*

                  $t = t_0$

              else

              $t = t + P (1/ \Delta t_s)$

            Diffusion *step for* $\Delta t = t - t_0$

            $t = t_0$

          Post *processing of subinterval*

       Post *processing of main interval*

     Post *processing of realization*

Post *processing*

Figure 3.3: ODT evolution algorithm

4

Primary breakup modeling in ODT

This chapter describes how One-Dimensional Turbulence is used to model relevant mechanisms that result in primary breakup. As discussed previously, breakup of a liquid jet is caused by instabilities that are caused by aerodynamic forces acting on the jet surface, turbulent motions inside the liquid, interfacial Rayleigh waves and cavitation. Capturing these mechanisms by ODT needs further extensions to the model discussed in previous chapter.

4.1   Surface tension modeling in ODT

Unbalanced cohesive forces at the liquid/gas interface lead to surface tension forces. According to an ODT based energetic view, this can be written as a volumetric energy density E_σ and is defined by

$$E_\sigma = \sigma \alpha, \tag{4.1}$$

where σ represents surface tension energy coefficient per unit area and α is the surface area per unit volume. To evaluate α for a given density number of inter-

faces along a line of sight, the interface is assumed to be a statistically isotropic random interface.

Because interfaces in ODT are isolated points on a line, geometric interpretation is required to obtain the area increase. In cases with surfaces that are highly wrinkled, local isotropy is closely approximated [23, 24]. Because of this, interfaces in our model are treated as random isotropic surfaces. On this basis, geometric analysis shows [25] that the number density n of interface intersections along a line of sight per unit length corresponds to an interface surface area α per unit volume of $2n$. This allows the volumetric energy density of a homogeneous, isotropic interface with surface tension σ to be expressed in the form

$$E_\sigma = 2\sigma n. \tag{4.2}$$

We introduce an additional variable which contains a marker of the phase for each cell to track the liquid-gas boundries. In addition, the diffusion process must be modified for two-phase flows. The velocity at the interface is obtained by having two conditions: 1) the velocities have to be identical on either side of the interface, i.e. $U^l = U^g$. 2) the tangential stress have to be same on either side of interface,i.e. $\mu^l \partial_y U^l = \mu^g \partial_y U^g$.

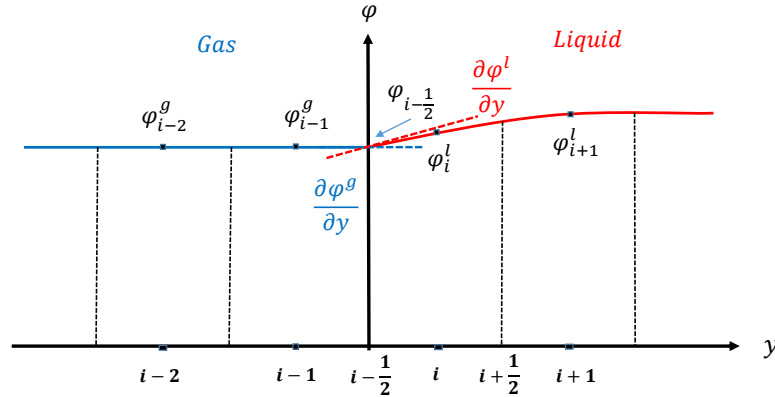As Figure 4.1 shows, these fluxes can be calculated at the interface location,

Figure 4.1: Sketch of phase interface between two immiscible fluids, φ_i is the value of property

resulting in the following equations,

$$\varphi_{f_i} = \frac{\varphi_i^l + \varphi_{i-1}^g \frac{y_i - y_{i-\frac{1}{2}}}{y_{i-\frac{1}{2}} - y_{i-1}} \frac{\mu_g}{\mu_l}}{1 + \frac{y_i - y_{i-\frac{1}{2}}}{y_{i-\frac{1}{2}} - y_{i-1}} \frac{\mu_g}{\mu_l}} \tag{4.3}$$

$$\partial \varphi_g / \partial y = \frac{\varphi_{i-\frac{1}{2}} - \varphi_{i-1}^g}{y_{i-\frac{1}{2}} - y_{i-1}} \tag{4.4}$$

$$\partial \varphi_l / \partial y = \frac{\varphi_i^l - \varphi_{i-\frac{1}{2}}}{y_i - y_{i-\frac{1}{2}}} \tag{4.5}$$

Generally, in ODT there are two possibilities for two phase eddies: 1) an eddy located at the jet boundary containing one interface, 2) an eddy containing the whole jet. Due to the triplet map implementation these number of interfaces are tripled as shown in Figure 4.2 for an eddy that contains one interface. When the triplet map operates, the number of interfaces within the eddy inter-
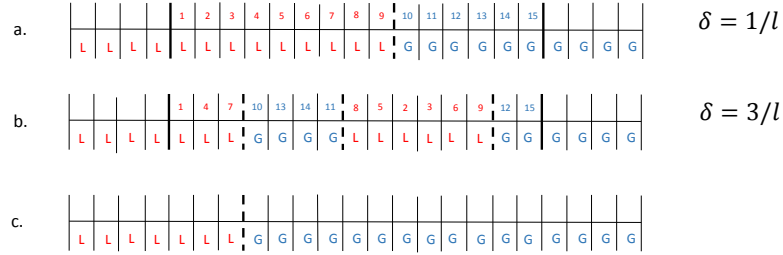
Figure 4.2: Multiphase eddy in ODT. (a) The spatial region between the thick solid lines is selected for eddy implementation. It is a multiphase eddy containing both phase L and G separated by one phase interface (thick dashed line). The spatial distribution of phase indices is time advanced only by triplet mapping. (b) A triplet map is implemented, illustrated by the reordering of cell indices within the eddy, resulting in three phase interfaces. (c) The newly formed droplet is re- moved and replaced by gas.

val is changed from N to N', and the surface tension energy change becomes

$\Delta E_\sigma = 2\sigma(N' - N)$, where N shows the density number of interfaces per length before and N' is the number of interfaces after triplet mapping.

As a result, based on the main hypothesis of the turbulent breakup theory, drops are formed from turbulent eddies when the kinetic energy of radial fluctuations of the eddy is larger than the surface energy required to form a drop of corresponding size. In terms of ODT, surface tension energy change can be explained as sink of the kinetic energy with the value equal to $-\Delta E_\sigma$. Therefore, as described in section 3.2.1, surface tension energy change, $(-\Delta E_\sigma)$ should be included in energy conservation equation (3.17) and also equation (3.33) to find the kernel amplitudes c_i, and b_i.

4.2 Rayleigh breakup regime in ODT

Rayleigh breakup of a liquid jet was first described by Plateau [26] and Lord Rayleigh [27] more than a century ago. A small surface disturbance will grow untill its amplitude exceeds the circumference of the jet and causes the jet to break. The optimum wave length for an inviscid liquid jet is expressed as $\lambda_{opt} = 2\sqrt{2}\pi r$ and is determined by the jet radius only [27]. The system automatically selects this optimum wave length and breaks up into fixed fragments of volume $\lambda_{opt}\pi r^2$.

ODT conserves properties along a transverse line at fixed x/d and has no inherent capability to represent the stream wise energy transfers associated with Rayleigh wave propagation.

In this context, it is simplest to incorporate the effect of Rayleigh wave energy by adding a corresponding available-energy term to the rate expression. As discussed earlier, in ODT the rate expression used to compute acceptance probabilities is motivated by eddy length and time scale. The same phenomenology is encapsulated in the Rayleigh time scale $\tau \sim (\rho l^3/\sigma)^{1/2}$, where ρ is the liquid density, σ is the surface tension, and τ can be interpreted as the time required for the amplitude of the Rayleigh wave reach size local jet size l. Wu et al. [28] proposed that τ is the time required for a size l droplet to form and detach.

On this basis, we proposed that the rate expression 3.39 should have an additional Rayleigh term $R = A(l/\tau)^2$, where A is an adjustable parameter, only for eddies that completely contain a liquid region, whose size is denoted as l. The usual rate expression with inclusion of Rayleigh wave energy then becomes $E = E_{Rayleigh} + E_{Kinetic} - E_{Surfacetension} - E_{Visc}$, representing Rayleigh energy,

kinetic energy, surface tension energy, and viscous penalty respectively. The ODT analog of this breakup mechanism is an eddy event containing the entire jet, which breaks the entire liquid region into three equal sized parts. In the current study, the simulation is terminated upon first occurance of a Rayleigh breakup event.

A trial Rayleigh eddy has an available energy $E_{Rayleigh}$, but this energy budget is based on a mechanism not represented whithin ODT line advancement. Therefore $E_{Rayleigh}$ should have no role in energy redistribution during implementing a Rayleigh eddy.

4.3   Shear-Driven Breakup within ODT

When values of jet exit Weber number significantly exceed 10^5, the turbulent liquid column or liquid core breakup mechanism is changed. At these condition turbulence distorts the liquid jet to a much greater degree than the jet diameter, leading to an aerodynamic turbulent liquid column breakup mechanism.

   Studies [14] showed that in that range aerodynamic effects at the liquid/gas interface do not have a significant influence on liquid phase velocities and turbulent properties prior to breakup: As noted by Sallam et al. [14] aerodynamic effects become important only when the liquid jet is in cross flow. For a jet with axial gas co-flow, this cross flow configuration arises when the jet undergoes large scale distortions due to large-scale instabilities.

Regarding the model implementation, in a place of the gas uniform cross-stream velocity, matching the liquid velocity at each phase interface, the uniform velocity profiles are replaced by a linear velocity profiles with slope S, where S is an adjustable parameter (Figure 4.3). Consequently, The new available kinetic energy based on the new velocity profile is calculated and updates equation (A.11) which influences the eddy acceptance probability.
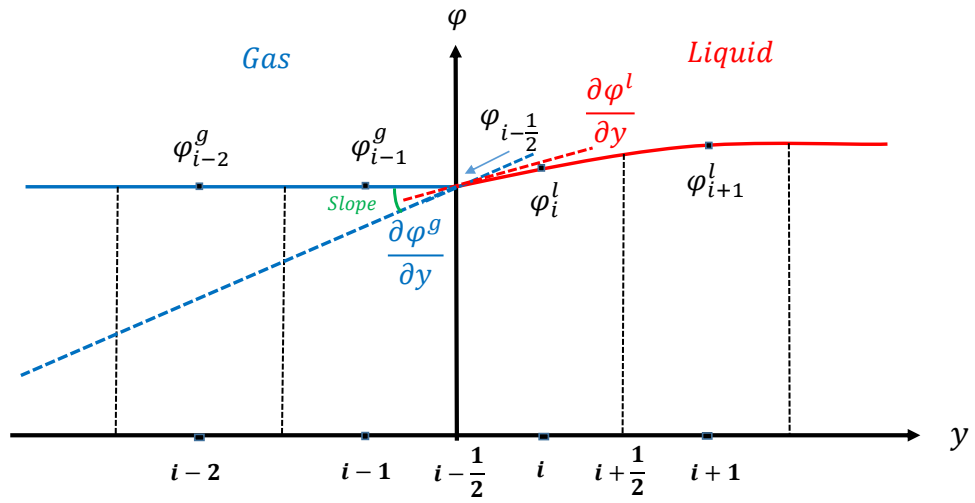
Figure 4.3: Sketch of phase interface between two immiscible fluids, solid blue line shows the old gas cross-stream velocity profile and blue dashed line shows new gas cross-stream velocity profile with slope S

5
Model assessment

Primary atomization of turbulent liquid jets is the process by which shear, turbulence and flow instabilities in a turbulent multiphase environment cause a liquid jet to be broken into smaller structures, which will then disintegrate further into dispersed drops, Figure 5.1. This process is critical to combustion applications, in which fine sprays are necessary to enhance evaporation of the liquid fuel to a gaseous state.

Depending on the application, a number of strategies can be employed to achieve efficient atomization in technical devices. In particular, two strategies are often encountered: either the liquid is accelerated to high velocities and injected into pressurized gas, as is done in direct injection systems, or the liquid fuel is injected at relatively low speeds with a coflow or cross flow of high speed gas, which is known as air blast atomization. This work investigates the former strategy, i.e. direct injection systems, where most of the momentum is carried by a highly turbulent liquid jet. Turbulent interfacial flows fluctuate on a broad range of length and time scales. This property makes the affordability of detailed numerical simulations of interfacial flows, e.g. direct numerical simulation (DNS) or highly resolved LES, challenging. A One-Dimensional
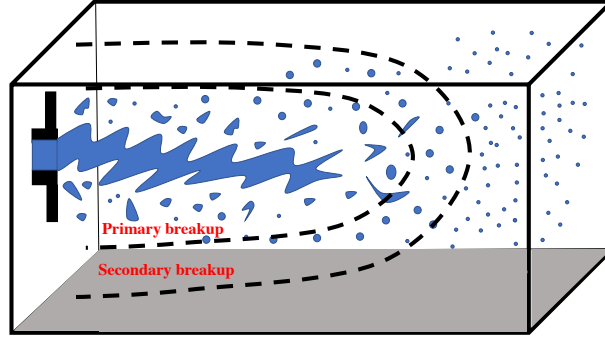
Figure 5.1: Liquid jet atomization regions

Turbulence (ODT) model is considered here as an affordable model for simulating liquid jet primary atomization at high Reynolds and Weber numbers. This chapter describes the steps taken to assess the ODT model as a new primary breakup model.

5.1 Simulation setup
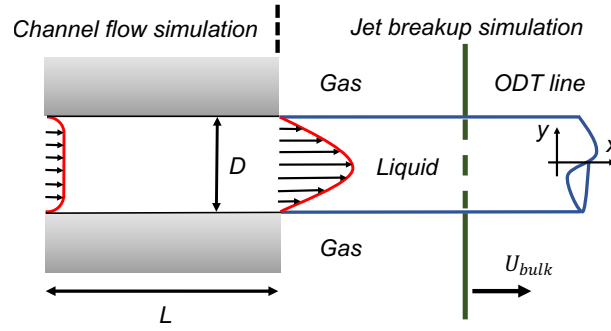
Figure 5.2: Liquid jet simulation setup

The simulation setup adopted in this work is illustrated in Figure 5.2. The ODT domain represents a lateral line of sight through the jet, which is assumed to be planar, and extends into the gaseous region on each side of the jet. The

ODT domain is treated as a Lagrangian object advected downstream with the liquid bulk velocity U_{bulk}.

As discussed in chapter 3, the property fields defined on the 1D domain evolve according to two mechanisms: (1) molecular diffusion and (2) a sequence of mapping operations, denoted eddy events, which represent the advection term in the Navier-Stokes equations along the ODT line.

In all cases studied here, the ODT simulation consists of two parts : a short temporal channel section (Figure 5.2 "channel flow simulation") and the jet section (Figure 5.2 "jet breakup simulation"). The simulation starts from a fully developed turbulent channel flow profile. The Dirichlet (no-slip) boundary condition is applied to the velocity components during the channel section. The channel flow is simulated for a time duration of $t = L/U_{bulk}$, where L denotes the channel length and U_{bulk} represents the bulk velocity. At this point the current flow properties are saved as new restart profiles for the next realization of the channel flow and are used as initial conditions for the jet portion of the simulation. The switch to jet simulation is done by changing the boundary condition of the current realization from no-slip to a Neumann (free-slip) boundary condition and increasing the domain length to 3D where D is the channel width. The domain length should be large enough so that the finite size of the domain does not affect the results; we found that a factor of 3 works well for the simulations considered here. The newly extended domain is initialized by stagnant air at the standard conditions. The optimization of the ODT parameters, C and Z is discussed in the next section.

5.2   Liquid jet with no breakup

Before investigating jet breakup behavior, the development of the turbulent intensity in the jet prior to breakup is examined. This ensures that the ODT model is capable of correctly predicting the level of turbulence prior to breakup within the jet. In practice, this requires a parameter study to optimize ODT model parameters C and Z to improve the simulation results compared to experiments. As discussed in chapter 3, C and Z are the ODT global parameters which have been kept constant for the liquid jet simulation both with and without breakup. More details of this parameter calibration is reported in Meiselbach [29] and Movaghar et al. [30].

5.3 Primary breakup regimes

Primary breakup of liquid jets in still gases at standard conditions have been studied experimentally since many years, for example Dai et al. [31, 32], Tseng et al. [33], Wu et al. [28, 34–36], Faeth et al. [37], Sallam et al. [14, 38, 39]. These studies used pulsed shadowgraphy and holography to measure the properties of turbulent primary breakup and showed that aerodynamic effects are small for liquid/gas density ratios greater than 500 (which is typical of injection of liquids into air and other light gases at NTP). This finding holds true except far from the jet exit where aerodynamic effects become strong due to the surrounding gas. They also showed that drop size distributions after turbulent primary breakup satisfied the universal root/normal distribution of simmons [40] and were completely defined by the Sauter mean diameter (SMD). Furthermore, drop velocities after turbulent primary breakup were independent of drop size and were instead related to mean velocities of the liquid at the jet exit. In addition, the SMD of drops after turbulent primary breakup progressively increased with increasing distance along the liquid surface and could be correlated by the Weber number based on simplified phenomenological analysis.
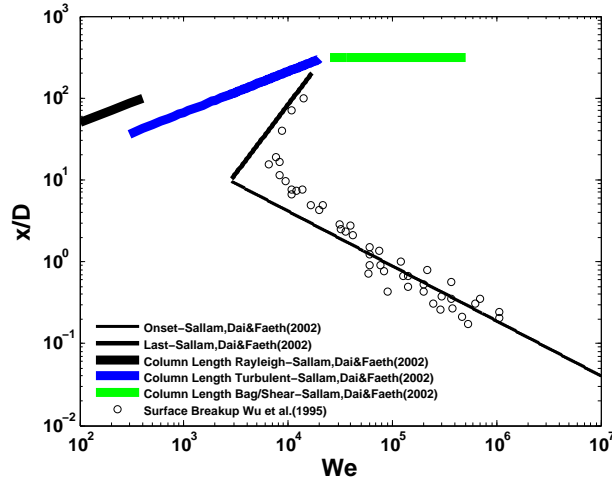

Figure 5.3: Breakup regime map

Further studies by Sallam et al. [14, 38] resulted in a breakup regime map

as shown in Figure 5.3. The map primarily devides the flow into surface and no surface breakup regimes. As illustrated in Figure 5.3, for $We < 5200$ the jet does not experience surface breakup which corresponds to the Rayleigh regime and the first wind induced breakup regime (Fig 2.2). For $5200 < We < 17000$ the liquid jet undergoes both onset and end of surface breakup before the liquid column breaks up as a whole. When the Weber number exceeds 17000, the turbulent liquid jet surface breakup begins progressively closer to jet exit, eventually reaching the atomization breakup regime where surface breakup starts close to the injector exit.

In addition to the surface breakup modes, three further modes of liquid column breakup are shown in Figure 5.3.

1- Weakly turbulent liquid column breakup (▬▬):

This mode occurs when the liquid jet Weber number (We) is lower than 500. For such conditions, the liquid column is not significantly distorted by turbulence and distortion of the liquid column is generally axisymmetric and involves Rayleigh-like breakup of the liquid column.

2 - Turbulent liquid column breakup (▬▬):

When the liquid turbulence at the jet exit is reasonably developed (Re > 10000) and the Weber number is high enough, this causes the liquid jet surface to become distorted in the cross stream direction. This process continues until the liquid jet fully breaks.

3- Aerodynamic/shear breakup (▬▬):

When the liquid jet Weber number (We) exceeds 17000, the small eddies seen close to the injector exit have already decayed. Thus, far downstream what remains are large-scale distortion of a nearly non turbulent liquid jet. These large scales place most of the liquid column elements in cross flow direction which gets distorted finally due to strong interfacial shear.

To assess the predictability of ODT to capture the various primary breakup modes, ODT simulations based on the discussed experimental conditions were carried out. The results are reported and discussed by Movaghar et al. [30] and Kerstein et al. [41] in detail.

5.3.1   Cases with high liquid/gas density ratio

Wu and Faeth [28] showed experimentally that aerodynamic phenomena for turbulent primary breakup are largely controlled by the liquid/gas density ratio. When this ratio is less than 500, aerodynamic phenomena affect the onset
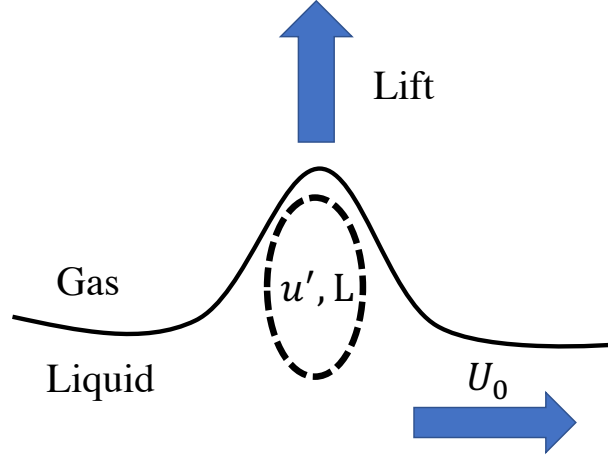
Figure 5.4: Liquid jet atomization

location of breakup, droplet sizes and velocities just after breakup. Figure 5.4 illustrates how lift enhances interfacial distruption and creating smaller droplets. In Figure 5.4, L is the turbulent eddy size, u' the turbulent eddy velocity, and it is assumed that the liquid structure moves at the bulk jet velocity U_0. Therefore, the followings scalings can be written:

- Kinetic energy of the liquid structure : $E_K \sim \rho_l u'^2$
- Energy through aerodynamic lift: $E_L \sim \rho_g U_0^2$
- Energy associated with surface tension: $E_{ST} \sim \sigma/L$

E_L and E_K need to overcome E_{ST} in order to lead to breakup. If the density ratio (ρ_l/ρ_g) is large, then it is justified to neglect aerodynamic lift. The important effects are then the turbulent kinetic energy and surface tension. For $E_K > E_{St}$, the interface is expected to deform. If the density ratio is small, then E_L will contribute to destabilizing the interface, enabling the creation of smaller droplets.

In this work, simulations with high liquid/gas density ratio, ($\rho_l/\rho_g > 500$, were limited to water injection into still air. Simulations were performed for the turbulent planar jet with jet exit liquid Weber numbers in the range $We = 10^2 - 10^7$ and for bulk Reynolds numbers of $Re_{bulk} = 11500$, 23000, 46000 and 92000. The simulation conditions are summerized in Table 5.2. Results were compared with Wu and Faeth [42] and Sallam et al. [14, 39].

Parameter	Value	
	Baseline	Variations
μ_l	8.94×10^{-4} kg/ms	$[4.47 - 17.88] \times 10^{-4}$ kg/ms
μ_g	18.5×10^{-5} kg/ms	$9.25 \times 10^{-5} - 37 \times 10^{-5}$ kg/ms
D	10.2 mm	10.2 mm
u_{bulk}	2 m/s	$[1,2,4,8]$ m/s
ρ_l/ρ_g	860	$16 - 860$
Re_{bulk}	23000	$11500, 23000, 46000, 92000$
We	10^7	$10^2 - 10^7$
Oh	0.0138	$0.0034 - 0.0138$

Table 5.1: Summary of simulation conditions for the liquid jet

The main results of this study are summerized in a breakup regime map, Figure 5.5. The plotted model results correspond to the baseline conditions shown in Table 5.1 except for We and Re_{bulk}, which vary as indicated in the plot. The vertical axis shows the axial position x normalized by the jet diameter (x/D). Onset, and column length refer to the location of the onset of breakup, i.e. the axial position of the first multiphase eddy, and the length of the liquid core respectively. Wu et al. [36] and Sallam et al. [14] suggested correlations for the onset and the length of the liquid core in terms of the liquid Weber number $We = \rho_l D u_0^2 / \sigma$, where ρ_l is the liquid density, u_0 is the average liquid velocity at the jet exit, and σ is the surface tension of the liquid. Three modes of liquid-column breakup were identified by Sallam et al. [14] for turbulent round liquid jets. As described in section 5.3, these modes are a weakly turbulent Rayleigh-like breakup mode observed at low jet exit Weber number, a turbulent breakup mode observed at moderate jet exit Weber number, and an aerodynamic bag/shear breakup mode observed at high jet exit Weber number. The breakup-length correlation shown by Sallam et al. [14] for each of these mechanisms is illustrated in Figure 5.5. ODT model simulation results are shown for both the median and the most probable location based on an ensemble of 1000 realizations for each Weber and Reynolds number, indicated in Figure 5.5 by solid and dashed lines, respectively. Since there is no clear indication that the correlations suggested by Sallam et al. [14] are based on the mean, most probable, or other locations statistic, both statistics are presented.

The results and validations compared to experiments including liquid breakup
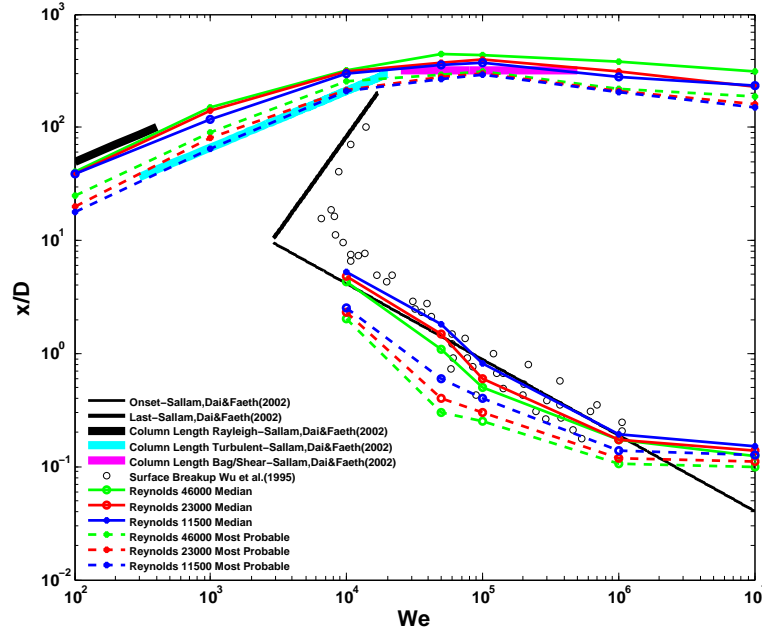
Figure 5.5: Breakup regime map.

lengths and turbulent breakup properties are presented in papers I and III. The major conclusions of this study follows:

- After parameter adjustments, column-breakup results reported formerly by Sallam et al. [14] and Wu et al. [36] encompassing the weakly turbulent Rayleigh-like breakup, turbulent breakup, and aerodynamic bag/shear breakup regimes. ODT model simulations reproduced the behaviors of experiments and correlations reported in the literature.

- Results for the onset of droplet breakup based on both ensemble averaging and most probable locations agree well with experiments in the range of Weber numbers [10^4 - 10^6].

Droplet statistics   To further elucidate the parameter dependences of droplet sizes and velocities, scatter plots of normalized droplet axial velocity against diameter from ODT model simulations and experiments are shown in Figure 5.6.
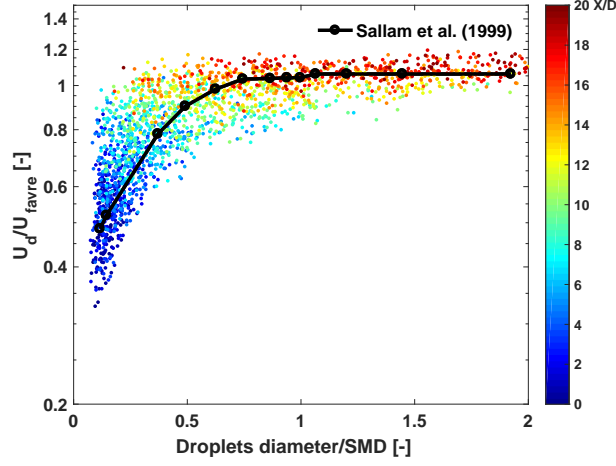
Figure 5.6: Scatter plot of droplet axial velocity, normalized by the favre velocity, versus diameter. The color indicates the distance from the jet inlet.

The velocities in this plot are normalized by the mass-weighted (Favre) averaged droplet velocities, U_{Favre}, while the drop diameters are normalized by the SMD. Color is used to indicate the axial location at the instant of droplet formation in the ODT simulation.

Values of U_d are seen to increase in magnitude with increasing d initially and then remain nearly unity in both ODT model simulations and experiments. The scatter plot Figure 5.6 shows that droplets close to the jet inlet have lower axial velocities than droplets farther downstream. This can be explained by the influence of the flow profile of the jet at the jet inlet plane: in the near field the velocities inside the liquid jet near the liquid-gas interface are still dominated by the boundary layer profile leading to low velocities in the droplet-generating region near the interface. Further downstream, radial turbulent transport within the jet tends to homogenize the lateral profile of the axial velocity, thereby increasing it near the liquid-gas interface.

5.3.2 Cases with low liquid/gas density ratio

We performed further simulations of a turbulent liquid jet injected into stagnant dense air to assess the predictability of ODT as a primary breakup model where

Parameter	Value
μ_l	1.7×10^{-3} kg/ms
μ_g	1.78×10^{-5} kg/ms
D	100 μm
u_{bulk}	100 m/s
ρ_l/ρ_g	34
Re_{bulk} (Reynolds)	5000
We (Weber)	17000
Oh (Ohnesorge)	0.026

Table 5.2: Simulation conditions for the case with low liquid/gas density ratio.

the liquid/gas density ratio is low. The simulation results were validated by comparison with the from DNS study of Herrmann [43]. Figure 5.7 shows the cyclindrical DNS computational domain used in this study. It extends 20 inlet diameters D downstream of the jet inlet and 8 diameter in the radial direction.
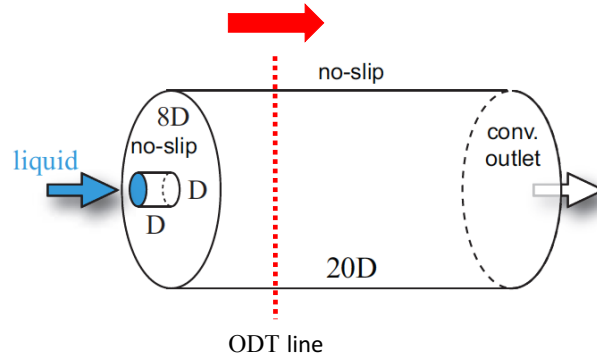
Figure 5.7: DNS and ODT computational setup

In the DNS computations no-slip boundary conditions are used on all boundary faces, except for a convective outflow at the right boundary and an inflow boundary condition at the injector pipe inlet. To represent accurately the turbulence of the liquid at the inlet, a DNS of a single-phase periodic pipe flow was performed using the injector-flow Reynolds number $Re_{bulk} = 5000$. The DNS results were stored in a database and then used as inflow boundary conditions for the atomization simulation. Table 5.2 summarizes the operating conditions

used in the ODT and the DNS simulations. The gas phase is initialized being
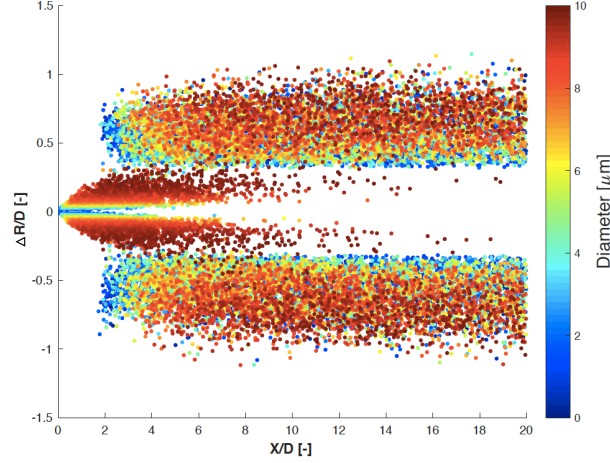
Figure 5.8: ODT droplet spatial distribution, where the ordinate is the distance ΔR of a droplet from the jet perimeter immediately after droplet formation, scaled by D is the nozzle diameter, and the color bar indicates the droplet diameter.

motionless.

Figure 5.8 shows a scatter plot summarizing the simulation results, where the lateral location is defined as the distance ΔR of the droplet from the liquid/gas interface immediately after droplet formation.

The sizes of droplet-forming ODT eddy events can be inferred from the $\Delta R/D$ values from the simulations. The small $\Delta R/D$ values in the near field reflect the persistence of the channel-flow inlet condition over some x/D range. The thin boundary layers at the edges of the channel flow evolve into regions of high liquid shear in the vicinity of the jet perimeter, albeit decaying due to turbulent transport that spreads velocity fluctuations laterally and droplet generation that removes strongly sheared liquid from the jet, in effect peeling away the boundary layer. This flow structure generates eddies comparable in scale to the thin high-shear regions. Some of these eddies generate droplets at locations that are relatively close to the jet perimeter as seen in Figure 5.8, which also shows the gradual reduction of this tendency with increasing x/D.

Farther downstream $(x/D > 10)$, a transition to droplet formation by larger

eddies occurs. This is consistent with the decay of the initial shear layers and increasing droplet formation by larger eddies, whose contribution is delayed due to the relatively long turnover times of these eddies. Both liquid bulk turbulence and aerodynamic shear can contribute to the occurrence of such eddies. Our results suggest that many of the droplets that are generated in the far field are small relative to the size of the eddies that produce them. These eddies are thus located primarily in the gas phase, and hence driven largely by aerodynamic shear, which is an important cause of far field droplet generation.
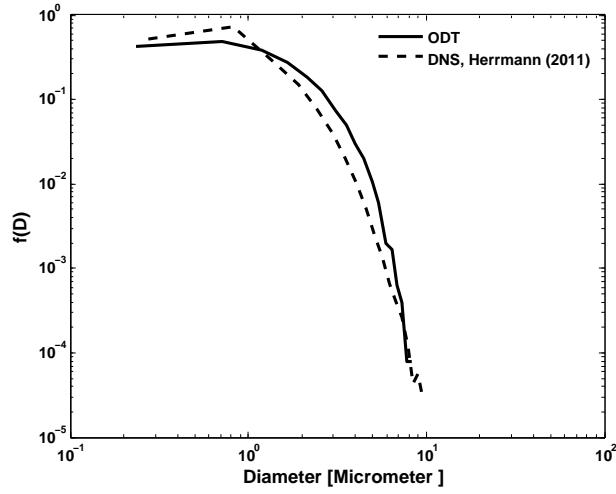
Figure 5.9: Droplet size distribution.

One of the main outputs of the primary-breakup simulations are droplet-size distributions. Figure 5.9 shows the droplet-size probability density function $f(D)$ resulting from primary breakup in DNS and ODT simulations compared to experimentally measured droplet sizes. The results of our simulation qualitatively match the experimental measurements, providing further validation of our model's utility.

5.3.3 Cases under real engine conditions

As discussed earlier, ODT can generate a distribution of droplet sizes and velocities which could be used as inputs for a standard Lagrangian spray model in RANS or LES simulations.

Parameter	ECN-Spray G	ECN-Spray A
Fuel type	$Iso-Octane$	$n-dodecane$
Fuel density	$669 \, kg/m^3$	$744 \, kg/m^3$
Nozzle diameter	133 μm	90 μm
Injection pressure	200 bar	1500 bar
Injection mass	13.6 mg	3.6 mg
Injection duration	780 μs	1.5 ms
Ambient gas density	$3.5 \, kg/m^3$	$22.8 \, kg/m^3$
Ambient gas pressure	0.6 Mpa	6 Mpa
Discharge coefficient	0.49	0.86

Table 5.3: Operating conditions.

Under real engine conditions, the liquid jet Reynolds and Weber number is quite high,(e.g. : ECN Spray A, $Re \sim 25000$, $We \sim 700000$) and fully resolving the breakup is not feasible computationally with DNS and LES simulations. In current industrial approaches instead of simulating primary breakup, a physical model is used which often imposes very large drops (or blobs) with specific momentum as the liquid fuel inlet condition. The blobs then break up into finer droplets and vaporize using accepted droplet breakup and vaporization models. These physical models for primary breakup contain parameters that are typically adjusted to match experimental results. To improve the accuracy in combustion models, a more general and portable physical model of the primary spray breakup process is needed, which requires more detailed investigation of the near field of the spray.

To validate the capability of ODT as a model for primary breakup in a standard Lagrangian spray simulation, ECN spray A and G are investigated here using a RANS turbulence model. Table 5.3 summarize the operating conditions used in the simulations. This approach is currently under study and outcomes will be a part of discussions in future publications.

6

A statistical study of turbulence/surface tension interaction

The liquid jet atomization encompasses different mechanisms. One way to understand them is by isolating different physical mechanisms relevant to to the atomization process. As a start point, we isolate the interplay between surface tension and fluid inertia by instering a single interface into in a decaying field of homogeneous isotropic turbulence. The simulations consist of identical fluids both above and below an initially flat interface. Such a configuration has been studied formerly by other researchers and can be regarded as a canonical flow configuration for the local interaction of turbulence and interfaces.

Trontin *et al.* [44] isolated the interaction between fluid inertia and surface tension in a box of three-dimensional decaying homogeneous turbulence and studied anisotropic effects of surface tension on the surrounding turbulence. Studies conducted by McCaslin *et al.* [16, 45], in a case similar to [44], showed that surface tension increases energy in the flow field at small scales and that interface corrugations are greatly suppressed at length scales smaller than the

surface tension cutoff length scale.

The investigations here were carried out using DNS performed by CTFlab at Cornell university and ODT. This work can be seen as an assessment for the ability of ODT to capture the interface breakup validated by DNS data.

6.1   Setup

The studied case evolves in two stages. First, the free decay of turbulence is simulated until it reaches the homogeneous isotropic turbulent (HIT) state. During this stage of the simulation S_{u_i} is equal to zero. After reaching HIT, an interface is inserted at the desired Taylor-microscale Reynolds number $Re_{\lambda_g} = u_{rms}\lambda_g/\nu$, where u_{rms} denotes the root-mean-square velocity fluctuation and $\lambda_g = \sqrt{10}(\eta^2 L_{int})^{1/3}$ is the Taylor microscale. Here, η is the Kolmogorov length scale and L_{int} is the characteristic length scale of the large eddies. In terms of the turbulent kinetic energy (TKE) k, which is $k = \frac{3}{2}u_{rms}^2$ for isotropic turbulence, and the TKE dissipation rate ε, these length scales are $\eta = (\nu^3/\varepsilon)^{1/4}$ and $L_{int} = k^{3/2}/\varepsilon$. In order to focus on turbulence-interface interactions, the same density and dynamic viscosity are assigned for both phases and a phase marker is used to identify each of them.

The nominal ODT domain length is 2π, which is same as the nominal domain size of intended DNS comparison cases [45]. The DNS data is generated using a full three-dimensional incompressible Navier-Stokes flow solver [12, 46]. Each phase is transported using an unsplit geometric semi-Lagrangian volume of fluid (VOF) method [47], with the curvature calculated through a mesh decoupled height function [48] and the pressure jump due to surface tension imposed using the ghost fluid method [49].

The initial velocity profile is taken as a sine wave $u(y,0) = u_0(\sin y + \cos y)$ so that the resulting turbulence integral scale will roughly match the comparison cases in nominal length units. Periodic boundary conditions are used at the ends of the domain. The ODT model parameters are chosen to be $C = 1.71$, $Z = 60$.

When turbulence decays to a prescribed Taylor-scale Reynolds number which in this study is 155, the second part of the simulation is initiated by inserting the phase interface into the middle of the box . The phase between each pair of

Case	Tool	Re_λ	We_λ
1	DNS, ODT	155	∞
2	DNS, ODT	155	21.06
3	DNS, ODT	155	8.47
4	DNS, ODT	155	1.36
5	ODT	155	100
6	ODT	500	100
7	ODT	1000	100

Table 6.1: Parameters that characterize the HIT/interface simultions.

adjacent interfaces is assigned a unique index. The results are based on 2000 realizations.

Density and viscosity are uniform in all phases to isolate the effects of turbulent inertia and surface tension. Two cases with different Weber numbers are simulated and the surface tension energy parameter σ is used to vary the Weber number, which is defined as $We_\lambda = \rho u_{rms}^2 \lambda / \sigma$. The simulation conditions are shown in Table 6.1, with example images from the DNS and ODT simulations at a time of $t/\tau = 0.5$ shown in Figure 6.1 for Cases [1-4], respectively. Where τ represents the large eddy turn over time.

In continue, the statistics of interface surface density and the two point autocorrelation function of phase index along the direction normal to the initial surface are studied and compared with corresponding DNS data generated by the CTFLab at Cornell University. The results are reported in detail as a manuscript attached to this thesis.

6.2 The surface tension cutoff length scale

In reference to Figure 6.2, an eddy of size l with characteristic velocity u' will stop overturning the interface when surface tension on that scale balances inertia, i.e., when the Weber number $We = \rho u'^2 l / \sigma \sim 1$. The limiting length scale $l_\sigma \sim \sigma / \rho u'^2$ emerges from this simple balance as a function of u'. According to Kolmogorov [50], the expression for the characteristic velocity u' will depend on where the critical length scale falls within the universal equilibrium range. The two expressions for the critical length scale in the dissipation range and

(a) $We_\lambda = \infty$

(b) $We_\lambda = 21.06$

(c) $We_\lambda = 8.47$

(d) $We_\lambda = 1.36$
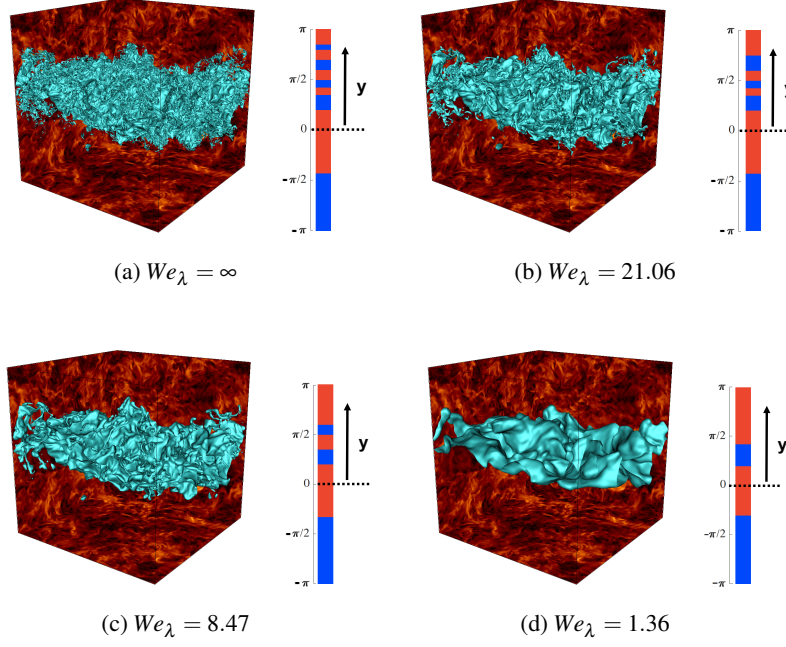
Figure 6.1: Interface for the DNS(left) and ODT(right) for cases [1-4] at time $t/\tau = 0.5$.
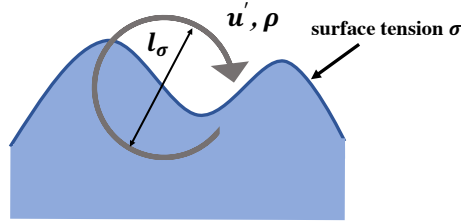
Figure 6.2: Critical length scale schematic.

in the inertial subrange become $l_\sigma \sim (\sigma v/(\rho \varepsilon))^{1/3}$ and $l_\sigma \sim (\sigma^3/(\rho^3 \varepsilon^2))^{1/5}$, respectively. The resulting l_σ from the ODT and the DNS simulations for cases 1 - 5 are compared to the predicted value given by [50] and shown in Figure

6.3.
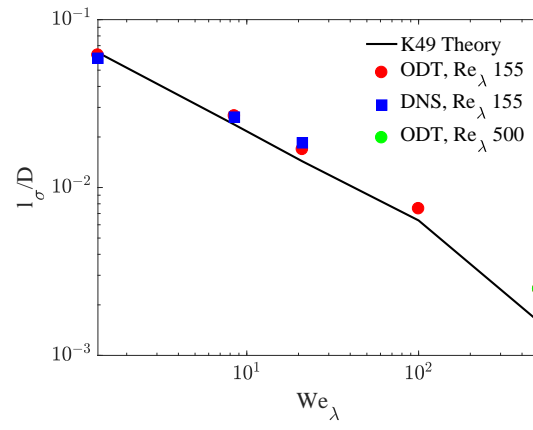
Figure 6.3: Comparison between critical length scale l_σ calculated from theory and simulations.

7

Virtual ODT for LES/VOF closure

7.1 Introduction

Predictive simulations with high spatial and temporal resolution, i.e., Direct Numerical Simulations (DNS), offer a rigorous way to study liquid-gas interface dynamics during primary breakup. Despite the significant benefits provided by DNS, the large computational cost precludes their use in many flows of engineering interests. Therefore, there is a need for appropriate interface dynamics models that make the computational cost of predicting the atomization process more feasible. While requiring physcial models for the small unresolved scales of the flow, Large-Eddy Simulation (LES) has shown to be a useful tool that can provide much more flexibility on resolution than DNS by introducing a spatial filter onto the governing equations and resolving only the scales larger than the filter width. However, the LES sub-filter models typically neglect the contribution of the surface tension term and are based on a cascade process hypothesis that may be questionable in the context of surface tension-driven atomization. This leads to proposing a new LES subgrid interface dynamics model.

A One-Dimensional Turbulence (ODT) model is considered here as an affordable model for simulating large Reynolds and Weber number flow configurations. ODT can be used both as a stand alone tool and as a sub-grid model for LES or RANS. This creates a possibility to use ODT as a subgrid resolution model in LES/VOF simulations to describe/model subgrid interface dynamics. This approach is described in detail in the following sections.

7.2 Governing equations

The flows investigated in this study are governed by the incompressible Navier-Stokes equations for immiscible two-phase flow. The momentum equation is given by

$$\frac{\partial u}{\partial t} + u \cdot \nabla u = -\frac{1}{\rho} \nabla p + \frac{1}{\rho} \nabla \cdot [\mu (\nabla u + \nabla^T u)] + \frac{1}{\rho} \sigma \gamma \delta(x - x_\Gamma) n, \quad (7.1)$$

where u is the velocity, ρ the density, p the pressure, and μ is the dynamic viscosity. The last term in equation (7.1) is the sinular surface tension force where γ denotes the curvature of the interface, δ is the Dirac delta function, x_Γ is the point on the interface Γ closest to the point x and n is the unit vector normal to Γ.

To compute the phase interface, in addition, a transport equation for the liquid volume fraction α in a computational cell is resolved

$$\frac{\partial \alpha}{\partial t} + \nabla \cdot (\rho u \alpha) = 0, \quad (7.2)$$

where $\alpha = 1$ represents a computational cell which is fully filled by liquid, and $\alpha = 0$ represents a computational cell which is fully filled by gas. The interface unit vector n and the interface curvature γ can be theoretically be expressed in terms of the the volume-of-fluid scalar as

$$n = \frac{\nabla \alpha}{|\nabla \alpha|}, \quad \gamma = \nabla \cdot n. \quad (7.3)$$

Following the continuum surface force approach [51] the surface tension force in equation (7.1) is modelled as

$$T_\sigma(x) = \sigma \gamma \delta(x - x_\Gamma) n = \sigma \gamma \nabla \alpha. \quad (7.4)$$

Using LES to simulate the flow field, the spatial filtering is applied into equation (7.1). In LES, the large scale structures are captured directly, whereas the small scale structures are filtered out. Applying any spatial filtering to equation (7.1), new terms appear, these are called sub-grid-scale (SGS) terms. LES is based on Kolmogorov's hypothesis: the large scale structures are dependent on the specific flow situation, whereas the behaviour of the small scale structures is isotropic and geometry independent, i.e, universal. If the scales that are filtered out are small enough to be considered as universal, the SGS terms can be closed by a model, e.g the smagorinsky model. However, these models typically neglect the contribution of the sub-filter surface tension term and are based on a cascade process hypothesis that may be questionable in the context of surface tension driven atomization.

In particular LES doesn't see interface wrinkles below its resolution scale, so the LES-resolved interface is much smoother and has less total surface area than the true interface. Therefore it doesn't fully account for the true total amount of stored surface-tension area. As Figure 7.1 illustrates when the Weber number is high enough there are some scales of interface wrinkling that are not resolved by the LES and they cause droplets generation. Following sections describe how ODT can be used to model these unresolved scales.
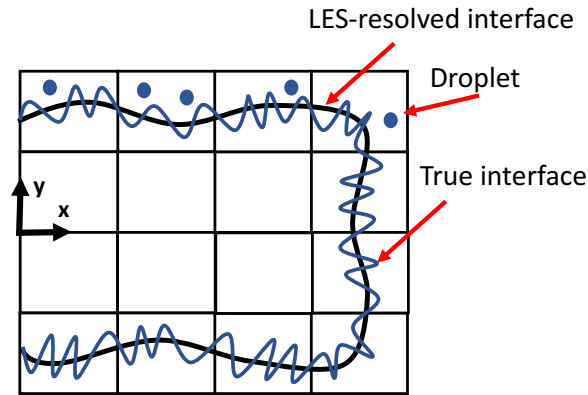
Figure 7.1: Sub-filter interfacial structures in LES simulation

As described earlier, ODT can be used as a stand alone computation tool. This creates a possibility to use ODT to compute a subgrid breakup table. As

shown in Figure 7.2 it is assumed that the ODT closure of LES/VOF can be formulated on an ODT domain locally normal to a given VOF interface element in every LES cell that contains an interface. For generality the interface is allowed here to be at any location $y = I$ on the ODT domain. ODT produces a size-conditioned as well as a total time rate of generation of droplets at a given VOF interface. At the LES level, the total droplet generation is interpreted as a rate $\dot{M}$ of mass conversion of LES-resolved liquid into unresolved droplets that are then deemed to reside in the gas phase. Accordingly, for a VOF interface element whithin a LES cell, droplet generation causes recession of the interface at a speed $\dot{M}/(A\rho_l)$ inserted as a source term into equation (7.2) and updates the LES governing equations. This approach, called Virtual ODT is described in this section.
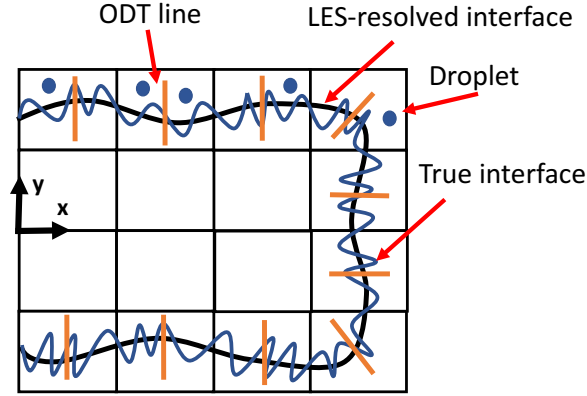
Figure 7.2: Using ODT as a sub-filter model for LES

7.3 Virtual ODT for VOF/LES closure

7.3.1 Implementation

As discussed earlier, ODT contains two main mechanisms, viscous time advancement and eddy events. For the tabulation purposes, we suppose there is no viscous advancement but only eddy sampling. Nevertheless, the accepted eddies are not implemented and just their statistics are collected. Because the

VODT state is not time advanced, the only effect of eddy events is droplet generation and the implied recession of the liquid surface. Therefore eddies entirely contained in one phase have no effect, so only multiphase (hence droplet-forming) eddies are considered. By not implementing the eddies, the eddy rate distribution is stationary. Thus the initial rate distribution is used to evaluate the rate of production of a droplet of any size. The effect of surface tension (and hence the *We* dependence), which does not appear in equation (3.20), is brought into the formulation through the physical modeling that specifies the eddy rate distribution.

A VODT droplet-forming eddy ranges from some location $y_0 < I$ to a location $y_0 + l > I$, which implies $l > I - y_0$. Based on the triplet-map definition, the eddy transfers $\frac{2}{3}$ of the liquid interval $[y_0, I]$ to the droplet, while the rest remains in liquid form as defined in VODT. The implied surface recession is then $\Delta y = \frac{2}{3}(I - y_0)$, corresponding to the LES-level volume conversion $\Delta V = A_s \Delta y$ where A_s is the surface area of VOF interface element.

Δy is the only available length scale from which the droplet diameter D can be inferred, so $D = B\Delta y$ is assumed, where B is a tunable parameter. Then the ODT droplet is deemed to represent N physical droplets, where $N = \Delta V / \left(\frac{\pi}{6}D^3\right)$ is based on assuming spherical droplets. Using $\Delta V = A_s D / B$, this gives $N = 6A_s/(\pi B D^2)$. N need not to be an integer because it is meaningful only in terms of droplet statistics.

At the LES level, it is assumed that the droplet spectrum in the gas phase is represented by a histogram based on either linear or geometric size bins. Uniform linear bins of size dD are assumed here for illustration, although the reasoning is more general. To complete the formulation of VODT outputs, the total generation rate $G(D)$ of droplets in the size range $[D, D+dD]$ is evaluated. To do this, the drop number probability distribution, $g(D) = \frac{dG}{dD}$ per unit diameter increment is first evaluated. Based on the results that follow, $g(D)$ can be integrated over dD intervals to obtain the binned generation rates $G(D)$.

In the Appendix, the ODT eddy rate distribution $\lambda(y_0, l)$ is evaluated for the specified VODT state. To evaluate $g(D)$, this distribution is integrated over its arguments subject to the constraint $D = B\Delta y = \frac{2}{3}B(I - y_0)$, re-expressed as $y_0 = I - \frac{3}{2}\frac{D}{B}$. Formally this involves insertion of $\delta(y_0 - I + \frac{3}{2}\frac{D}{B})$ into the integral over dy_0, and thus

$$g(D) = N(D) \int_{\frac{3}{2}\frac{D}{B}}^{h-I+\frac{3}{2}\frac{D}{B}} dl \int dy_0 \, \lambda(y_0, l) \delta(y_0 - I + \frac{3}{2}\frac{D}{B})$$

$$= \frac{6A_s}{\pi B D^2} \int_{\frac{3}{2}\frac{D}{B}}^{h-I+\frac{3}{2}\frac{D}{B}} dl \, \lambda(I - \frac{3}{2}\frac{D}{B}, l).$$

The moments of the drop number probability distribution are then defined by

$$G_i(D) = \int_{D_{min}}^{D_{max}} g(D) D^i dD.$$

G_0 is the total number of drops per unit time, G_1 is the total sum of diameter of the drops per unit time, $4\pi G_2$ is the total surface area of the drops per unit time and $4\pi G_3/2$ is the total volume of the drops per unit time.

7.3.2 VODT initial and boundary conditions

In virtual ODT simulations, the liquid-gas shear ratio is found by the tangential stress balance $\nu_l \rho_l (du/dy)|_l = \nu_g \rho_g (du/dy)|_g$ at the phase interface. The ODT domain length, h and the velocity difference, Δu across the ODT domain are given by the LES control-volume size and the LES-resolved shear. Furthermore, to keep the simplicity of the model only the u velocity component is nonzero.

$u(y)$ is assumed to be linear in each phase with $u(0) = 0$, so $u(I) = \gamma_l I$ and $u(h) = u(I) + \gamma_g(h - I)$. Rewriting the latter relation as $\Delta u = \gamma_l I + \gamma_g(h - I)$ and applying the interfacial matching condition $\mu_l \gamma_l = \mu_g \gamma_g$, where $\mu_{l,g} = \nu_{l,g}\rho_{l,g}$, the slopes γ_l and γ_g are determined.

For tabulation using ODT, Neumann boundary conditions at both ends of the ODT domain are preferable because the Dirichlet conditions would imply a Couette flow and associated wall boundary layers, which are unphysical in the present context. More broadly, the shear is the main governing LES parameter, so it is natural to communicate it to the ODT simulation by means of the boundary as well as initial conditions.

7.3.3 VODT inputs and outputs

For tabulation based on VODT, the VODT runs separately to generate the tables needed in the LES simulation. This brings out the issue of the table dimensionality which will be discussed in this section.

The inputs required by VODT are those needed to specify the VODT state and those needed to compute the associated droplet statistics. Some of these depend on the local LES state, so in a tabulation, they would be the coordinates of the table array. Others have no such dependence, so although they affect the VODT outputs, they do not affect the size of the table. Based on the formulation as outlined, the latter category includes the following: σ, v_l, ρ_l, the ODT/VODT parameters C, Z, and B, and possibly h (if the LES mesh is regular enough so that CV size variations can be ignored). The CV-specific parameters are then v_g, ρ_g, and Δu. Though only $\mu_g = v_g \rho_g$ is needed for the VODT initial condition, v_g and ρ_g individually are needed for the computation of droplet statistics. Then for the simplest application, the table is three-dimensional, or four-dimensional if mesh irregularity requires h to be an additional table coordinate.

7.4   Results and Conclusion

In the Appendix, it is shown that VODT for this simple application reduces to an algebraic system that is economical enough for on-the-fly runtime implementation. This makes VODT a computationally affordable tool to study different atomization processes. Figure 7.3 shows a normalized droplet atomization rate of interfacial breakup in different Reynolds and Weber numbers. The droplet generation rate, G_0, shows the total number of drops in time and is normalized by local shear $\Delta u / h$. As seen in the Figure 7.3, for relatively low injection velocities the atomization rate is primarily governed by the liquid surface tension. Figure 7.4 shows the normalized Sauter Mean Diameter (SMD) of droplets normalized by the cell size, h. The plot shows where $\rho_l / \rho_g = 1$ the SMD of droplets satys in a same order of magnitude in by changing the Reynolds and Weber numbers. In Figure 7.3 the density and viscosity ratios are both equal to 1. By varying the liquid/gas density ratio and keeping the viscosity ratio constant, Figure 7.5 is generated which shows how the atomization rate depends on the liquid/gas density ratio.

As discussed earlier the main scope of this section is to propose VODT as a subgrid model for VOF/LES simulations. Like ODT, VODT has three adjustable parameters C, Z, B that need to be calibrated for this planar shear layer application.

A possible basis for this that does not require external input is to run
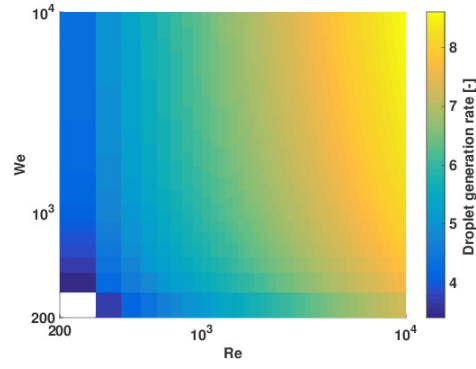
Figure 7.3: Normalized droplet generation rate [-]
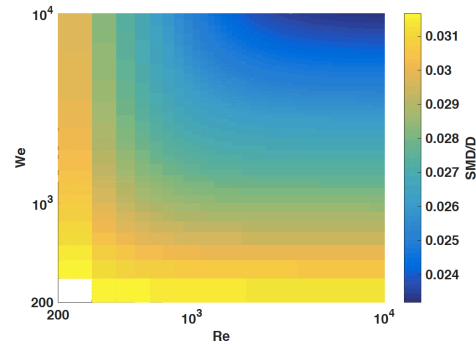
Figure 7.4: Normalized droplet Sauter Mean Diameter (SMD)
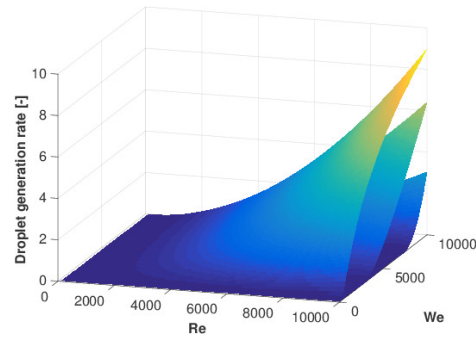
Figure 7.5: Normalized droplet generation rate at $\rho_l/\rho g = 1, 10, 100$ with $\mu_l/\mu_g = 100$

VOF/LES/VODT at different LES resolutions for the same case. If VODT is a good closure, then these results should all predict the same flow development and droplet statistics. As resolution improves, some of the droplet generation seen at the VODT level at coarse LES resolution should become LES-resolved, with VODT still giving the same results as at lower LES resolution for droplets not resolved by the higher-resolution LES. In effect, VODT parameters can be set within LES/VOF/VODT on the basis of overall consistency. This approach is currently under study and outcomes will be a part of discussions in future publications.

8
Summery of papers

This chapter gives summaries of the appended papers, outlining their aim and a brief summary.

8.1 Paper I

Sensitivity of VOF Simulations of the Liquid Jet Breakup to Physical and Numerical Parameters

Aim: To study the characteristics of the primary breakup of liquid jet in changes of the liquid-gas properties

Summary: We applied the Volumes of Fluids (VOF) approach utilizing the Direction Averaged Curvature (DAC) model, to estimate the interface curvature, and the Direction Averaged Normal (DAN) model, to propagate the interface. The influence of varying the fluid properties, namely liquid-gas density and viscosity ratio, and injection conditions is discussed related to the required

grid resolution. Resulting droplet sizes are compared to distributions obtained through the One-Dimensional Turbulence (ODT) model.

8.2 Paper II

Numerical Investigation of Turbulent-jet Primary Breakup Using One-Dimensional Turbulence

Aim: This paper summarizes the extensions of the ODT model to simulate geometrically simple jet breakup problems.

Summary: A new model to predict primary breakup of liquid jets is proposed in this paper. The model is based on extensions to the stochastic one-dimensional turbulence model (ODT) that incorporate surface tension and its interaction with liquid-phase turbulence, Rayleigh waves and aerodynamic shear. Simulations are per formed, starting with a liquid jet with no breakup to investigate turbulence levels inside a jet and followed by a jet with primary breakup. Each jet breakup simulation consists of a short temporal channel section to initialize a turbulent velocity profile at the nozzle exit followed by an adjacent jet section. The simulations were carried out for jet exit Reynolds number in the range of $[1.1 \times 10^4 - 9.2 \times 10^4]$ while the Weber number is varied within the range $[10^2 - 10^7]$. We presented results on breakup statistics including spatial locations of droplet release, droplet sizes and liquid core length. The results on primary breakup are compared to experimental results and models. ODT results for the most probable and the median location of onset of breakup show agreement with the experiments, including sensitivity to Weber number.

8.3 Paper III

Parameter Dependences of the Onset of Turbulent Liquid-jet Breakup

Aim: To propose a new correlation to predict the onset location and the SMD in terms of liquid jet Reynolds number and Weber number

Summary: In this paper, it's proposed that breakup onset is controlled by the residual presence of the boundary-layer structure of the nozzle flow in the near

field of the jet. Assuming that the size of the breakup-inducing eddy is within the scale range of the log-law region, We^{-1} dependence of both the onset location and the SMD at onset is predicted. These dependences agree with the available measurements more closely than those previously predicted. To predict the dependences on the Reynolds number Re, either the friction velocity in conjunction with the Blasius friction law or the bulk velocity can be used, where the former yields $Re^{3/8}$ and $Re^{1/4}$ dependence of the onset location and the SMD at onset respectively, while the latter implies no Re dependence of either. The latter result is consistent with the available measurements, but the boundary-layer analysis indicates that the velocity scaling should be based on the friction velocity rather than the bulk velocity and needs further investigation.

8.4 Paper IV

Modeling and Numerical Study of Primary Breakup Under Diesel Conditions

Aim: To assess the ability of ODT to capture the primary jet breakup under diesel conditions

Summary: The ODT model for numerical simulation of primary jet breakup is evaluated here by comparing model predictions to DNS results for primary jet breakup under diesel conditions. Multiple realizations are run to gather ensemble statistics that are compared to DNS results. The model as previously formulated, including the assigned values of tunable parameters, is used here without modification in order to test its capability to predict various statistics of droplets generated by primary breakup. This test is enabled by the availability of DNS results that are suitable for model validation. Properties that are examined are the rate of bulk liquid mass conversion into droplets, the droplet size distribution, and the dependence of droplet velocities on droplet diameter. Quantities of greatest importance for engine modeling are found to be predicted with useful accuracy.

8.5   Paper V

Assessment of an Atomization Model Based on One-Dimensional Turbulence using Direct Numerical Simulation of a Decaying Turbulent Interfacial Flow

Aim: To assess the ability of ODT to capture the interface breakup with DNS data for further improvements.

Summary: Here, ODT is used to investigate the interaction of turbulence with an initially planar interface. The notional interface is inserted into a periodic box of decaying homogeneous isotropic turbulence at the targeted value of the Taylor-microscale Reynolds number $Re_{\lambda_g} = 155$, simulated for a variety of Weber numbers ($We_{\lambda_g} = \infty$, 21.06, 8.47, 1.36) . Unity density and viscosity ratios are used in order to isolate the interaction between fluid inertia and the surface-tension force. Statistics of interface surface density, two-point correlations of phase index, and turbulent kinetic energy budgets along the direction normal to the initial surface are compared with corresponding DNS data. Mesh-convergence studies that are impractical using DNS are performed using ODT, indicating that it can affordably resolve the interface at Reynolds and Weber numbers that are beyond the reach of DNS ($Re_{\lambda_g} = 500, We_{\lambda_g} = 100$).

8.6   Paper VI

A Subgrid-Scale Model for Large-Eddy Simulation of Liquid/Gas Interfaces Based on One-Dimensional Turbulence

Aim: Applying ODT as a subgrid resolution model in LES/VOF simulations to describe/model subgrid interface dynamics.

Summary: A new approach based on One-Dimensional turbulence (ODT) developed to describe the subgrid interface dynamics. This new approach called VODT produces a size-conditioned as well as a total time rate of generation of droplets for given flow conditions at an interface. At the LES level, the total droplet generation from VODT is interpreted as a rate of mass conversion of LES-resolved liquid into unresolved droplets. For this purpose a setup of a

planar-shear-layer analogue to an LES cell developed and simulated. Preliminary results of applying VODT are discussed at the end of the paper. The total number of droplets and the total volume of the droplets per unit time presented in a form of tables dimensionalized by Reynolds number, Weber number, density ratio and viscosity ratio in every cell.

9

Concluding remarks and future work

In this study we present a new model for the prediction of primary break up of liquid jets. The model is based on the stochastic One Dimensional Turbulence model (ODT) and extends previous formulations of ODT to gas-liquid multiphase flow. The ODT formulation has been discussed briefly in chapter 2.

Most CFD Lagrangian spray models that have been developed lately to describe spray breakup can accurately predict global spray characteristics, but they embrace considerable uncertainties regarding important processes that occur close to the nozzle. One major outcome of this study was to identify these dominant processes and further attempts to model them within the ODT modeling framework. On this basis, the main mechanisms that influence the droplet formation have been developed within ODT and were discussed in chapter 3. These new extensions enable ODT to deal with surface tension energy and turbulence interface interaction, capturing Rayleigh wave effects and also shear-driven breakup.

For model assessment, this project was divided into three different phases. In the first phase, the cases with liquid/gas ratio higher than 500 were considered.

Here, the author had access to the wide range of experimental data. The ODT model was generalized to capture the physical mechanisms related to primary breakup. This introduced additional modeling parameters in the ODT formulation. Further parameter studies and their optimization against the available experiments were discussed in papers I and II. Despite the predictability that ODT showed against those experiments, some of the discrepancies noted in the model validation reflected the inherent physics of ODT that is largely based on one dimensional reasoning. For example, shear driven breakup formulation. Extended in this manner, ODT is capable of generating droplet formation statistics that are otherwise available only from costly multidimensional flow simulations.

Furthermore, the author thinks by exploiting advanced measurement techniques, e.g. ballistic imaging, there would be more detailed droplet data available in future. This will allow furthermore detailed validation of the modeling approach presented in this thesis and thereby indicate its future prospects for becoming a robust predictive simulation tool.

The second phase referred to the cases where the liquid/gas density and viscosity ratio is in the order of engine applications but still affordable by detailed numerical simulations. In this stage, the ODT primary breakup model reproduced accurately some available DNS data, in particular droplets size and velocity distributions.

In this regime, the author deliberately avoided any adjustment of parameter values determined in the previous phase so that the model could be evaluated on a predictive basis. This established a baseline performance demonstration that can be used for further modifications to improve the model representation of the physics involved in primary breakup, for example, aerodynamic effects which should be considered as a dominant break up mechanism in the cases with low liguid/gas density ratio. The author does not rule out the possibility that model parameters could be retuned so as to fit to both DNS or future experiments.

Finally, in the last phase, in order to evaluate the performance of the model under real diesel engine conditions, the so-called ECN Spray-A based on the Engine Combustion Network (ECN) configurations was simulated. The ODT

primary breakup results were coupled as an input with Lagrangian spray models in OpenFoam. Global spray characteristics such as liquid length and vapor penetration are validated against available experimental data.

The last phase should be looked at as a first step to develop a new multicomponent spray evaporation model. As discussed earlier, the ODT model can provide droplet size and velocity distributions from primary breakup, but the subsequent spray development is influenced by mechanisms affecting droplet trajectories such as drag and droplet collisions. At this stage, there is no suitable way to time advance droplets' motion and interactions on the 1D Lagrangian domain by stand alone ODT. In this sense, the ODT primary break up results are provided as an input to a Lagrangian spray model. Furthermore, the proposed ODT model has the potential to include further physical mechanisms influencing primary breakup, e.g. evaporation, multi-component fuels, and breakup under supercritical conditions. These new extensions could be considered in future investigations.

This study showed that the ODT primary breakup model could be considered as an affordable LES subgrid model for simulating large Reynolds and Weber number flow configurations. This outcome led the author to propose a strategy to use ODT as a subgrid resolution model in LES/VOF simulations to describe/model unresolved subgrid interface dynamics. This new approach called VODT was described in chapter 6 and needs to be investigated further in the future.

Appendices

A

Appendix

Evaluation of the eddy rate distribution for the VODT state

The variable-density ODT formulation of [17] specialized to the VODT state will be discussed in this section.

The eddy event is formally represented as

$$v_i(y) \to v_i(f(y)) + b_i J(y) + c_i K(y) \qquad (\text{A.1})$$

and

$$\rho(y) \to \rho(f(y)), \qquad (\text{A.2})$$

where $f(y)$ is the inverse of the triplet map, $K = y - f(y)$, $J = |K|$, and b_i and c_i are assigned based on physical modeling. v_i is the ith velocity component. In VODT there is only one component, denoted u, so the subscript i is omitted in what follows.

It is now convenient to introduce the notations ρ' and u' to denote the profiles of density and of velocity components after triplet mapping, and the notation $u'' = u' + bJ + cK$ to denote the velocity profiles after the subsequent energy-change operation. Thus, ρ' and u'' represent the flow configuration upon eddy completion, though in VODT they are computed only to evaluate λ.

The values of b and c that correspond to a given change ΔE in the kinetic energy of the u profile, subject to momentum conservation, are now expressed in terms of ρ', u', and the kernels J and K. The relations determining b and c are momentum conservation,

$$\int \rho' u'' \, dy = \int \rho' u' \, dy, \tag{A.3}$$

and energy conservation,

$$
\begin{aligned}
\Delta E &= \frac{1}{2} \int \rho'(u''^2 - u'^2) \, dy, \\
&= \frac{1}{2} \int \rho'[(bJ + cK)^2 + 2u'(bJ + cK)] \, dy. \\
&= \frac{b^2}{2} \underbrace{\int \rho' J^2 \, dy}_{\rho_{JJ}} + \frac{c^2}{2} \underbrace{\int \rho' K^2 \, dy}_{\rho_{KK}} + \frac{bc}{2} \underbrace{\int \rho' JK \, dy}_{\rho_{JK}} + b \underbrace{\int \rho' u' J \, dy}_{\rho_{uJ}} + c \underbrace{\int \rho' u' K \, dy}_{\rho_{uK}}
\end{aligned}
\tag{A.4}
$$

These equations can be recast in terms of the quantities below that are used to solve for b and c. Each equation stated in its general form and then specialized to the VODT state. Superscripts $<$ and $>$ indicate the case $I < y_0 + \frac{l}{2}$ and $I > y_0 + \frac{l}{2}$, respectively. Moreover, the notations γ_l and γ_g refer to the shear slopes in the liquid and the gas phase, respectively.

$$\rho_J \equiv \int \rho' J \, dy$$

$$= \frac{4}{9} \int_{y_0}^{y_0+\frac{l}{2}} (l + y_0 - y)\rho(y) \, dy + \frac{4}{9} \int_{y_0+\frac{l}{2}}^{y_0+l} (y - y_0)\rho(y) \, dy$$

$$\rho_J^< = \frac{4\rho_l}{9} \int_{y_0}^{I} (l + y_0 - y) \, dy + \frac{4\rho_g}{9} \int_{I}^{y_0+\frac{l}{2}} (l + y_0 - y) \, dy + \frac{4\rho_g}{9} \int_{y_0+\frac{l}{2}}^{y_0+l} (y - y_0) \, dy$$

$$= \frac{4\rho_l}{9} \left[(I - y_0)(l + y_0) - \frac{1}{2}(I^2 - y_0^2) \right] +$$

$$\frac{4\rho_g}{9} \left[(y_0 + \frac{l}{2} - I)(l + y_0) - \frac{1}{2}((y_0 + \frac{l}{2})^2 - I^2) + \frac{1}{2}((y_0 + l)^2 - (y_0 + \frac{l}{2})^2) - y_0 \frac{l}{2} \right]$$

$$= \frac{4\rho_l}{9} \left[(I - y_0)(l + y_0) - \frac{1}{2}(I^2 - y_0^2) \right] +$$

$$\frac{4\rho_g}{9} \left[(y_0 + \frac{l}{2} - I)(l + y_0) - (y_0 + \frac{l}{2})^2 + \frac{1}{2}((y_0 + l)^2 + I^2 - y_0 l) \right]$$

$$\rho_J^> = \frac{4\rho_l}{9} \int_{y_0}^{y_0+\frac{l}{2}} (l + y_0 - y) \, dy + \frac{4\rho_l}{9} \int_{y_0+\frac{l}{2}}^{I} (y - y_0) \, dy + \frac{4\rho_g}{9} \int_{I}^{y_0+l} (y - y_0) \, dy$$

$$= \frac{4\rho_g}{9} \left[\frac{1}{2}((l + y_0)^2 - I^2) - y_0(l - I + y_0) \right] +$$

$$\frac{4\rho_l}{9} \left[(\frac{l}{2} + y_0 - I)(l + y_0) - (y_0 + \frac{l}{2})^2 + \frac{1}{2}((y_0 + l)l + I^2 + y_0^2) \right]$$

$$\rho_K \equiv \int \rho' K \, dy$$

$$= \frac{4}{9} \int_{y_0}^{y_0+l} [l - 2(y - y_0)]\rho(y) \, dy$$

$$\rho_K = \frac{4\rho_l}{9} \int_{y_0}^{I} [l - 2(y - y_0)] \, dy + \frac{4\rho_g}{9} \int_{I}^{y_0+l} [l - 2(y - y_0)] \, dy$$

$$= \frac{4\rho_l}{9} \left[I^2 + l y_0 - I(2y_0 + l) + y_0^2 \right] + \frac{4\rho_g}{9} \left[-I^2 - l y_0 + I(2y_0 + l) - y_0^2 \right]$$

$$\rho_{KK} \equiv \int \rho' K^2 \, dy = \int \rho' J^2 \, dy$$

$$= \frac{8}{27} \int_{y_0}^{y_0+l} [l^2 - 3l(y - y_0) + 3(y - y_0)^2]\rho(y) \, dy$$

$$\rho_{KK} = \frac{8\rho_l}{27}\int_{y_0}^{I}[l^2 - 3l(y-y_0) + 3(y-y_0)^2]\,\mathrm{d}y + \frac{8\rho_g}{27}\int_{I}^{y_0+l}[l^2 - 3l(y-y_0) + 3(y-y_0)^2]\,\mathrm{d}y$$

$$= \frac{8\rho_l}{27}\left[l^2 I - \frac{3lI^2}{2} + \frac{2I^3}{3} + y_0(3lI - l^2 - 2I^2) + y_0^2(2I - \frac{3l}{2}) - \frac{2y_0^3}{3}\right]$$

$$+ \frac{8\rho_g}{27}\left[-l^2 I + \frac{3lI^2}{2} - \frac{2I^3}{3} - y_0(3lI - l^2 - 2I^2) - y_0^2(2I - \frac{3l}{2}) + \frac{2y_0^3}{3}\right]$$

$$\rho_{JK} \equiv \int \rho' JK\,\mathrm{d}y$$

$$= \frac{8}{27}\int_{y_0}^{y_0+\frac{l}{2}}[l^2 - 3l(y-y_0) + 2(y-y_0)^2]\rho(y)\,\mathrm{d}y$$

$$+ \frac{8}{27}\int_{y_0+\frac{l}{2}}^{y_0+l}(y-y_0)[l - 2(y-y_0)]\rho(y)\,\mathrm{d}y$$

$$\rho_{JK}^{<} = \frac{8\rho_l}{27}\int_{y_0}^{I}[l^2 - 3l(y-y_0) + 2(y-y_0)^2]\,\mathrm{d}y + \frac{8\rho_g}{27}\int_{I}^{y_0+\frac{l}{2}}[l^2 - 3l(y-y_0) + 2(y-y_0)^2]\,\mathrm{d}y$$

$$+ \frac{8\rho_g}{27}\int_{y_0+\frac{l}{2}}^{y_0+l}(y-y_0)[l - 2(y-y_0)]\,\mathrm{d}y$$

$$= \frac{-5l^3\rho_g}{81} + \frac{8\rho_l}{27}\left[\frac{5l^3\rho_g}{24} - l^2 I + \frac{3lI^2}{2} - \frac{2I^3}{3} + y_0(l^2 - 3Il + 2I^2) + y_0^2(2I - \frac{3I}{2}) - \frac{2y_0^3}{3}\right]$$

$$+ \frac{8\rho_g}{27}\left[l^2 I - \frac{3lI^2}{2} + \frac{2I^3}{3} - y_0(l^2 - 3Il + 2I^2) - y_0^2(2I - \frac{3I}{2}) + \frac{2y_0^3}{3}\right]$$

$$\rho_{JK}^{>} = \frac{8\rho_l}{27}\int_{y_0}^{y_0+\frac{l}{2}}[l^2 - 3l(y-y_0) + 2(y-y_0)^2]\,\mathrm{d}y + \frac{8\rho_l}{27}\int_{y_0+\frac{l}{2}}^{I}(y-y_0)[l - 2(y-y_0)]\,\mathrm{d}y$$

$$+ \frac{8\rho_g}{27}\int_{I}^{y_0+l}(y-y_0)[l - 2(y-y_0)]\,\mathrm{d}y$$

$$= \frac{5l^3\rho_l}{81} + \frac{8\rho_l}{27}\left[-\frac{l^3}{24} + \frac{lI^2}{2} - \frac{2I^3}{3} + y_0(2I^2 - Il) + y_0^2(\frac{l}{2} - 2I) + \frac{2y_0^3}{3}\right]$$

$$+ \frac{8\rho_g}{27}\left[\frac{l^3}{24} - \frac{lI^2}{2} + \frac{2I^3}{3} - y_0(2I^2 - Il) - y_0^2(\frac{l}{2} - 2I) - \frac{2y_0^3}{3}\right]$$

$$\rho_{uJ} \equiv \int \rho' u' J\,\mathrm{d}y$$

$$= \frac{4}{9}\int_{y_0}^{y_0+\frac{l}{2}}(l + y_0 - y)\rho(y)u(y)\,\mathrm{d}y + \frac{4}{9}\int_{y_0+\frac{l}{2}}^{y_0+l}(y-y_0)\rho(y)u(y)\,\mathrm{d}y$$

$$\rho_{uJ}^< = \frac{4\rho_l}{9}\int_{y_0}^{I}(l+y_0-y)u(y)\,dy + \frac{4\rho_g}{9}\int_{I}^{y_0+\frac{l}{2}}(l+y_0-y)u(y)\,dy + \frac{4\rho_g}{9}\int_{y_0+\frac{l}{2}}^{y_0+l}(y-y_0)u(y)\,dy$$

$$= \frac{\rho_g}{54}(l-2I+2y_0)\left[2l^2\gamma_g + l(-5I\gamma_g+5\gamma_g y_0+9u(I))+2(I-y_0)(I\gamma_g-\gamma_g y_0-3u(I))\right]$$

$$+ \frac{4\rho_g}{9}\left[\frac{7l^3\gamma_g}{24}-\frac{3}{8}l^2 I\gamma_g+\frac{3}{8}l^2\gamma_g y_0+\frac{3l^2 u(I)}{8}\right]$$

$$+ \frac{2\rho_l}{27}(I-y_0)\left[3l(I\gamma_l-\gamma_l y_0+2u(y_0))-(I-y_0)(2I\gamma_l-2\gamma_l y_0+3u(y_0))\right]$$

$$\rho_{uJ}^> = \frac{4\rho_l}{9}\int_{y_0}^{y_0+\frac{l}{2}}(l+y_0-y)u(y)\,dy + \frac{4\rho_l}{9}\int_{y_0+\frac{l}{2}}^{I}(y-y_0)u(y)\,dy + \frac{4\rho_g}{9}\int_{I}^{y_0+l}(y-y_0)u(y)\,dy$$

$$= \frac{2\rho_g}{27}(l-I+y_0)\left[2l^2\gamma_g + l(-I\gamma_g+\gamma_g y_0+3u(I))-(I-y_0)(I\gamma_g-\gamma_g y_0-3u(I))\right]$$

$$+ \frac{4\rho_l}{9}\left(-\frac{l^3\gamma_l}{24}-\frac{l^2 u(y_0)}{8}+\frac{l^3\gamma_l}{3}-I^2\gamma_l y_0+\frac{I^2 u(y_0)}{2}+I\gamma_l y_0^2\right)$$

$$+ \frac{4\rho_l}{9}\left(-Iu(y_0)y_0-\frac{\gamma_l y_0^3}{3}+\frac{u(y_0)y_0^2}{2}+\frac{l^3\gamma_l}{12}+\frac{3l^2 u(y_0)}{8}\right)$$

$$\rho_{uK} \equiv \int \rho'u'K\,dy$$

$$= \frac{4}{9}\int_{y_0}^{y_0+l}[l-2(y-y_0)]\rho(y)u(y)\,dy$$

$$\rho_{uK} = \frac{4\rho_l}{9}\int_{y_0}^{I}[l-2(y-y_0)]u(y)\,dy + \frac{4\rho_g}{9}\int_{I}^{y_0+l}[l-2(y-y_0)]u(y)\,dy$$

$$= \frac{2\rho_l}{27}(I-y_0)\left[3l(I\gamma_l-\gamma_l y_0+2u(y_0))-2(I-y_0)(2I\gamma_l-2\gamma_l y_0+3u(y_0))\right]$$

$$- \frac{2\rho_g}{27}(l-I+y_0)\left[l^2\gamma_g+l\gamma_g(I-y_0)-2(I-y_0)(I\gamma_g-\gamma_g y_0-3u(I))\right]$$

$$H^< \equiv \rho_K/\rho_J^<$$
$$H^> \equiv \rho_K/\rho_J^>$$
$$P^< \equiv \rho_{uK}-H^<\rho_{uJ}^<$$
$$P^> \equiv \rho_{uK}-H^>\rho_{uJ}^>$$
$$T^< \equiv \frac{1}{2}(H^{<2}+1)\rho_{KK}-H^<\rho_{JK}^<$$
$$T^> \equiv \frac{1}{2}(H^{>2}+1)\rho_{KK}-H^>\rho_{JK}^>.$$

Momentum conservation then gives

$$b = -Hc. \tag{A.5}$$

For constant density, $\rho_K = 0$ and therefore $b = 0$, showing that the function J is needed to enforce momentum conservation only if the density profile is not constant in y.

In equation (A.5), integrals have been expressed in terms of postmap (primed) and premap (unprimed) quantities. The latter representation enabled straight-forward derivations of the simple expressions shown for the VODT flow state.

Energy conservation is now expressed in the form

$$\Delta E = Pc + Tc^2. \tag{A.6}$$

The solution for c is

$$c = \frac{1}{2S}\left[-P + \mathrm{sgn}(P)\sqrt{P^2 + 4T\Delta E}\right], \tag{A.7}$$

where the sign of the discriminant term is chosen so that c approaches zero as ΔE approaches zero. Equation (A.7) is not used in VODT because the u-profile changes prescribed by the eddy event rate not implemented. Only the likelihood of occurrence of each possible multiphase eddy is needed to generate the VODT output statistics.

The available energy Q is determined by minimizing the right-hand side of equation (A.6) with respect to c, giving

$$Q = \frac{P^2}{4T}. \tag{A.8}$$

The reasoning that determines the time scale τ used in the eddy-selection procedure is restated in the present terminology and notation. Interpreting the triplet map as motion occurring over a time period τ (although the actual implementation is instantaneous), the associated kinetic energy can be expressed as $\frac{1}{2\tau^2}\int\rho'(y)\Delta^2(y)\,\mathrm{d}y$, where $\Delta(y)$ is the displacement of a fluid element that is moved to location y by the triplet map. Based on the definition of K, this energy is equal to $\rho_{KK}/(2\tau^2)$. This energy is assumed to scale as the available energy of the u velocity upon completion of eddy implementation, here denoted Q'', minus a viscous penalty.

As explained in the erratum to Ashurst and Kerstein (2005) [52], the requirement that the present variable-density formulation reduces to the conventions adopted in the constant-density formulation (which is convenient because the meanings of the model parameters are then unchanged) implies

$$\frac{27}{4}\frac{\rho_{KK}}{\tau^2} = \frac{8}{27}Q'' - Z\frac{\mu_{eddy}^2}{\rho_{eddy}l}, \tag{A.9}$$

where ρ_{eddy} is the average density within the eddy, μ_{eddy} is the harmonic average of the dynamic viscosity within the eddy, and

$$Q'' = Q + \Delta E. \tag{A.10}$$

Equation (A.9) is written as an equality although it is based on scaling concepts rather than exact properties because the required overall coefficient of proportionality is subsumed into the parameter C in the relation

$$\lambda = C/(l^2\tau) \tag{A.11}$$

determining the rate distribution.

Finally, ΔE is evaluated as the surface-tension-induced reduction of kinetic energy due to the eddy-induced increase of interface surface area. Following Movaghar et al. [53], this gives

$$\Delta E = -\frac{4\sigma}{\rho_{eddy}l}. \tag{A.12}$$

Because ΔE and the last term in equation (A.9) are both negative, the right-hand side of that equation can be negative but the left-hand side must be positive. This is an indication that the selected eddy is energetically forbidden, corresponding to $\lambda = 0$ for such eddies.

Bibliography

[1] Norman Chigier, William Bachalo, Rolf D Reitz, Josette Bellan, and Marcus Herrmann, "Spray control for maximizing energy efficiency and reducing emission in combustion engines," *Atomization and Sprays*, vol. 21, no. 7, 2011.

[2] M. Linne, "Imaging in the optically dense regions of a spray: a review of developing techniques," *Progress in Energy and Combustion Science*, vol. 39, no. 5, pp. 403–440, 2013.

[3] Mark Linne, Megan Paciaroni, Tyler Hall, and Terry Parker, "Ballistic imaging of the near field in a diesel spray," *Experiments in fluids*, vol. 40, no. 6, pp. 836–846, 2006.

[4] Mattias Rahm, Megan Paciaroni, Zhenkan Wang, David Sedarsky, and Mark Linne, "Evaluation of optical arrangements for ballistic imaging in sprays," *Optics express*, vol. 23, no. 17, pp. 22444–22462, 2015.

[5] A Kastengren, J Ilavsky, Juan Pablo Viera, Raul Payri, DJ Duke, A Swantek, F Zak Tilocco, N Sovis, and CF Powell, "Measurements of droplet size in shear-driven atomization using ultra-small angle x-ray scattering," *International Journal of Multiphase Flow*, vol. 92, pp. 131–139, 2017.

[6] Daniel J Duke, Alan L Kastengren, Katarzyna E Matusik, Andrew B Swantek, Christopher F Powell, Raul Payri, Daniel Vaquerizo, Lama Itani, Gilles Bruneaux, Ronald O Grover Jr, et al., "Internal and near nozzle measurements of engine combustion network âĂIJspray gâĂİ gasoline direct injectors," *Experimental Thermal and Fluid Science*, vol. 88, pp. 608–621, 2017.

[7] GM Magnotti and CL Genzale, "Detailed assessment of diesel spray atomization models using visible and x-ray extinction measurements," *International Journal of Multiphase Flow*, vol. 97, pp. 33–45, 2017.

[8] P. O'Rourke and A. Amsden, "The tab method for numerical calculation of spray droplet breakup," Tech. Rep., SAE Technical Paper, 1987.

[9] FX. Tanner, "Liquid jet atomization and droplet breakup modeling of non-evaporating diesel fuel sprays," Tech. Rep., SAE Technical Paper, 1997.

[10] R. Reitz, "Modeling atomization processes in high-pressure vaporizing sprays," *Atomisation Spray Technology*, vol. 3, pp. 309–337, 1987.

[11] Carsten Baumgarten, *Mixture formation in internal combustion engines*, Springer Science & Business Media, 2006.

[12] Olivier Desjardins, Jeremy McCaslin, Mark Owkes, and Peter Brady, "Direct numerical and large-eddy simulation of primary atomization in complex geometries," *Atomization and Sprays*, vol. 23, no. 11, 2013.

[13] M. Herrmann, "Detailed numerical simulations of the primary atomization of a turbulent liquid jet in crossflow," *Journal of Engineering for Gas Turbines and Power*, vol. 132, no. 6, pp. 061506, 2010.

[14] K. Sallam, Z. Dai, and G. Faeth, "Liquid breakup at the surface of turbulent round liquid jets in still gases," *International Journal of Multiphase Flow*, vol. 28, no. 3, pp. 427–449, 2002.

[15] Christophe Dumouchel, "On the experimental investigation on primary atomization of liquid streams," *Experiments in fluids*, vol. 45, no. 3, pp. 371–422, 2008.

[16] Jeremy McCaslin, "Development and application of numerical methods for interfacial dynamics in turbulent liquid-gas flows," 2015.

[17] Wm. T. Ashurst and A. R. Kerstein, "One-dimensional turbulence: Variable-density formulation and application to mixing layers," *Physics of Fluids (1994-present)*, vol. 17, no. 2, pp. 025107, 2005.

[18] A. R. Kerstein and S. Wunsch, "Simulation of a stably stratified atmospheric boundary layer using one-dimensional turbulence," *Boundary-layer meteorology*, vol. 118, no. 2, pp. 325–356, 2006.

[19] A. R. Kerstein, "One-dimensional turbulence: model formulation and application to homogeneous turbulence, shear flows, and buoyant stratified flows," *Journal of Fluid Mechanics*, vol. 392, pp. 277–334, 1999.

[20] D. Lignell, A.R. Kerstein, G. Sun, and EI. Monson, "Mesh adaption for efficient multiscale implementation of one-dimensional turbulence," *Theoretical and Computational Fluid Dynamics*, vol. 27, no. 3-4, pp. 273–295, 2013.

[21] Peter A Lewis and Gerald S Shedler, "Simulation of nonhomogeneous poisson processes by thinning," *Naval Research Logistics (NRL)*, vol. 26, no. 3, pp. 403–413, 1979.

[22] Randall J McDermott, *Toward one-dimensional turbulence subgrid closure for large-eddy simulation*, Department of Chemical Engineering, University of Utah, 2005.

[23] Susumu Goto and Shigeo Kida, "Enhanced stretching of material lines by antiparallel vortex pairs in turbulence," *Fluid Dynamics Research*, vol. 33, pp. 403–431, 2003.

[24] Susumu Goto and Shigeo Kida, "Reynolds-number dependence of line and surface stretching in turbulence: folding effects," *Journal of Fluid Mechanics*, vol. 586, pp. 59–81, 2007.

[25] Sung Nok Chiu, Dietrich Stoyan, Wilfrid S Kendall, and Joseph Mecke, *Stochastic geometry and its applications*, John Wiley & Sons, 2013.

[26] Joseph Antoine Ferdinand Plateau, *Statique expérimentale et théorique des liquides soumis aux seules forces moléculaires*, vol. 2, Gauthier-Villars, 1873.

[27] Lord Rayleigh, "On the instability of jets," *Proceedings of the London mathematical society*, vol. 1, no. 1, pp. 4–13, 1878.

[28] P. Wu and G. Faeth, "Aerodynamic effects on primary breakup of turbulent liquids," *Atomization and Sprays*, vol. 3, no. 3, 1993.

[29] Falko T Meiselbach et al., "Application of odt to turbulent flow problems," 2015.

[30] A Movaghar, M Linne, M Oevermann, F Meiselbach, H Schmidt, and Alan R Kerstein, "Numerical investigation of turbulent-jet primary breakup using one-dimensional turbulence," *International Journal of Multiphase Flow*, vol. 89, pp. 241–254, 2017.

[31] Z Dai, W-H Chou, and GM Faeth, "Drop formation due to turbulent primary breakup at the free surface of plane liquid wall jets," *Physics of Fluids*, vol. 10, no. 5, pp. 1147–1157, 1998.

[32] Z Dai, LP Hsiang, and G Faeth, "Spray formation at the free surface of turbulent bow sheets," in *Proc. 21st ONR Symp. on Naval Hydrodynamics*, 1997, pp. 490–505.

[33] L-K Tseng, GA Ruff, and GM Faeth, "Effects of gas density on the structure of liquid jets in still gases," 1992.

[34] P-K Wu, L-K Tseng, and GM Faeth, "Primary breakup in gas/liquid mixing layers for turbulent liquids," *Atomization and Sprays*, vol. 2, no. 3, 1992.

[35] P-K Wu, RF Miranda, and GM Faeth, "Effects of initial flow conditions on primary breakup of nonturbulent and turbulent round liquid jets," *Atomization and sprays*, vol. 5, no. 2, 1995.

[36] P. Wu and G. Faeth, "Onset and end of drop formation along the surface of turbulent liquid jets in still gases," *Physics of Fluids (1994-present)*, vol. 7, no. 11, pp. 2915–2917, 1995.

[37] GM Faeth, L-P Hsiang, and P-K Wu, "Structure and breakup properties of sprays," *International Journal of Multiphase Flow*, vol. 21, pp. 99–127, 1995.

[38] KA Sallam, Z Dai, and GM Faeth, "Drop formation at the surface of plane turbulent liquid jets in still gases," *International journal of multiphase flow*, vol. 25, no. 6, pp. 1161–1180, 1999.

[39] KA Sallam and GM Faeth, "Surface properties during primary breakup of turbulent liquid jets in still air," *AIAA journal*, vol. 41, no. 8, pp. 1514–1524, 2003.

[40] HC Simmons, "The correlation of drop-size distributions in fuel nozzle sprays," *J. Eng. Power*, vol. 99, no. 3, pp. 309–319, 1977.

[41] Alan R Kerstein, Amirreza Movaghar, and Michael Oevermann, "Parameter dependences of the onset of turbulent liquid-jet breakup," *Journal of Fluid Mechanics*, vol. 811, 2017.

[42] DH. Wolf, FP. Incropera, and R. Viskanta, "Measurement of the turbulent flow field in a free-surface jet of water," *Experiments in fluids*, vol. 18, no. 6, pp. 397–408, 1995.

[43] Marcus Herrmann, "On simulating primary atomization using the refined level set grid method," *Atomization and Sprays*, vol. 21, no. 4, 2011.

[44] P Trontin, S Vincent, JL Estivalezes, and JP Caltagirone, "Direct numerical simulation of a freely decaying turbulent interfacial flow," *International Journal of Multiphase Flow*, vol. 36, no. 11, pp. 891–907, 2010.

[45] JO McCaslin and O Desjardins, "Theoretical and computational modeling of turbulence/interface interactions," in *Proceedings of the Summer Program*, 2014, p. 79.

[46] Olivier Desjardins, Guillaume Blanquart, Guillaume Balarac, and Heinz Pitsch, "High order conservative finite difference scheme for variable density low mach number turbulent flows," *Journal of Computational Physics*, vol. 227, no. 15, pp. 7125–7159, 2008.

[47] M. Owkes and O. Desjardins, "A computational framework for conservative, three-dimensional, un-split, geometric transport with application to the volume-of-fluid (VOF) method," *Journal of Computational Physics*, vol. 270, pp. 587–612, 2014.

[48] M. Owkes and O. Desjardins, "A Mesh-decoupled Height Function Method for Computing Interface Curvature," *Journal of Computational Physics*, vol. 281, 2015.

[49] R. Fedkiw, T. Aslam, B. Merriman, and S. Osher, "A non-oscillatory Eulerian approach to interfaces in multimaterial flows (the ghost fluid method)," *J. Comput. Phys.*, pp. 457–492, 1999.

[50] AN Kolmogorov, "On the breakage of drops in a turbulent flow," *Doklady Akademii Nauk SSSR*, vol. 66, pp. 825828, 1949.

[51] JU Brackbill, Douglas B Kothe, and Charles Zemach, "A continuum method for modeling surface tension," *Journal of computational physics*, vol. 100, no. 2, pp. 335–354, 1992.

[52] Wm T Ashurst and Alan R Kerstein, "Erratum:âĂIJone-dimensional turbulence: Variable-density formulation and application to mixing layersâĂİ[phys. fluids 17, 025107 (2005)]," *Physics of Fluids*, vol. 21, no. 11, pp. 119901, 2009.

[53] A Movaghar, M Linne, M Herrmann, AR Kerstein, and M Oevermann, "Modeling and numerical study of primary breakup under diesel conditions," *International Journal of Multiphase Flow*, vol. 98, pp. 110–119, 2018.

[54] AKMF Hussain and WC Reynolds, "Measurements in fully developed turbulent channel flow," *Journal of Fluids Engineering*, vol. 97, no. 4, pp. 568–578, 1975.

[55] R. Lebas, T. Menard, P.A. Beau, A. Berlemont, and F. Demoulin, "Numerical simulation of primary break-up and atomization: Dns and modelling study," *International Journal of Multiphase Flow*, vol. 35, no. 3, pp. 247–260, 2009.

[56] M. Linne, M. Paciaroni, E. Berrocal, and D. Sedarsky, "Ballistic imaging of liquid breakup processes in dense sprays," *Proceedings of the Combustion Institute*, vol. 32, no. 2, pp. 2147–2161, 2009.

[57] M. Linne, "Analysis of x-ray phase contrast imaging in atomizing sprays," *Experiments in fluids*, vol. 52, no. 5, pp. 1201–1218, 2012.

[58] A. Mansour and N. Chigier, "Turbulence characteristics in cylindrical liquid jets," *Physics of Fluids*, vol. 6, no. 10, pp. 3380–3391, 1994.

[59] R. Moser, J. Kim, and N. Mansour, "Direct numerical simulation of turbulent channel flow up to re= 590," *Phys. Fluids*, vol. 11, no. 4, pp. 943–945, 1999.

[60] R. Schmidt, A. R. Kerstein, S. Wunsch, and V. Nilsen, "Near-wall les closure based on one-dimensional turbulence modeling," *Journal of Computational Physics*, vol. 186, no. 1, pp. 317–355, 2003.

[61] F. Schulz, Ch. Glawe, H. Schmidt, and A. R. Kerstein, "Toward modeling of co2 multi-phase flow patterns using a stochastic multi-scale approach," *Environmental earth sciences*, vol. 70, no. 8, pp. 3739–3748, 2013.

[62] J. Shinjo and A. Umemura, "Simulation of liquid jet primary breakup: Dynamics of ligament and droplet formation," *International Journal of Multiphase Flow*, vol. 36, no. 7, pp. 513–532, 2010.

[63] Sh. Ross et al., *Stochastic processes*, vol. 2, John Wiley & Sons New York, 1996.

[64] G. Sun, D. Lignell, J. Hewson, and C. Gin, "Particle dispersion in homogeneous turbulence using the one-dimensional turbulence model," *Physics of Fluids*, vol. 26, no. 10, pp. 103301, 2014.

[65] A. Movaghar, M. Linne, M. Oevermann, F. Meiselbach, H. Schmidt, and A. R. Kerstein, "Numerical study of liquid breakup at the surface of turbulent liquid jets using one-dimensional turbulence," in *ILASS âĂŞ Europe 2014, 26th Annual Conference on Liquid Atomization and Spray Systems*, 2014.

[66] Olivier Desjardins, Heinz Pitsch, et al., "Detailed numerical investigation of turbulent atomization of liquid jets," *Atomization and Sprays*, vol. 20, no. 4, pp. 311, 2010.

[67] Olivier Desjardins, Vincent Moureau, and Heinz Pitsch, "An accurate conservative level set/ghost fluid method for simulating turbulent atomization," *Journal of Computational Physics*, vol. 227, no. 18, pp. 8395–8416, 2008.

[68] Olivier Desjardins, *Numerical methods for liquid atomization and application in detailed simulations of a diesel jet*, Stanford University, 2008.

[69] G Agbaglah, R Chiodi, and O Desjardins, "Numerical simulation of the initial destabilization of an air-blasted liquid layer," *Journal of Fluid Mechanics*, vol. 812, pp. 1024–1038, 2017.

[70] Mikhael Gorokhovski and Marcus Herrmann, "Modeling primary atomization," *Annu. Rev. Fluid Mech.*, vol. 40, pp. 343–366, 2008.

[71] Zachary Falgout, Mattias Rahm, David Sedarsky, and Mark Linne, "Gas/fuel jet interfaces under high pressures and temperatures," *Fuel*, vol. 168, pp. 14–21, 2016.

[72] Terry Parker et al., "Two-dimensional droplet size and volume fraction distributions from the near-injector region of high-pressure diesel sprays," *Atomization and Sprays*, vol. 16, no. 7, 2006.

[73] S Som and SK Aggarwal, "Effects of primary breakup modeling on spray and combustion characteristics of compression ignition engines," *Combustion and Flame*, vol. 157, no. 6, pp. 1179–1193, 2010.

[74] Alan R Kerstein, Wm T Ashurst, Scott Wunsch, and Vebjorn Nilsen, "One-dimensional turbulence: vector formulation and application to free shear flows," *Journal of Fluid Mechanics*, vol. 447, pp. 85–109, 2001.

[75] F Ben Rayana, A Cartellier, and E Hopfinger, "Assisted atomization of a liquid layer: investigation of the parameters affecting the mean drop size prediction,(paper iclass06-190)," *CD Proc. ICLASS*, 2006.

[76] Philippe Marmottant and Emmanuel Villermaux, "On spray formation," *Journal of fluid mechanics*, vol. 498, pp. 73–111, 2004.

[77] Zhaorui Li and Farhad A Jaberi, "Turbulence-interface interactions in a two-fluid homogeneous flow," *Physics of Fluids*, vol. 21, no. 9, pp. 095102, 2009.

[78] S. V. Apte, K. Mahesh, M. Gorokhokhovski, and P. Moin, "Stochastic modeling of atomizing spray in a complex swirl injector using large eddy simulation," vol. 32, pp. 2257–2266, 2009.

[79] A. Vallet, A. A. Burluka, and R. Borghi, "Development of an Eulerian model for atomization of a liquid jet," vol. 11, pp. 619–642, 2001.

[80] R. Lebas, G. Blokkeel, P.-A. Beau, and F. X. Demoulin, "Coupling vaporization model with the Eulerian-Lagrangian spray atomization (ELSA) model in diesel engine conditions," vol. 2005-01-0213, 2005.

[81] W. Ning, R. D. Reitz, A. M. Lippert, and R. Diwakar, "Development of a next-generation spray and atomization model using an Eulerian-Lagrangian methodology," in *17th International Multidimensional Engine Modeling User's Group Meeting*, Detroit, MI, 2007.

[82] A. R. Kerstein, W. T. Ashurst, S. Wunsch, and V. Nilsen, "One-dimensional turbulence: Vector formulation and application to free shear flow," vol. 447, pp. 85–109, 2001.

[83] T. Echekki, A. R. Kerstein, J.-Y. Chen, and T. D. Dreeben, "One-dimensional turbulence simulation of turbulent jet diffusion flames: Model formulation and illustrative applications," *Combustion and Flame*, vol. 125, pp. 1083–1105, 2001.

[84] Esteban D Gonzalez-Juez, Rodney C Schmidt, and Alan R Kerstein, "ODTLES simulations of wall-bounded flows," *Physics of Fluids*, vol. 23, pp. 125102, 2011.

[85] Mikhael Gorokhovski, "The stochastic Lagrangian model of drop breakup in the computation of liquid sprays," *Atomization and Sprays*, vol. 11, pp. 1514–1524, 2001.

[86] Dana W Lee and Robert C Spencer, *Photomicrographic studies of fuel sprays*, vol. 454, NACA, 1933.

[87] Behrouz Chehroudi, Shih-Hsiung Chen, Frediano V Bracco, and Yoshiaki Onuma, "On the intact core of full-cone sprays," *SAE Technical Paper*, vol. 850126, 1985.

[88] W. T. Ashurst and A. R. Kerstein, "Erratum to One-dimensional turbulence: Variable-density formulation and application to mixing layers," *Physics of Fluids*, vol. 21, pp. 119901, 2009.

[89] S. V. Apte, M. Gorokhokhovski, and P. Moin, "LES of atomizing spray with stochastic modeling of secondary breakup," *International Journal of Multiphase Flow*, vol. 29, pp. 1503–1522, 2003.

[90] K. Mahesh, G. Constantinescu, S. Apte, G. Iaccarino, F. Ham, and P. Moin, "Large-eddy simulation of reacting turbulent flows in complex geometries," *Journal of Applied Mechanics*, vol. 73, pp. 374–381, 2006.

[91] J. Chesnel, T. Ménard, J. Réveillon, and F.-X. Demoulin, "Subgrid analysis of liquid jet atomization," 2011.

[92] R. Jhavar and C. J. Rutland, "Using large eddy simulations to study mixing effects in early injection diesel engine combustion," *SAE Technical Paper*, vol. 2006-01-0871, 2006.

[93] N. Van Dam and C. Rutland, "Adapting diesel large-eddy simulation spray models for direct-injection spark-ignition applications," vol. in press, 2015.

[94] S. Toninin, M. Gavaises, and A. Theodorakakos, "Modelling high-pressure dense diesel sprays with adaptive local grid refinement," *International Journal of Heat and Fluid Flow*, vol. 29, pp. 427–448, 2008.

[95] AN Kolmogorov, "On the breakage of drops in a turbulent flow," in *Dokl. Akad. Navk. SSSR*, 1949, vol. 66, pp. 825–828.

[96] Stephen B Pope, "Turbulent flows," 2001.

[97] J Hinze, "0. 1975 turbulence," 1938.

[98] Hendrik Tennekes and John Leask Lumley, *A first course in turbulence*, MIT press, 1972.

[99] Hermann Schlichting, "Boundary-layer theory," 1968.

[100] Christoph Glawe, Falko T Schulz, Esteban D Gonzalez-Juez, Heiko Schmidt, and Alan R Kerstein, "Odtles simulations of turbulent flows through heated channels and ducts," in *TSFP DIGITAL LIBRARY ONLINE*. Begel House Inc., 2013.

[101] Thibault Ménard, Sebastien Tanguy, and Alain Berlemont, "Coupling level set/vof/ghost fluid methods: Validation and application to 3d simulation of the primary break-up of a liquid jet," *International Journal of Multiphase Flow*, vol. 33, no. 5, pp. 510–524, 2007.

[102] JP Fuster and S Marty Matas, "S. popinet, hoepffner j., a. cartellier, and s. zaleski. instability regimes in the primary breakup instability regimes in the primary breakup instability regimes in the primary breakup region of planar coflowing sheets," *J. Fluid Mech*, vol. 736, pp. 150–176, 2013.

[103] Thomas Otto, Maurice Rossi, and Thomas Boeck, "Viscous instability of a sheared liquid-gas interface: Dependence on fluid properties and basic velocity profile," *Physics of Fluids*, vol. 25, no. 3, pp. 032103, 2013.

[104] M Herrmann and M Gorokhovski, "An outline of a les subgrid model for liquid/gas phase interface dynamics," *Proceedings of the 2008 CTR Summer Program*, pp. 171–181, 2008.

[105] S He and M Seddighi, "Turbulence in transient channel flow," *Journal of Fluid Mechanics*, vol. 715, pp. 60–102, 2013.

[106] Xiaohua Wu and Parviz Moin, "A direct numerical simulation study on the mean velocity characteristics in turbulent pipe flow," *Journal of Fluid Mechanics*, vol. 608, pp. 81–112, 2008.

[107] Holger Grosshans, *Large eddy simulation of atomizing sprays*, 2013.

[108] H Grosshans, A Movaghar, L Cao, M Oevermann, R-Z Szász, and Laszlo Fuchs, "Sensitivity of vof simulations of the liquid jet breakup to physical and numerical parameters," *Computers & Fluids*, vol. 136, pp. 312–323, 2016.

[109] Sourabh V Apte, Krishnan Mahesh, Michael Gorokhovski, and Parviz Moin, "Stochastic modeling of atomizing spray in a complex swirl injector using large eddy simulation," *Proceedings of the Combustion Institute*, vol. 32, no. 2, pp. 2257–2266, 2009.

[110] V Moureau and O Desjardins, "A second-order ghost-fluid method for the primary atomization of liquid fuel in air-blast type injectors," in *Proceedings of the Summer Program*, 2008, vol. 143.

[111] MG Pai, I Bermejo-Moreno, O Desjardins, and H Pitsch, "Role of weber number in primary breakup of turbulent liquid jets in crossflow," *Center for Turbulence Research Annual Research Briefs*, pp. 145–158, 2009.

[112] Jennifer C Beale and Rolf D Reitz, "Modeling spray atomization with the kelvin-helmholtz/rayleigh-taylor hybrid model," *Atomization and sprays*, vol. 9, no. 6, 1999.

[113] Todd D Fansler and Scott E Parrish, "Spray measurement technology: a review," *Measurement Science and Technology*, vol. 26, no. 1, pp. 012002, 2014.

[114] Franz X Tanner, "Development and validation of a cascade atomization and drop breakup model for high-velocity dense sprays," *Atomization and sprays*, vol. 14, no. 3, 2004.

[115] MA Gorokhovski and VL Saveliev, "Analyses of kolmogorovâĂŹs model of breakup and its application into lagrangian computation of liquid sprays under air-blast atomization," *Physics of Fluids*, vol. 15, no. 1, pp. 184–192, 2003.

[116] Mikhael Gorokhovski, J Jouanguy, and A Chtab-Desportes, "Stochastic model of the near-to-injector spray formation assisted by a high-speed coaxial gas jet," *Fluid dynamics research*, vol. 41, no. 3, pp. 035509, 2009.

[117] MR Turner, SS Sazhin, JJ Healey, Cyril Crua, and SB Martynov, "A breakup model for transient diesel fuel sprays," *Fuel*, vol. 97, pp. 288–305, 2012.

[118] SP Lin and RD Reitz, "Drop and spray formation from a liquid jet," *Annual Review of Fluid Mechanics*, vol. 30, no. 1, pp. 85–105, 1998.

[119] Norman Dombrowski and PC Hooper, "The effect of ambient density on drop formation in sprays," *Chemical Engineering Science*, vol. 17, no. 4, pp. 291–305, 1962.

[120] H Grosshans, Elias Kristensson, R-Z Szász, and Edouard Berrocal, "Prediction and measurement of the local extinction coefficient in sprays for 3d simulation/experiment data comparison," *International Journal of Multiphase Flow*, vol. 72, pp. 218–232, 2015.

[121] Ragnar Lárusson, *Modal Analysis of Supersonic Flow Separation in Nozzles*, PhD dissertation, Chalmers University of Technology, 2017.

[122] Athanasios Papoulis, *Probability & statistics*, vol. 2, Prentice-Hall Englewood Cliffs, 1990.

Part II

PAPERS

PAPER I

Sensitivity of VOF Simulations of the Liquid Jet Breakup
to Physical and Numerical Parameters

Sensitivity of VOF simulations of the liquid jet breakup to physical and numerical parameters

H. Grosshans [a,e,*], A. Movaghar [b], L. Cao [c], M. Oevermann [b], R.-Z. Szász [a], L. Fuchs [d]

[a] Division of Fluid Mechanics, Lund University, Lund, Sweden
[b] Department of Applied Mechanics, Chalmers University of Technology, Gothenburg, Sweden
[c] Key Laboratory for Aerosol-Cloud-Precipitation of China Meteorological Administration, Nanjing University of Information Science & Technology, Nanjing, China
[d] Department of Mechanics, KTH, Stockholm, Sweden
[e] Institute of Mechanics, Materials and Civil Engineering, Université catholique de Louvain, Louvain-la-Neuve, Belgium

ARTICLE INFO

ABSTRACT

In this paper the characteristics of the primary breakup of a liquid jet is analyzed numerically. We applied the Volumes of Fluids (VOF) approach utilizing the Direction Averaged Curvature (DAC) model, to estimate the interface curvature, and the Direction Averaged Normal (DAN) model, to propagate the interface. While being used for the first time to predict liquid atomization, this methodology showed a high accuracy. The influence of varying the fluid properties, namely liquid-gas density and viscosity ratio, and injection conditions is discussed related to the required grid resolution. Resulting droplet sizes are compared to distributions obtained through the One-Dimensional Turbulence (ODT) model.

1. Introduction

Atomizing liquid jets are frequently occurring in industrial applications. For example, in combustion devices driven by liquid fuel, a fuel jet is injected in the combustion chamber. Before the combustion process takes place, the liquid jet needs to break up into small droplets, evaporate and mix with the surrounding air. The characteristics of the primary breakup of the fuel jet, i.e. liquid breakup length, local droplet diameter or velocity distributions, is crucial for the efficiency and exhaust level of the subsequent combustion process.

Due to its importance, these flows have been analyzed extensively by means of experiments in the last decades. For instance, Hiroyasu and Kadota [29] found an empirical best-fit relation between the fuel injection pressure, the ambient air density, the fuel mass flow rate and the Sauter Mean Diameter (SMD) of the resulting droplet distribution. In the following years Elkotb [9], Varde et al. [76] and Faeth et al. [10] included additionally the effects of liquid viscosity, liquid density and surface tension in the study. Furthermore, Reitz and Bracco [58] derived correlations for the breakup length of the liquid core.

Farth et al. [11] identified the implosion of cavitation bubbles, turbulence in the liquid jet and aerodynamic liquid-gas interaction to be the most dominant mechanisms for liquid jet atomization. Since the first and second mechanisms are related to phenomena occurring inside the injection nozzle, a number of researchers elucidated the influence of the in-nozzle flow on the following jet break-up. For example, Martínez-Martínez et al. [48] reported a high dependence of the spray penetration length on the nozzle diameter. Moreover, Suh and Lee [72] found that an increase in the nozzle length to width ratio enhances the generation of cavitation bubbles in the nozzle and fuel atomization.

Extensive reviews summarizing the knowledge concerning the fundamental aspects of the physics of the disintegration of liquid jets have been provided by Sirignano and Mehring [69] and Eggers and Emmanuel [8].

However, due to the large number of droplets, experimental measurements in these flow regions are very challenging. Especially when looking at droplet size distributions in optically dense sprays, results are blurred due to multi-scattering effects. Aiming to remove these effects, new experimental techniques have been developed in the recent years. Its potential to tackle this problem has been demonstrated by a group of methods based on Structured Laser Illumination Planar Imaging (SLIPI) [3]. A further advancement represents Dual-SLIPI [36] which even proved to be an adequate method to validate numerical models [20,21].

* Corresponding author.
   E-mail address: holger.grosshans@uclouvain.be (H. Grosshans).

Somewhat similar to SLIPI is an approach called ballistic imaging. However, in ballistic imaging the photons affected by multi-scattering are rejected before the camera, while they are rejected by image processing after the images have been recorded in SLIPI. Ballistic imaging has been used successfully to image the liquid/gas interface of intact liquid structures inside the dense spray region [see the review of Linne [43]].

Despite all experimental effort, the influence of the fluid properties on the liquid jet break-up is not yet fully understood. This is not only due to the optical density but also the full parameter range has not been studied so far. In particular, data concerning the effect of the viscosity of the surrounding gas is rare.

Furthermore, an important disadvantage of experiments is the difficulty to assess isolated effects. For this reason it is difficult to derive conclusions concerning the physics of the flow. For example from the above discussed experimental works it can not be concluded if the influence of the injection conditions on the jet break-up is caused by the changes in the in-nozzle flow, aerodynamic instabilities or something else.

Numerical simulations give the possibility to obtain results of a higher resolution and for isolated effects. The approaches usually applied to simulate sprays include the Eulerian–Eulerian and Lagrangian Particle Tracking (LPT) method. Both assume the liquid phase to be dispersed. The primary breakup of the liquid jet is not resolved, at its best it can be included in the simulation by modeling assumptions.

To simulate the primary breakup the liquid-gas interface is required to be resolved on the numerical grid. Following van Wachem and Schouten [75], methods that resolve the liquid-gas interface can be grouped into surface tracking methods and volume tracking methods. Surface tracking methods include the front tracking [74] and the level-set method [53,64]. These methods solve for the position of the interface while the volume of each phase is reconstructed. Therefore, surface tracking methods suffer in their original formulations from inaccuracies in the volume reconstruction. Also, the liquid volume in the domain is not conserved.

Volume tracking methods are the marker and cell [27] and the Volumes of Fluids (VOF) method [30]. These methods solve for the volume of each phase while the interface is reconstructed. Consequently, volume tracking methods suffer in their original formulations from errors in the interface curvature.

Recent reviews summarizing the available computational models used to describe the atomization of jets were given by Gorokhovski and Herrmann [18] and Jiang et al. [32]. However, all attempts to resolve a strongly curved interface require a very high grid resolution. Therefore, only in the recent years sufficient computational capabilities are available to perform this kind of simulations.

Important implementations include the one by Desjardins et al. [6] and Desjardins and Pitsch [7] who applied a version of level-set which aims to be nearly mass conservative. To handle the high gradients at the liquid-gas interface, they implemented the ghost-fluid method. Furthermore, a combined VOF/level-set method was used by Le Chenadec and Pitsch [38]. To improve the grid quality at the interface they allowed mesh deformations. Fuster et al. [13] utilized the VOF method and improved the grid resolution at the interface, depending on its curvature, applying the octree adaptive grid refinement. A further combination of methods was proposed by Menard et al. [50] who exploited the advantages of each the VOF, level-set and ghost-fluid approach. When compared to experimental data of Diesel injection [39], they recovered well the influence of the surrounding gas temperature. Shinjo and Umemura [65–67] developed a numerical method that applies the level-set method and an improved VOF formulation to combine the benefits of both. They analyzed the isolated aerodynamic breakup effect of a jet injected into still air while the in-nozzle flow was not taken into account. Through computing on a very fine grid (the nozzle diameter was resolved by 285 grid points) they could observe the ligament formation both from the mushroom tip edge and the liquid core surface. The droplet formation occurred from the ligament tip mostly by the short-wave mode.

Some researches aimed to evaluate the influence of the in-nozzle flow on the jet break-up. Som et al. [71] simulated only the nozzle flow solving the RANS (Reynolds Averaged Navier–Stokes) equations. The mass flow at the nozzle exit was analyzed depending on the fuel type, the injection pressure and the needle lift position. The subsequent coupling of RANS simulations of a nozzle flow to a liquid jet was performed by Yuan and Schnerr [80]. They demonstrated the enhancement of atomization due to cavitation by comparing a case applying a cavitation model with a case without. Moreover, recent time resolved Large Eddy Simulations (LES) by Ghiji et al. [16] of the flow inside a simplified nozzle and the subsequent atomization indicated a good agreement with experiments during early stages of Diesel injection. An approach without resolving the in-nozzle flow was recently followed by Xiao et al. [78]. They implemented the Rescaling and Recycling Method to facilitate generation of appropriate unsteady LES inlet conditions. The method was applied to replicate the turbulent nozzle outflow and to investigate its influence on the liquid jet. Siamas et al. [68], on the other hand, focused on evaluating the effect of swirl created inside the nozzle on the flow field of annular gas-liquid jets using detailed VOF simulations. They identified the swirling motion to be responsible for the development of a central recirculation zone.

Besides the above discussed model developments, a new formulation of the VOF approach utilizing the Direction Averaged Curvature (DAC) and Direction Averaged Normal (DAN) models was proposed by Lörstad and Fuchs [47]. However, the method was so far only applied to compute bubbles and not yet to liquid jets. Nevertheless, its accuracy when describing bubbles was intensively tested by Lörstad et al. [45,46]. It was reported to remedy some of the main issues in the VOF method: the DAC model was shown to model the surface tension forces highly accurate for high Reynolds number flows. Furthermore, the DAN model proved to be second-order accurate, mass conservative, without over- or undershoots of the phase variable, and, most important, non-diffusive.

A simplified approach to resolve a turbulent flow, which is worth mentioning, is called One-Dimensional Turbulence (ODT). It has been originally proposed by Kerstein [33] and was extended by Kerstein et al. [34] and Ashurst and Kerstein [2]. The major advantage compared to the above discussed methods lies in its computational efficiency which allows to explore flow regimes (Reynolds and Weber numbers here) which are not accessible by LES or Direct Numerical Simulation (DNS) methods. This methodology was used by Movaghar et al. [51] to study the outcome of liquid atomization. Despite the limitation of the model to simulate topologically simple flows with one dominant flow direction, e.g. simple jets or boundary layers, the method has proven to correctly predict many different scaling laws in turbulent flow.

To sum up, the theoretical research until today focuses mainly on the improvement of the computational methodology. So far only a few investigations focused on gaining physical insight.

In the present study for the first time the VOF/DAC/DAN method was applied to the case of an atomizing liquid jet. In this paper the capabilities of the VOF/DAC/DAN method to accurately model the primary breakup of a liquid jet in relation to the required grid resolution are discussed. The method is utilized to study the influence of the fluid properties, such as liquid-gas density and viscosity ratio, and the injection profiles on the flow. The results are compared to data generated by the ODT model. The comparison is based on the resulting droplet diameter distribution, which is most sensitive to the resolution of the applied grid.

2. Description of the VOF/DAC/DAN approach

The VOF method is used to handle the liquid and the gaseous phase. The flow field is described in an Eulerian framework by the incompressible, isothermal Navier–Stokes equations for multiphase flows without phase changes. The non-dimensional mass and momentum conservation equations are given by

$$\frac{\partial u_i}{\partial x_i} = 0 \tag{1}$$

$$\rho \frac{\partial u_i}{\partial t} + \rho u_j \frac{\partial u_i}{\partial x_j} = -\frac{\partial p}{\partial x_i} + \frac{1}{Re_{\text{jet}}} \frac{\partial}{\partial x_j} \left(\mu \left(\frac{\partial u_i}{\partial x_j} + \frac{\partial u_j}{\partial x_i} \right) \right) + \frac{\kappa \delta n_i}{We_{\text{jet}}} . \tag{2}$$

Herein u_i, p, ρ and μ denote the velocity components, the pressure, the density and the dynamic viscosity of the fluid, respectively. The last term on the right hand side of the momentum equation represents forces due to the surface tension, where δ is a Dirac function which vanishes everywhere except at the interface, κ the interface curvature and n_i the interface unit normal.

In the above equation, the jet Reynolds number, Re_{jet}, and the jet Weber number, We_{jet}, are based on the injection velocity U_{inj} and the nozzle diameter d_{noz}, namely

$$Re_{\text{jet}} = \frac{\rho_l U_{\text{inj}} d_{\text{noz}}}{\mu_l} \quad \text{and} \quad We_{\text{jet}} = \frac{\rho_g U_{\text{inj}}^2 d_{\text{noz}}}{\sigma} . \tag{3}$$

In this equation σ denotes the surface tension and the indices l and g the liquid and the gas phase, respectively. The fluid properties in Eqs. (2) and (3) are calculated linearly dependent on the phase variable α as

$$\rho = \rho_g + (\rho_l - \rho_g)\tilde{\alpha} \quad \text{and} \quad \mu = \mu_g + (\mu_l - \mu_g)\tilde{\alpha} \tag{4}$$

where $\tilde{\alpha}$ is a smoothed field of α using a smoothing function described by Rudman [62].

The governing equations are discretized by the finite differences method. The convective terms are approximated by a third-order accurate upwind scheme, the diffusive and pressure terms by fourth-order central schemes and the time derivatives by an implicit second order backward scheme. A coupling between the pressure and the velocity is used which is based on the simultaneous update of the dependent variables. The approach is SIMPLE like and described in detail for single-phase flows by Fuchs and Zhao [12].

2.1. Turbulence modeling

The turbulent flow field is simulated by performing a LES, where the discretization scheme applied on the grid acts as a low-pass filter. A detailed discussion concerning LES can be found, for instance, in the textbooks of Pope [55] or Sagaut [63]. The grid size, h, is considerably smaller than the largest flow scales but it is larger than the Kolmogorov eddies ($l_0 \gg h \gg \eta$) for large Reynolds numbers. Therefore, the large scale structures are captured, while the small scale structures are filtered out. When applying any spatial filtering to the governing equations, new terms appear; these are called Sub-Grid-Scale (SGS) terms. LES is based on Kolmogorov's hypothesis: the large scale structures are dependent on the specific flow situation, while the behavior of the small scale structures is isotropic and geometry independent, i.e. universal. If the scales that are filtered out are small enough to be considered as universal, the SGS terms can be closed by a turbulence model.

A large number of models have been formulated in the past out of which many are based on the simple Smagorinsky model [70]. A widely used variant is the dynamic calculation of the Smagorinsky constant [15] using the least-square technique and averaging

in one direction as proposed by Lilly [42]. This approach has been implemented to study a wide range of flows such as pneumatic conveying [22], reactive flows [40] or the atmospheric boundary layer [35], just to name a few.

As an indicator for the definition of an appropriate grid size the size of the Taylor scale eddies can be used, as they are defined to be located between integral scale and Kolmogorov scale eddies. In general it can be stated that the smaller the filter size is the smaller is the contribution of the SGS terms and the more accurate the solution will be. If the grid is fine enough, the contribution of SGS terms even vanishes and can therefore be neglected.

The SGS terms have a function of dissipating energy that is transferred by the energy cascade. To account for dissipation in this work the 'implicit turbulence model' [4] with no explicit SGS expression is used. By not including explicit dissipation, the overall dissipative properties of the discrete system are reduced. The neglected dissipative effects of an eventual explicit SGS model are accounted for by using dissipative numerical schemes. It must be emphasized that one may rely on such a model only if the resolution is fine enough, i.e. a considerable part of the turbulence energy spectrum is resolved.

The implicit LES approach has been successfully applied in comparable works as well, e.g. by Desjardins et al. [6]. In our simulations the grid is chosen to be approximately three times finer than the size of Taylor scale eddies. It is shown in Section 4.1 that the influence of the unresolved scales on the velocity field can be considered negligible. In fact, the limiting parameter for the grid resolution in the herein studied cases are apparently not the turbulent scales but the droplet sizes. Therefore, the preference of the simple implicit LES over a more complex model is justified.

2.2. Surface tension modeling and motion of the phase interface

Following the Continuum Surface Force (CSF) model as described in [5], the Dirac function and the interface unit normal in Eq. (2), are replaced by

$$\delta n_i = \frac{\partial \alpha}{\partial x_i} . \tag{5}$$

The normal direction of the interface, which is needed for the phase transport and the curvature, is derived from the α field using the DAN model as presented by Lörstad and Fuchs [47]. To reduce the computational effort, the calculations are carried out in the direction of the largest component of the normal vector. A distance function, Λ, is introduced which is estimated based on the volume fractions of the neighboring cells. These volume fractions are summed up in the calculation direction. It gives the distance of the interface in the neighboring cells to the center of the current cell. For the z-direction this leads to the expression for the interface normal, namely

$$n = \begin{pmatrix} n_x \\ n_y \\ n_z \end{pmatrix} = \frac{\frac{\partial \alpha}{\partial x_z}}{\left| \frac{\partial \alpha}{\partial x_z} \right|} \cdot \begin{pmatrix} -\frac{\partial \Lambda}{\partial x_x} \\ -\frac{\partial \Lambda}{\partial x_y} \\ 1 \end{pmatrix} . \tag{6}$$

This procedure, as it considers only the largest normal component, is simpler and faster as comparable methods, for example those proposed by Puckett et al. [57] or Renardy and Renardy [59].

Finally, the curvature is calculated applying the DAC model, as given by Lörstad and Fuchs [47]. As for the DAN model, the computational effort is reduced by carrying out the calculations in the direction of the largest normal component. In a similar way a distance function Λ is established. For the z-direction the expression for the interface curvature is given by

$$\kappa = \frac{n_z}{|n_z|} \left(\frac{\Lambda_{ii}}{|n|} - \frac{\Lambda_i \Lambda_j \Lambda_{ij}}{|n|^3} \right) . \tag{7}$$

To apply the surface tension forces to the flow equations, the topology of the gas-liquid interface needs to be known. Therefore, for the phase field, α, which represents the liquid volume fraction, the transport equation

$$\frac{\partial \alpha}{\partial t} + \frac{\partial u_i \alpha}{\partial x_i} = 0 \qquad (8)$$

is solved. When solving this equation it is of utmost importance to be not too diffusive in order to keep the liquid gas interface sharp and to use a stable approach at the same time.

Several approaches have been proposed and compared by Rudman [61] and Gopala and van Wachem [17]. In both papers the ability to keep the interface sharp and the mass conserved has been studied with simplified advection and shear flow cases and a case capturing the progression of the Rayleigh–Taylor instability. Rudman [61] reported the superior behavior of the direction split method proposed by Young [79] compared to the Simplified Line Interface Calculation (SLIC) method [52], the original VOF method [30] and the flux-corrected transport (FCT) method proposed by Rudman [61]. Gopala and van Wachem [17] considered the Lagrangian Piecewise Linear Interface Construction (PLIC) [75], the CICSAM [73] and the inter-gamma differencing scheme [31] to be preferable over the above mentioned FCT method.

Based on the discussion above, the direction split method proposed by Young [79], extended from 2D to 3D is applied in this work. For details concerning the implementation, the reader is referred to the original paper by Lörstad [44].

Lörstad et al. [45,46], Lörstad and Fuchs [47] and Lörstad [44] reported several test cases which prove the quality of the above described VOF methodology. A three-dimensional Stokes flow (Re = 10^{-6}) past a fix liquid sphere represents one of them. The simulations for different viscosity ratios were compared to analytical solutions given by Panton [54]. For a viscosity ratio of unity the results indicated that the flow solution is second order accurate [47]. However, the viscosity model (c.f. Eq. (4)) seems to introduce a first order error. The same conclusions were drawn when the velocity of a bubble rising in a quiescent liquid due to gravity was computed on different grid resolutions.

Furthermore, three-dimensional advection tests similar to the one used by Aniszewski et al. [1] and the two-dimensional tests by Rudman [62] and Gerlach et al. [14] were performed [47]. Herein, a liquid of an initially spherical shape is deformed by a pre-defined flow field. After a certain period of time the flow is reversed which would result, in the case of a perfect advection scheme, in a liquid of the initial shape. This type of tests evaluate the phase transport model and the DAN model. Second order accuracy was found for unidirectional and rotating flow fields while the accuracy showed to reduce slightly for large deformations.

The results of a commonly used case [e.g. by [1,14,37,49,56,59,77]] to test the surface tension modeling are given by Lörstad et al. [45,46]. Therein, a droplet is placed in a zero velocity field as initial and boundary condition. The solution is usually subjected to spurious unphysical currents. The order of accuracy showed to be the same than for the immersed boundary method and the PROST VOF-model by Renardy and Renardy [59] even though the magnitude of the error is slightly larger. However, the spurious currents diminished with time. Moreover, the test revealed that, if the droplet is resolved by ten cells over the diameter, the maximum error for κ is approximately 4%. As the Weber numbers in engines are usually large, the error originating from the surface tension term is considered to be small.

Additionally to the above discussed tests, the VOF/DAC/DAN approach has been successfully compared to experimental results for air bubbles rising in water due to gravity (by Lörstad and Fuchs [47] for a similar set-up than the one used by Popinet [56]) and air injection into a water channel [44].

3. Description of the ODT model

For comparison of the droplet size distributions obtained by the VOF approach, in the present study the ODT model is applied. The model is summarized in the following section. However, for a detailed description of the method, the reader is referred to its original formulation by Kerstein [33] and its extensions by Kerstein et al. [34] and Ashurst and Kerstein [2].

ODT is a stochastic model resolving a turbulent flow along a notional line of sight through a 3-dimensional flow. The main advantages of such a one-dimensional stochastic simulation approach are twofold. First, a one-dimensional formulation enables affordable simulations of high Reynolds number turbulence over the full range of relevant length and time scales. On the contrary, computational cost considerations often limit the application of DNS to flows of moderate Reynolds numbers. Second, the model has proven to successfully capture diverse flow behaviors. Furthermore, it permits high resolution of property gradients, which is needed to capture details of, e.g., boundary layers, flame structures and flow structures close to phase boundaries.

ODT has recently been used by Movaghar et al. [51] to model the primary breakup of statistically stationary turbulent liquid jets. This was achieved by extending ODT to deal with the interaction between turbulence and surface tension energy. Moreover, Rayleigh type wave instabilities and shear driven breakup mechanism were accounted for.

The flow on an ODT line is time-advanced by solving a set of equations given by

$$\frac{Du_i(y,t)}{Dt} = \nu \frac{\partial^2 u_i(y,t)}{\partial y^2} - S_{u_i} \qquad (9)$$

$$\frac{D\phi(y,t)}{Dt} = \varrho \frac{\partial^2 \phi(y,t)}{\partial y^2} - S_\phi . \qquad (10)$$

Here, u_i are the velocity components and ϕ is a passive scalar. The coefficients ν and ϱ denote the molecular viscosity and mass diffusivity, respectively. S_{u_i} and S_ϕ represent source terms. In the present application the turbulent jet decays and S_{u_i} is equal to zero.

In ODT turbulent advection is modeled by a series of stochastic eddy events. Each eddy event is modeled by applying an instantaneous mapping of the property field, called triplet map [c.f. [51]]. ODT samples eddy events from an instantaneous eddy event rate distribution that evolves with the flow. These events are individually parameterized by the position y_0 and the size l. The reconstruction of the distribution every time an eddy event or an advancement of Eq. (9) takes place is computationally expensive. Therefore, for computational efficiency in ODT eddy events are sampled using an equivalent Monte-Carlo numerical procedure called thinning which was originally proposed by Lewis and Shedler [41]

4. Results and discussion

The VOF simulations presented herein were run in simple cuboid domains as sketched in Fig. 1. A Dirichlet condition was applied at the inlet, i.e. the velocity vector is given. The velocity components and scalars at the outlet correspond to a zero-gradient condition. At the walls no-slip and zero-gradient was imposed for the velocity components and the scalars, respectively.

The computed operation conditions are oriented on realistic parameters of Diesel injection. However, to improve numerical stability, the liquid-gas viscosity and density ratio were reduced. The inlet nozzle was assumed to have a diameter of $d_{noz} = 10^{-4}$ m. A uniform velocity profile at the nozzle orifice of $U_{inj} = 500$ m/s was
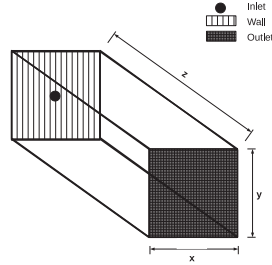
Fig. 1. Geometry of the domain used in the VOF simulations and boundary conditions.

Fig. 2. Average liquid volume fraction along the jet centerline. The jet is considered to be atomized at a downstream position of $z = 30 \, d_{noz}$. The parameters of the jet are $Re_{jet} = 15,000$, $We_{jet} = 10,000$, $\rho_l/\rho_g = 10$ and $\mu_l/\mu_g = 3.42$.

Fig. 3. Average streamwise velocity at a downstream position of $z = 30 \, d_{noz}$ for different grid resolutions. The simulations performed with a grid resolution of $h = 0.05 \, d_{noz}$ are considered to give grid independent results for the velocity. The parameters of the jet are $Re_{jet} = 15,000$, $We_{jet} = 10,000$, $\rho_l/\rho_g = 10$ and $\mu_l/\mu_g = 3.42$.

considered. All results presented within this paper are normalized to d_{noz} and U_{inj}.

In the following section the sensitivity of results obtained by VOF to numerical parameters, namely the grid resolution and domain size, is assessed. Afterwards the effect of varying the liquid-gas density and viscosity ratio is evaluated. Further, the results are compared to data obtained using the ODT method. Finally, the influence of in-nozzle flow on the jet development is studied.

4.1. Sensitivity of VOF to numerical parameters

The objective of the present study is to study the primary break-up of a liquid jet. For this purpose, a plane normal to the *z*-axis was introduced in the domain where the liquid phase which passes by is analyzed. The algorithm to extract information concerning the liquid is based on the algorithm described by Herbert et al. [28] and extended by Grosshans et al. [23–25] to time dependent problems. By identifying the connected liquid phase which passes the layer per timestep, the total volume of each liquid structure is determined. This quantity is used to calculate the radius equivalent to a spherical droplet.

To capture the characteristics of the fully atomized jet, this plane needs to be placed far enough downstream of the injector. On the other hand, it shall be close enough to the nozzle so the droplets are large enough to be accurately described by the VOF approach.

To define the appropriate position for this plane, a jet of $Re_{jet} = 15,000$ and $We_{jet} = 10,000$ was simulated. Moreover, a liquid-gas density and viscosity ratio of 10 and 3.42, respectively, were maintained. For this configuration the speed of sound is estimated to be 1500 m/s inside the liquid and 660 m/s inside the gas. Thus, the flow can be considered incompressible within the largest part of the domain. The dimensions of the computational domain were $x \times y \times z = 16 \times 16 \times 55 \, d_{noz}$ containing cells of a uniform size of $h = 0.05 \, d_{noz}$. It is shown below that this numerical set-up is well chosen.

The resulting average liquid volume fraction along the jet centerline, see Fig. 2, is chosen as the criterion to identify the position of the jet break-up. For regions of the intact liquid jet a liquid volume fraction of unity is observed. Thus, the jet starts to break up after a downstream position of $z = 13 \, d_{noz}$. It is decided to consider the jet to be fully broken up when the centerline liquid volume fraction is below 0.25. Thus, in the following the characteristics of the atomization is assessed at a downstream position of $z = 30 \, d_{noz}$.

To test the grid sensitivity of the results, the VOF equations were solved on different resolutions including cell sizes of 0.2, 0.1 and 0.05 d_{noz}. The resulting average streamwise velocity profiles at a downstream position of $z = 30 \, d_{noz}$ are shown in Fig. 3. The
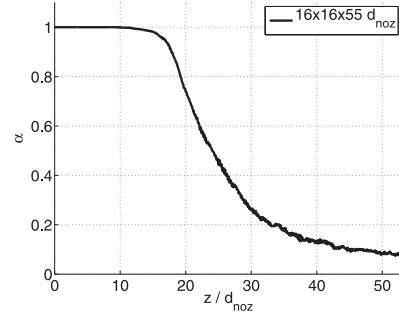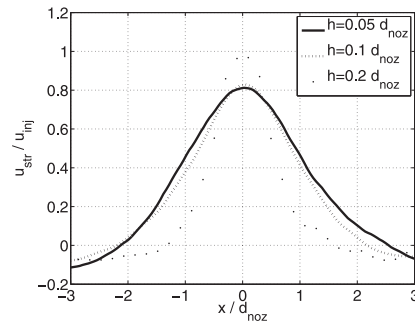
coarsest grid in the case of $h = 0.2 \, d_{noz}$ causes high numerical diffusion which damps turbulence. Thus, the spray does not widen up as much as it can be seen for finer grids. The velocity profiles relating to grid resolutions of $h = 0.1 \, d_{noz}$ and $h = 0.05 \, d_{noz}$ are very similar. Comparing their centerline velocity a difference of less than 4% is observed. Therefore, the simulations performed with a grid resolution of $h = 0.05 \, d_{noz}$ are considered to give grid independent results for the velocity.

This is supported by a Richardson extrapolation [according to the procedure described by Roache [60]] concerning the same simulations which has been reported by Grosshans [19] and Grosshans et al. [26]. They evaluated the average streamwise velocity for three points in the domain. In summary, the apparent order of discretization showed to be between 2.5 and 3.7, which is in the expected range. The relative errors for $h = 0.05 \, d_{noz}$ were considered to be sufficiently low.

Besides the velocities, also the grid sensitivity of the resulting drop size distributions was analyzed. The high sensitivity of the droplet diameters to the used grid resolution has been pointed out earlier, e.g. by Gorokhovski and Herrmann [18]. Results extracted at $z = 30 \, d_{noz}$ are presented in Fig. 4. Further to the above reported grid resolutions, an even finer grid, namely $h = 0.0375 \, d_{noz}$, was included in the study. It is interesting to note that the droplet diameter distributions obtained with a cell size of $h = 0.05 \, d_{noz}$ are relatively reliable down to a droplet diameter of $d_d/h = 2$. This confirms the excellent ability of the DAC/DAN method to capture the curvature of the liquid-gas interface. Nevertheless, smaller
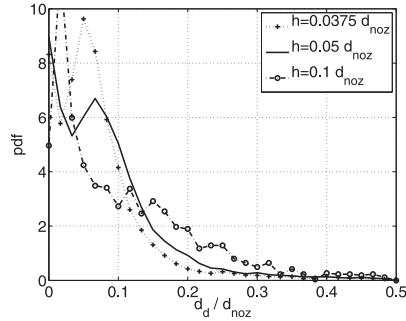
Fig. 4. Droplet diameter distributions at a downstream position of $z = 30\ d_{noz}$ for different grid resolutions. The results confirm the ability of the DAC/DAN approach to capture the curvature of the liquid-gas interface down to droplet sizes of $d_d/h = 2$. Smaller droplets are, however, not resolved. The parameters of the jet are $Re_{jet} = 15,000$, $We_{jet} = 10,000$, $\rho_l/\rho_g = 10$ and $\mu_l/\mu_g = 3.42$.

Fig. 5. Average streamwise velocity at a downstream position of $z = 30\ d_{noz}$ for different domain sizes. The velocity profiles in spanwise direction of $\pm 2\ d_{noz}$ are nearly identical. Thus, a domain of the size of $8\ d_{noz}$ in x and y-direction is judged to be sufficient. The parameters of the jet are $Re_{jet} = 15,000$, $We_{jet} = 10,000$, $\rho_l/\rho_g = 10$ and $\mu_l/\mu_g = 3.42$.

droplets are not properly resolved. However, the droplets which are smaller than $d_d/h = 2$ contribute only 0.87% to the total liquid mass at the considered downstream position. The low liquid mass carried by the unresolved droplets carries, due to their small size, little kinetic energy. Thus, the related error is small.

On the other hand all investigated cases are of a high Weber number. Therefore, the surface tension term, and consequently the interface curvature has a low contribution to the momentum equation, c.f. Eq. (2). This explains why the velocity profiles presented in Fig. 3 show a better convergence than the corresponding droplet diameter distributions.

Following the above discussions, the simulations described in the following were run on a grid with a cell size of $h = 0.05\ d_{noz}$.

Not only the grid resolution but also the domain size is investigated. Therefore, the above described jet was run is run in a domain of the size of 8, 12 and 16 d_{noz} in x and y-direction. The average streamwise velocity profiles at a downstream position of $z = 30\ d_{noz}$ are shown in Fig. 5. It can be seen that the velocities at the centerline and in an area in spanwise direction of $\pm$ 2 d_{noz} are nearly identical. This is the region where by far most of the liquid mass is transported. Thus, a domain of the size of 8 d_{noz} in x and y-direction is judged to be sufficient and was considered in the following simulations.

4.2. Liquid-gas density ratio and comparison to ODT

To assess the sensitivity of the atomization on the fluid properties, simulations with liquid-gas density ratios of 10, 20 and 30 were performed. The other conditions are identical to those described in the previous section, namely $Re_{jet} = 15,000$, $We_{jet} = 10,000$ and $\mu_l/\mu_g = 3.42$.

Snapshots of the penetration of the liquid jet of a liquid-gas density ratio of 10 are shown in Fig. 6. Fig. 6(b) depicts the jet very short after the beginning of the injection forming a mushroom cap shape. In Fig. 6(c) a detail of the liquid core at later stage is enlarged. One can see the formation of Kelvin–Helmholtz instabilities at the surface. These lead to the stripping off of small droplets from the jet surface. As these droplets are small, their Stokes number is also small, hence their trajectories are strongly influenced by turbulent eddies, which leads to the dispersion of the spray.

The droplet diameter distributions for different liquid-gas density ratios are presented in Fig. 7. The results of the VOF simulations (Fig. 7(a)) are compared to the results of the ODT simulations (Fig. 7(b)).
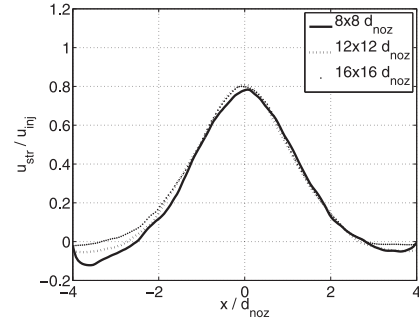
In opposite to the ODT simulations, the VOF distributions stemming from the simulations show two peaks. The first peak is located around $d_d/d_{noz} \approx 0.02$ and the second peak around $d_d/d_{noz} \approx 0.08$. While the second peak is close to the resolution limit of the method, the first peak is clearly beneath. In the resolved region, both simulation types give distributions of a similar shape. However, the droplets predicted by ODT are generally larger that those resulting from the VOF simulations. This is also related to the method to analyze the droplets: the sizes predicted by ODT relate to droplets which are generated directly by the primary break-up. Thus, they did not experience any secondary break-ups which further decrease the droplet size. The droplets presented in Fig. 7(b) are, therefore, not related to a fixed position in space. Instead the distribution includes all droplets which are separated at any time from the liquid core. The VOF results (Fig. 7(a)), on the other hand, represent droplet distributions obtained at a fixed plane in space. Therefore, also a certain amount of secondary breakups is included in the results. Consequently, the distributions predicted by VOF show smaller droplets compared to ODT.

While the limitation of the VOF results correspond to the applied grid resolution, the leading order error in the ODT is assumed to be related to not capturing 3-dimensional effects. Thus, the effect of swirls or vortices are not reflected in the results presented in Fig. 7(b).

Comparing the simulations of different liquid-gas density ratios with each other, both VOF and ODT show little differences. Thus, both approaches indicate a low sensitivity of the droplet size distributions to the range of studied conditions. However, the VOF approach predicts more large, i.e. resolved, droplets the higher the liquid-gas density ratio is. For lower liquid-gas density ratios the jet breaks up faster, generating smaller droplets through secondary breakup.

The streamwise and spanwise droplet velocities of the three cases predicted by VOF are presented in Fig. 8. The case of the highest density ratio shows the fastest and the case of the lowest density ratio the slowest droplets, c.f. Fig. 8(a). This is reasonable since larger droplets have a higher inertia and therefore their trajectories are the least disturbed by turbulent eddies. In the case of the low density ratio, the droplets are the smallest and the aerodynamic drag force acting on the droplets is the highest due to a high gas density. However, the spanwise droplet velocity distribution (Fig. 8(b)) is only little influenced in the range of studied conditions.

(a) The complete jet at $t = 42.6$. The blue surface describes the isosurface of $\alpha = 0.5$.
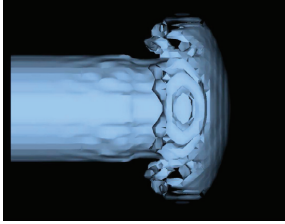
(b) The jet at $t = 1.1$, forming a mushroom cap shape.
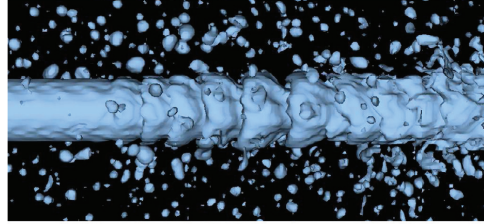
(c) Detail of the jet between $z = 8$ and $z = 16$ at $t = 58.6$, forming Kelvin-Helmholtz instabilities on the liquid surface.

Fig. 6. Snapshots of the jet penetration of case of $Re_{jet} = 15{,}000$, $We_{jet} = 10{,}000$, $\rho_l/\rho_g = 10$ and $\mu_l/\mu_g = 3.42$. (For interpretation of the references to colour in this figure legend, the reader is referred to the web version of this article.)

(a)

(b)

Fig. 7. Droplet diameter distributions at a downstream position of $z = 30\ d_{noz}$ resulting from the VOF (a) and the ODT (b) simulations for variations of the liquid gas density ratio. The parameters of the jet are $Re_{jet} = 15{,}000$, $We_{jet} = 10{,}000$ and $\mu_l/\mu_g = 3.42$.

4.3. Liquid-gas viscosity ratio

Further, the influence of the liquid-gas viscosity ratio on the primary break-up was computed using VOF. For this purpose liquid jets of the properties $\mu_l/\mu_g = 1$, 2 and 7 were simulated. The other conditions are identical to those described in the previous section, namely $Re_{jet} = 15{,}000$ and $We_{jet} = 10{,}000$ while ρ_l/ρ_g was set to 10.

The resulting droplet diameter distributions are presented in Fig. 9. In opposite to the results for different density ratios, the distributions for different viscosity ratios differ significantly from each other. The case of the smallest liquid-gas viscosity ratio creates the largest droplets, while the case of the highest liquid-gas viscosity ratio creates the smallest droplets. As the jet Reynolds number is kept constant for the three cases, an increase in the liquid-gas viscosity ratio results in an increase of the Reynolds

Fig. 8. Streamwise (a) and spanwise (b) droplet velocity distributions at a downstream position of $z = 30\ d_{noz}$ resulting from the VOF simulations for variations of the liquid gas density ratio. The parameters of the jet are $Re_{jet} = 15,000$, $We_{jet} = 10,000$ and $\mu_l/\mu_g = 3.42$.
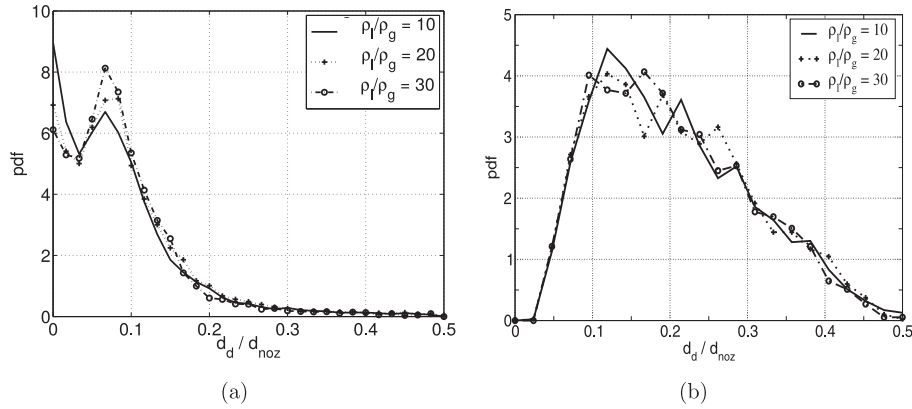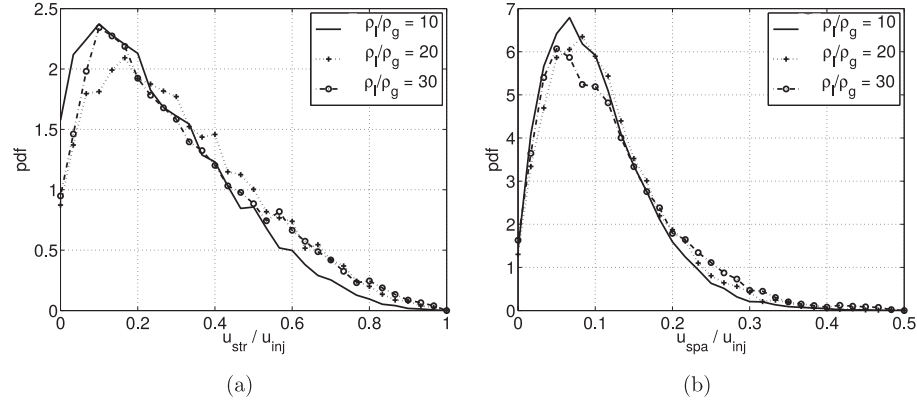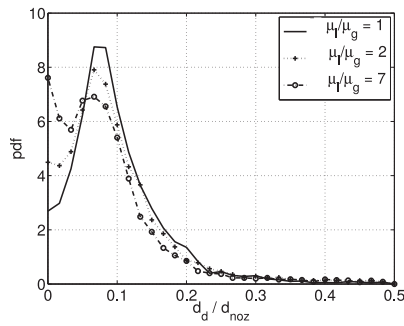

Fig. 9. Droplet diameter distributions at a downstream position of $z = 30\ d_{noz}$ resulting from the VOF simulations for variations of the liquid gas viscosity ratio. The parameters of the jet are $Re_{jet} = 15,000$, $We_{jet} = 10,000$ and $\rho_l/\rho_g = 10$.

Fig. 10. Spanwise droplet velocity distributions at a downstream position of $z = 30\ d_{noz}$ resulting from the VOF simulations for variations of the liquid gas viscosity ratio. The parameters of the jet are $Re_{jet} = 15,000$, $We_{jet} = 10,000$ and $\rho_l/\rho_g = 10$.
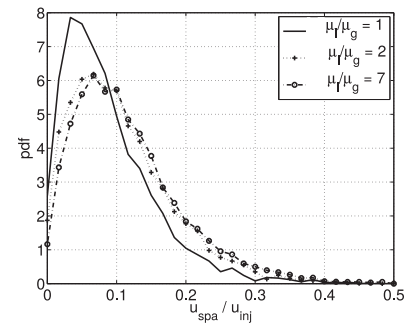
number of the gaseous phase. This leads to more turbulent structures in the gas, which enhance the instability mechanisms acting on the liquid surface. These instabilities cause breakups and, consequently, smaller droplets.

Since small droplets have less inertia than large droplets, thus, their trajectories are more influenced by turbulent eddies. Furthermore, in cases of a viscosity ratio of 2 and 7, for which the smallest droplets occur, the gaseous phase contains the most turbulent structures. For this reason the droplets are the most dispersed in these cases and their spanwise velocities, (c.f. Fig. 10) are the highest.

The average streamwise velocity profiles as function of variations of the liquid-gas viscosity ratio are depicted in Fig. 11. The negative streamwise velocities in this region account for the backflow which is caused by the air entrained by the spray. The cases containing the largest droplets, i.e. for a low viscosity ratio, show the highest centerline velocity, due to the high inertia of the droplets. The smaller the droplets, the lower the centerline velocity and the more the spray is widened up due to turbulent dispersion.

4.4. In-nozzle flow

The cases considered so far employ a uniform velocity profile as inlet condition for the liquid jet. To assess the jet development
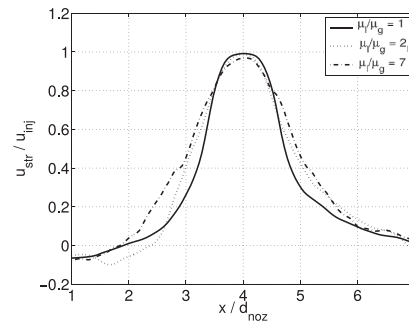
Fig. 11. Average streamwise velocity at a downstream position of $z = 30\ d_{noz}$ for different liquid gas viscosity ratio resulting from the VOF simulations. The parameters of the jet are $Re_{jet} = 15,000$, $We_{jet} = 10,000$ and $\rho_l/\rho_g = 10$.

under conditions closer to real fuel injection, the influence of the flow inside the nozzle is taken into account.

In a separate simulation the flow inside a nozzle was computed and provided by Altimira (2013)[1] using the OpenFOAM solver

---

[1] Personnal communication.

in-nozzle   in-nozzle, hot fuel

$t = 71$

$t = 142$

$t = 213$
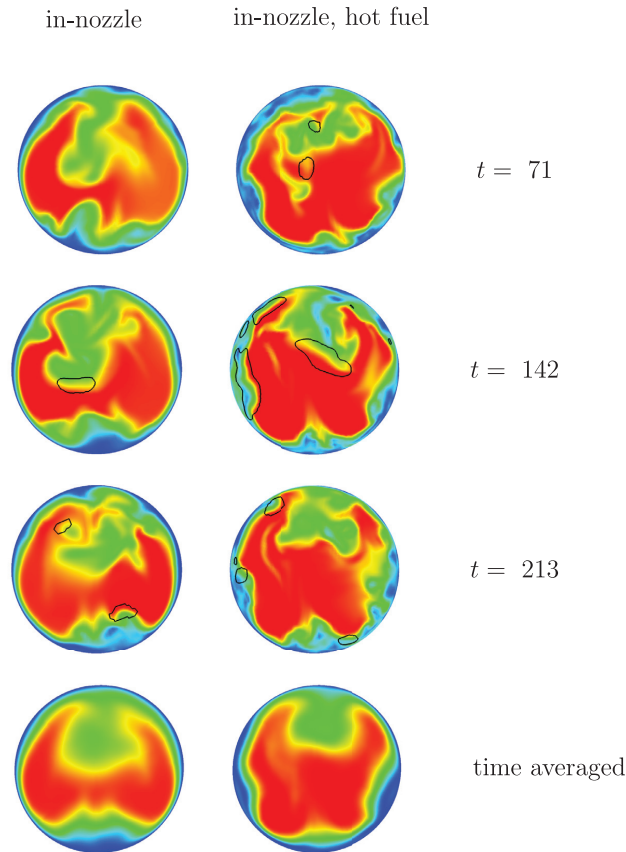
time averaged

Fig. 12. Instantaneous and time averaged fields at the nozzle orifice plane which are used as starting condition of the jet to simulate the effect of the in-nozzle flow (left) and the in-nozzle flow of hot fuel (right). The color gives the velocity magnitude where the blue color corresponds to zero and the red color to the maximum velocity. The black lines indicate the location of cavitation bubbles. (For interpretation of the references to colour in this figure legend, the reader is referred to the web version of this article.)

interPhaseChangeFoam. The chosen geometry corresponds to a representative Diesel nozzle of an orifice diameter of 130 μm.

The in-nozzle simulation applied a LES-VOF approach taking into account the generation of cavitation bubbles. Two different inlet flow fields were considered which both reflect the turbulence and cavitation inside the nozzle. However, while the liquid in one simulation is at ambient temperature (298 K), the second simulation accounts a liquid temperature of 348 K. The results of these simulations in terms of velocity profiles and liquid volume fractions served as instantaneous inlet conditions for the jet simulations presented herein. Instantaneous snapshots and time averages of the inlet conditions at the orifice plane are given in Fig. 12. For both cases the asymmetry of the profiles caused by the in-nozzle geometry can be observed. For comparison, a third case is run applying a uniform velocity profile at the inlet.

All three cases have a jet Reynolds number of 8000 and a jet Weber number of 330. The density ratio of the liquid and the cavitation vapor bubbles was 480 in the in-nozzle simulations. The corresponding ratio of viscosity was 88. Due to numerical stability issues, the liquid-gas density and viscosity ratios are reduced to 18 in the liquid jet simulation. For simplification, the vapor bubbles, originated from cavitation in the nozzle, are assumed to be of the

same properties as the surrounding gas phase. It is recalled from Section 2 that no phase change model is applied.

With the discussion in the introduction in mind, it is expected that the in-nozzle flow will create disturbances transported through the liquid jet and leading to a faster break-up. This is confirmed when looking at the snapshots of the jet development in Fig. 13. While the jet started with a top-hat profile propagates straight, the jets of the cases accounting for in-nozzle turbulence are stronger disturbed and propagate slower. As the collapse of cavitation bubbles is not modeled here, this effect is caused by turbulent structures created inside the nozzle. Also, the gas bubbles inside the liquid jet caused by cavitation in the nozzle enhance the break-up. The propagation of the tip of the liquid jets over time is shown in Fig. 14. The figure confirms that the undisturbed jet propagates faster, while the effect of the increased liquid temperature is small.

Further, the influence of the in-nozzle flow on the liquid gas mixing is evaluated. The instantaneous mixing is quantified based on a mixing indicator proposed by Grosshans [19], Grosshans et al. [26]. This indicator is based on the rms of the liquid volume fraction in the complete domain, rms(α). rms(α) is normalized to the theoretical value of the rms of the liquid volume fraction,
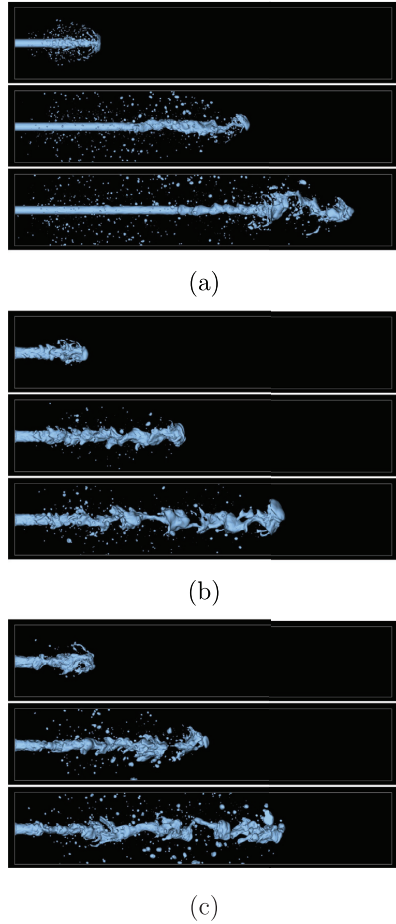
(a)

(b)

(c)

Fig. 13. Liquid jet evolution, started with a top hat profile (a), accounting for in-nozzle turbulence, (b) and accounting for in-nozzle turbulence plus increased liquid temperature (c). Each case is shown for $t = $ 11.5, 32.6 and 55.7. The parameters of the jets are $Re_{jet} = 8000$, $We_{jet} = 330$, $\rho_l/\rho_g = 18$ and $\mu_l/\mu_g = 18$.
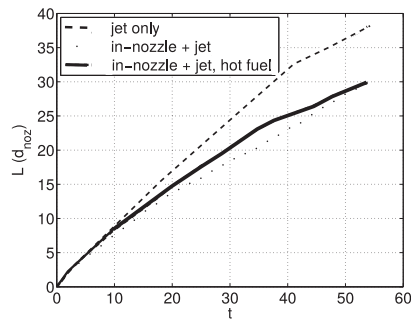

Fig. 14. Liquid penetration over time in non-dimensional units. The undisturbed jet propagates faster, while the effect of the increased liquid temperature is small. The parameters of the jets are $Re_{jet} = 8000$, $We_{jet} = 330$, $\rho_l/\rho_g = 18$ and $\mu_l/\mu_g = 18$.
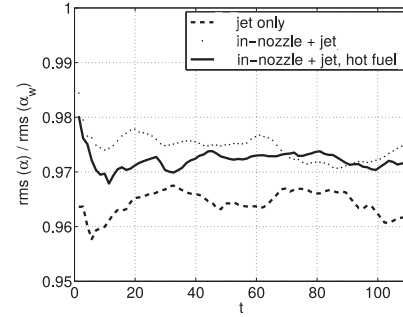
Fig. 15. Time evolution of the liquid-gas mixing. The relative velocity at the liquid-gas interface after the injection is reduced for the cases considering the in-nozzle flow. Thus, less small droplets are sheared of and the liquid-gas mixing reduces in comparison to the case employing a top hat profile at the inlet. The parameters of the jets are $Re_{jet} = 8000$, $We_{jet} = 330$, $\rho_l/\rho_g = 18$ and $\mu_l/\mu_g = 18$.

relating to the liquid which is currently in the domain, if no mixing would occur at all, denoted as rms(α_w). Thus, the mixing indicator is always between unity and zero, whereas a decrease in the mixing indicator corresponds to a better liquid-gas mixing in the domain. The time evolution of this indicator is shown in Fig. 15 for the three simulated cases. The curves reveal that when employing a top-hat profile, the mixing is significantly better compared to the other two cases. This is due to the higher relative velocity at the liquid-gas interface after the injection. Consequently, small droplets are sheared off at the liquid surface. These small droplets can also be observed when comparing the snapshots of the three cases in Fig. 13.

5. Conclusions

The outcome of liquid injection into a stagnant gas has been evaluated depending on the physical and numerical parameters. It has been demonstrated in this paper that the VOF/DAC/DAN method represents an accurate and efficient alternative to simulate the primary breakup of a liquid jet. For comparison, three cases of different liquid-gas density ratios have been calculated using the ODT model. Both methods predict similar features of the droplet size distributions, indicating that the disintegration of the liquid core into ligaments and droplets due to aerodynamic instabilities has been captured. However, the comparison also showed the limitation of the VOF approach to resolve small droplets depending on the grid resolution.

The influence of varying the liquid-gas density ratio between 10 and 30 on the aerodynamic break-up was demonstrated to be low. On the other hand, the reduction of the liquid-gas viscosity ratio from 7 to 1 resulted in smaller droplets and consequently a stronger dispersion. This is attributed to the increased turbulence in the gas phase, enhancing instabilities at the liquid-gas interface. Furthermore, in-nozzle turbulence and cavitation bubbles was shown to quicken the liquid core break-up.

Acknowledgments

References

[1] Aniszewski W, Ménard T, Marek M. Volume of fluid (VOF) type advection methods in two-phase flow: A comparative study. Comput Fluids 2014;97:52–73.

[2] Ashurst W, Kerstein A. One-dimensional turbulence: Variable-density formulation and application to mixing layers. Phys Fluids 2005;17.

[3] Berrocal E, Kristensson E, Richter M. Application of structured illumination for multiple scattering suppression in planar laser imaging of dense sprays. Opt Express 2008;16:17870–81.

[4] Boris J, Grinstein F, Oran E, Kolbe R. New insights into large eddy simulation. Fluid Dyn Res 1992;100:199–228.

[5] Brackbill J, Kothe D, Zemach C. A continuum method for modeling surface tension. J Comput Phys 1992;100:335–54.

[6] Desjardins O, Moureau V, Pitsch H. An accurate conservative level set/ghost fluid method for simulating turbulent atomization. J Comput Phys 2008;227:8395–416.

[7] Desjardins O, Pitsch H. Detailed numerical investigations of the turbulent atomization of liquid jets. Atomiz Sprays 2010;20:311–36.

[8] Eggers J, Emmanuel V. Review of theory of distortion and disintegration of liquid streams. Rep Prog Phys 2008;71:1–79.

[9] Elkotb M. Fuel atomization for spray modelling. Prog Energy Combust Sci 1982;8:61–91.

[10] Faeth G, Hsiang L-P, Wu P. Structure and breakup properties of sprays. Int J Multiphase Flow 1995;21:99–127.

[11] Farth A, Fettes C, Leipertz A. Investigation of the diesel spray break-up close to the nozzle at different injection conditions. The fourth international symposium COMODIA 98; 1998.

[12] Fuchs L, Zhao H-S. Solution of three-dimensional viscous incompressible flows by a multi-grid method. Int J Num Meth Fluids 1984;4:539–55.

[13] Fuster D, Bague A, Boeck T, Le Moyne L, Leboissetier A, Popinet S, et al. Simulation of primary atomization with an octree adaptive mesh refinement and VOF method. Int J Multiphase Flow 2009;35:550–65.

[14] Gerlach D, Tomar G, Biswas G, Durst F. Comparison of volume-of-fluid methods for surface tension-dominant two-phase flows. Int J Heat Mass Transfer 2006;49:740–54.

[15] Germano M, Piomelli U, Moin P, Cabot W. A dynamic subgridscale eddy viscosity model. Phys Fluids 1991:1760–5.

[16] Ghiji M, Goldsworthy L, Brandner P, Garaniya V, Hield P. Numerical and experimental investigation of early stage diesel sprays. Fuel 2016;175:274–86.

[17] Gopala V, van Wachem B. Volume of fluid methods for immiscible-fluid and free surface flows. Chem Eng J 2008;141:204–21.

[18] Gorokhovski M, Herrmann M. Modeling primary atomization. Annu Rev Fluid Mech 2008;40:343–66.

[19] Grosshans H. Large eddy simulation of atomizing sprays. Lund University; 2013. Ph.d. thesis.

[20] Grosshans H, Berrocal E, Kristensson E, Szász R-Z, Fuchs L. Correlating results from numerical simulation to SLIPI-based measurements for a non-combusting diesel spray. 12th triennial international conference on liquid atomization and spray systems (ICLASS), 2–6 September 2012, Heidelberg, Germany; 2012.

[21] Grosshans H, Kristensson E, Szász R-Z, Berrocal E. Prediction and measurement of the local extinction coefficient in sprays for 3d simulation/experiment data comparison. Int J Multiphase Flow 2015;72:218–32.

[22] Grosshans H, Papalexandris M. Evaluation of the parameters influencing electrostatic charging of powder in a pipe flow. J Loss Prev Process Ind 2016;43:83–91.

[23] Grosshans H, Szász R-Z, Fuchs L. Development of a combined VOF-LPT method to simulate two-phase flows in various regimes. 7th international symposium on turbulence and shear flow phenomena, July 28–31, 2011, Ottawa, Canada; 2011.

[24] Grosshans H, Szász R-Z, Fuchs L. Full spray simulation-coupled volume of fluid and lagrangian particle tracking methods. 24th european conference liquid atomization and spray system, September 5–7, 2011, Estoril, Portugal; 2011.

[25] Grosshans H, Szász R-Z, Fuchs L. Development of an efficient statistical volumes of fluid–lagrangian particle tracking coupling method. Int J Num Meth Fluids 2014;74(12):898–918.

[26] Grosshans H, Szász R-Z, Fuchs L. Enhanced liquid–gas mixing due to pulsating injection. Comput Fluids 2015;107:196–204.

[27] Harlow F, Welch J. Numerical calculation of time-dependent viscous incompressible flow of fluid with free surface. Phys Fluids 1965;8(12):2182–9.

[28] Herbert D, Schmidt D, Knaus D, Philips S, Magari P. Parallel VOF spray droplet identification in an unstructured grid. ILASS Americas, Orlando, Florida, May 2008; 2008.

[29] Hiroyasu H, Kadota T. Fuel droplet size distribution in diesel combustion chamber. SAE 1974. 740725

[30] Hirt C, Nichols B. Volume of fluid (VOF) method for the dynamics of free boundaries. J Comput Phys 1981;39:201–25.

[31] Jasak H., Weller H.. Interface-tracking capabilities of the intergamma differencing scheme. 1995. Technical Report.

[32] Jiang X, Siamas G, Jagus K, Karayiannis T. Physical modelling and advanced simulations of gas-liquid two-phase jet flows in atomization and sprays. Prog Energy Combust Sci 2010;36:131–67.

[33] Kerstein A. One-dimensional turbulence: Model formulation and application to homogeneous turbulence, shear flows, and buoyant stratified flows. J Fluid Mech 1999;392:277–334.

[34] Kerstein A, Ashurst W, Wunsch S, Nilsen V. One-dimensional turbulence: Vector formulation and application to free shear flow. J Fluid Mech 2001;447:85–109.

[35] Kirkpatrick M, Ackerman A, Stevens DE, Mansour N. On the application of the dynamic smagorinsky model to large-eddy simulations of the cloud-topped atmospheric boundary layer. J Atmos Sci 2005;63:526–46.

[36] Kristensson E, Berrocal E, Alden M. Extinction coefficient imaging of turbid media using dual structured laser illumination planar imaging. Opt Lett 2011;36(9):1656–8.

[37] Lafaurie B, Nardone C, Scardovelli R, Zaleski G. Modeling merging and fragmentation in multiphase flows with SURFER. J Comput Phys 1994;113:134–47.

[38] Le Chenadec V, Pitsch H. A 3d unsplit forward/backward volume-of-fluid approach and coupling to the level set method. J Comput Phys 2013;233:10–33.

[39] Lebas R, Menard R, Beau P, Berlemont A, Demoulin F. Numerical simulation of primary break-up and atomization: DNS and modelling study. Int J Multiphase Flow 2009;39:247–60.

[40] Lessani B, Papalexandris M. Time-accurate calculation of variable density flows with strong temperature gradients and combustion. J Comput Physics 2006;212:218–46.

[41] Lewis P, Shedler G. Simulation of nonhomogeneous poisson processes by thinning.. Nav Res Log 1979;26(3):403–13.

[42] Lilly DK. A proposed modification of the germano subgrid-scale closure method. Phys Fluids A 1992;4(3):633–5.

[43] Linne M. Imaging in the optically dense regions of a spray: A review of developing techniques. Prog Energy Combust Sci 2013;39(5):403–40.

[44] Lörstad D.. Numerical modeling of deforming bubble transport related to cavitating hydraulic turbines. 2003. PhD Thesis

[45] Lörstad D, Francois M, Shyy W, Fuchs L. Volume of fluid and immersed boundary investigations of a single rising droplet. In: AIAA, 41st aerospace science meeting and exibition; 2003. p. 1282.

[46] Lörstad D, Francois M, Shyy W, Fuchs L. Assessment of volume of fluid and immersed boundary methods for droplet computations. Int J Num Meth Fluids 2004;46:109–25.

[47] Lörstad D, Fuchs L. High order surface tension VOF-model for 3d bubbly flows with high density ratio. J Comput Phys 2004;200:153–76.

[48] Martínez-Martínez S, Sánchez-Cruz F, Riesco-Ávila J, Gallegos-Muñoz A, Aceves S. Liquid penetration length in direct diesel fuel injection. Appl Therm Eng 2008;28(14–15):1756–62.

[49] Meier M, Yadigaroglu G, Smith B. A novel technique for including surface tension in PLIC-VOF methods. Eur J Mech B/Fluids 2002;21:61–73.

[50] Menard T, Tanguy S, Berlemont A. Coupling level set/VOF/ghost fluid methods: Validation and application to 3d simulation of the primary break-up of a liquid jet. Int J Multiphase Flow 2006;33:510–24.

[51] Movaghar A, Linne M, Oevermann M, Meiselbach F, Schmidt H, Kerstein AR. Numerical study of liquid breakup at the surface of turbulent liquid jets using one-dimensional turbulence. ILASS - Europe 2014, 26th annual conference on liquid atomization and spray systems, 8–10 Sep. 2014, Bremen, Germany; 2014.

[52] Noh W, Woodward P. SLIC (Simple Line Interface Calculation). Lect Notes in Phys 1976;59:330–40.

[53] Osher S, Sethian J. Fronts propagating with curvature-dependent speed: Algorithms based on hamilton-jacobi formulations. J Comput Phys 1988;79:234–46.

[54] Panton R. Incompressible flow. New York: John Wiley & Sons; 1996.

[55] Pope S. Turbulent flows. New York: Cambridge University Press; 2000.

[56] Popinet S. An adaptive solver for surface-tension-driven interfacial flows. J Comput Phys 2009;228:5838–66.

[57] Puckett E, Almgren A, Bell J, Marcus D, Richter W. A high-order projection method for tracking fluid interfaces in variable density incompressible flows. J Comput Phys 1997;130:269–82.

[58] Reitz R, Bracco F. Mechanism of atomization of liquid jets. Phys Fluids 1982;25:1730–42.

[59] Renardy Y, Renardy M. Prost: a parabolic reconstruction of surface tension for the volume of fluid method. J Comput Phys 2002;183:400–21.

[60] Roache P. Quantification of uncertainity in computational fluid dynamics. Ann Rev Fluid Mech 1997;29:123–60.

[61] Rudman M. Volume-tracking methods for interfacial flow calculations. Int J Num Meth Fluids 1997;24:671–91.

[62] Rudman M. A volume-tracking method for incompressible multifluid flows with large density variations. Int J Num Meth Fluids 1998;28:357–78.

[63] Sagaut P. Large eddy simulation for incompressible flows: An introduction. 2nd edition. Berlin and Heidelberg: Springer; 2004.

[64] Sethian J. A fast marching level-set method for monotonically advancing fronts. Proc Natl Acad Sci USA 1996;93. 1591–95

[65] Shinjo J, Umemura A. Simulation of liquid jet primary breakup: Dynamics of ligament and droplet formation. Int J Multiphase Flow 2010;36:513–32.

[66] Shinjo J, Umemura A. Detailed simulation of primary atomization mechanisms in diesel jet sprays (isolated identification of liquid jet tip effects). Proc Combust Inst 2011;33:2089–97.

[67] Shinjo J, Umemura A. Surface instability and primary atomization characteristics of straight liquid jet sprays. Int J Multiphase Flow 2011;37:1294–304.

[68] Siamas GA, Jiang X, Wrobel LC. Direct numerical simulation of the near-field dynamics of annular gas-liquid two-phase jets. Phys Fluids 2009;21(042103):1–14.

[69] Sirignano W, Mehring C. Review of throry of distortion and disintegration of liquid streams. Prog Energy Combust Sci 2000;26:609–55.

[70] Smagorinsky J. General circulation experiments with the primitive equations: I. the basic equations. Mon Weather Rev 1963;91:99–164.

[71] Som S, Aggarwal S, El-Hannouny E, Longman D. Investigation of nozzle flow and cavitation characteristics in a diesel injector. J Eng Gas Turbines Power 2010;132(4):042802.

[72] Suh H-K, Lee C. Effect of cavitation in nozzle orifice on the diesel fuel atomization characteristics. Int J Heat Mass Transfer 2008;29:1001–9.

[73] Ubbink O.. Numerical prediction of two fluid systems with sharp interfaces. 1997. PhD Thesis

[74] Unverdi S, Tryggvarson G. A front tracking method for viscous incompressible multi-fluid flows. J Comput Phys 1992;100:25–37.

[75] van Wachem B, Schouten J. Experimental validation of a 3-d lagrangian VOF model: Bubble shape and rise velocity. AIChE J 2002;48(12):2744–53.

[76] Varde K, Popa D, Varde L. Spray angle and atomization in diesel sprays. SAE Tech Pap 1984. 841055

[77] Williams M, Kothe D, Puckett E. Accuracy and Convergence of Continuum Surface-Tension Models. In: Shyy W, Narayanan R, editors. Fluid dynamics at interfaces. Cambridge university Press; 1999. p. 295–305.

[78] Xiao F, Dianat M, McGuirk J. LES of turbulent liquid jet primary breakup in turbulent coaxial air flow. Int J Multiphase Flow 2014;60:103–18.

[79] Young D. Time-dependent multi-material flow with large fluid distortion. Num Meth Fluid Dyn 1982:273–85.

[80] Yuan W, Schnerr GH. Numerical simulation of two-phase flow in injection nozzles: Interaction of cavitation and external jet formation. J Fluids Eng 2003;125(6):963–9.

PAPER II

Numerical Investigation of Turbulent Jet Primary Breakup
Using One-Dimensional Turbulence

Numerical investigation of turbulent-jet primary breakup using one-dimensional turbulence

CrossMark

A. Movaghar [a,*], M. Linne [b], M. Oevermann [a], F. Meiselbach [c], H. Schmidt [c], Alan R. Kerstein [d]

[a] Department of Mechanics, Chalmers University of Technology, Gothenburg, Sweden
[b] School of Engineering, University of Edinburgh, Edinburgh, UK
[c] Faculty of Mechanical Engineering, Electrical and Energy Systems, Brandenburg University of Technology Cottbus - Senftenberg, Germany
[d] 72 Lomitas Road, Danville, CA 94526, USA

ABSTRACT

Primary breakup to form droplets at liquid surfaces is an important fundamental process to study as it determines the initial properties of the dispersed phase, which affect mixing rates, secondary breakup, droplet collisions, and flow separation within the dispersed flow region. Primary breakup can be regarded as one of the least developed model components for simulating and predicting liquid jet breakup. However, it is of paramount importance in many technical applications, e.g. fuel injection in engines and spray painting. This paper presents a numerical investigation of primary breakup of a turbulent liquid jet in still air at standard conditions using the one-dimensional turbulence (ODT) modeling framework. ODT is a stochastic model that simulates turbulent flow evolution along a notional 1D line of sight by applying instantaneous maps to represent the effect of individual turbulent eddies on property profiles. An important feature of ODT is the resolution of all relevant scales, both temporal and spatial. The restriction to one spatial dimension in ODT permits affordable high resolution of interfacial and single-phase property gradients, which is key to capturing the local behavior of the breakup process and allows simulations at high Reynolds and Weber numbers that are currently not accessible to direct numerical simulations (DNS).

This paper summarizes our extensions of the ODT model to simulate geometrically simple jet breakup problems, including representations of Rayleigh wave breakup, turbulent breakup, and shear-driven breakup. Each jet breakup simulation consists of a short temporal channel section to initialize a turbulent velocity profile at the nozzle exit followed by an adjacent jet section. The simulations are carried out for jet exit Reynolds number of 11,500, 23,000, 46,000 and 92,000 while the Weber number is varied within the range 10^2–10^7. We present results on breakup statistics including spatial locations of droplet release, droplet sizes and liquid core length. The results on primary breakup are compared to experimental results and models.

© 2016 Elsevier Ltd. All rights reserved.

1. Introduction

The breakup of liquid jets is of paramount importance in many technical processes, e.g. injection of liquid fuel in engines, spray painting, and spray forming of metals. In the case of liquid fuel injection into engines, primary breakup determines initial droplet sizes and velocities and therefore impacts all subsequent processes such as secondary breakup, droplet collisions, droplet evaporation, and ultimately fuel–air mixing, which plays a central role in combustion efficiency and emissions.

The important influence of the atomization process on the overall system performance has led many researchers to focus on modeling and simulating liquid jet breakup and subsequent droplet formation with approaches ranging from fundamental investigations using DNS (Desjardins et al., 2008; Herrmann, 2011; Lebas et al., 2009; Shinjo and Umemura, 2010; 2011) and large-eddy simulation (LES) (Apte et al., 2003; Chesnel et al., 2011; Dam and Rutland, 2015; Jhavar and Rutland, 2006; Mahesh et al., 2006) to more applied engineering models based on the Reynolds averaged Navier Stokes (RANS) equations (O'Rourke and Amsden, 1987; Reitz, 1987; Tanner, 1997; Toninin et al., 2008).

In the latter engineering approach the gaseous phase is solved in an Eulerian frame whereas the dispersed phase is typically by modeled via Lagrangian parcels, each of which represents many

---

droplets of a single size or a size distribution. The spray breakup process in these Eulerian–Lagrangian simulations can be modeled using standard deterministic breakup models based on Taylor analogy breakup (TAB) (O'Rourke and Amsden, 1987; Tanner, 1997) or wave models (Reitz, 1987). In both models, liquid blobs the size of the injector diameter are introduced into the simulation and undergo secondary breakup and atomization based on the balance between aerodynamic and surface tension forces acting on the liquid phase. Tuning is usually necessary every time the flow conditions are changed to achieve satisfactory results.

Apte et al. (2003) developed a stochastic secondary breakup model based on Kolmogorov's discrete model of breakup. The breakup process is simulated via a stochastic Fokker–Planck equation for the droplet radius. The model creates a broad spectrum of droplet sizes and the parameters of the model are computed dynamically based on the local Weber number, i.e. with less tuning than the standard blob model. However, the simulation starts by introducing computational blobs as in the models above. The model is applied in Apte et al. (2009) to simulate the atomization process in a gas-turbine swirl injector.

The above mentioned DNS and LES approaches are in principle capable of predicting primary breakup processes but due to computational costs they are usually limited to low Reynolds and Weber numbers. The number of grid points in a DNS needed to capture the physics increases with increasing Reynolds number, scaling as $Re^{9/4}$, which makes DNS (and LES in many cases as well) unfeasible for typical industrial applications with high Reynolds numbers and high Weber numbers.

There are only a few (simplified) models available for engineering applications which are actually simulating primary breakup. All have in common the use of an Eulerian description of the liquid phase close to the nozzle. The goal is to describe realistically the dense zone of the spray and its atomization. In the ELSA (Eulerian–Lagrangian spray atomization) model (Vallet et al., 2001), additional Eulerian transport equations for the liquid mass and the liquid surface density are solved. Production and destruction of liquid surface density due to shear, turbulence, collisions, and evaporation are accounted for via modeled source terms (Lebas et al., 2005; Ning et al., 2007). Besides the Eulerian zone describing the dense region of the spray, the model features a transition zone to switch from the Eulerian to the Lagrangian calculation and a Lagrangian zone with classical tracking of droplets. The ELSA model is usually implemented in conjunction with RANS turbulence models. Although the model and its further developments and variants have been an important step forward in modeling the dense region of the spray it still needs tuning and the form of the interface density equation that is used remains open to discussion.

The lack of predictive primary breakup models is partly due to our incomplete knowledge of the underlying physics close to the nozzle. Only recently have experimental techniques like ballistic imaging (Linne, 2013; Linne et al., 2009) enabled detailed investigation of phenomena in the optically dense region of the liquid core of a jet. In addition, DNS (Herrmann, 2010; Lebas et al., 2009; Shinjo and Umemura, 2010) is now able to provide in-depth knowledge of primary breakup for moderate Reynolds and Weber numbers, which will help to develop and validate new models. Certainly, the development of a predictive model for primary breakup is highly desirable not only from an application point of view but also to gain a better understanding of the relevant physical processes.

The main objective of the present paper is the development of a new computational model for primary jet breakup that is both computationally efficient and more predictive than other low-cost approaches. We propose a new model for simulating and predicting primary jet breakup that is based on a stochastic one-dimensional approach, namely one-dimensional turbulence

(ODT). We describe our extensions of the original ODT formulation (Ashurst and Kerstein, 2005; Kerstein, 1999) to gas–liquid multiphase flow to capture breakup mechanisms such as Rayleigh breakup, turbulence induced breakup, and shear-driven breakup. The low computational costs of ODT compared to fully resolved three-dimensional DNS overcomes the limitation of DNS to moderate Reynolds and Weber numbers and therefore allows exploration of the full parameter range of technically relevant breakup regimes while maintaining high spatial and temporal resolution of relevant phenomena.

We apply our method to the simulation of the stationary breakup process of a planar jet in air at standard conditions and present results for the location of the onset of breakup at the jet surface, the liquid column length, and parameter dependences of droplet sizes. The main results are presented in the form of a breakup regime map as presented by Wu and Faeth (1995) and Sallam et al. (2002) and are compared to their experimental results.

The paper is organized as follows: after a description of the ODT model in the next section, we present a validation study of ODT for turbulence decay in a liquid jet without breakup based on comparison of the results to measurements. The validation is followed by the investigation and discussion of liquid jet breakup for a range of Weber numbers.

2. ODT formulation

2.1. Background and objectives

The ODT model of Kerstein used in this study is briefly described in this section. For a fully detailed description we refer to Kerstein (1999), Kerstein et al. (2001), and the variable-density extension by Ashurst and Kerstein (2005). ODT is a stochastic model of turbulent flows that solves the unsteady one-dimensional transport equations for mass, momentum, and optionally other scalars such as species mass fractions.

The main advantage of using one-dimensional unsteady stochastic simulation is that it enables affordable simulation of high-Reynolds-number turbulence over the full range of dynamically relevant length scales. In particular, it affordably resolves property gradients needed to capture details of jet primary breakup. DNS provides such information for moderate Reynolds numbers but with much higher computational cost and a limited range of scales.

Meaningful applications of ODT are limited to relatively simple flow configurations, e.g. boundary layer flows (Kerstein, 1999), jets (Echekki et al., 2001) and mixing layers (Ashurst and Kerstein, 2005; Kerstein et al., 2001). For those flow problems ODT has been shown to produce the correct scaling laws and often to provide qualitatively and quantitatively good agreement with measurements and DNS results.

The present work focuses on modeling primary breakup along liquid turbulent jet surfaces and needs further extension of the ODT modeling approach. The successful application of ODT to multiphase flows may provide an additional tool for investigating such flows, especially if combined with DNS and experimental data.

2.2. Governing equations

The flows investigated in this study are governed by the incompressible lorred Navier–Stokes equations for immiscible two-phase flow. The momentum equation is given by

$$\frac{\partial u}{\partial t} + u \cdot \nabla u = \frac{1}{\rho} \nabla p + \frac{1}{\rho} \nabla \cdot [\mu (\nabla u + \nabla^T u)] + \frac{1}{\rho} T_\sigma, \qquad (1)$$

where u is the velocity, ρ the density, p the pressure, μ the dynamic viscosity and T_σ the surface tension force which is nonzero
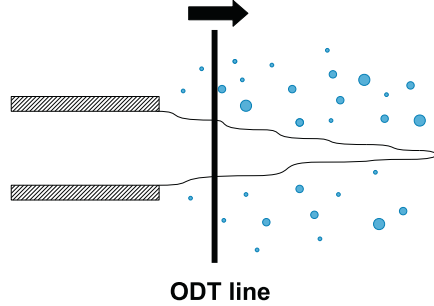
Fig. 1. ODT line configuration for primary breakup simulations.

only at the phase interphase. All fluid properties are considered to be constant in each phase.

2.3. ODT configuration

In the ODT modeling approach we are not aiming at solving (1) directly, which is the target of direct numerical simulations (DNS), but instead look at a model analog for certain simple flow configurations. Here we are focusing on liquid jets into quiescent air. For such a flow configuration the ODT domain represents a lateral line of sight through the jet, which is assumed to be planar, and extends into the gaseous region on each side of the jet, see Fig. 1. The ODT domain is treated as a Lagrangian object advected downstream with the liquid bulk velocity u_{bulk}. The fields defined on the 1D domain evolve then by two mechanisms: (1) molecular diffusion, and (2) a sequence of mapping operations, denoted eddy events, which represent the advection term in the Navier–Stokes equation along the ODT line. These eddy events occur over a large range of length scales, with frequencies that depend on instantaneous flow states. These mechanisms are described in detail in the following sections.

The liquid initial condition, representing the flow state at the nozzle orifice, is generated by a channel flow simulation that is run to a fully developed statistically stationary state. During the subsequent jet simulation, liquid segments representing newly formed droplets are detached from the segment representing the residual liquid jet core. The detached segments are removed from the ODT domain, so at all times the multiphase representation consists of one liquid segment between two gaseous regions.

In the Lagrangian reference frame, a simulated ODT realization of the breaking jet represents advancement along the space-time trajectory $x = u_{bulk}t$. (Note the distinction between this and the flow state at a given instant, which is a function of the lateral coordinate y.) It is therefore not possible to capture x and t dependences individually, and in particular, transient jet development is not represented. Here, the model is applied solely to statistically stationary jets, but it is possible that the model could represent transient jets usefully by empirically tuning model parameters to match measured transient states.

2.4. ODT time-advancement mechanisms

In contrast to common approaches based on the Navier–Stokes equations, ODT uses a set of time advancement mechanisms modeling different physical effects phenomenologically on a 1D line of sight through the turbulent flow.

The first mechanism is standard time evolution of flow properties by molecular diffusion, source terms, gravity, etc. described by a set of partial differential equations, but excluding advection.

In this study of liquid jet breakup we assume constant densities ρ_l and ρ_g in the liquid and the gaseous phase, respectively. The only property transported across the phase interface is momentum. Therefore, the only flow properties that are time advanced by the first mechanism are the velocity components u_i governed by the truncated momentum equation

$$\frac{\partial u_i}{\partial t} - v_p \frac{\partial^2 u_i}{\partial y^2} = S_{p,i}, \tag{2}$$

where v_p is the kinematic viscosity and the indices $i = 1, 2, 3$ denote streamwise, lateral and spanwise direction, respectively, with corresponding spatial coordinates (x, y, z). The subscript p is the phase label l for liquid and g for gaseous. In the present study, the 1D ODT line represents a lateral line of sight in the direction normal to a fixed wall (for channel flow) or to the gas–liquid interfaces of the planar liquid jet and its surrounding gas. For the channel flow simulation that initializes the flow state of the jet, the forcing term $S_{l,1}$ is assigned a fixed value

$$S_{l,1} = -\frac{1}{\rho_l} \frac{\partial p}{\partial x}$$

chosen such that the fully developed state matches corresponding experimental values of the jet exit Reynolds number and $S_{l,2}$ and $S_{l,3}$ are set to zero. Here $\partial p / \partial x$ is the mean pressure gradient that drives the channel flow. In the free jet part of the simulation no forcing is applied, i.e. the turbulence decays, except to the extent that possible shear in the gas phase contributes to liquid-phase turbulence through interfacial momentum coupling.

The second mechanism in ODT uses instantaneous maps to represent advection by 3D turbulent eddies. This eddy mechanism itself is divided into two mathematical operations representing turbulent advection and energy redistribution.

The first operation is a measure-preserving map, termed the triplet map, that represents stirring by a notional turbulent eddy. The second operation is a modification of the velocity profiles in order to implement momentum-conserving energy changes. Using the caret symbol to denote the post-eddy state, these operations can be written as

$$\hat{u}_i(y, t) = u_i(f(y), t) + b_i J(y) + c_i K(y) \tag{3}$$

and

$$\hat{\rho}(y, t) = \rho(f(y), t), \tag{4}$$

where as noted, ρ for given y and t has one of the two values ρ_l and ρ_g.

According to this formulation, fluid at location $f(y)$ is moved to location y by the mapping operation, thus defining the map in terms of its inverse $f(y)$. The terms $b_i J(y) + c_i K(y)$ affect only the velocity components and are used to capture pressure-induced energy redistribution among velocity components and other energy-conversion processes.

The triplet map compresses the original profile to one third of its original length l, pastes three identical compressed copies into the eddy range $[y_0, y_0 + l]$ and reverses the middle copy to avoid velocity discontinuities. The map can be summarized as

$$f(y) = y_0 + \begin{cases} 3(y - y_0), & \text{if } y_0 \leq y \leq y_0 + (l/3), \\ 2l - 3(y - y_0), & \text{if } y_0 + (l/3) \leq y \leq y_0 + (2l/3), \\ 3(y - y_0) - 2l, & \text{if } y_0 + (2l/3) \leq y \leq y_0 + l, \\ y - y_0, & \text{otherwise} \end{cases} \tag{5}$$

This mathematical formulation of the map satisfies measure preservation (conservation property) and continuity of mapped profiles.

In Eq. (3), $K(y)$ is a kernel function that is defined as $K(y) = y - f(y)$, i.e., corresponding to the distance the local fluid element is displaced. It is non-zero only within the eddy interval. $J(y) =$

$|K(y)|$ is an additional kernel whose coefficients b_i have a specified functional dependence on c_i and the density profile within the eddy that enforces momentum conservation. Hence the coefficients b_i do not introduce additional degrees of freedom and therefore the coefficients c_i are the unknowns to be determined through modeling.

The kinetic energy of an individual velocity component i is

$$E_i = \frac{1}{2} \int \rho(y) v_i^2(y) dy,$$

where the integration is restricted to the eddy interval, in which the eddy induces energy transfer and conversion. The amplitudes c_i in Eq. (3) are determined for each eddy individually by applying the following conditions:

1. The total kinetic energy $E \equiv \Sigma_i E_i$ is changed as needed to keep the total system energy constant, e.g. accounting for surface-tension potential-energy changes within the multiphase treatment.

2. The two additional needed conditions are obtained by requiring that the net available kinetic energy, defined as the total kinetic energy minus the lowest attainable kinetic energy based on unconstrained variation of the amplitudes c_i, is equally distributed among the three velocity components in order to simulate the tendency of turbulence to drive the flow toward isotropy, see Ashurst and Kerstein (2005) and Ashurst and Kerstein (2009) for details.

The jet is represented on the ODT domain as a single contiguous liquid region within some interval $[y_1, y_2]$. If the eddy range $[y_0, y_0 + l]$ is entirely within this interval or entirely outside this interval we have a single-phase eddy whose implementation is the same as in previous ODT formulations. If instead the eddy range contains one or both of the interfacial locations y_1 and y_2, we have a multiphase eddy requiring an extension of the ODT methodology; see below.

2.5. Eddy selection in ODT

ODT samples eddy events from an instantaneous distribution that evolves with the flow. These events are individually parameterized by position y_0 and size l.

The number of events during a time increment dt for eddies whose left boundary is located within the interval $[y_0, y_0 + dy_0]$ on the ODT line in the size range $[l, l + dl]$ is

$$\lambda(t; y_0, l) \, dy_0 \, dl \, dt,$$

where the event rate density λ can be expressed as

$$\lambda(t; y_0, l) = \frac{C}{l^2 \tau(y; y_0, l)}, \qquad (6)$$

with dimension $1/(\text{length}^2 \text{ time})$. The adjustable parameter C scales the overall eddy event frequency and τ denotes the eddy time scale. The eddy time scale $\tau(y; y_0, l)$ is evaluated using dimensional reasoning via

$$(l/\tau)^2 \sim E_{final} - Z(\nu^2/l^2), \qquad (7)$$

where l denotes the eddy size and the first term on the right hand side is the final value of the available kinetic energy per unit mass, denoted E_{kin} in the absence of surface-tension effects, and the second term involving the parameter Z suppresses unphysically small eddies.

In practice it would be computationally unaffordable to reconstruct the distribution every time an eddy event or an advancement of Eq. (3) takes place. Therefore eddy events are sampled using an equivalent Monte–Carlo numerical procedure called thinning, see Ross (1996) for details.
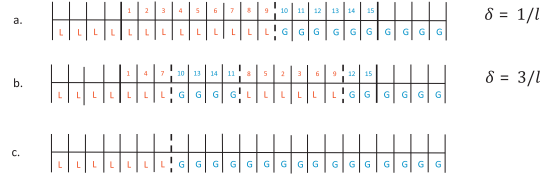

Fig. 2. Multiphase eddy treatment in ODT. (a) The spatial region between the thick solid lines is selected for eddy implementation. It is a multiphase eddy containing both liquid (L) and gas (G) separated by one phase interface (thick dashed line). (b) A triplet map is implemented here as a permutation of the cells of a uniform spatial discretization of the 1D domain, illustrated by the reordering of cell indices within the eddy. Now there are three phase interfaces. (c) The newly formed droplet is removed and replaced by gas. Information about removed droplets can be transferred to a secondary-breakup sub-model within a comprehensive spray simulation.

2.6. Multiphase eddy implementation in ODT

As discussed above, if the eddy range contains one or both of the gas–liquid phase boundaries the eddy is treated as a multiphase eddy. Fig. 2a shows an eddy which contains a phase change and hence is a multiphase eddy. Based on the main hypothesis of turbulent breakup theory, droplets can be formed by turbulent eddies only when the kinetic energy of the eddy fluctuations is larger than the surface tension energy required to form a droplet of size corresponding the eddy that produces it. This needs modeling in ODT to account for the change of surface tension energy via an eddy. Incorporation of this into ODT starts from the volumetric energy density of surface tension $\sigma\alpha$, where σ is the surface tension energy per unit area and α is the surface area per unit volume. This gives an energy density

$$E_\sigma = \sigma \alpha / \bar{\rho} \qquad (8)$$

per unit mass, where $\bar{\rho}$ is the mean density. The meaning and evaluation of α and $\bar{\rho}$ in ODT are considered.

Since an interface in ODT is represented by an isolated point on a line, geometric interpretation is required in order to obtain the area increase in the case of breakup. A plausible assumption for highly turbulent cases involving wrinkled interfaces is that the interface is a statistically homogeneous isotropic random surface. This does not necessarily apply to the jet breakup problems considered here, but it is convenient to adopt it as a universal assumption rather than to attempt a case-by-case treatment. Based on geometric analysis (Chiu et al., 2013) showing that the number density n of interface intersections along a line of sight corresponds to an interface area per unit volume of $\alpha = 2n$, this assumption gives

$$E_\sigma = 2n\sigma / \bar{\rho}. \qquad (9)$$

Because there are always exactly two phase interfaces on the ODT domain, the number of interfaces within any eddy is 0, 1, or 2, corresponding to number densities $n = 0$, $1/l$ or $2/l$, respectively, within the eddy. Triplet mapping of a phase interphase within an eddy produces three such interfaces. This is shown in Fig. 2b and can be interpreted as a tripling of interfacial area. In the Fig. 2b, δ is defined as the increase of number density of interfaces due to triplet mapping which will be 0, $2/l$ or $4/l$ for the mentioned cases. Based on the stated assumption, the respective increases in interfacial area per unit volume are then 0, $3/l$, or $6/l$.

Multiplication of the area per unit volume increase δ by the surface tension σ gives the surface tension potential energy per unit volume that is stored in the newly created interfaces. This implies the surface tension energy change per unit mass

$$\Delta E_\sigma = 2\sigma \delta / \bar{\rho}, \qquad (10)$$

where $\bar{\rho}$ is now identified as the mean density with the eddy range.

As noted earlier, conservation of total energy requires an equal and opposite change of the final kinetic energy. For a multiphase eddy, surface tension energy change is seen as a kinetic energy sink with the value $-\Delta E_\sigma$. Therefore the total energy formulation is re-written in the form

$$E_{final} = E_{kin} - \Delta E_\sigma. \tag{11}$$

As we focus on modeling primary breakup, droplets are removed from the computational domain as triplet maps create them by separating liquid from the jet, see Fig. 2b. Fig. 2c shows that the resulting gaps are set to gas-phase conditions, as explained later. Except for breakup events that contain the entire liquid region (the model analog of liquid-column disintegration; see below), a triplet map can create only one droplet.

Droplets are removed because there is no suitable way to time advance their motion and interactions on the 1D Lagrangian domain. In any case, their subsequent fate is a question beyond the scope of the primary-breakup phenomenon addressed here. The ultimate goal of the present study is to develop a primary-breakup model in which the released droplets are inputs to a spray model of conventional form that then time advances droplet populations using probability distribution functions or other standard tools. With such coupling, the spray model could be used to characterize the droplet-laden gaseous medium in the ODT primary-breakup model, resulting in two-way coupling of the primary-breakup model and the spray model.

2.7. Jet disintegration mechanisms

The occurrence of an ODT eddy containing the entire jet is the model analog of jet disintegration, also termed liquid-core breakup. In the literature, three jet-disintegration mechanisms, each of which is dominant in a range of Weber numbers, with little dependence on Reynolds number, are usually reported (Sallam et al., 2002; Wu and Faeth, 1993, 1995).

At low Weber numbers, the growth of Rayleigh waves on the liquid surface leads to eventual breakup. In the vicinity of Weber number 400, measurements suggest a transition to a different mechanism termed turbulent breakup. This regime has the same dependence of liquid-core length on x/D as the Rayleigh regime, but with a somewhat lower prefactor. The shift is subtle, and in earlier work the two regimes were subsumed in a single empirical correlation. Likewise, there is no attempt here to distinguish the two regimes. They are subsumed within a Rayleigh-breakup treatment that is described in Section 2.8.

At Weber number of approximately 30,000, there is another transition to the third mechanism, termed bag/shear breakup, which is aerodynamically driven. The modeling of this mechanism is described in Section 2.9 as part of a more general treatment of aerodynamic effects, though the approach is designed mainly to capture aerodynamically driven jet disintegration.

2.8. Rayleigh term in ODT

A Rayleigh breakup term is incorporated into the ODT rate expression to model the effect of longitudinal surface waves that eventually cause disintegration of the jet, in contrast to the release of droplets due to the smaller-scale influences of turbulent fluctuations. The modified rate expression is

$$(l/\tau)^2 = E_{final} - Zv^2/l^2 + A(D/t_R)^2. \tag{12}$$

In the new Rayleigh energy term, A is an adjustable parameter, D is the local jet diameter and $t_R = \sqrt{\rho_l D^3/\sigma}$ is the Rayleigh time

scale, defined as the time required for the Rayleigh jet instability to grow to size D, resulting in jet breakup (Wu and Faeth, 1993).

The Rayleigh term is included only for eddies that entirely contain one contiguous liquid region, which in the present application must be the jet region because droplets are removed from the simulation upon separation from the jet, as explained shortly. The Rayleigh term models the effect of longitudinal surface waves that eventually cause disintegration of the jet, in contrast to the release of droplets due to the smaller-scale influences of turbulent fluctuations.

2.9. Shear-driven breakup in ODT

At values of the jet exit Weber number exceeding 10^5, there is a transition to a different turbulent liquid column breakup mechanism (Sallam et al., 2002). At these conditions, turbulence distorts the liquid jet to a sufficient degree that an aerodynamic turbulent liquid column breakup mechanism becomes dominant.

As noted by Sallam et al. (2002) aerodynamic effects become important only when the liquid jet is in cross flow. For a jet with axial gas co-flow, this cross-flow configuration arises locally when the jet undergoes large scale distortions due to large scale instabilities. As these large distortions of the liquid jet are not captured by ODT, a model analog is needed to capture the effect on primary breakup.

The cross-flow effect is emulated by assuming a linear profile of the spanwise (z-directed) component gas phase velocity with linear time dependence $\pm St$ of the slope, where t is the simulation time. This corresponds to a linear increase of shear with distance from the nozzle. The slope has opposite signs on opposite sides of the liquid core so that the formulation obeys statistical reflection symmetry with respect to the jet centerline. The shear coefficient S is tuned so that the simulation produces high Weber number liquid column breakup consistent with experimental observations; see Section 3.2. The other two velocity components are spatially uniform in the gas phase. All gas velocity profiles are continually adjusted to match the corresponding liquid-phase velocity component at the liquid surface.

Time advancement governed by Eq. (2) includes momentum flux across the phase interface, so after each advancement step, the gas velocity profile deviates from linearity. Thereupon, the gas velocity profile is reset to the prescribed linear form on each side of the liquid core, shifted so that the gas and liquid velocities are equal at the liquid surface. The momentum transfer out of the liquid thus follows from Eq. (2), but the parameterization of the gas velocity profile supersedes the evolution of that profile resulting from the time advancement of Eq. (2). This reflects the physical picture that the gas flow is subject to external influences beyond the scope of the model that are subsumed in profile parameterization involving a tunable parameters. For present purposes, detailed physical modeling is needed only in the liquid phase.

Jet streamwise momentum change due to interfacial momentum transfer implies x dependence of the bulk velocity u_{bulk}. Indeed, droplet release also changes u_{bulk} because the droplet streamwise velocity (based on the average of u_1 over the droplet interval) is in general different from the jet bulk velocity. u_{bulk} in the relationship $x = u_{bulk}t$ is nevertheless held fixed at its value at the nozzle because these effects are small. Note that this relationship affects only the conversion from t to x for the purpose of gathering output statistics. Exact evaluation of $u_{bulk}(t)$ will be performed in the future if warranted.

The model representation of gas-phase shear promotes jet disintegration by contributing to the available energy of eddy events containing the entire jet core. Unlike the modeling of the Rayleigh disintegration mechanism in Section 2.8, which is applied only to that sub-class of multiphase eddies, the gas-phase representation

is included in all multiphase eddies, meaning that it also contributes to the available energy of multiphase eddies that detach droplets from the jet core rather than encompassing the entire core. When such an eddy is implemented, the gas velocity profile is modified by triplet mapping, by the kernel operation, and by droplet removal, which implies introduction of gas into the void left by this removal. All these changes in the gas phase are superseded by immediate restoration of the prescribed linear shear, as is done also after each time-advancement step of the momentum equation.

Thus, the most fundamental difference between the Rayleigh-breakup treatment and the gas-phase treatment is that the former is used solely to model a mechanism of jet disintegration while the latter affects all time-advancement mechanisms and thus is a general-purpose though minimal treatment of the aerodynamic coupling. The aforementioned lack of information about external influences on the gas flow is subsumed in the parameter S that is tuned to reproduce the most important single effect of aerodynamical coupling on breakup, namely shear-induced jet disintegration.

Recalling from Section 2.3 that the model represents a statistically stationary jet, the linear profile of gas velocity on either side of the jet can be viewed as a simple representation of the shear associated with jet-driven large scale secondary flow structures within the gas phase. To represent instead an early stage of unsteady injection, the time dependence of the imposed shear can be modified to reflect the high shear near the gas–liquid interface during the initial transient. As noted in Section 2.3, modeling of transient regimes is not attempted here.

This physical interpretation implies shearing of the streamwise velocity profile, but in the model, the shear is applied to the spanwise profile. As noted, this is intended to represent the cross-flow shearing effect. Because ODT does not have a representation of local rotation of the interface orientation, the cross-flow configuration is represented by rotating the gas shearing so as to emulate a cross flow relative to jet streamwise motion.

The gradual time development of secondary flow structures in the jet motivates the adopted cross-flow representation involving time-increasing shear. In addition to being simple and convenient, the assumed linear time dependence of the shear implies a dependence of the liquid column breakup length on ρ_l/ρ_g that has previously been derived theoretically and confirmed experimentally.

To estimate the density-ratio dependence implied by the model, consider an idealization of the flow state within some eddy that induces liquid column breakup. It has some size L that is of order D, where it is assumed that the size of the liquid core region is not much less than its initial value D when the breakup occurs. For estimation purposes, the eddy interval is assumed to consist of liquid and gas regions that are roughly equal in size, where, as assumed, the spanwise shear in the gas region is uniform with magnitude St at the breakup time t. The liquid region has velocity fluctuations that are much smaller in scale than L due to turbulent homogenization of the large-scale (order-D) lateral flow structure of the jet during the time interval t. Any interfacial layers induced by the gas-phase shear are likewise much smaller than L.

As indicated by Eq. (7), the eddy time scale τ is determined by a measure E_{final} of the kinetic energy content of the ODT velocity profiles within the eddy interval and by a viscous correction that mainly affects small eddies and therefore is neglected for estimation purposes. In Eq. (11), E_{final} is expressed as a kinetic energy term E_{kin} minus a quantity representing eddy-induced kinetic-energy conversion to surface-tension potential energy. The latter term is likewise neglected, corresponding to a high-Weber-number assumption, so the right-hand side of Eq. (7) reduces to E_{kin}.

E_{final} is a measure of the kinetic energy associated with velocity variations of order-L spatial extent within the eddy interval. Specifically, it is the net available kinetic energy determined us-

ing the kernel procedure outlined in item 2 of the enumeration in Section 2.4. Indeed, this procedure is formulated specifically for the purpose of capturing only the contributions by velocity variations of order-L spatial extent because these are the flow features that provide the shear forcing for size-L eddy turnover.

In Eq. (7), simplified as stated so that the right-hand side reduces to E_{kin}, energy is expressed per unit mass. The simplified equation is recast in terms of volume-integrated energy within the eddy interval. Here, the eddy volume is taken to be the ODT eddy size L times a nominal cross-sectional area that multiplies both sides of the equation and therefore is dropped. On this basis, the left-hand side scales as $\rho_l L^3/\tau^2$, where the average density within the eddy interval is taken to be of order ρ_l because $\rho_g \ll \rho_l$. On the right-hand side, the eddy-integrated available energy is denoted Q for consistency with Ashurst and Kerstein (2005). Q is analogous to Q_2'' in Eq. (1) of Ashurst and Kerstein (2009), where the subscript indicates that τ was evaluated based on the net available kinetic energy of component 2, but for reasons explained in Section 3.4 of Kerstein and Wunsch (2006), the net available kinetic energy Q summed over velocity components has been used in subsequent work, including the present study.

Q is the sum of the component available energies Q_i that are defined by Eq. (26) of Ashurst and Kerstein (2005). Expanding that equation based on the definitions of the terms on the right-hand side (subject to the corrections in Ashurst and Kerstein, 2009), various integrals over ρ or ρv_i times powers of J and K are introduced. For the representative case under consideration, the integrals involving ρ scale as ρ_l because $\rho_l \gg \rho_g$. Those involving ρv_i scale as ρ_g because the small-scale fluctuations of v_i within the jet effectively nullify the contribution from the liquid region. (Nonzero spatially uniform contributions are similarly nullified due to a subtraction operation mentioned in item 2 of the enumeration in Section 2.4.) The net outcome is that Q scales as $\frac{\rho_g^2}{\rho_l} L^3 (St)^2$.

The various estimates of quantities in the simplified form of Eq. (7) give, after rearrangement, $St\tau \propto \rho_l/\rho_g$. Jet column breakup is deemed to occur when the turnover time τ of the typical breaking eddy matches the elapsed time t. Therefore t is substituted for τ, giving $t \propto (S^{-1}\rho_l/\rho_g)^{1/2}$. Owing to the near constancy (here approximated as exact constancy) of the jet bulk velocity, x is proportional to the fluid residence time t, so the jet column breakup length is estimated to be proportional to $(\rho_l/\rho_g)^{1/2}$.

In Section 3.2.2 it is noted that this square-root dependence of the breakup length on the density ratio has been observed experimentally and explained theoretically based on elementary considerations. This dependence is not an intrinsic property of ODT because it is contingent on the assumption that the aerodynamic shear resulting from the postulated cross-flow mechanism is linear in t and therefore in x. Though simple and plausible, this assumption has no first-principles justification. However, the fact that it yields a scaling property that is independently known to be valid can be viewed as an *a posteriori* fundamental justification, thus indicating that the assumed linearity is not entirely arbitrary. This does not establish that jet instabilities do in fact lead to a linear-in-time effective aerodynamic shear coupling because ODT does not fully capture the relevant underlying physics. It remains to be investigated whether the ODT jet-breakup behavior that follows from linear-in-time shear is anything more than purely fortuitous. The model parameters are summarized in Table 1.

3. Results

3.1. Liquid jet with no breakup

Before investigating jet breakup behavior, the evolution of turbulent intensity in the jet prior to breakup is examined. This en-

Table 1

Summary of ODT breakup model parameters.

ODT parameter	Value
C (eddy frequency)	12.5
Z (viscous term)	50
A (rayleigh term)	1.5
S (shear)	40 1/s^2
β (elapsed time criterion)	0.14

Fig. 3. Mean streamwise velocity profiles (where $y = 0$ denotes the mid-plane) at several spatial positions for $Re_{bulk} = 23,000$.

sures that ODT is capable of correctly predicting the level of turbulence prior to breakup within the jet. The investigations are similar to those presented in Schulz et al. (2013) with some important changes of the ODT setup to improve the results. These new changes are based on a parameter study done by the authors to optimize ODT model parameters C and Z to improve the simulation results compared to experiments. As discussed in Section 2.5, C and Z are the ODT global parameters which have been kept at the same value for liquid jet both with and without breakup. More details of this parameter calibration are reported in Meiselbach (2015).

Wolf et al. (1995) performed measurements of the mean velocity and turbulence intensity for a rectangular jet of water ejecting under isothermal conditions into ambient gas at streamwise locations up to 30 nozzle widths, which is where breakup starts at the jet surface. The primary nozzle is a parallel plate channel with a rectangular cross section of width 10.2 mm in the narrower direction. The liquid jet has low Weber number. This leads to no droplet generation at the surface of liquid jet until it breaks beacuse of the Rayleigh waves.

The ODT representation of this experiment consists of two parts: a short temporal channel section and the jet section. The simulation starts from a fully developed turbulent channel flow profile of water at standard conditions. The Dirichlet (no-slip) boundary condition is applied to the velocity components during the channel section. The channel flow is simulated for a time duration of $t = D/u_{bulk}$, where D denotes the channel width and u_{bulk} represents the bulk velocity. At this point the current flow properties are saved as new restart profiles for the next realization of the channel flow and are used as initial conditions for the jet portion of the simulation. The switch to jet simulation done by changing the boundary condition of the current realization from no-slip to a Neumann (free-slip) boundary condition. This precludes any momentum exchange with the surrounding gas across the phase boundary, reflecting the near absence of momentum transfer to the gas in the experimental configuration, so the liquid jet is effectively a self-contained entity and no representation of the gas phase is required.

For the channel flow portion of the simulation, the model parameters are adjusted to match the results of the DNS channel flow simulation by Moser et al. (1999) and measurements by Hussain and Reynolds (1975), giving $C = 7$ and $Z = 400$. Previous ODT channel-flow simulations are reported by Schmidt et al. (2003) and Schulz et al. (2013). Here, as in those studies, the largest eddy size is $l = D/2$ in the channel portion.

For comparison of ODT results with the experiments by Wolf et al. (1995), the imposed mean pressure gradient in the channel part was chosen to match the experimental bulk Reynolds number. For the jet part, the simulations were carried out with model constants set to $C = 12.5$, $Z = 50$, and largest eddy size D, values that were chosen by Schulz et al. (2013) for a good fit to the Wolf et al. measurements.

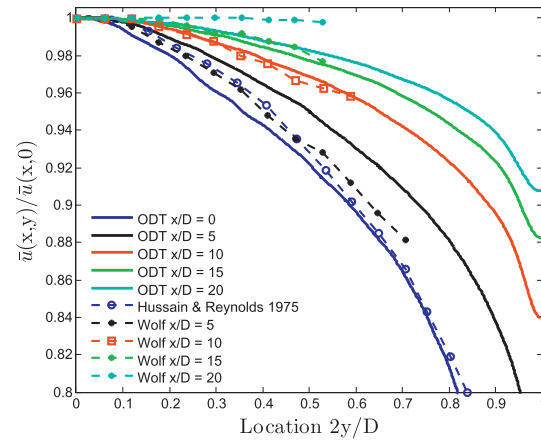Based on the available experimental data for two different Reynolds numbers, $Re_{bulk} = 23,000$ and $46,000$, two main flow simulation results are of interest, namely mean velocity profiles and profiles of the turbulence intensity.

Fig. 3 presents the mean velocity profile at different axial locations for $Re_{bulk} = 23,000$. As it shows, the initial profile reflects quite well the result of Hussain and Reynolds (1975) for the fully developed channel flow. The profiles at positions $x/D = 10$, 15 have the best fit with the experiments. The curve at $x/D = 5$ has the same tendency but shows a noticeable deviation from the experiments done by Wolf et al. (1995). This can be explained by the fact that ODT is a 1D model and that it cannot capture 3D effects at the outlet of the channel caused by changes of the boundary conditions and the pressure field. Another such 3D effect is the so called *bending effect* discussed in Lignell et al. (2013). The ODT model domain is interpreted as a straight line advected at the bulk velocity without distortion. In reality, a straight Lagrangian line at the nozzle exit would be bent due to the lateral variation of the mean axial velocity. This effect, which is most prominent in the near field where the lingering influence of the channel flow is greatest, is ignored here with the consequence that the outer regions of the ODT domain are advected too rapidly, so they have less time to undergo turbulence decay than expected after being advected a given streamwise distance from the nozzle exit.

The ODT results for $x/D = 20$ show a higher slope than the experiments. As discussed in Schulz et al. (2013) and Gonzalez-Juez et al. (2011), in confined flows with a free-slip surface, DNS predicts an increase of the tangential velocity fluctuations near the free-slip surface while ODT predicts a decrease since it cannot capture the mechanism that causes this, which is development of quasi-2D flow near the free-slip surface. The jet simulated in this paper behaves similarly near free-slip surface, explaining why ODT cannot predict the experiments accurately in the far field.

Fig. 4 shows the spatial evolution of the turbulence intensity at lateral positions $2y/D = 0.0$, 0.3 and 0.6 for Reynolds numbers 23,000 and 46,000. Whereas the slopes, i.e. the decay rate of turbulence, are well captured by ODT, the onset of the decay for different lateral positions shows substantial deviations from the experiments of Wolf et al. The computed curve for $2y/D = 0.6$, however, shows reasonable agreement with the measurements. The capability of ODT to capture decaying turbulence close to an interface qualitatively and quantitatively correctly is important for the liquid jet breakup simulation below in order to correctly capture the contribution of liquid-phase turbulence to droplet release. Therefore,
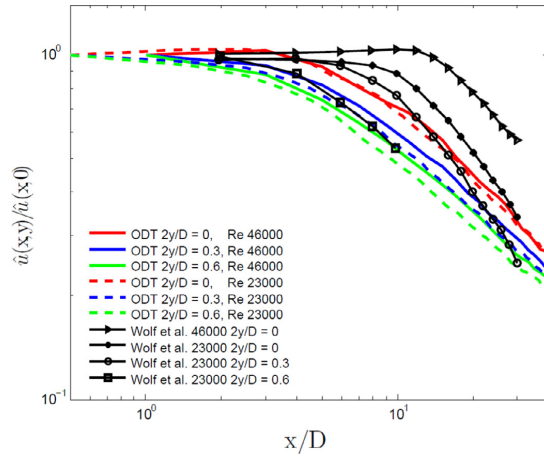
Fig. 4. Comparisons of streamwise turbulence intensity $\hat{u}(x, y) = u_{rms}(x, y)/\bar{u}(x, y)$ with measurements by Wolf et al. at different lateral positions for different Reynolds numbers $Re_{bulk} = 23,000$, $Re_{bulk} = 46,000$.

Fig. 5. Jet velocity field and eddy occurrences for a simulated realization at Weber number 10^7. The liquid region is bounded above and below by black solid lines. Color in the liquid region indicates streamwise velocity in meter per second. Green lines representing streamwise velocity profiles at $x/D = 0, 10$, and 20 show that the streamwise gas velocity is taken to be uniform and to match the liquid velocity at each phase interface. Color in the gas region indicates lateral velocity, whose spatial variation reflects the imposed linear z dependence, with slope on either side that increases linearly in time, and hence in x. The black bars indicate eddy sizes, and locations. (For interpretation of the references to color in this figure legend, the reader is referred to the web version of this article.)

the empirical ODT parameters have been tuned to match turbulence decay close to the gas–liquid interface and not, as usual, at the centerline.

A comparison of the experimental results for two different Reynolds numbers shows that with increasing Reynolds numbers the turbulence decay rate is decreasing and the onset of decay is delayed. The corresponding simulation results show weaker Reynolds-number dependence.

3.2. Liquid jet with breakup

3.2.1. Numerical implementation

As noted earlier in Section 3.1 the liquid jet simulation contains two part, a short temporal channel section followed bu temporal jet section. At liquid jet with breakup simulation the change between sections is implemented by changing the boundary condition, from Dirichleth boundary condition during the channel simulation to free slip boundary condition during the jet simulation. The interfacial flux matching condition is conserved during jet simulation. The change between sections is implemented by changing the boundary condition and increasing the domain length to 3D, where D is the channel width. The domain length should be large enough so that the finite size of the domain does not affect the results. For the jet part, the simulation was carried out with model constants same as Section 3.1, $C = 12.5$, $Z = 50$.

3.2.2. Streamwise development of the breaking jet

The validation in Section 3.1 of ODT for the cases prior to breakup initiation was a foundation for application of ODT to breakup cases, in particular enabling the tuning of model parameters based on liquid-phase turbulence measurements that have not been performed during jet breakup. Generalizing the model to capture the physical mechanisms related to breakup introduced additional modeling parameters in the ODT formulation which need to be optimized. Some of these modeling parameters were discussed in Section 2. Another is discussed next.

For the jet section the eddies inside the liquid core are always be smaller than the local jet diameter but multiphase eddies larger than the jet local diameter are allowed. The elapsed-time criterion described in Echekki et al. (2001) limits the allowed sizes of the multiphase eddies during the jet simulation. The criterion excludes
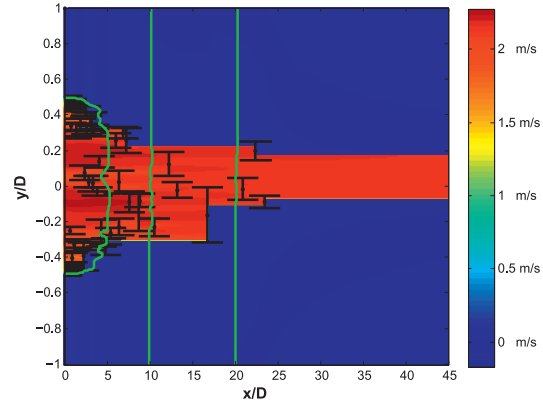
multiphase eddies whose τ value violates the requirement $\tau > \beta t$, where t is the elapsed time since the start of the jet part and β is an adjustable parameter.

The physical justification of this restriction is that an ODT eddy event is interpreted as the completion of an eddy motion of finite time duration. Therefore the event should be allowed only if the elapsed time exceeds the turnover time of the corresponding physical eddy. The adjustable parameter is introduced because this is a scaling concept rather than an exact physical relationship.

Turbulent eddies entirely contained within the liquid phase turbulence already became fully developed during the channel flow simulation that precedes the jet simulation, so no waiting time is required for these eddies to complete their turnovers in the jet region. This criterion is the ODT analog of previous dimensional estimation of breakup onset locations based on the relevant eddy turnover time or other applicable time scales such as the Rayleigh time scale as described in Wu and Faeth (1993).

In ODT, liquid-column breakup corresponds to the occurrence of an eddy containing the whole liquid region. As discussed in the modeling section, for such eddies a Rayleigh term is included in the expression determining eddy likelihood. The parameter A in the ODT Rayleigh term has been adjusted to obtain quantitative agreement of two statistical measures of ODT column length with those lines, which roughly represent the experimental observations of liquid-column breakup at relatively low Weber number. Likewise, the shear parameter S has been adjusted to match experimental observations of liquid-column breakup in the high-Weber-number regime. The test conditions of the current study are summarized in Table 2.

Simulations were performed for the turbulent planar jet with jet exit liquid Weber numbers in the range $We = 10^2$–10^7 and for bulk Reynolds numbers of $Re_{bulk} = 11,500, 23,000$ and $46,000$. The bulk Reynolds numbers are varied by varying u_{bulk}. The ranges of variation of the other variables in the current study are summarized in Table 2. Results are compared with Wu and Faeth (1995) and Sallam et al. (2002).

Table 2
Summary of simulation conditions for the liquid jet.

Parameter	Value	
	Baseline	Variations
μ_l (liquid absolute viscosity)	8.94×10^{-4} kg/ms	$[4.47 - 17.88] \times 10^{-4}$ kg/ms
μ_g (gas absolute viscosity)	18.5×10^{-5} kg/ms	$9.25 \times 10^{-5} - 37 \times 10^{-5}$ kg/ms
D (initial jet diameter)	10.2 mm	10.2 mm
u_{bulk} (jet exit mean velocity)	2 m/s	$[1, 2, 4, 8]$ m/s
ρ_l/ρ_g (liquid/gas density ratio)	860	16–860
$Re_{bulk} = \rho_l u_{bulk} D/\mu_l$ (Reynolds)	23,000	$11,500, 23,000, 46,000, 92,000$
$We = \rho_l u_{bulk}^2 D/\sigma$ (Weber)	10^7	$10^2 - 10^7$
$Oh = \mu_l/(\rho_l D\sigma)^{0.5}$ (Ohnesorge)	0.0138	0.0034–0.0138

Fig. 6. Breakup regime map.

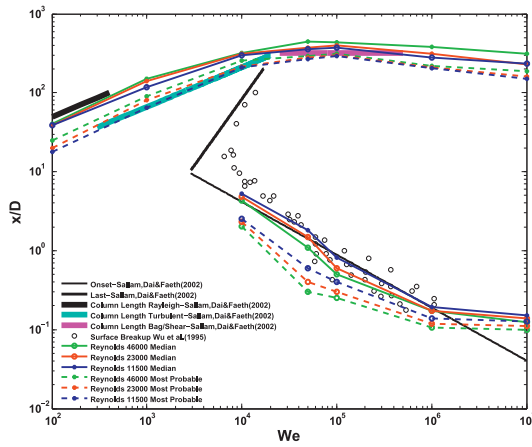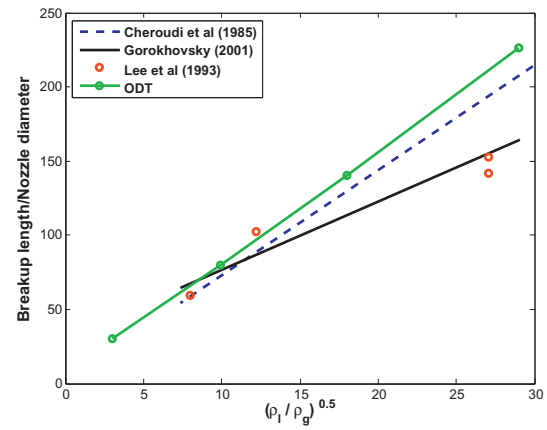**Fig. 7.** Breakup length as a function of the square root of the liquid/gas density ratio.

Fig. 5 shows the velocity field for a single simulated jet realization at a Weber number of 10^7 and the baseline values for the other variables that are shown in Table 2. In the figure, the streamwise location of the temporal evolving solution on the ODT line is based on the liquid bulk velocity times the elapsed simulation time. The liquid phase region in Fig. 5 is separated from the gas phase by the black solid line. The black bars show the locations and the sizes of the accepted eddies. The absence of detached droplets in Fig. 5 reflect their removal upon detachment, as discussed earlier. The green lines are streamwise velocity profiles at $x/D = 0, 10,$ and 20.

Fig. 6 summarizes the main results of this study in a breakup regime map. The plotted model results correspond to the baseline conditions shown in Table 2 except for We and Re_{bulk}, which vary as indicated in the plot. The vertical axis shows the axial position x normalized by the jet diameter. Onset, and column length refer to the location of the onset of breakup, i.e. the axial position of the first multiphase eddy, and the length of the liquid core respectively. Wu and Faeth (1995) and Sallam et al. (2002) suggested correlations for the onset and the length of the liquid core in terms of the liquid Weber number $We = \rho_l D u_0^2/\sigma$, where ρ_l is the liquid density, u_0 is the average liquid velocity at the jet exit, and σ is the surface tension of the liquid. Three modes of liquid-column breakup were identified by Sallam et al. (2002) for turbulent round liquid jets, as described in Section 2.7: a weakly turbulent Rayleigh-like breakup mode observed at low jet exit Weber number, a turbulent breakup mode observed at moderate jet exit Weber number, and an aerodynamic bag/shear breakup mode observed at high jet exit Weber number. The breakup-length correla-

tion shown by Sallam et al. (2002) for each of these mechanisms is illustrated in Fig. 6. ODT results are shown for both the median and the most probable location based on an ensemble of 1000 realizations for each Weber and Reynolds number, indicated in Fig. 6 by solid and dashed lines, respectively. Since there is no clear indication that the correlations suggested by Sallam et al. (2002) are based on the mean, most probable, or other location statistic, both statistics are presented.

The Rayleigh term in the expression determining eddy likelihood is compatible in formulation with the theory of the Rayleigh and turbulent regimes of liquid-column breakup, and accordingly the ODT results match the slopes of the corresponding experimental correlations. As mentioned above, the heights of the experimental trend lines were matched by tuning the ODT Rayleigh parameter A. Likewise, the insensitivity of the liquid-column breakup length to Weber number in the bag/shear regime is reproduced by ODT and the height of the experimental trend line is matched by adjustment of the parameter S.

Fig. 7 shows the effect of the liquid/gas density ratio on the liquid-column breakup length of the jet. The range of studied density ratios is shown in Table 2. In addition to ODT results, theoretical studies by Gorokhovski (2001) and measurements by Lee and Spencer (1933) and Chehroudi et al. (1985) are shown. The Weber number of the liquid jet in the ODT simulations and the experimental value is $5*10^5$. The liquid jet Reynolds number is 23,000. The vertical axis shows the jet breakup length normalized by the nozzle diameter and the horizontal axis shows the square root of the liquid/gas density ratio. Although the absolute numbers exhibit considerable scatter, the results show that both ODT and the
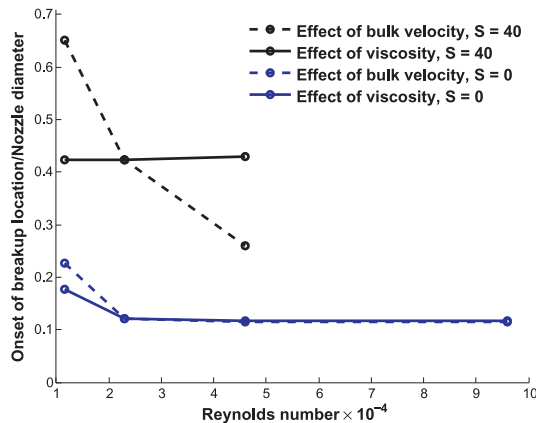
Fig. 8. Re_{bulk} dependence of breakup onset location for $We = 10^5$.

measurements obey the theoretical square-root dependence on the density ratio. The origin of this behavior in ODT is explained in Section 2.9. The explanation is predicated on neglect of surface-tension effects (among other assumptions), explaining why the ODT representation of high-Weber-number jet breakup is insensitive to Weber number, a result that is supported by the Weber-number insensitivity of the jet breakup length seen in Fig. 6 at high Weber numbers.

The ODT numerical results indicate that the analysis in Section 2.9, which assumes $\rho_l/\rho_g \gg 1$, is valid for values of this ratio at least as low as 10. This is not necessarily an indication that the square-root scaling is physically valid for such a low ratio, and presently there does not appear to be any clear evidence in this regard.

3.2.3. Onset and termination of droplet release

Turning from the topic of jet breakup length to the statistics of droplet release from the intact liquid core, Fig. 6 indicates reasonable agreement of ODT results for the onset of droplet release with measurements. The degree of agreement depends on the statistical data reduction that is performed. The ODT simulations did not provide a discernible indication of the termination of droplet release, corresponding to the three highest data points of the plotted measurements by Wu et al. The lines labeled onset and last are based on their theoretical analysis of the onset and termination mechanisms. Termination refers to the last turbulent breakup occurring at the jet surface before the jet intact core fully breaks. The elaped-time criterion parameter β is tuned to the value 0.14 for best agreement with the onset of breakup measurements. ODT dynamics capture the measured trend with respect to Weber number irrespective of the precise choice of β.

Fig. 8 shows the dependence of the onset location on Re_{bulk} for Weber number fixed at 10^5 and other parameters assigned their baseline values, except that additional cases are shown for which $S = 0$ instead of its baseline value. The dependence is evaluated based on variation of Re_{bulk} by varying either u_{bulk} or the liquid viscosity. The Re_{bulk} value that falls outside the plot frame is 92,000.

For the baseline S value, the dependence is sensitive to the method of varying Re_{bulk}, indicating that some other parameter in addition to Re_{bulk} and We is needed to collapse the normalized properties of the breakup process. Reduction of the aerodynamic coupling by choosing $S = 0$ greatly reduces this sensitivity, indicating that aerodynamic coupling, which can introduce additional

length and time scales and thus, e.g., an additional Reynolds number, is the cause of the sensitivity.

Faeth and coauthors do not discuss the Re_{bulk} dependence of breakup onset location but the measurements shown on their regime map and the information in their legends enable Re_{bulk} to be inferred for each measurement. The collection of cases was not configured to enable straightforward determination of the Re_{bulk} dependence for fixed We, but a detailed inference procedure allowed this determination. The specifics of the procedure and the various implications of the results are beyond the scope of the work presented here so they will be reported elsewhere. What is pertinent here is the conclusion that no statistically significant dependence on Re_{bulk} could be discerned but a mild dependence might exist below the threshold of statistical significance.

On this basis, the $S = 0$ results in Fig. 8 are consistent with the Re_{bulk} dependence implied by the measurements but the results for the baseline S value are not. Thus the baseline S value, though suitable for obtaining the correct jet length at high We, results in too much near-field aerodynamic shear. This indicates that the linear-in-time shear model, notwithstanding the beneficial feature that it introduces the correct dependence of jet length on the density ratio, is too simple for a correct near-field treatment and needs some elaboration in that regard. This will be addressed in future work.

Aerodynamic shear has two effects on jet breakup. The most important far-field effect is to augment breakup by promoting jet instability. In the near field, the model results imply that a more important effect is to promote the viscous transport of liquid momentum to the gas phase, with effects on the flow structure that delay the onset of breakup. This is indicated by the earlier onset of breakup when the aerodynamic effect is reduced. This not necessarily physically realistic and further motivates future improvement of the shear treatment. Any such change is likely to require modification of the parameter β in order to maintain the ODT onset location versus We curve at the experimentally observed level.

3.2.4. Droplet statistics

ODT can generate a distribution of droplet sizes which, e.g., can serve as an input for subsequent secondary breakup models in CFD simulations. However, as ODT as presented here provides droplet sizes from primary breakup only, comparisons with experiments, which usually cannot separate droplets from primary and secondary breakup, should be regarded as tentative. Here we use a study by Sallam and Faeth (2003) for a qualitative comparison and scaling results.

Fig. 9 shows droplet diameters at the onset of their formation along the surface of the jet at different Weber numbers. This study is based on the baseline values summarized in Table 2 except the Weber number values which are in the range of 10^4–10^7. The black solid line shows the best fit correlation of the measurements reported by Sallam and Faeth (2003). The vertical axis shows the droplet Sauter Mean Diameter (SMD) normalized by Λ, which is the cross stream integral length scale of the flow at the jet exit. Based on Sallam and Faeth (2003), Λ scales with the hydraulic diameter d_h which corresponds to the channel diameter here. The horizontal axis shows the jet exit Weber number based on Λ. Results show consistency versus experiments but with a lower rate of decrease as Weber number increases. This might be due to the above mentioned fact that ODT considers droplets resulting from primary breakup only whereas the experimental results will contain secondary breakup effects as well, leading to overall smaller droplets.

Physical modeling described in the appendix is needed in order to infer physical droplet statistics from the statistics of ODT droplet-formation events. This modeling introduces a tunable parameter B in Appendix A.3 that relates ODT and physical droplet sizes. For the data comparison shown in Fig. 9, an equivalent tun-
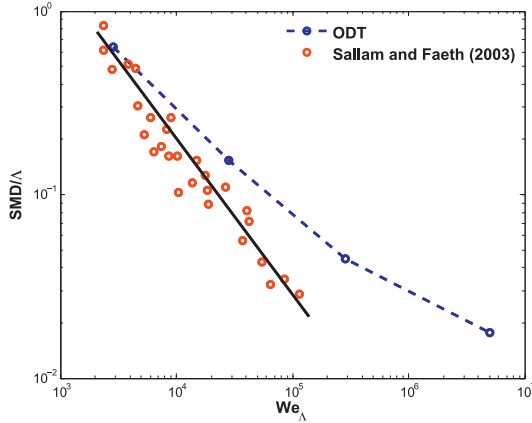
Fig. 9. Droplet diameters at the onset of their formation along the surface of liquid jet as a function of the Weber number.
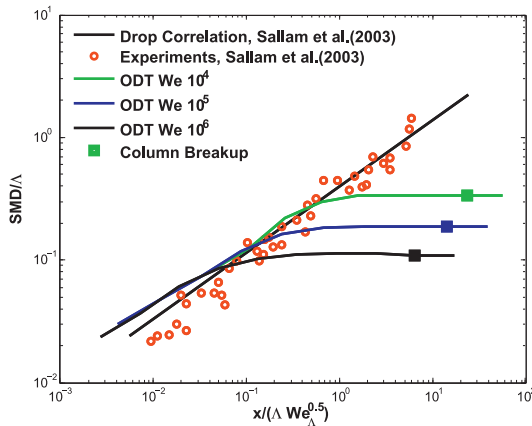

Fig. 10. Droplet diameters along the surface of liquid jet function of Weber number and distance from the nozzle. The square symbols show the most probable location of column breakup at different Weber numbers.

ing was performed by adjusting the value of Λ such that the ratio Λ/D is equal to 2/7.

Fig. 10 shows the variation of the Sauter Mean Diameter (SMD) of droplets released via primary breakup as a function of the distance from the nozzle for different Weber numbers. This study is based on the baseline values summarized in Table 2 except the Weber number values which are in the range of 10^4–10^6. The vertical axis shows the SMD normalized by Λ and the horizontal axis shows the distance from the nozzle normalized by $\Lambda We_\Lambda^{1/2}$. The circular symbols show the measurements by Sallam and Faeth (2003) with the jet exit Weber number within the range 200–300,000. The square symbols represents the most probable location of column breakup for different Weber numbers. As results show ODT curves extend beyond column breakup location because that refers to the most probable location in 2000 realization and therefore breakup extends beyond that point for some realizations. The droplet statistics are collected cumulatively as has been described in Appendix A.3. As the results show, the droplet size linearly increases with increasing distance from the nozzle. This process continues until far downstream where aerodynamic shear

breakup mechanism dominates. The model representation of this mechanism, which is formulated to reproduce the *We* and density-ratio dependence of column breakup length, fails to capture the measured upward continuation of the SMD trend far downstream in Fig. 10. This discrepancy is not surprising given the rudimentary treatment of aerodynamic shear effects in the model.

Advanced measurement techniques and numerical simulations are progressing toward achieving the capability to generate size distributions of primary-breakup droplets. This will allow detailed, unambiguous validation of the modeling approach presented here and thereby indicate its future prospects for becoming a robust predictive tool.

4. Conclusion

In this study, we propose a new model to predict primary breakup of liquid jets. The model is based on extensions to the stochastic one-dimensional turbulence model (ODT) that incorporate surface tension and its interaction with liquid-phase turbulence, Rayleigh waves and aerodynamic shear. Simulations are performed, starting with a liquid jet with no breakup to investigate turbulence levels inside a jet and followed by a jet with primary breakup. The simulations span the Weber number range $[10^2$–$10^7]$ at three different Reynolds numbers: 11,500, 23,000 and 46,000. The liquid/gas density ratio ranges from 10 to 860.

The major conclusions of this study are as follows:

- After parameter adjustments, ODT reproduced column-breakup results reported previously by Wu and Faeth (1995) and Sallam et al. (2002) encompassing the weakly turbulent Rayleigh-like breakup, turbulent breakup, and aerodynamic bag/shear breakup regimes.
- ODT results for the most probable and the median location of onset of breakup show agreement with the experiments, including sensitivity to Weber number but not to Reynolds number. The latter result reflects an apparent deficiency of the aerodynamic shear treatment in the near field.
- Based on an assumed rate of streamwise increase of the strength of aerodynamic shear effects, ODT yields a square-root dependence of the jet column-breakup length on the liquid-to-gas density ratio in the shear-dominated (high Weber number) regime, as found experimentally and explained by previous analysis.
- The Sauter mean diameter of the droplets at the onset of their formation decreases with increasing Weber number. The ODT results show the same trend as experiments but with lower slope.

Some of the noted results reflect incorporation into ODT of empirical phenomenology that is largely based on dimensional reasoning. Extended in this manner, ODT is capable of generating droplet formation statistics that are otherwise available only from costly multidimensional flow simulations. This enables model application over a broader parameter range than is affordable using other methods.

The proposed model has the potential to include further physical mechanisms influencing primary breakup, e.g. viscosity and surface-tension variability due to thermal non-uniformity, and effects of evaporation, including compositional non-uniformity due to fractional distillation of multi-component fuels. Extensions to cavitating and supercritical conditions are also envisioned.

Appendix A. Interpretation of ODT droplet statistics

A1. Overview

In the ODT breakup model, the ODT domain nominally represents a lateral line of sight through the liquid jet. ODT is formulated to represent flows that are statistically homogeneous in directions normal to the ODT domain, so the physical configuration to which the ODT breakup model most directly applies is the planar jet. Nevertheless, it is possible to apply the breakup model to round jets in a physically and mathematically consistent way.

For some purposes, this is straightforward. The regime map in Section 3.2 shows the Weber-number dependence of the streamwise location of the occurrence of particular stages of breakup (onset of breakup, final jet breakup). The determination of these locations in ODT breakup simulations is straightforward. However, determination of the physical quantities corresponding to ODT droplet statistics requires detailed consideration, as follows.

An ODT multiphase eddy breaks the liquid region into either two or three disconnected segments, where the latter case is interpreted as the occurrence of final jet breakup. Final jet breakup does not contribute to the droplet statistics presented here, so only the case of breakup into two segments is considered. As illustrated in Fig. 2, this corresponds to a situation in which the eddy initially contains only one phase interface. The triplet map then creates three compressed copies of the liquid region that it contains, one of which remains attached to the liquid core while the other two, which are contiguous, form a newly separated liquid region that is deemed to be a released droplet.

Two aspects of model interpretation are addressed. One is the enforcement of conservation laws, in particular, mass conservation. The second is the interpretation of the ODT domain as a transverse line that is swept downstream at the liquid bulk velocity u_{bulk}, such that droplet releases can be detected only at the streamwise location $x = u_{bulk}t$ at any given time t.

To address the first point, a geometrical interpretation of ODT application to a round jet is invoked. The ODT breakup simulation is initialized with a liquid segment of lateral extent D corresponding to the jet diameter at the injector orifice. Accordingly, the lateral extent $D(x)$ of the ODT liquid core at any $x \geq 0$ is deemed to represent the jet diameter at x, where $D(0)$ corresponds to D with no argument. For all x, the jet cross-section is assumed to be circular. Assuming that the liquid bulk velocity u_{bulk} is constant in x, the jet streamwise mass flux at x is $\frac{\pi}{4}u_{bulk}\rho_l D^2(x)$. The decrease of $D(x)$ with x due to droplet releases implies reduction of the jet streamwise mass flux and a commensurate increase of the streamwise mass flux of the dispersed liquid (the released droplets).

This interpretation implicitly addresses the second point. Namely, advancement of an ODT realization in time t is interpreted for statistical purposes advancement along the streamwise coordinate $x = u_{bulk}t$. On this basis, each ODT realization is deemed to specify an x-dependent steady (time-invariant) jet streamwise mass flux. Then release of an ODT droplet corresponds to a reduction of the jet streamwise mass flux at the release location, implying a commensurate rate of conversion of jet mass into droplet mass. Based on a determination of droplet size that is explained in Appendix A.3, the statistics of droplet releases during an ensemble of ODT realizations are used to determine both the mean rate of statistically steady droplet creation as a function of x and the droplet size distribution.

A2. Liquid core mass-loss rate

The most fundamental breakup statistic is the rate of breakup-induced mass loss from the jet. To show how this is inferred from ODT output, the jet mass-loss rate is first evaluated for a single ODT droplet release at some location $\hat{x}$. That release abruptly reduces $D(x)$ from $D_-(\hat{x})$ to $D_+(\hat{x})$, where the subscripts $-$ and $+$ denote values upstream and downstream of the discontinuity, respectively. Based on the constant liquid bulk velocity u_{bulk}, the associated change of jet streamwise mass flux at $\hat{x}$ is $\phi = \frac{\pi}{4}u_{bulk}\rho_l[D_+{}^2(\hat{x}) - D_-{}^2(\hat{x})]$. $-\phi$, which is positive, is interpreted as the associated increase of the streamwise droplet mass flux. Henceforth, the minus sign is dropped and ϕ is taken to be the absolute value of the indicated expression.

This result assumes that the ODT release event represents a steady process of jet-to-droplet mass-flux conversion at $\hat{x}$, or more generally, at the locations x_i of the droplet releases during one ODT realization. As in experiments, the quantity of interest is the time-averaged rate of streamwise mass-flux transfer from the jet to the droplets as a function of x.

As explained in Appendix A.1, each ODT realization generates, in effect, a representation of droplet releases along the space-time trajectory $x = u_{bulk}t$. Any epoch t corresponds to one location $x(t)$ along this trajectory. Therefore ODT cannot directly provide time-averaged information as a function of x. However, an ensemble of ODT realizations can provide ensemble statistics as a function of x, which constitute an equivalent representation of droplet statistics gathered during measurements of statistically steady jet breakup, assuming ergodicity of both the model and the corresponding physical process.

On this basis, the x dependence of the mean rate of core-to-droplet mass conversion is determined from ODT output as follows. The fundamental quantity of interest the cumulative jet-to-droplet mass-flux conversion $\Phi(x)$ within the streamwise interval $[0, x]$. For one ODT realization, this can be expressed as $\Phi(x) = \sum_{i=1}^{I(x)}\phi_i$, where $\phi_i = \frac{\pi}{4}u_{bulk}\rho_l|D_+{}^2(x_i) - D_-{}^2(x_i)|$ is the jet-to-dispersed-phase streamwise mass-flux conversion associated with the ith droplet release and $I(x)$ is the largest value of i for which the location x_i of the release does not exceed x. Φ is piecewise constant in x with a discontinuity wherever $x = x_i$ for some i.

Each member j of a collection of J ODT realizations yields the output $\Phi_j(x)$ for the realization. Averaging over j gives an estimate $\langle\Phi(x)\rangle_J$ of the desired ensemble average $\langle\Phi(x)\rangle$. For any finite J, $\langle\Phi(x)\rangle_J$ is piecewise constant, but for large J, this estimate converges to the ensemble ($J = \infty$) limit, which is a continuous function of x. A differentiable approximant of $\langle\Phi(x)\rangle$ can be obtained by filtering or by fitting a smooth function to $\langle\Phi(x)\rangle_J$.

This enables estimation of the ensemble average rate of jet-to-dispersed-phase streamwise mass-flux conversion per unit streamwise distance $\langle\phi\rangle = \frac{d}{dx}\langle\Phi\rangle$. $\langle\phi\rangle$ could be estimated directly in terms of the collection of quantities ϕ for J realization, but evaluating it using $\langle\Phi\rangle$ is convenient because it circumvents the handling of discontinuities, as in the estimation of a probability density function from data by differentiating a smoothed estimate of the cumulative distribution.

$\langle\Phi(x)\rangle$ can be interpreted as the droplet mass flux at x only if the streamwise velocity of all droplets at all x is u_{bulk}, which is generally incorrect owing to liquid–gas momentum and mass exchange and other effects. Therefore model results evaluate only the contribution $\langle\phi(x)\rangle$ of newly released droplets to the droplet mass flux. Further modeling beyond the present scope is needed to evaluate droplet evolution after release.

A3. Droplet size distribution

$\langle\phi(x)\rangle$ can be used to determine the mean rate $r(x)$ of droplet releases per unit streamwise distance based on droplet size information. For example, if the droplets are monodisperse with mass m, then $r(x) = m^{-1}\langle\phi(x)\rangle$, where $m(s) = \frac{\pi}{6}\rho_l s^3$ for droplet diameter s.

Upon release, a given ODT droplet occupies some length-l_d interval of the ODT domain. As explained shortly, l_d is used to identify an associated physical droplet diameter s and mass $m(s)$. s is assumed to be the diameter of each of the physical droplets comprising the steady mass flux attributed to the ODT droplet release event.

Each of these events yields a different ODT droplet size l_d and therefore a different physical diameter s. The collection of events during an ensemble of ODT realizations thus generates a polydispersion. To gather the associated droplet-size statistics, the range of droplet diameters s is discretized into bins $k = 1, \ldots, K$, where each bin is assigned a nominal diameter s_k and mass m_k.

The events that produce droplets within the diameter range of bin k constitute a size-conditioned subset of all droplet release events. Accordingly, the formal development in Appendix A.2 is applied on a size-conditioned basis. Namely, $\Phi_k(x)$ is the jet mass-flux loss attributed to events that release droplets in the bin-k diameter range. $\langle\phi_k\rangle$ is obtained from $\langle\Phi_k\rangle$ in the same manner as $\langle\phi\rangle$ is obtained from $\langle\Phi\rangle$. This enables the determination of the bin quantities $\langle r_k(x)\rangle = m_k^{-1}\langle\phi_k(x)\rangle$. By dividing each quantity $\langle r_k(x)\rangle$ by $\sum_{k=1}^{K}\langle r_k(x)\rangle$, the normalized histogram (discrete form of the probability density function) of droplet diameter is obtained. Specifically, this determines the size distribution of droplets released at the streamwise location x.

The remaining consideration is to associate a diameter s with a given droplet release in ODT. The available physical input is the size l_d of the liquid interval representing the droplet. This is a physically relevant length scale because it reflects the scale of the physical mechanisms of droplet separation from the liquid core as they are represented in ODT (see Section 2). However, the modeling of these mechanisms does not capture behavior in directions not aligned with the ODT domain such as the distortion of the shape of the phase interface as the droplet is formed. Therefore the size of the droplet in ODT is at best a rough estimate of the physical droplet diameter. Accordingly, the droplet diameter s is expressed as $s = Bl_d$, where B is a tunable coefficient. Because B is a single number that can hopefully be assigned a case-independent value while the droplet generation rate is a function of streamwise location, Weber number, ρ_l/ρ_g, and other quantities, there is ample scope to fit B to a subset of the available data and subsequently validate the various parameter dependences predicted by the model.

A4. Discussion

As noted in Appendix A.1, ODT has a consistent physical interpretation as a representation of flows that are statistically homogeneous in directions normal to the ODT domain. The application of ODT to a round jet is not fully consistent by construction, but it approaches physical consistency in a particular limit, as described next.

The physically consistent limit of the round-jet application described here is the regime $l_d \ll D$. The ODT droplet scale l_d is the scale of the physical mechanisms of droplet generation. At scales much less than D, the mean shape of the perimeter of the liquid core is planar to a good approximation, so modeling of processes that generate small droplets using a planar-jet picture is a reasonable idealization. Those processes are of course coupled to the core flow and therefore are in principle geometry dependent, but this introduces at most an order-one error that is subsumed into parameter adjustments.

These considerations justify the physical interpretation of ODT primary-droplet generation from a dimensional scaling viewpoint, but they do not account for the intermediate step of ligament formation, followed by ligament breakup into droplets. A possible empirical representation of this process would be to treat ODT droplet

release as physical droplet release farther downstream, reflecting the time required for ligament breakup. Ligament lifetime determination as in Sallam and Faeth (2003) could be the basis for such a representation.

References

Apte, S.V., Gorokhokhovski, M., Moin, P., 2003. LES of atomizing spray with stochastic modeling of secondary breakup. Int. J. Multiph. Flow 29, 1503–1522.

Apte, S.V., Mahesh, K., Gorokhokhovski, M., Moin, P., 2009. Stochastic modeling of atomizing spray in a complex swirl injector using large eddy simulation. Proc. Combust. Inst. 32, 2257–2266.

Ashurst, W.T., Kerstein, A.R., 2005. One-dimensional turbulence: Variable-density formulation and application to mixing layers. Phys. Fluids 17, 025107.

Ashurst, W.T., Kerstein, A.R., 2009. Erratum to one-dimensional turbulence: Variable-density formulation and application to mixing layers. Phys. Fluids 21, 119901.

Chehroudi, B., Chen, S.-H., Bracco, F.V., Onuma, Y., 1985. On the Intact Core of Full–cone Sprays. SAE Technical Paper 850126.

Chesnel, J., Ménard, T., Réveillon, J., Demoulin, F.-X., 2011. Subgrid analysis of liquid jet atomization. Atom. Sprays 21, 41–67.

Chiu, S.N., Stoyan, D., Kendall, W.S., Mecke, J., 2013. Stochastic Geometry and its Applications. John Wiley & Sons.

Dam, N.V., Rutland, C., 2015. Adapting diesel large-eddy simulation spray models for direct-injection spark-ignition applications. Int. J. Engine Res. doi:10.1177/1468087415572034.

Desjardins, O., Moureau, V., Pitsch, H., 2008. An accurate conservative level set/ghost fluid method for simulating turbulent atomization. J. Comput. Phys. 227, 8395–8416.

Echekki, T., Kerstein, A.R., Chen, J.-Y., Dreeben, T.D., 2001. One-dimensional turbulence simulation of turbulent jet diffusion flames: Model formulation and illustrative applications. Combust. Flame 125, 1083–1105.

Gonzalez-Juez, E.D., Schmidt, R.C., Kerstein, A.R., 2011. ODTLES simulations of wall-bounded flows. Phys. Fluids 23, 125102.

Gorokhovski, M., 2001. The stochastic Lagrangian model of drop breakup in the computation of liquid sprays. Atom. Sprays 11, 1514–1524.

Herrmann, M., 2010. Detailed numerical simulations of the primary atomization of a turbulent liquid jet in crossflow. J. Eng. Gas Turb. Power 132, 061506.

Herrmann, M., 2011. The influence of density ratio on the primary atomization of turbulent liquid jet in crossflow. Proc. Combust. Inst. 33, 2079–2088.

Hussain, A., Reynolds, W., 1975. Measurements in fully developed turbulent channel flow. J. Fluids Eng. 97, 568–578.

Jhavar, R., Rutland, C. J., 2006. Using Large Eddy Simulations to Study Mixing Effects in Early Injection Diesel Engine Combustion. SAE Technical Paper 2006-01-0871.

Kerstein, A., Wunsch, S., 2006. Simulation of a stably stratified atmospheric boundary layer using one-dimensional turbulence. Bound. Layer Meteorol. 118, 325–356.

Kerstein, A.R., 1999. One-dimensional turbulence: Model formulation and application to homogeneous turbulence, shear flows, and buoyant stratified flows. J. Fluid Mech. 392, 277–334.

Kerstein, A.R., Ashurst, W.T., Wunsch, S., Nilsen, V., 2001. One-dimensional turbulence: Vector formulation and application to free shear flow. J. Fluid Mech. 447, 85–109.

Lebas, R., Blokkeel, G., Beau, P.-A., Demoulin, F. X., 2005. Coupling Vaporization Model with the Eulerian–Lagrangian Spray Atomization (ELSA) Model in Diesel Engine Conditions. SAE Technical Paper 2005-01-0213.

Lebas, R., Menard, T., Beau, P., Berlemont, A., Demoulin, F.-X., 2009. Numerical simulation of primary break-up and atomization: DNS and modelling study. Int. J. Multiph. Flow 35, 247–260.

Lee, D.W., Spencer, R.C., 1933. Photomicrographic Studies of Fuel Sprays, 454. NACA.

Lignell, D., Kerstein, A., Sun, G., Monson, E., 2013. Mesh adaption for efficient multi-scale implementation of one-dimensional turbulence. Theor. Comput. Fluid Dyn. 27, 273–295.

Linne, M., 2013. Imaging in the optically dense regions of a spray: A review of developing techniques. Progress Energy Combust. Sci. 39, 403–440.

Linne, M.A., Paciaroni, M., Berrocal, E., Sedarsky, D., 2009. Ballistic imaging of liquid breakup processes in dense sprays. Proc. Combust. Inst. 32, 2147–2161.

Mahesh, K., Constantinescu, G., Apte, S., Iaccarino, G., Ham, F., Moin, P., 2006. Large-eddy simulation of reacting turbulent flows in complex geometries. J. Appl. Mech. 73, 374–381.

Meiselbach, F.T., 2015. Application of ODT to Turbulent Flow Problems. Ph.D. thesis, Brandenburg University of Technology, Cottbus, Germany.

Moser, R.D., Kim, J., Mansour, N.N., 1999. Direct numerical simulation of turbulent channel flow up to Re=590. Phys. Fluids 11, 943–945.

Ning, W., Reitz, R.D., Lippert, A.M., Diwakar, R., 2007. Development of a next-generation spray and atomization model using an Eulerian–Lagrangian methodology. In: Proceedings of the Seventeenth International Multidimensional Engine Modeling User's Group Meeting. Detroit, MI.

O'Rourke, P. J., Amsden, A. A., 1987. The TAB Method for Numerical Calculation of Spray Droplet Breakup. SAE Technical Paper 872089.

Reitz, R.D., 1987. Modeling atomization processes in high-pressure vaporizing sprays. Atom. Spray Technol. 3, 309–337.

Ross, S.M., 1996. Stochastic Processes, second ed. John Wiley & Sons New York.

Sallam, K., Dai, Z., Faeth, G., 2002. Liquid breakup at the surface of turbulent round liquid jets in still gases. Int. J. Multiph. Flow 28, 427–449.

Sallam, K., Faeth, G., 2003. Surface properties during primary breakup of turbulent liquid jets in still air. AIAA J. 41, 1514–1524.

Schmidt, R.C., Kerstein, A.R., Wunsch, S., Nilsen, V., 2003. Near-wall LES closure based on one-dimensional turbulence modeling. J. Comput. Phys. 186, 317–355.

Schulz, F.T., Glawe, C., Schmidt, H., Kerstein, A.R., 2013. Toward modeling of CO_2 multi-phase flow patterns using a stochastic multi-scale approach. Environ. Earth Sci. 70, 3739–3748.

Shinjo, J., Umemura, A., 2010. Simulation of liquid jet primary breakup: Dynamics of ligament and droplet formation. Int. J. Multiph. Flow 36, 513–532.

Shinjo, J., Umemura, A., 2011. Detailed simulation of primary atomization mechanism in Diesel jet sprays (isolated identification of liquid jet tip effects). Proc. Combust. Inst. 33, 2089–2097.

Tanner, F., 1997. Liquid Jet Atomization and Droplet Breakup Modeling of Non-Evaporating Diesel Fuel Sprays. SAE Technical Paper 970050.

Toninin, S., Gavaises, M., Theodorakakos, A., 2008. Modelling high-pressure dense diesel sprays with adaptive local grid refinement. Int. J. Heat Fluid Flow 29, 427–448.

Vallet, A., Burluka, A.A., Borghi, R., 2001. Development of an Eulerian model for atomization of a liquid jet. Atom. Sprays 11, 619–642.

Wolf, D., Incropera, F., Viskanta, R., 1995. Measurement of the turbulent flow field in a free-surface jet of water. Exp. Fluids 18, 397–408.

Wu, P.-K., Faeth, G., 1993. Aerodynamic effects on primary breakup of turbulent liquids. Atom. Sprays 3, 265–289.

Wu, P.-K., Faeth, G., 1995. Onset and end of drop formation along the surface of turbulent liquid jets in still gases. Phys. Fluids 7, 2915–2917.

PAPER III

Parameter Dependences of the Onset of Turbulent Liquid-jet Breakup

JFM RAPIDS
journals.cambridge.org/rapids
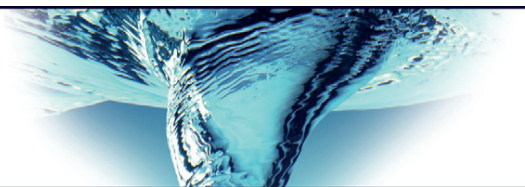
Parameter dependences of the onset of turbulent liquid-jet breakup

Alan R. Kerstein[1,†], **Amirreza Movaghar**[2] **and Michael Oevermann**[2]

[1]72 Lomitas Road, Danville, CA 94526, USA

[2]Department of Applied Mechanics, Chalmers University of Technology, Gothenburg, Sweden

Previous studies have predicted $We^{-2/5}$ dependence of the streamwise location at which primary breakup of turbulent liquid jets begins and $We^{-3/5}$ dependence of the Sauter mean diameter (SMD) of droplets released at that location, where We is the jet Weber number. Measured deviations from these predictions were attributed to measurement uncertainties and to the simplicity of the analysis, which invoked turbulence inertial-range phenomenology. Here, it is proposed that breakup onset is instead controlled by the residual presence of the boundary-layer structure of the nozzle flow in the near field of the jet. Assuming that the size of the breakup-inducing eddy is within the scale range of the log-law region, We^{-1} dependence of both the onset location and the SMD at onset is predicted. These dependences agree with the available measurements more closely than those previously predicted. To predict the dependences on the Reynolds number Re, either the friction velocity in conjunction with the Blasius friction law or the bulk velocity can be used, where the former yields $Re^{3/8}$ and $Re^{1/4}$ dependence of the onset location and the SMD at onset respectively, while the latter implies no Re dependence of either. The latter result is consistent with the available measurements, but the boundary-layer analysis indicates that the velocity scaling should be based on the friction velocity rather than the bulk velocity, so the origin of the measured lack of Re dependence merits further investigation. A plausible hypothesis is that pressure effects associated with the transition from wall-bounded nozzle flow to jet free-slip boundary conditions induce a transient large-scale flow modification that counteracts the Re dependence of the nozzle flow while preserving the logarithmic flow structure near the jet surface. Notwithstanding the absence of direct evidence supporting this hypothesis, the new analysis and comparisons of its predictions with measurements suggest that transient effects such as the residual influence of the nozzle-flow structure are the likely explanations of the observed parameter dependences.

Key words: jets, multiphase flow, turbulent boundary layers

† Email address for correspondence: alan.kerstein@gmail.com

A. R. Kerstein, A. Movaghar and M. Oevermann

1. Introduction

Primary breakup of turbulent liquid jets is subject to multiple influences such as aerodynamic shear, interfacial instabilities and cavitation as well as turbulence within the liquid jet. Various experiments have been performed in order to identify the effects of individual mechanisms. It has proven especially useful to focus on the onset of jet breakup. For high liquid-to-gas density ratios and inlet conditions for which cavitation and aerodynamic shear are negligible, this near-field process is controlled mainly by liquid-phase turbulence.

For this regime, Wu & Faeth (1995), here denoted WF, correlate the breakup-onset location x_i scaled by the jet diameter D in terms of the jet Weber number We using a theory based on the phenomenology of homogeneous isotropic turbulence (HIT), yielding the prediction $x_i/D \propto We^{-2/5}$. They fit a power-law dependence of x_i/D on We to measurements of x_i/D versus We, giving $x_i/D \propto We^{-0.67}$, where the range of reasonable agreement with the measurements begins at $We = 5 \times 10^4$. They deem this to be acceptable agreement of the theory with the measurements considering the simplicity of the theory.

Sallam & Faeth (2003), here denoted SF, note that the theory also predicts that the Sauter mean diameter (SMD) of droplets released at the onset location scales as $We^{-3/5}$. They find that the best power-law fit to their measurements is $We^{-0.94}$. They do not consider the deviation from the theoretical prediction to be statistically significant.

Here, a different physical picture of the mechanism of onset is proposed which is based on the flow state at the injector orifice. Prediction of the relevant mean properties of this state is based on classical boundary-layer (BL) phenomenology. It is assumed that the portion of the injector flow that is closest to the injector walls controls the eventual occurrence of breakup onset during the subsequent evolution of the liquid jet. The justification is that this is the region of highest mean shear, which tends to promote breakup. This is a strong assumption because this shear rapidly decays after the flow transitions from no-slip boundary conditions in the nozzle to free-slip boundary conditions (to a good approximation provided that the liquid-to-gas density ratio is large) upon exiting the nozzle. Nevertheless, it is assumed that the jet retains sufficient residual influence of the initial jet state so that scaling analysis based on that state is applicable to the estimation of the parameter dependences of breakup onset.

The BL analysis is used to estimate the local mean shear as a function of distance y from the injector wall. The shear is expressed as the inverse of a time scale that is interpreted as the turnover time t of the eddy that induces breakup onset, which is adopted as an estimate of the elapsed time from issuance of fluid from the nozzle to the onset of breakup. WF proceed similarly, except that they evaluate the turnover time t of the breakup-inducing eddy using inertial-range turbulence phenomenology that does not invoke a mean shear.

The analysis is explained first in terms of t without specifying its parameter dependences, and then the parameter dependences of t are derived by expressing t as a length scale L divided by a velocity scale V. It is shown that the parameter dependences of L and V determine the dependences of x_i/D and the SMD at onset on We and Re respectively. This allows unambiguous comparisons of the implications of the HIT and BL pictures of the turbulence phenomenology governing breakup onset.

Although the role of liquid-phase BL phenomenology that is proposed here is novel, effects of the gas-phase boundary layer are recognized and understood in the

context of air-assisted liquid-jet breakup (Raynal 1997; Varga, Lasheras & Hopfinger 2003; Kourmatzis & Masri 2014). That regime typically involves liquid injection into a high-speed laminar or turbulent gas stream, in contrast to the liquid jets in still air that have been used to study breakup dominated by liquid-phase turbulence. Since there is a continuous (although not necessarily monotonic) variation of the relative aerodynamic and liquid-phase contributions as the gaseous co-flow is increased, the two contributions are comparable in importance under some conditions. Therefore, a complete theory of breakup onset would need to encompass both contributions, such that the behaviour in the limiting cases of dominance by one or the other contribution is recovered.

In principle, the present study facilitates this synthesis by providing evidence that the liquid-phase contribution to breakup onset might be more analogous to the aerodynamic mechanism than previously supposed. It will be noted, however, that the new BL picture is not fully consistent with observations, so future steps towards the attainment of a fully satisfactory theory of the liquid-phase-dominated regime are recommended, which would establish the foundation for subsequent incorporation of aerodynamic phenomenology to obtain a comprehensive theory.

2. Analysis

Both here and in WF, t is a monotonically increasing function of eddy size, so the relevant t value is the turnover time of the smallest allowed eddies, whose size is denoted l_e. It is assumed that l_e approximates the size of droplets formed by such eddies.

The Rayleigh criterion $t_s \sim (\rho l_d^3/\sigma)^{1/2}$, where ρ is the liquid density and σ is the surface tension, determines the minimum size l_d of droplets that can be generated by a given shear $1/t_s$. Substituting l_e for l_d and t for t_s based on assumptions thus far,

$$t \sim (\rho l_e^3/\sigma)^{1/2} \tag{2.1}$$

is obtained, establishing a relationship between t and the smallest possible eddy size, l_e, which is not yet known. To evaluate l_e, modelling is used to obtain another relationship between t and l_e.

For this purpose, WF use HIT phenomenology. To obtain their breakup-onset scaling, the inertial-range scaling of t is expressed as $t \sim (D/U)(l_e/D)^{2/3}$, where U is the jet bulk velocity. This is equivalent to the specialization of equation (2) of WF to the inertial range. Substitution of this into (2.1) gives $l_e/D \sim We^{-3/5}$, where $We = \rho U^2 D/\sigma$. From this, the inertial-range scaling of t is used to obtain $t \sim (D/U)We^{-2/5}$.

Based on the assumption in §1 that the eddy turnover time t approximates the elapsed time until breakup onset, the onset location x_i scales as Ut, so

$$x_i/D \sim Ut/D. \tag{2.2}$$

The WF result for t then yields $x_i/D \sim We^{-2/5}$. The assumption that l_e approximates the size l_d of droplets released at onset then gives $l_d/D \sim We^{-3/5}$.

The analysis based on the BL picture differs from the foregoing only in the modelling that determines the l_e dependence of t. The first step is to evaluate the shear at the nozzle wall using the Blasius friction law $2(u_\tau/U)^2 = CRe^{-1/4}$ (Schlichting & Gersten 2000), where u_τ is the friction velocity, $Re = UD/\nu$, ν is the kinematic viscosity, and the empirical coefficient $C = 0.079$ and other numerical factors are

henceforth omitted from scaling estimates. Substitution of the definition of Re and the definition $u_\tau^2 = \nu(\partial u/\partial y)$, where $u(y)$ is the streamwise mean velocity profile and its partial derivative is evaluated at the wall, into the friction law gives the wall-shear scaling $\partial u/\partial y \sim (U^2/\nu)Re^{-1/4}$ and thus

$$u_\tau \sim U\,Re^{-1/8}. \tag{2.3}$$

The mean shear is derived as a function of y using the law of the wall, expressed as $u(y)/u_\tau = \kappa^{-1}\ln(yu_\tau/\nu) + B$, where B and the von Kármán constant κ are empirical coefficients. From this, $\mathrm{d}u/\mathrm{d}y \sim u_\tau/y$, corresponding to the time scale $t_s \sim y/u_\tau$.

It is assumed that size-l_d droplets are formed by liquid extending a distance $y = l_d$ inward from the jet boundary. Combined with the substitution of l_e for l_d and t for t_s based on prior assumptions, the expression for t_s becomes $t \sim l_e/u_\tau$. This allows l_e to be evaluated using (2.1), giving $l_e \sim \sigma/\rho u_\tau^2$, which is substituted back into $t \sim l_e/u_\tau$ to obtain $t \sim \sigma/\rho u_\tau^3$. Then, (2.3) is used to obtain

$$t \sim \frac{\sigma}{\rho U^3}Re^{3/8}. \tag{2.4}$$

Substituting this into (2.2) and using the definition of We,

$$x_i/D \sim We^{-1}Re^{3/8} \tag{2.5}$$

is obtained. Likewise, (2.3), the scaling of l_e, the definition of We and substitution of l_d for l_e give

$$l_d/D \sim We^{-1}Re^{1/4}. \tag{2.6}$$

In § 3, it is shown that the We dependences predicted by (2.5) and (2.6) are well supported by measurements, but the measurements give no indication of Re dependences as strong as predicted. In fact, they do not exclude the possibility that there is no dependence on Re.

Formally, the absence of Re dependence can be obtained by assuming $V = U$ instead of $V = u_\tau$ in the relation $t \sim L/V$, which eliminates the Re dependences without affecting the We dependences. In this regard, note that here and also in the HIT analysis, the dependence of L on l_e (and a power of D that maintains dimensional consistency) determines, through (2.1), the We dependence of l_e/D and consequently of x_i/D and l_d/D, while the velocity scale V that is adopted determines the Re dependences of x_i/D and l_d/D.

This raises the question of what physical mechanism could explain the dependence $t \sim y/U$. A definitive answer is not yet in hand, but a plausible candidate is the near-field structure of the mean pressure field. In the fully developed nozzle flow that has been implicitly assumed, the mean pressure gradient is constant and axially oriented. Upon exiting the nozzle, the flow becomes transient, and so the mean pressure field also varies radially. Since the flow is subsonic, mean pressure effects extend over large scales, implying possible large-scale adjustments of flow features such as the velocity normalization in the law of the wall. The available large-scale velocity is the bulk velocity U. This motivates the hypothesis that such adjustment suppresses the inlet-flow Re dependence partially or entirely while preserving the logarithmic cross-stream structure near the jet perimeter. This hypothesis is testable through either measurements or detailed numerical simulations, which are therefore recommended as further steps towards complete understanding of near-field turbulent jet behaviours that affect the onset of breakup.

FIGURE 1. Image of near-field breakup in a 95 % ethanol jet issuing from a 1 cm diameter nozzle at a bulk velocity of 15 m s^{-1}, corresponding to $Re = 72\,000$ and $We = 78\,000$.

3. Comparison with measurements

In the published experimental studies whose implications are revisited here, care was taken to assure that the nozzle flow closely approximated fully developed pipe flow, as explained, e.g., by WF and Wu, Miranda & Faeth (1995). This does not guarantee that the flow state downstream of the nozzle orifice is fully determined by the nozzle flow. The injector tube necessarily has a finite thickness, implying the possible formation of one or more recirculation zones downstream of the end face of the tube. For the high liquid-to-gas density ratios in the experiments, the high inertia of the jet implies that these are gas-phase recirculation zones. This is supported by the image in figure 1, which suggests negligible near-field influence of the ambient air on the jet. Farther downstream, any aerodynamic coupling should be further mitigated by jet-induced gas flow, which tends to reduce interfacial shear that might affect the liquid flow. However, these attributes can be sensitive to details such as the tube thickness and the degree of planarity and smoothness of the tube face. The possibility that some liquid is entrained into the recirculation zones, which would increase their momentum coupling to the jet, cannot be ruled out. These points illustrate that it is difficult to construct a precisely canonical experimental configuration. In this regard, detailed numerical simulations of cases with nominally zero-thickness tubes might be advantageous for obtaining definitive resolution of the ambiguities noted in §2.

WF presented the results of several experimental studies in a plot of x_i/D versus *We*. The reported measurements of breakup-onset location are replotted in figure 2, along with line segments representing the HIT prediction $We^{-2/5}$ and the BL prediction We^{-1}. The BL prediction is in better agreement with the measurements than the HIT prediction.

WF do not state the *Re* values corresponding to the data points, but they can be inferred from their plotted data, information in the plot legends and the definitions of *We* and *Re*. On this basis, figure 3 is obtained. The vertical axis is compensated so that any apparent dependence on *Re* cannot be caused by a correlation between
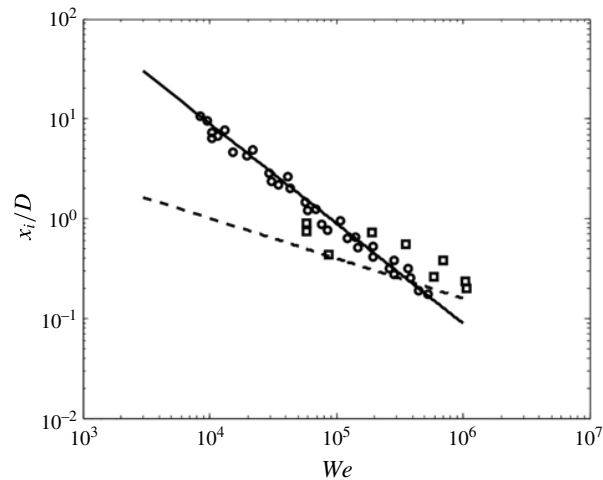
FIGURE 2. Measured Weber-number dependence of the normalized breakup-onset location x_i/D from the data compilation by WF. Data points designated by open squares are deemed to be outliers, as explained in the text. Solid line, We^{-1} dependence (BL prediction); dashed line, $We^{-2/5}$ dependence (HIT prediction).
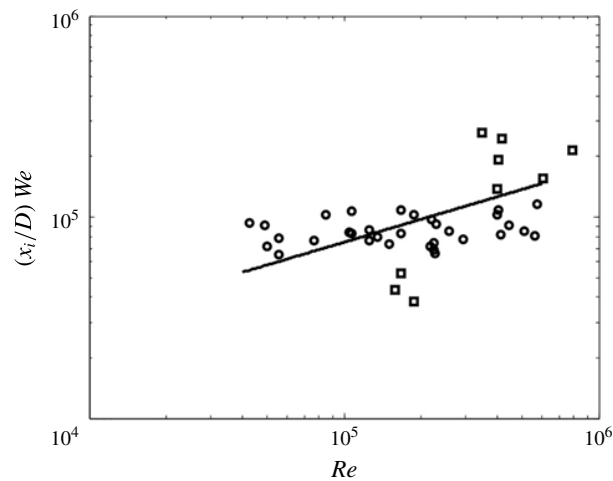
FIGURE 3. Reynolds-number dependence of the We-compensated normalized breakup-onset location. The Re values of the individual data points are deduced from information provided by WF, as explained in the text. Data points designated by open squares correspond to the similarly designated data points in figure 2. Solid line, $Re^{3/8}$ dependence (BL prediction).

the We and Re values of the chosen experimental cases. The plot gives no definitive indication of Re dependence, though it is possible that a mild dependence is masked by the statistical scatter of the data.

To reduce this scatter, selected outlier cases relative to the We^{-1} correlation line, designated by open squares in figure 2, are similarly designated in figure 3.

FIGURE 4. Measurements of the Weber-number dependence of the droplet SMD at onset, normalized by the cross-stream integral scale Λ, from the data compilation by SF. Solid line, We^{-1} dependence (BL prediction); dashed line, $We^{-3/5}$ dependence (HIT prediction).

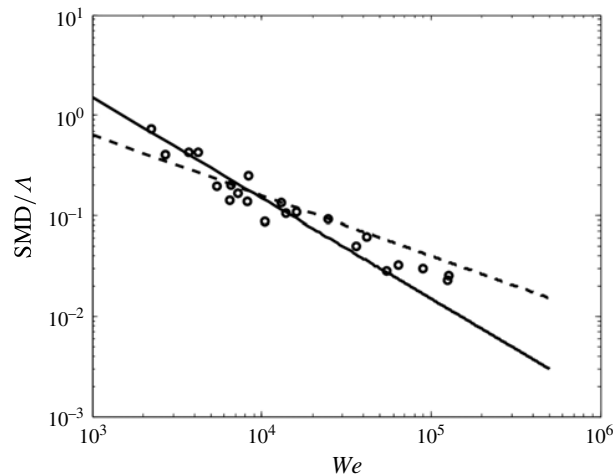The clustering of the outliers in both figures suggests that the cause of their deviations from the overall trends in these figures is systematic rather than statistical. Because these points are farthest from the We^{-1} correlation line in figure 2, the compensation factor used in figure 3 is least effective in removing their We dependence. This contributes to their deviations from collapse of the data in figure 3 as a function of Re. Without these cases, it is seen that a systematic dependence on Re can be ruled out with increased precision. On this basis, the $Re^{3/8}$ dependence predicted by the BL analysis, shown in the plot, is clearly inconsistent with the measurements, although the data can be plausibly interpreted as indicating a weaker dependence. In what follows, the theoretical interpretation is based on the default assumption that x_i/D does not depend on Re.

SF report measurements from various sources as well as their own measurements of droplet SMD at onset as a function of We. They normalized the SMD using the cross-stream integral scale Λ, for which they adopted the circular-pipe empirical correlation $\Lambda = D/8$. Their data are replotted in figure 4 with superimposed line segments whose slopes correspond to the HIT and BL predictions.

SF propose that the droplet diameter should correlate with the ligament diameter, for which they obtain $We^{-0.94}$ dependence based on a best fit to data. They then show that this empirical dependence likewise fits their droplet SMD data very well. (This procedure is used rather than a direct fit to the droplet data because the ligament data conform to power-law behaviour more closely than the droplet data.) The $We^{-0.94}$ dependence that they thus infer is substantially closer to the BL prediction than to their HIT prediction.

Insufficient information is provided to back-calculate Re for the individual points, so Re dependence cannot be evaluated quantitatively. However, the fairly good collapse of the data as a function of We suggests that any Re sensitivity is likely to be weak, which does not necessarily exclude the $Re^{1/4}$ dependence predicted by the BL analysis.

The correlation lines in figures 2 and 4 serve not only to demonstrate that the BL predictions are more consistent with measured We dependences than the HIT

predictions, but also to provide improved theory-based inputs to empirical models of jet breakup that might be used in engineering and other applications. For this purpose, the correlations

$$x_i/D = 9 \times 10^4 We^{-1} \tag{3.1}$$

and

$$\mathrm{SMD}/\Lambda = 1.5 \times 10^3 We^{-1}, \tag{3.2}$$

corresponding to the solid lines plotted in the respective figures, are recommended.

An additional perspective on the BL analysis is obtained by expressing the typical droplet size at onset in wall units. The BL analysis assumes that the distance from the jet perimeter at which shear acts to form a droplet scales with the droplet size, and that this location is within the log layer of the precursor nozzle flow. For $Re = 10^4$, the location at which the log layer is deemed to begin is nominally 30 in wall units (Pope 2000). The log law shows little Re dependence at Re values higher than this, so this lower bound on the logarithmic region is a generic high-Re value.

Based on $\Lambda = D/8$ and the data in figure 4, 0.01 is taken to be a representative value of l_d/D. The Blasius friction law can be expressed to a good approximation as $u_\tau = 0.2 U Re^{-1/8}$. It follows that $l_+ \equiv l_d u_\tau / \nu = 0.2(l_d/D)Re^{7/8}$. This exceeds 30 for $Re > 6 \times 10^5$, which is more that four times larger than the high end of the Re range of the SF experimental cases. This brings into question the applicability of the BL analysis to the measurements.

There are several ambiguities that obscure the interpretation of this result. One is that the liquid region that is subject to the droplet-forming shear might not be detached in its entirety to form a droplet. Droplet release might involve an action–reaction mechanism in which a portion of the liquid rebounds and thus remains with the jet. Another is that large-scale transients possibly associated with the absence of Re dependence of the breakup-onset location might also negate the applicability of standard law-of-the-wall phenomenology to the estimation of the extent of the log layer. These points further motivate future study of the details of breakup onset in order to clarify the governing mechanisms.

4. Discussion

The analysis presented here involves the representation of the turnover time t of the breaking eddy in terms of the inverse of a velocity times a power of the eddy size l_e (and the power of the jet diameter D that maintains dimensional consistency). The physical picture on which the modelling is based determines which velocity scale and what power of l_e are applicable. The choice of velocity scale determines the Re dependences of breakup-onset location and SMD at onset, and the power of l_e determines the We dependences of these quantities.

It has been shown that We^{-1} dependence of both quantities, which is well supported by the available measurements, is obtained if the dependence of t on l_e is linear. Since droplets are released from the perimeter of the jet, it is assumed that the breaking eddy occurs in a size-l_e region adjacent to the perimeter. Within this region, t is the inverse of a shear that can be estimated as $\partial u/\partial y$ evaluated at a distance $y = l_e$ from the jet perimeter. To obtain linear dependence of t on l_e, the partial derivative must scale as y^{-1}, implying logarithmic dependence of u on y. This reversal of the derivation in §2 shows that, starting from the empirical evidence and some plausible assumptions, the logarithmic y dependence of u can be deduced. It is natural to infer that this dependence is a residual effect of the logarithmic structure of the near-wall nozzle flow.

Proceeding therefore to more systematic (versus empirically driven) reasoning, as in §2, the *Re* dependences of the onset properties are also predicted, but in this case the results disagree with the available measurements. As noted, the *Re* dependences reflect the choice of velocity scale. Choice of the bulk velocity *U* instead of the friction velocity implied by the BL analysis yields agreement with the observed insensitivity of onset location to *Re* and predicts that SMD at onset is likewise insensitive to *Re*, but the latter result has not yet been stringently tested. A plausible explanation is that transients in the near field of the jet modify the flow structure in a way that changes the velocity scale while preserving the logarithmic *y* dependence of *u* near the jet perimeter. As yet, this hypothesis is not supported by any detailed reasoning or direct evidence.

The partial success of the BL picture suggests both future needs and opportunities. It would be beneficial to measure the liquid-phase flow in order to clarify why the predicted *We* dependences are obeyed but the predicted lack of *Re* dependence is not. Such measurements are challenging. Even in non-breaking jets, well-resolved flow measurements near the jet perimeter have not yet proven feasible (Mansour & Chigier 1994; Wolf, Incropera & Viskanta 1995). Numerical simulations would be especially suitable for clarifying the flow features that account for the observed parameter dependences, but any resulting modification of the theory would have to be tested experimentally due to the need for parameter variations beyond the range of computationally affordable simulations.

In §1, it is noted that a sufficiently improved theory of the breakup regime dominated by liquid-phase turbulence could enable further steps towards the unification of this liquid-phase BL treatment and the gas-phase BL treatment that has proven useful for interpreting features of air-assisted jet breakup. It is also noteworthy that studies of the latter regime (Raynal 1997; Varga *et al.* 2003; Kourmatzis & Masri 2014) involve coaxial flow configurations in which the speed of the co-flowing air is known and controllable. In contrast, the data used in the present study are from jets into still air, in which details of the jet-induced air flow are typically sensitive to uncontrolled influences such as far-field conditions. This ambiguity is inconsequential for breakup governed solely by the liquid-phase flow, although it does raise the concern that the exclusion of significant aerodynamic effects might not be definitive in the absence of gas flow measurements. Based on these considerations, it would be beneficial to study the liquid-phase-dominated regime using the coaxial configuration because it would enable better control and characterization of aerodynamic effects and it would also allow systematic increase of aerodynamic influence in order to identify the intermediate behaviours that occur as the breakup mechanism transitions to eventual aerodynamic dominance. The ultimate benefit of this investigation would be a more comprehensive theory of breakup onset, although challenges such as the treatment of cavitation effects would remain.

Several conclusions can be drawn from the analysis and results presented here. First, logarithmic flow structure near the jet perimeter provides a straightforward explanation of the experimentally observed *We* dependence of both onset location and SMD at onset. Second, the origins of this flow structure and of the velocity scaling implied by the measured insensitivity of onset location to *Re* can be clarified in the future by measurements and detailed numerical simulations that focus on this question. Third, the HIT picture of breakup onset, heretofore accepted as the definitive interpretation of breakup onset, is now seen to be neither the unique nor the most plausible physical picture of this phenomenon.

A. R. Kerstein, A. Movaghar and M. Oevermann

Acknowledgements

References

KOURMATZIS, A. & MASRI, A. R. 2014 Air-assisted atomization of liquid jets in varying levels of turbulence. *J. Fluid Mech.* **764**, 95–132.

MANSOUR, A. & CHIGIER, N. 1994 Turbulent characteristics in cylindrical liquid jets. *Phys. Fluids* **6**, 3380–3391.

POPE, S. B. 2000 *Turbulent Flows*. Cambridge University Press.

RAYNAL, L. 1997 Instabilite et entrainment a l'interface d'une couche de melange liquid-gaz. PhD thesis, Universite Joseph Fourier, Grenoble, France.

SALLAM, K. A. & FAETH, G. M. 2003 Surface properties during primary breakup of turbulent liquid jets in still air. *AIAA J.* **41**, 1514–1524.

SCHLICHTING, H. & GERSTEN, K. 2000 *Boundary-Layer Theory*, 8th edn. Springer.

VARGA, C. M., LASHERAS, J. C. & HOPFINGER, E. J. 2003 Initial breakup of a small-diameter liquid jet by a high-speed gas stream. *J. Fluid Mech.* **497**, 405–434.

WOLF, D. H., INCROPERA, F. P. & VISKANTA, R. 1995 Measurements of the turbulent flow field in a free-surface jet of water. *Exp. Fluids* **18**, 397–408.

WU, P.-K. & FAETH, G. M. 1995 Onset and end of drop formation along the surface of turbulent liquid jets in still gases. *Phys. Fluids* **7**, 2915–2917.

WU, P.-K., MIRANDA, R. F. & FAETH, G. M. 1995 Effects of initial flow conditions on primary breakup of nonturbulent and turbulent liquid jets. *Atomiz. Sprays* **5**, 175–196.
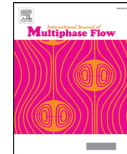
PAPER IV

Modeling and Numerical Study of Primary Breakup Under Diesel Conditions

Modeling and numerical study of primary breakup under diesel conditions

A. Movaghar [a],[*], M. Linne [b], M. Herrmann [c], A.R. Kerstein [d], M. Oevermann [a]

[a] Department of Mechanics, Chalmers University of Technology, Gothenburg, Sweden
[b] School of Engineering, University of Edinburgh, Edinburgh, UK
[c] Department of Mechanical and Aerospace Engineering, Arizona State University, Tempe, AZ, USA
[d] Consultant, 72 Lomitas Road, Danville, CA 94526, USA

ARTICLE INFO

ABSTRACT

A recently introduced stochastic model for reduced numerical simulation of primary jet breakup is evaluated by comparing model predictions to DNS results for primary jet breakup under diesel conditions. The model uses one-dimensional turbulence (ODT) to simulate liquid and gas time advancement along a lateral line of sight. This one-dimensional domain is interpreted as a Lagrangian object that is advected downstream at the jet bulk velocity, thus producing a flow state expressed as a function of streamwise and lateral location. Multiple realizations are run to gather ensemble statistics that are compared to DNS results. The model incorporates several empirical extensions of the original ODT model that represent the phenomenology governing the Weber number dependence of global jet structure. The model as previously formulated, including the assigned values of tunable parameters, is used here without modification in order to test its capability to predict various statistics of droplets generated by primary breakup. This test is enabled by the availability of DNS results that are suitable for model validation. Properties that are examined are the rate of bulk liquid mass conversion into droplets, the droplet size distribution, and the dependence of droplet velocities on droplet diameter. Quantities of greatest importance for engine modeling are found to be predicted with useful accuracy, thereby demonstrating a more detailed predictive capability by a highly reduced numerical model of primary jet breakup than has previously been achieved.

© 2017 Elsevier Ltd. All rights reserved.

1. Introduction

Most concepts for current and future high efficiency, low emission internal combustion engines use direct injection of fuel via sprays. Understanding the breakup of the fuel spray is of high interest to further improve engine combustion. When fuel is injected into the engine, the relatively low density ratio between liquid fuel and gas creates strong aerodynamic interactions. The liquid surface becomes unstable and droplets are formed. This process is called primary breakup. Droplets formed from primary breakup break into smaller and smaller droplets in a process called atomization. Fuel droplets evaporate and the fuel vapor mixes with the ambient air to form a fuel–air mixture which ignites either via self-ignition (diesel engine) or spark ignition (gasoline engine). Complete control of fuel–air mixing from primary breakup to turbulent mixing of the fuel vapor with the air in the cylinder is of utmost impor-

tance to achieve clean and efficient combustion. As the highly consequential first step in this process, primary breakup plays a special role but is the least well understood.

Due to its technical importance, the breakup of turbulent jets has been investigated experimentally in great detail and many models have been proposed to simulate the breakup process. Eulerian–Lagrangian models are the current workhorses for practical engineering simulations of spray processes including fuel injection in engines. In the majority of these simulations primary breakup is not actually simulated. Instead, simple liquid blobs of the size of the injector diameter are introduced into the simulation. Further breakup of these blobs via secondary breakup is simulated with phenomenological models such as the Taylor analogy breakup (TAB) (O'Rourke and Amsden, 1987; Tanner, 1997) or wave models (Reitz, 1987). Nevertheless, due to the limited understanding of primary breakup, current numerical spray models for Reynolds-averaged Navier–Stokes simulations (RANS) or large-eddy simulations (LES) involve significant simplifications, and tuning is usually necessary every time the flow conditions are changed to achieve satisfactory results.

---

* Corresponding author.
  E-mail address: movaghar@chalmers.se (A. Movaghar).

The limited understanding of primary breakup is due to the fact that experimental observation of the high-density region close to jet inlet is extremely difficult. As a result, much of the underlying physics leading to primary breakup is still unclear. Recently, sophisticated imaging techniques such as ballistic imaging and high speed shadow imaging have been able to provide more details of the primary breakup region (Linne, 2013; Rahm et al., 2015). Those new imaging techniques support the development of more predictive primary breakup models.

Direct numerical simulations (DNS) or high resolution large-eddy simulations (LES) offer an alternative way to study liquid–gas interface dynamics during primary breakup. Spatial and temporal resolution is limited only by the available computational resources, which have improved significantly over the past decades. Ménard et al. (2007) and Lebas et al. (2009) performed detailed simulations of jet breakup using a coupled level set/volume-of-fluid method with a ghost fluid approach. However they did not provide quantitative comparisons such as droplet size distributions with experimental data. Desjardins et al. (2010) and Desjardins et al. (2013) simulated the primary breakup using a conservative level set/ghost fluid approach. They used realistic turbulent boundary conditions at the injector inflow but no droplet size distributions were reported. Herrmann (2011) studied primary breakup of turbulent liquid jet under diesel conditions using the refined level set grid approach. He reported droplet size distributions and results of a grid refinement study providing detailed physical insight into primary breakup for moderate Weber and Reynolds numbers, which is difficult to acquire with experimental studies. However, routine use of DNS for industrial ranges of Weber and Reynolds numbers is still beyond the capacity of today's computers (Herrmann, 2010).

For practical simulations of engineering interest as well as to investigate the physics and scalings of primary breakup beyond the parameter range of DNS studies, a predictive and computationally affordable low-order model for simulating primary breakup is highly desirable. For this purpose, the one-dimensional turbulence (ODT) model has been proposed recently by Movaghar et al. (2017) as a primary breakup model. This stochastic modeling approach provides high lateral resolution by affordably resolving all relevant scales in that direction. The low computational cost of ODT compared to fully resolved three-dimensional DNS overcomes the limitation of DNS to moderate Reynolds and Weber numbers. As Movaghar et al. (2017) showed, after parameter tuning ODT has the capability to reproduce the results of experiments by Wu and Faeth (1995) and Sallam et al. (2002) for cases with high liquid/gas density ratio ($\rho_l/\rho_g > 500$). However, under real engine conditions liquid/gas density ratios are relatively low and aerodynamic effects have a significant effect on primary breakup.

In this work we apply the ODT approach presented in Movaghar et al. (2017) to the simulation of primary breakup of a round turbulent liquid jet injected into stagnant high pressure air under diesel-engine-like conditions. The main results, presented in the form of droplet size and velocity distributions as well as an axial profile of the mass rate of conversion from bulk liquid to droplets, are compared to the DNS study of Herrmann (2011).

The flows investigated in this study are governed by the incompressible Navier-Stokes equations for immiscible two-phase flow. The momentum equation is given by

$$\frac{\partial u}{\partial t} + u \cdot \nabla u = \frac{1}{\rho} \nabla p + \frac{1}{\rho} \nabla \cdot [\mu(\nabla u + \nabla^T u)] + \frac{1}{\rho} T_\sigma, \tag{1}$$

where u is the velocity, ρ the density, p the pressure, μ is the dynamic viscosity and T_σ the surface tension force which is nonzero only at the phase interface. All fluid properties are considered to be constant in each phase, allowing the viscous term to be simplified as shown below.

The one-dimensional turbulence model is outlined briefly in Section 2. A complete description of the ODT formulation used here is provided in Movaghar et al. (2017). The DNS formulation is discussed in detail in Herrmann (2008).

2. One-dimensional turbulence model

2.1. Time advancement processes

ODT is a stochastic model simulating the evolution of turbulent flow along a notional line of sight through a three-dimensional flow. Here it is used to simulate a nominally planar jet. The round-jet interpretation of this planar configuration is explained in Movaghar et al. (2017) and additional details of the execution of the simulations are discussed in Section 3.2. Denoting the jet streamwise direction as *x*, the ODT line of sight is oriented in the lateral (*y*) direction. This setup provides high lateral resolution of the relevant physics near the interface.

A Lagrangian picture is adopted, such that time advancement of ODT processes is interpreted as streamwise advancement based on assumed streamwise displacement of the ODT domain at the jet bulk velocity, denoted u_{bulk}. Taking the jet inlet to be the time origin in the ODT simulation, the ODT state at any later time *t* is interpreted as the state of the jet at streamwise location $x = u_{bulk}t$. Since the ODT state at given *t* represents the profile in *y* of all properties that are time advanced during the simulation, a single ODT realization can be interpreted as a representation of the instantaneous state of the jet in the $x - y$ plane. (In Movaghar et al., 2017, an array of *y* profiles of streamwise velocity, plotted at various *x* locations, illustrates this interpretation.) Each simulated ODT realization is initialized at the jet inlet with a size-*D* interval of liquid, where *D* is the inlet diameter of the round jet represented by the ODT simulation, and gas on both sides of the liquid.

Viscous transport on the ODT line is time advanced by solving

$$\partial u_i(y,t)/\partial t = \nu \partial^2 u_i(y,t)/\partial y^2, \tag{2}$$

where u_i with $i \in 1, 2, 3$ are the three velocity components and ν is the kinematic viscosity. The right-hand side of Eq. (2) is a specialization of the viscous transport in Eq. (1) based on the stated assumption of fixed fluid properties in each phase. A different ν value is needed in each of the phases and the liquid–gas density ratio is involved in the interfacial momentum–flux matching condition. Consistent with the idealized nature of the flow modeling, the gas-phase flow is parameterized rather than time advancing it using Eq. (2), as explained in Movaghar et al. (2017).

In ODT, turbulent advection is modeled by a stochastic sequence of events. These events represent the impact of turbulent eddies on property fields (velocity and any scalars that might be included) along the one-dimensional domain. During each eddy event, an instantaneous map termed the 'triplet map,' representing the effect of a turbulent eddy on the flow, is applied to all property fields. It occurs within the spatial interval $[y_0, y_0 + l]$, where y_0 represents the eddy location on the ODT line and *l* is the eddy size. A triplet map shrinks each property profile within $[y_0, y_0 + l]$, to one-third of its original length, pastes three identical compressed copies into the eddy range, and reverses the middle copy to ensure the continuity of each profile. The map mimics the eddy-induced folding effect and increase of property gradients. Formally, the new velocity profiles after a map are given by

$$\hat{u}_i(y,t) = u_i(f(y),t), \tag{3}$$

here conveniently expressed in terms of the inverse map

$$f(y) = y_0 + \begin{cases} 3(y - y_0), & \text{if } y_0 \leq y \leq y_0 + (1/3)l, \\ 2l - 3(y - y_0), & \text{if } y_0 + (1/3)l \leq y \leq y_0 + (2/3)l, \\ 3(y - y_0) - 2l, & \text{if } y_0 + (2/3)l \leq y \leq y_0 + l, \\ y - y_0, & \text{otherwise,} \end{cases} \tag{4}$$

which is single-valued. (The forward map is multi-valued.)

The triplet map is measure preserving, which implies that all integral properties of the flow field, such as mass, momentum and kinetic energy, are identical before and after applying the map. Various cases, such as buoyant stratified flow, involve sources and sinks of kinetic energy due to equal-and-opposite changes of one or more other forms of energy. Even in the simplest cases, viscosity converts kinetic energy into thermal energy. The resulting dissipation of kinetic energy is captured by Eq. (2). Energy-conversion mechanisms other than viscous dissipation are incorporated by introducing an additional operation during the eddy event.

In the present formulation, the triplet map can increase the number of phase interfaces within the eddy interval, as illustrated in Section 2.3, resulting in an increase ΔE_σ of surface-tension energy that must be balanced by an equal-and-opposite decrease of kinetic energy ΔE_{kin}, such that the total eddy-induced energy change $\Delta E = \Delta E_{kin} + \Delta E_\sigma$ is zero.

Accordingly, the formal statement of the eddy-induced flow change is generalized to

$$\hat{u}_i(y, t) = u_i(f(y), t) + c_i K(y) + b_i J(y) \tag{5}$$

and

$$\hat{\rho}(y, t) = \rho(f(y), t). \tag{6}$$

Here, $K(y) \equiv y - f(y)$ is the map-induced displacement of the fluid parcel that is mapped to location y and $J(y) \equiv |K(y)|$.

Eq. (6) indicates that density is triplet mapped but is not subject to addition of the kernels J and K, reflecting the fact that incompressible advection, and therefore its representation by eddy events, does not change the density ρ of fluid elements. (As noted, ρ for given y and t has one of the two values ρ_l and ρ_g.)

The six coefficients b_i and c_i are evaluated by enforcing the prescribed kinetic-energy change based on the surface-tension energy change E_σ, which is zero if the eddy interval contains only one phase. Momentum conservation in each direction i implies three more constraints. The two additional needed constraints are obtained by modeling the eddy-induced redistribution of kinetic energy among the velocity components. In accordance with return-to-isotropy phenomenology, these additional constraints impose a degree of equalization of the component kinetic energies.

2.2. Eddy selection

ODT samples eddy events from an eddy event rate distribution that depends on the instantaneous flow state and therefore evolves with the flow. Thus, there is no predetermined frequency of occurrence of eddy events collectively nor of a particular eddy type corresponding to a given location y_0 and size l.

The mean number of events during a time increment dt for eddies located within the interval $[y_0, y_0 + dy]$ in the size range $[l, l + dl]$ is denoted $\lambda(y_0, l; t) \, dy_0 \, dl \, dt$. The relation

$$\lambda(y_0, l; t) = C/(l^2 \tau(y_0, l; t)). \tag{7}$$

defines an adjustable parameter C that scales the overall eddy frequency and an eddy time scale τ, where the argument t appearing on both sides of the equation indicates that both λ and τ vary with time for given values of y_0 and l because τ depends on the time-varying instantaneous flow state in the manner described next. (With this understanding, the arguments of τ are henceforth

suppressed.) The dimensions of the event rate distribution λ are (length$^2 \times$ time)$^{-1}$. To find the eddy time scale τ, the square of the implied eddy velocity l/τ is modeled as

$$(l/\tau)^2 \sim E_{final} - Z(\nu^2/l^2), \tag{8}$$

where the first term, which is dependent on the instantaneous flow state, is specified by Eq. (12) in Section 2.3 and the second term involving the parameter Z suppresses unphysically small eddies. (The coefficient implied by the proportionality is absorbed into C.) In practice it would be computationally unaffordable to reconstruct the rate distribution every time an eddy event or an advancement of Eq. (2) takes place. Therefore eddy events are sampled using an equivalent Monte-Carlo numerical procedure called thinning (Ross, 1996).

2.3. Multiphase eddy implementation in ODT

As discussed in Section 2.1, if the eddy range contains one or both of the liquid–gas interfaces, the eddy is treated as a multiphase eddy. Fig. 1a shows an eddy that contains a phase interface and hence is a multiphase eddy. Based on the main hypothesis of turbulent breakup theory, droplets can be formed by turbulent eddies only when the kinetic energy of the velocity fluctuations is larger than the surface-tension energy required to form a droplet of size corresponding the eddy that produces it. This needs modeling in ODT to account for the eddy-induced change of surface-tension energy.

Incorporation of this into ODT starts from the volumetric density $\sigma\alpha$ of surface-tension energy, where σ is the surface-tension energy per unit area and α is the surface area per unit volume. This gives an energy density

$$E_\sigma = \sigma\alpha/\bar{\rho} \tag{9}$$

per unit mass, where $\bar{\rho}$ is the mean density. The meaning and evaluation of α and $\bar{\rho}$ in ODT are considered.

Since an interface in ODT is represented by an isolated point on a line, geometric interpretation is required in order to obtain the area increase in the case of breakup. A plausible assumption for highly turbulent cases involving wrinkled interfaces is that the interface is a statistically homogeneous isotropic random surface. For such a surface, a number density n of interface intersections along a line of sight corresponds to an interface area per unit volume $\alpha = 2n$ (Chiu et al., 2013). On this basis,

$$E_\sigma = 2n\sigma/\bar{\rho}. \tag{10}$$

This assumption might not be precisely accurate for the jet breakup problems considered here, but it is convenient to adopt it as a universal assumption rather than to attempt a case-by-case treatment. The assumption is used only to evaluate E_σ for jet-breaking eddies, which are typically small relative to the jet diameter in the axial range considered here. The tendency for the turbulent cascade to induce small-scale homogeneity and isotropy is well established (Goto and Kida, 2003; 2007).

Because there are always exactly two phase interfaces on the ODT domain at the inception of an eddy event, the number of interfaces within any eddy is 0, 1, or 2, corresponding to number densities $n = 0$, $1/l$ or $2/l$, respectively, within the eddy. Triplet mapping of a phase interface within an eddy produces three such interfaces. This is shown in Fig. 1b and is interpreted as a tripling of interfacial area. The eddy-induced increase δ of the number density of interfaces due to triplet mapping which will be 0, $2/l$ or $4/l$ for the mentioned cases. Based on the relation $\alpha = 2n$, the interfacial area increase per unit volume is 2δ. Multiplication by the surface tension σ gives the surface tension potential energy per unit volume that is stored in the newly created interfaces. This implies the surface tension energy change per unit mass

$$\Delta E_\sigma = 2\sigma\delta/\bar{\rho}, \tag{11}$$
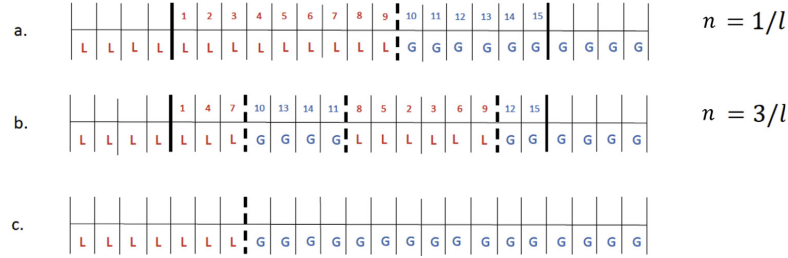
$n = 1/l$

$n = 3/l$

Fig. 1. Multiphase eddy treatment in ODT. (a) The size-l spatial region between the thick solid lines is selected for eddy implementation. It is a multiphase eddy containing both liquid (L) and gas (G) separated by one phase interface (thick dashed line), corresponding to $n = 1/l$. (b) A triplet map is implemented here as a permutation of the cells of a uniform spatial discretization of the 1D domain, illustrated by the reordering of cell indices within the eddy. Now there are three phase interfaces, corresponding to $n = 3/l$ and thus $\delta = 2/l$. (c) The newly formed droplet is removed and replaced by gas. Information about removed droplets can be transferred to a secondary-breakup sub-model within a comprehensive spray simulation.

where $\bar{\rho}$ is now identified as the mean density with the eddy range. This explanation corrects an erroneous discussion of these points in Movaghar et al. (2017), but the final result, Eq. (11), is unchanged.

Conservation of total energy requires an equal and opposite change of the final kinetic energy. Here this implies

$$E_{final} = E_{kin} - \Delta E_\sigma, \qquad (12)$$

where E_{kin} and E_{final} are the available kinetic energy per unit mass before and after the change, respectively. Here, available means the maximum amount extractable by adding weighted J and K kernels to the instantaneous velocity profiles as shown in Eq. (5). The change is implemented by similarly modifying the velocity profiles using weighted J and K kernels, but in this instance extracting the energy ΔE_σ from the flow field within the eddy interval, as described in Section 2.1.

As we focus on modeling primary breakup, droplets are removed from the computational domain as triplet maps create them by separating liquid from the jet, see Fig. 1b. Fig. 1c shows that the resulting gaps are set to gas-phase conditions. Except for breakup events that contain the entire liquid region (the model analog of liquid-column disintegration), a triplet map can create only one droplet.

Droplets are removed because there is no suitable way to time advance their motion and interactions on the 1D Lagrangian domain. In any case, their subsequent fate is a question beyond the scope of the primary-breakup phenomenon addressed here. The ultimate purpose of the ODT primary-breakup model is to use the statistics of the released droplets as inputs to a spray model of conventional form that then time advances droplet populations using probability distribution functions or other standard tools. With such coupling, the spray model could be used to characterize the droplet-laden gaseous medium in the ODT primary-breakup model, resulting in two-way coupling of the primary-breakup model and the spray model.

The above description covers the essentials of the ODT primary-breakup formulation. In order to capture global features of breaking liquid jets such as the Weber-number dependence of the liquid column length, Eq. (8) was supplemented with additional terms idealizing the Rayleigh and aerodynamic-shear mechanisms of liquid-column disintegration. The present study retains all these details, including the assigned values of adjustable parameters, as described in Movaghar et al. (2017), so the reader is referred to that publication for a complete discussion. The intent here is to determine the extent to which this formulation, designed and validated with reference to global jet structure, is able to capture local features such as the size distribution of droplets produced by primary breakup.
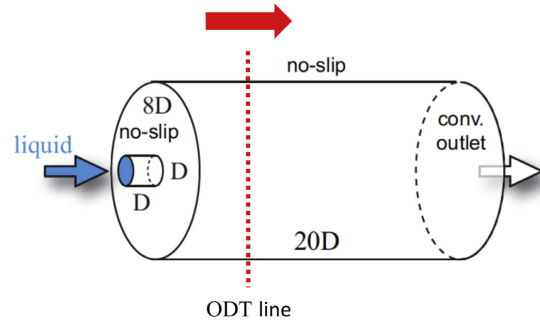

Fig. 2. DNS and ODT computational setups.

Table 1
Simulation conditions for the liquid jet.

Parameter	Value
μ_l (Liquid absolute viscosity)	1.7×10^{-3} kg/ms
μ_g (Gas absolute viscosity)	1.78×10^{-5} kg/ms
D (Initial jet diameter)	100 µm
u_{bulk} (Jet inlet mean velocity)	100 m/s
ρ_l/ρ_g (Liquid/gas density ratio)	34
$Re_{bulk} = \rho_l u_{bulk} D/\mu_l$ (Reynolds)	5000
$We = \rho_l u_{bulk}^2 D/\sigma$ (Weber)	17000
$Oh = \mu_l/(\rho_l D \sigma)^{0.5}$ (Ohnesorge)	0.026

3. Operating conditions and computational setups

3.1. Operating conditions and DNS computational setup

Simulations have been performed of the primary breakup of a turbulent liquid jet injected into stagnant dense air under diesel engine conditions. Fig. 2 shows the cylindrical DNS computational domain. It extends 20 inlet diameters D downstream of the jet inlet and 4 diameters in the radial direction.

In the DNS, which is described in detail in Herrmann (2011), no-slip boundary conditions are used on all boundary faces, except for a convective outflow at the right boundary and an inflow boundary condition at the injector pipe inlet. To accurately represent the turbulence of the liquid at the inlet, DNS of single-phase periodic pipe flow was performed using the injector-flow Reynolds number $Re_{bulk} = 5000$. The DNS results were stored in a database and then used as inflow boundary conditions for the atomization simulation.

Table 1 summarizes the operating conditions used in the simulations. The gas phase is initialized to be motionless.

3.2. ODT computational setup

As explained in Section 2.1 and illustrated in Fig. 2, the ODT line is interpreted as a Lagrangian object advected downstream at velocity u_{bulk} during a simulated realization. The ODT simulation setup in this study involves first, the generation of initial property profiles at the jet inlet plane, and second, the time advancement of the jet breakup simulation.

The initial velocity profiles u_i for the jet breakup simulation are obtained by performing a channel-flow simulation representing the turbulent flow in the injector pipe. During the channel-flow simulation, Dirichlet boundary conditions are applied at both endpoints of the ODT line (representing no-slip wall boundary conditions) and the ODT parameters are chosen to be $C = 5.2$ and $Z = 10$ as in Movaghar et al. (2017). The ODT flow state at the end of the channel simulation is saved for initialization of the next simulated channel-flow realization that generates a new initial condition for the next jet simulation.

With this procedure, each profile at the jet inlet plane represents an instantaneous flow state along a wall-normal line of sight within a fully developed channel flow. (See the cited reference for additional details concerning the model formulation and parameter settings in the jet portion of the simulation.) Each simulated ODT realization of the jet is performed for a computational time corresponding to a streamwise distance $x/D = 20$, which is the axial extent of the DNS domain. Statistics are presented either as a function of x/D or on the basis of all droplets generated by the ensemble of simulations.

The ODT results presented here are based on an ensemble of 10,000 simulated realizations, corresponding to a total CPU time of 24 hours, which is lower by a factor of 10,000 than the CPU time for the DNS comparison case. This does not fully indicate the cost advantage of ODT because adequate statistics could have been obtained with significantly fewer simulated realizations, but 10,000 realizations were nevertheless run because it was convenient to do so. (For visual clarity, scatter plots shown here are based on data from 500 realizations. Those plots demonstrate that fewer realizations are sufficient for ample output statistics.) However, the DNS run time cannot be substantially reduced without reducing numerical accuracy and thereby degrading the fidelity of the results.

As discussed by Herrmann (2011), in the DNS it takes approximately 4 μs for the turbulent pipe flow to reach the jet inlet plane and thereafter influence the liquid/gas interface. Before this stage, breakup occurs in a fully laminar environment and by mechanisms that are beyond the scope of this paper. For the comparison we limit ourselves to conditions of statistically stationary turbulent breakup. The ODT formulation is inherently limited to representation of statistically stationary conditions because ODT time advancement is a surrogate for streamwise advancement according to the Lagrangian interpretation adopted here, so there is no representation of transient jet development at a given streamwise location.

4. Results

4.1. Droplet mass generation rate

The most basic quantitative signature of primary breakup is the rate of liquid jet mass loss due to droplet generation by primary breakup. Fig. 3 shows the cumulative jet-to-droplet mass conversion rate $\dot{m}_d$ as a function of x/D, meaning that $\dot{m}_d$ for given x/D is the axial mass flux of all droplets generated between the jet inlet
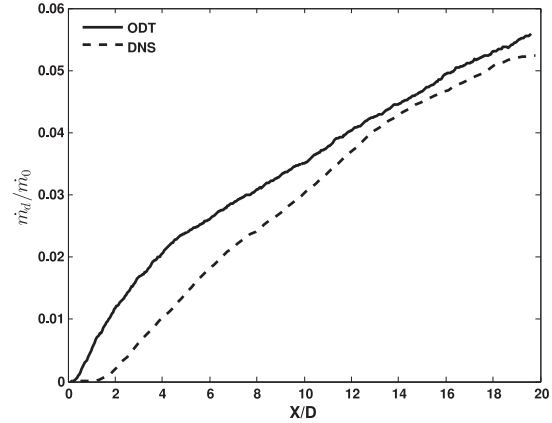

Fig. 3. Cumulative jet-to-droplet mass conversion rate due to primary breakup normalized by the liquid jet mass flux at the jet inlet plane.

and x/D. In the plot, $\dot{m}_d$ is normalized by the liquid jet mass flux $\dot{m}_0$ at the jet inlet plane.

In the far field, the ODT results agree quite well with the DNS. The main difference between the two curves is that the near-field jet-to-droplet mass conversion rate is larger for ODT than for DNS, followed by bending of the ODT curve to a shallower slope near $x/D = 4$, while for DNS this bending does not occur until $x/D = 13$. The ODT near-field conversion rate is thus higher than for DNS, but does not extend as far as the DNS near-field transient before bending to a lower rate. These two effects nearly cancel, such that the ODT droplet mass flux at $x/D = 13$ nearly matches the DNS value, after which the nearly equal (and roughly constant) slopes of the two curves indicate that the ODT far-field conversion rate is equal to the DNS rate within the statistical precision of the curves.

There are at least two possible causes of the near-field discrepancies. One is that the transition at the jet inlet plane from confined flow with no-slip walls to a free liquid interface coupled to the gas flow is likely to induce local three-dimensional pressure fluctuations beyond the scope of phenomenology captured by ODT. Another is that primary breakup is deemed to occur in ODT at the instant of separation of a liquid parcel from the jet, but in the DNS, such separation is primarily by ligament formation, and droplet formation is deemed to occur only when droplets separate from the ligaments. This delays the attribution of liquid mass loss until larger x/D, which might partially explain the shallower but more extended near-field transient indicated by the DNS. In principle it is possible to introduce an analogous delay of mass-loss attribution in ODT that might bring the near-field results into better agreement. However, this would be only a bookkeeping adjustment that does not introduce any physically based representation of droplet generation mediated by ligament formation into ODT. Moreover, it would involve model and parameter adjustments that would deviate from the present focus on strictly predictive application of the previously reported model formulation. For these reasons, it is not attempted here.

With regard to prediction, two points are noteworthy. First, the model was designed and validated with emphasis on the global jet structure, as explained in Section 2.3, but the comparisons in Fig. 3 and results that follow focus on local details of breakup that test the broader applicability of the model. Second, the lower ρ_l/ρ_g value for the present case than for the ambient-pressure cases previously used to calibrate the model tests the robustness of its parameter-space extrapolation.
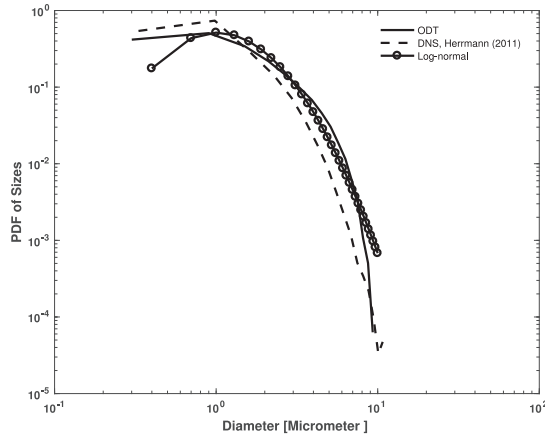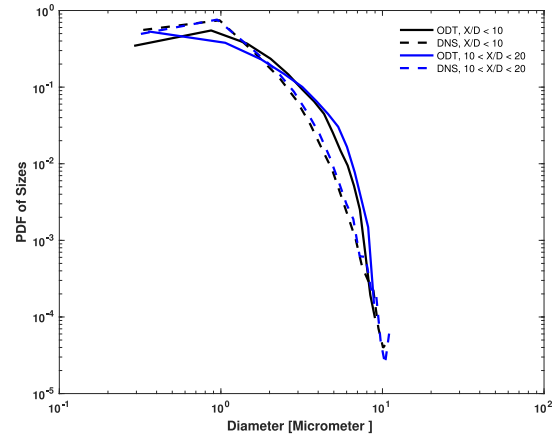
Fig. 4. Droplet size distribution.

Fig. 5. Droplet size distribution.

4.2. Droplet size distribution

One of the main outputs of the primary-breakup simulations is droplet-size information. Due to its computational affordability, ODT can be used in the future to generate droplet-size distributions as inputs for a standard Lagrangian spray model.

ODT is numerically implemented using a specially designed adaptive mesh that does not limit the droplet size resolution, so arbitrarily small droplets can be released, as prescribed by the physics. Neither the numerics nor the physical modeling inherently constrain the range of droplet sizes whose primary breakup can be predicted using ODT, but model simplifications and omissions of physical mechanisms that influence the process imply that the predictions cannot be deemed reliable without adequate validation. The present study compares ODT predictions to DNS results as a contribution to this objective.

In DNS (or any grid based method) simulations generally, the minimum size of droplets depends on the grid size—droplets smaller than the grid size cannot be represented by interface tracking methods such as volume of fluids (VOF) or level-set methods unless inherent subgrid resolution is used as described by Herrmann (2008). In Herrmann (2011) the resolution of the level set is finer than the flow solver to minimize the impact of the grid size on the breakup process. A grid resolution of $0.0039D$ is used for resolving the interface and $0.01D$ for the flow. For comparison, a similar resolution should be used for the ODT simulations. We have chosen the smallest eddy size allowed in the ODT simulation to be $0.002D$ and suppress all eddies of smaller size (though the generation of smaller droplets is still not completely ruled out because an eddy can overlap an arbitrarily small liquid interval and form a droplet from a portion of that interval).

As discussed in Section 2.3, a multiphase eddy detaches a liquid interval of some length l_d from the bulk liquid. For breakup of a round jet, the ODT droplet size is not the same as the length of the liquid interval l_d. Instead we define $S = Bl_d$ as the size of the droplet, where B is a tunable coefficient. In Movaghar et al. (2017), tuning of B to match measurements of high-density-ratio (ambient-pressure) jet breakup gave the optimum value $B = 0.2$. The same value is used here in order to test the robustness of that parameter fit (and of the other features of the ODT formulation).

On this basis, Fig. 4 shows the droplet-size probability density function $f(D)$ resulting from primary breakup in DNS and ODT sim-

ulations. The distributions are histograms that partition the diameter range into 20 bins. The results show good agreement of the ODT and DNS results, notably including the relatively rare production of large droplets.

Fig. 4 shows also a log-normal distribution fitted to the ODT results. It provides a rough but reasonable representation of the ODT distribution. Thus, if ODT is used to develop a parameterized tabulation of droplet size distributions, log-normal fits might be suitable for condensing the information, e.g. for use in subgrid closures of coarse-grained simulations of primary atomization.

Since Fig. 4 is based on the aggregate of droplets throughout the x/D range [0, 20], it does not reflect variation of the size distribution as the jet develops spatially. To capture this, several representations of the streamwise variation of droplet statistics are presented.

First, in Fig. 5, DNS and ODT results for $f(D)$ are shown for two subranges of the streamwise range of the simulations. It is seen that there is little difference between the distributions in the two subranges. Further subdivision of the near-field data into x/D subranges [0, 5] and [5, 10] (not shown) indicates some greater degree of x/D dependence of the ODT results but hardly any such dependence of the DNS results. However, the results shown next indicate transient behaviors not captured by this comparison.

Droplet Sauter Mean Diameter (SMD) is shown as a function of x/D in Fig. 6. There is rough (30% maximum deviation) quantitative agreement of ODT with the DNS results at all x/D, but reflecting the observation in the previous paragraph, ODT shows markedly greater near-field x/D dependence than the DNS.

To examine these tendencies in greater detail, scatter plots of droplet diameter versus x/D are shown in Fig. 7. The main difference between the ODT and DNS results is the absence of significant droplet generation for $x/D < 1$ in the DNS, while the ODT results indicate no discernible delay of the onset of droplet generation.

Parameter dependences of the x/D value for onset of droplet generation were examined in Movaghar et al. (2017) for ambient pressure conditions corresponding to a liquid/gas density ratio of order 1000. In that case, ODT was found to underestimate the onset distance by roughly a factor of two relative to experimental results for values of Reynolds number and Weber number close to those for the present case. (Onset distance was defined as the most probable onset location based on the distribution of onset locations generated by an ensemble of ODT realizations. The median of this
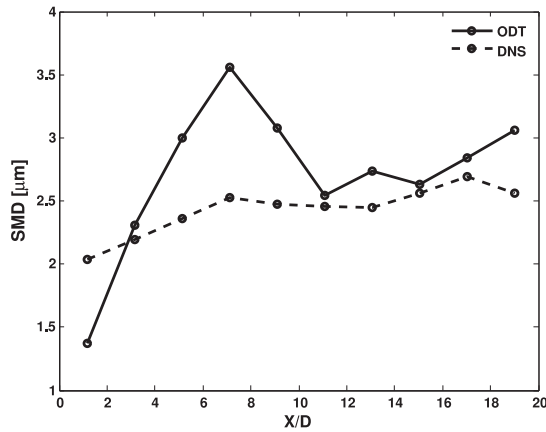
Fig. 6. Droplet Sauter Mean Diameter (SMD) versus distance from the jet inlet.

distribution likewise gave an underestimate, but was not as far below the measurements.)

For the present case, the liquid/gas density ratio is lower and both DNS and ODT indicate onset closer to the inlet than for ambient conditions, with ODT again underestimating the onset distance. The implication is that aerodynamic coupling, which is enhanced by an increase of the gas density, promotes early onset of droplet generation. ODT appears to exaggerate this tendency.

The ODT behavior is further elucidated by Fig. 8, which is a scatter plot of axial and lateral droplet location, with lateral location expressed as droplet distance R from the jet perimeter immediately after droplet formation. Droplet sizes are color-coded.

This plot captures all the information shown in Fig. 7a as well as the lateral droplet locations relative to the jet perimeter upon droplet formation. However, the available DNS output does not allow a comparable rendering of DNS results, which is why Fig. 7 is also shown.

R/D values provide an indication of the sizes of the droplet-forming ODT eddy events. The small R/D values in the near field reflect the persistence of the channel-flow inlet condition over some x/D range. The thin boundary layers at the edges of the channel flow evolve into regions of high liquid shear in the vicinity of the jet perimeter, albeit decaying due to turbulent transport that spreads velocity fluctuations laterally and droplet generation that removes strongly sheared liquid from the jet, in effect peeling away the boundary layer. This flow structure generates eddies comparable in scale to the thin high-shear regions. Some of these eddies generate droplets at locations that are relatively close to the jet perimeter as seen in Fig. 8, which also shows the gradual reduction of this tendency with increasing x/D.

Farther downstream, a transition to droplet formation by larger eddies is apparent, consistent with decay of the initial shear layers and increasing droplet formation by larger eddies, whose contribution is delayed due to the relatively long turnover times of these eddies. Both liquid bulk turbulence and aerodynamic shear can contribute to the occurrence of such eddies. It is seen that many of the droplets that are generated in the far field are small relative to the size of the eddies that produce them. (Note in Table 1 that $D = 100$ μm.) These eddies are thus located primarily in the gas phase, and hence driven largely by aerodynamic shear, which is thus an important if not dominant cause of far-field droplet generation. Indeed, the aerodynamic shear treatment introduced in Movaghar et al. (2017) is formulated to increase the strength of this droplet-generation mechanism with increasing x/D.
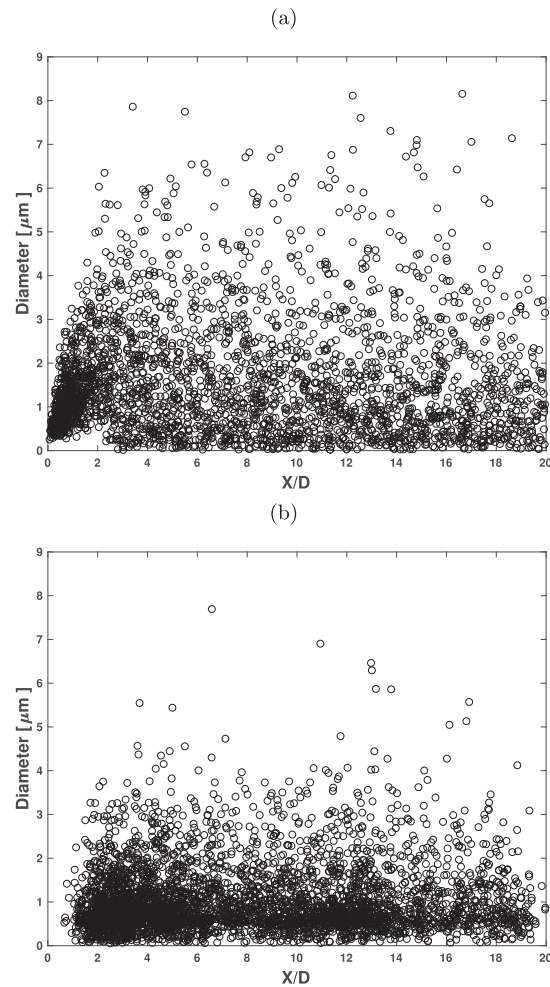

Fig. 7. Scatter plots of droplet diameter versus distance from the jet inlet. (a) ODT, (b) DNS.

This strengthening droplet-generation mechanism is supplemented by the contribution of liquid bulk turbulence, which decays with increasing x/D. Figs. 7a and 8 indicate that the net effect is gradually decreasing but generally stable droplet generation, as seen also in the DNS results in Fig. 7b. The slight decreasing tendency is quantified on a mass basis in Fig. 3.

The overall impression is that droplet generation by relatively large eddies is reasonably well represented by the model, but there is excessive near-field droplet formation by small eddies induced by locally strong shear originating in the inlet flow. This discrepancy was evident to some extent in previous work focusing on very high liquid/gas density ratios, but is more pronounced in the present model application to a case with a lower, though still high, density ratio. In the model, the gas streamwise velocity is spatially uniform with a value that matches the liquid streamwise velocity at the phase interface. On this basis, higher gas density more effectively counteracts the increase of the liquid velocity at the phase interface caused by lateral homogenization of the liquid
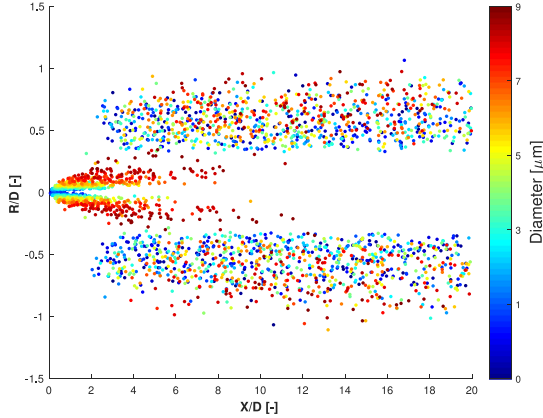
Fig. 8. ODT droplet spatial distribution, where the ordinate is the distance R of a droplet from the jet perimeter immediately after droplet formation, scaled by D, and the color bar indicates the droplet diameter in μm. (For interpretation of the references to color in this figure legend, the reader is referred to the web version of this article.)

Fig. 9. Normalized droplet mean axial velocity conditioned on droplet diameter. U_0 is the liquid bulk velocity at the jet inlet.

Fig. 10. Droplet kinetic energy in the lateral plane, conditioned on droplet diameter. The normalizing velocity is defined as in Fig. 9.

jet by bulk turbulence. Therefore inaccurate modeling of the aerodynamic coupling has more severe consequences as the liquid/gas density ratio is reduced. The aerodynamic coupling was formulated in Movaghar et al. (2017) to match far-field rather than near-field behavior, so present results might motivate future modification of the near-field aerodynamic coupling in the model.

Notwithstanding the nuances of aerodynamic coupling, the notion that the liquid-phase contribution to breakup is initially boundary-layer controlled and subsequently controlled by homogeneous turbulence is intrinsically plausible. A recent study that re-examined experimental results on the parameter dependences of liquid-jet breakup onset found evidence supporting the relevance of both of these mechanisms (Kerstein et al., 2017). Though the initial flow state of the liquid is an input to the ODT jet simulation, its subsequent development is governed by the ODT representation of turbulence dynamics, which broadly captures the main features in this as in other model applications.

4.3. Droplet velocity distribution

Fig. 9 shows the droplet mean axial velocity conditioned on droplet diameter for ODT and DNS. The distributions are discretized using 10 bins over the range of droplet diameters. The profiles are normalized by the liquid bulk velocity at the jet inlet plane. ODT captures the overall magnitude and trend of the DNS results (note that the vertical origin is a positive value and the maximum ODT error is under 30%), but the curves have different shapes.

This may occur for several reasons but we believe that ligament formation prior to droplet generation, which ODT cannot emulate (as discussed in Section 4.1) is the leading effect. Another consideration is that droplet velocities are influenced by the return-to-isotropy representation in ODT that is described in Section 2.1. This idealization of an effect stemming from complicated pressure-fluctuation effects is rough at best, so ODT predictions of droplet velocities might be less reliable than droplet-size predictions.

ODT results for a normalized measure of droplet kinetic energy in the plane normal to the axial direction, shown in Fig. 10, grossly underpredict the DNS results. In addition to the possible causes described above, another possible cause of this underprediction is
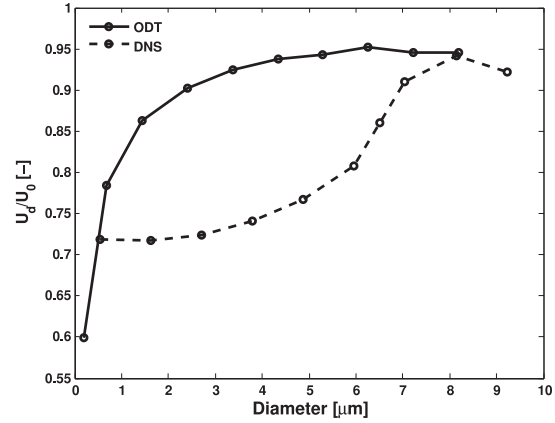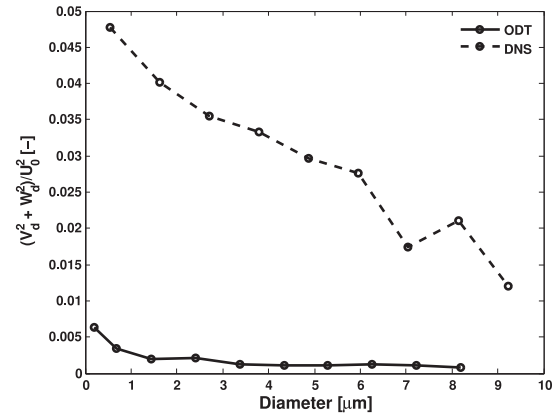
the inability of ODT to capture radial undulations of the liquid-gas interface, which might contribute to the DNS radial velocity.

To further elucidate the parameter dependences of droplet velocity, scatter plots of normalized droplet axial velocity against diameter from ODT and DNS computations are shown in Fig. 11. Color is used to indicate the axial location at the instant of droplet formation, as defined for ODT and DNS in Section 4.1.

The ODT scatter plot shows that droplets close to jet inlet have lower axial velocities than droplets farther downstream. This can be explained by the influence of the flow profile of the jet at the jet inlet plane: in the near field the velocities inside the liquid jet near the liquid-gas interface are still dominated by the boundary layer profile leading to low velocities in the droplet-generating region near the interface. Farther downstream, radial turbulent transport within the jet tends to homogenize the lateral profile of axial velocity, thereby increasing it near the liquid-gas interface.

Though this is a physically reasonable trend, the DNS scatter plot indicates that any such trend is dominated by a much larger scatter of velocity values than is produced in ODT. The likely cause is the greater complexity of the three-dimensional breakup process than its one-dimensional ODT analog, as discussed in Section 4.1.
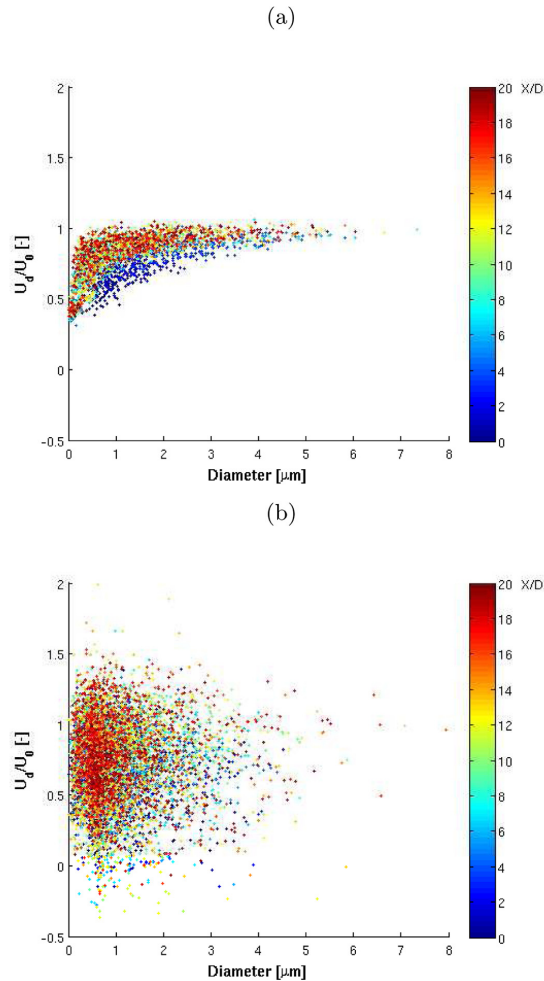
(a)

(b)

Fig. 11. Scatter plots of droplet axial velocity, normalized by the injection velocity, versus diameter. The color indicates the distance from the jet inlet. (a) ODT, (b) DNS. (For interpretation of the references to color in this figure legend, the reader is referred to the web version of this article.)

Notable in this regard is the occurrence of negative axial velocities in Fig. 11.b, which might be due to a viscoelastic action-reaction mechanism when axially oriented ligaments decompose into droplets, propelling some droplets forward (note the large positive axial velocity values) and others backward.

5. Conclusion

The recently introduced primary-breakup model of Movaghar et al. (2017) based on the one-dimensional turbulence (ODT) model was used here to simulate the primary breakup of a turbulent jet under diesel-like conditions. The results have been compared to droplet statistics from a direct numerical simulation (DNS).

The results show that ODT reproduces the rate of bulk liquid mass conversion into droplets and the droplet-size distribution produced by the DNS to a useful degree of accuracy. Some quan-

titative and qualitative discrepancies of the dependence of droplet velocities on droplet diameter were observed.

The significance of the present results stems from the fact that the model formulation of Movaghar et al. (2017) was used here without any modification or parameter resetting. The model involves numerous parameters that were tuned to match global properties, such as the Weber number dependence of the liquid jet length, that were determined experimentally for ambient-pressure conditions. As noted in section 4, an additional parameter was tuned in that study to match measured values of the droplet Sauter mean diameter (SMD) at the onset of breakup over a range of Weber numbers and other SMD measurements as a function of axial location. Though the ability to capture these SMD parameter dependences based on a single parameter adjustment indicates some degree of model fidelity with regard to droplet statistics, this does not constitute a definitive demonstration of quantitative predictive capability.

Having fully specified the model in this manner in previous work, the present evaluation of more detailed droplet statistics produced by ODT by comparing them to DNS results provides a clear assessment of predictive capability. In some important respects, predictive accuracy is confirmed. The lower accuracy of droplet-velocity predictions is understandable in view of the simplified ODT treatment of turbulent energy redistribution among velocity components and the inability of ODT to represent explicitly the effects of ligament formation and destabilization processes that mediate droplet formation.

Indeed, it is perhaps surprising that overall bulk liquid conversion and the droplet-size distribution are so well predicted in view of the latter caveat. To rule out the possibility of agreement due to, e.g., fortuitous cancellation of errors, it will be important to compare ODT predictions to other DNS cases as they become available. Based on the results presented here and in Movaghar et al. (2017), it can nevertheless be concluded that the evidence in hand constitutes a more convincing demonstration of detailed predictive capability by a highly reduced numerical model of primary jet breakup than has previously been achieved.

References

Chiu, S.N., Stoyan, D., Kendall, W.S., Mecke, J., 2013. Stochastic Geometry and Its Applications. John Wiley & Sons.

Desjardins, O., McCaslin, J., Owkes, M., Brady, P., 2013. Direct numerical and large-eddy simulation of primary atomization in complex geometries. Atomization Sprays 23, 1001–1048.

Desjardins, O., Pitsch, H., et al., 2010. Detailed numerical investigation of turbulent atomization of liquid jets. Atomization Sprays 20, 311–336.

Goto, S., Kida, S., 2003. Enhanced stretching of material lines by antiparallel vortex pairs in turbulence. Fluid Dyn. Res. 33, 403–431.

Goto, S., Kida, S., 2007. Reynolds-number dependence of line and surface stretching in turbulence: folding effects. J. Fluid Mech. 586, 59–81.

Herrmann, M., 2008. A balanced force refined level set method for two-phase flows on unstructured flow solver grids. J. Comput. Phys. 227, 2674–2706.

Herrmann, M., 2010. Detailed numerical simulations of the primary atomization of a turbulent liquid jet in crossflow. J. Eng. Gas Turbines Power 132, 061506.

Herrmann, M., 2011. On simulating primary atomization using the refined level set grid method. Atomization Sprays 21, 283–301.

Kerstein, A.R., Movaghar, A., Oevermann, M., 2017. Parameter dependences of the onset of turbulent liquid-jet breakup. J. Fluid Mech. 811, R5.

Lebas, R., Menard, T., Beau, P., Berlemont, A., Demoulin, F.-X., 2009. Numerical simulation of primary break-up and atomization: DNS and modelling study. Int. J. Multiphase Flow 35, 247–260.

Linne, M., 2013. Imaging in the optically dense regions of a spray: a review of developing techniques. Prog. Energy Combust. Sci. 39, 403–440.

Ménard, T., Tanguy, S., Berlemont, A., 2007. Coupling level set/VOF/ghost fluid methods: validation and application to 3D simulation of the primary break-up of a liquid jet. Int. J. Multiphase Flow 33, 510–524.

Movaghar, A., Linne, M., Oevermann, M., Meiselbach, F., Schmidt, H., Kerstein, A.R., 2017. Numerical investigation of turbulent-jet primary breakup using one-dimensional turbulence. Int. J. Multiphase Flow 89, 241–254.

O'Rourke, P. J., Amsden, A. A., 1987. The TAB method for numerical calculation of spray droplet breakup. SAE Technical Paper 872089.

Rahm, M., Paciaroni, M., Wang, Z., Sedarsky, D., Linne, M., 2015. Evaluation of optical arrangements for ballistic imaging in sprays. Opt. Express 23, 22444–22462.

Reitz, R.D., 1987. Modeling atomization processes in high-pressure vaporizing sprays. Atomisation Spray Technol. 3, 309–337.

Ross, S.M., 1996. Stochastic Processes, second ed John Wiley & Sons.

Sallam, K., Dai, Z., Faeth, G., 2002. Liquid breakup at the surface of turbulent round liquid jets in still gases. Int. J. Multiphase Flow 28, 427–449.

Tanner, F., 1997. Liquid jet atomization and droplet breakup modeling of non-evaporating diesel fuel sprays. SAE Technical Paper 970050.

Wu, P.-K., Faeth, G., 1995. Onset and end of drop formation along the surface of turbulent liquid jets in still gases. Phys. Fluids 7, 2915–2917.

PAPER V

Assessment of an Atomization Model Based on One-Dimensional Turbulence using Direct Numerical Simulation of a Decaying Turbulent Interfacial Flow

Assessment of an Atomization Model Based on One-Dimensional Turbulence using Direct Numerical Simulation of a Decaying Turbulent Interfacial Flow

A. Movaghar,[1, a)] R. Chiodi,[2] M. Oevermann,[1] O. Desjardins,[2] and A. R. Kerstein[3]

[1)]*Department of Mechanics, Chalmers University of Technology, Gothenburg, Sweden*

[2)]*Sibley School of Mechanical and Aerospace Engineering, Cornell University, Ithaca, New York 14853, USA*

[3)]*Consultant, 72 Lomitas Road, Danville, CA 94526, USA*

The interaction between turbulence and surface tension is studied numerically using the one-dimensional-turbulence (ODT) model. ODT is a stochastic model simulating turbulent flow evolution along a notional one-dimensional line of sight by applying instantaneous maps that represent the effects of individual turbulent eddies on property fields. It provides affordable high resolution of interface creation and property gradients within each phase, which are key for capturing the local behavior as well as overall trends, and has been shown to reproduce the main features of an experimentally determined regime diagram for primary jet breakup. Here, ODT is used to investigate the interaction of turbulence with an initially planar interface. The notional flat interface is inserted into a periodic box of decaying homogeneous isotropic turbulence, simulated for a variety of turbulent Reynolds and Weber numbers. Unity density and viscosity ratios are used in order to isolate the interaction between fluid inertia and the surface-tension force. Statistics of interface surface density, two-point correlations of phase index, and turbulent kinetic energy budgets along the direction normal to the initial surface are compared with corresponding DNS data. Allowing the origin of the lateral coordinate system to follow the location of the median interface element improves the agreement between ODT and DNS, reflecting the absence of lateral non-vortical displacements in ODT. Mesh-convergence studies that are impractical using DNS are performed using ODT, indicating that it can affordably resolve the interface at Reynolds and Weber numbers that are beyond the reach of DNS.

I. INTRODUCTION

The interface/turbulence interaction between two fluids in a turbulent environment has an important role in many technical processes, e.g. spray painting and primary liquid atomization in combustion devices. Primary atomization has a significant role in spray formation and its characteristics. Combustion performance such as efficiency and emissions creation is extremely dependent on spray characteristics. For these reasons, primary atomization has been studied theoretically and experimentally for a long time[1–3], but our understanding of liquid atomization is still inadequate.

Atomization in turbulent environments involves a vast range of length and time scales. Predictive simulations with high spatial and temporal resolution, i.e direct numerical simulations (DNS) and high resolution large-eddy simulations (LES) are used to study liquid-gas interface dynamics during primary breakup, but resolution of all relevant scales is limited by the available computational resources[4–6].

Consequently, for practical simulations of engineering interest as well as to investigate the physics and scalings of primary breakup beyond the parameter range of DNS studies, a predictive and computationally affordable interface dynamics model is highly desirable.

Former studies showed that the surface instability on the liquid jet core has a critical role in the jet breakup process. These instabilities are interpreted mainly by using linear analysis[7–10], but recent studies show that the assumptions of linear stability analysis are violated in the presence of a significant non-zero normal velocity at the interface. Therefore such a formulation is not sufficient for describing atomizing liquids in complex geometries or at high Reynolds numbers.

So other approaches are needed to understand and model the interactions between two immiscible fluids in a turbulent environment. Such turbulence-interface interactions have been studied by several researchers.

Li & Jaberi[11] studied the interplay between surface tension and baroclinity near the interface and their impact on turbulent kinetic energy dissipation. Trontin *et al.*[12] isolated the interaction between fluid inertia and surface tension in a box of three-dimensional decaying homogeneous turbulence and studied anisotropic effects of surface tension on the surrounding turbulence. Studies conducted by McCaslin *et al.*[13,14] for a case similar to [12] showed that surface tension increases energy in the flow field at small scales and that interface corrugations are greatly suppressed at length scales smaller than the critical radius at which there is a balance between strain-induced wrinkling and surface-tension-induced smoothing of corrugations.

One objective of this study is to support the devel-

[a)]Electronic mail: movaghar@chalmers.se

opment of a new modeling approach for turbulent jet breakup induced by surface instabilities based on the one-dimensional-turbulence (ODT) model. ODT was recently used[15] to reproduce the main features of an experimentally determined regime diagram for primary jet breakup. This stochastic modeling approach provides high resolution affordably by resolving all relevant scales only in the direction normal to the phase interface using a modeling construct that captures three-dimensional effects. The low computational cost of ODT compared to fully resolved three-dimensional DNS overcomes the limitation of DNS to moderate Reynolds and Weber numbers.

Here, the ODT model representation of phase-interface motion within turbulent flow is assessed using available DNS data for a regime that isolates just the interactions between surface tension and turbulence. In both DNS and ODT simulations, a planar interface is inserted into a box of decaying homogeneous isotropic turbulence (HIT). The flow-induced deformation of the initially planar interface and response of the flow to the associated surface-tension effects are examined.

The flows investigated in this study are governed by the incompressible Navier-Stokes equations for immiscible two-phase flow in which all fluid properties are considered to be constant and identical in the two phases. For this case, the momentum equation is given by

$$\frac{\partial \mathbf{u}}{\partial t} + \mathbf{u} \cdot \nabla \mathbf{u} = \frac{1}{\rho}\nabla p + \nu\nabla^2\mathbf{u} + \frac{1}{\rho}T_\sigma, \qquad (1)$$

where $\mathbf{u}$ is the velocity, ρ the density, p the pressure, ν the kinematic viscosity and T_σ the surface tension force, which is nonzero only at the phase interface.

This study involves two different approaches, solution of the flow equations by DNS and numerical modeling of the flow using ODT. These approaches are described briefly in further sections.

II. FLOW CONFIGURATION

The studied case involves two stages. First, the free decay of turbulence is simulated until it reaches the homogenous isotropic state. After reaching HIT, an interface is inserted at the targeted value of the Taylor-microscale Reynolds number $Re_{\lambda_g} = u_{rms}\lambda_g/\nu$, where u_{rms} denotes the root-mean-square velocity fluctuation and $\lambda_g = \sqrt{10}(\eta^2 L_{int})^{1/3}$ is the Taylor microscale. Here, η is the Kolmogorov length scale and L_{int} is the characteristic length scale of the large eddies. In terms of the turbulent kinetic energy (TKE) k per unit mass, which is $k = \frac{3}{2}u_{rms}^2$ for isotropic turbulence, and the TKE dissipation rate ϵ, these length scales are $\eta = (\nu^3/\epsilon)^{1/4}$ and $L_{int} = k^{3/2}/\epsilon$. In order to focus on turbulence-interface interactions, the same density and viscosity are assigned for both phases and a phase index is used to distinguish them.

TABLE I: Parameters that characterize the HIT/interface simulations. DNS simulations limited to cases 1-4 and ODT performed for cases 1-6.

Case	Re_{λ_g}	We_{λ_g}
1	155	∞
2	155	21.06
3	155	8.47
4	155	1.36
5	155	100
6	500	100

When turbulence decays to a prescribed Taylor-scale Reynolds number Re_{λ_g}, which in this study is 155 (except for some ODT results for $Re_{\lambda_g} = 500$), the second part of the simulation is initiated by inserting a planar phase interface into the middle of the box. The phase on each side of the interface is assigned a unique index. Four cases with different values of surface tension σ are studied, corresponding to a range of turbulent Weber numbers, defined as $We_{\lambda_g} = \rho u_{rms}^2 \lambda_g/\sigma$, evaluation at the instant of interface insertion. Table I summarizes the simulated cases.

III. METHODS

A. One-dimensional turbulence

The ODT formulation used in this study is described briefly in Appendix A. For a fully detailed introduction, see the publication by Kerstein[16] and its extensions by Ashurst & Kerstein[17] and by Movaghar et al.[15,18]. The advantages of a turbulence model formulated as a one-dimensional unsteady stochastic simulation are twofold. First, a one-dimensional formulation enables affordable simulation of high-Reynolds-number turbulence over the full range of dynamically relevant length scales, resolving the interactions between turbulent advection and microphysical processes such as viscous dissipation. Second, this approach permits high resolution of properties in the direction of the most significant gradients or flow-structure variations, here denoted by the spatial coordinate y, and on that basis is found to reproduce diverse flow behaviors.

In contrast to common approaches based on the Navier-Stokes equations, ODT uses a set of mechanisms modeling the physical effects phenomenologically on a 1D line of sight through the domain. The property fields defined on the one-dimensional domain evolve by two mechanisms: molecular evolution and a stochastic process representing advection. The stochastic process consists of a sequence of 'eddy events,' each of which involves an instantaneous transformation of the velocity and and any other property fields. In this application the only other property field is the phase index, which is subject to advection but not molecular evolution. During the time

interval between each event and its successor, molecular evolution occurs, governed by the equation

$$\partial u_i(y,t)/\partial t = \nu \partial^2 u_i(y,t)/\partial y^2, \qquad (2)$$

where u_i with $i \in 1, 2, 3$ are the three velocity components.

The eddy events representing advection may be interpreted as the model analog of individual turbulent eddies. In ODT each eddy event is characterized by a length scale (the eddy size) and a time scale. The stochastic sampling of occurrences of eddies is based on the interpretation of the eddy time scale as the mean time until the next occurrence of an eddy of given size at a given location. The unique feature is that the time scale is based on the instantaneous flow state within the spatial extent of the eddy, so it is different for each sampled eddy rather than being based on a mean-field relationship. Thus, the velocity profiles $u_i(y,t)$ do not advect fluid along the y coordinate, but they indirectly influence advection through their role in determining the time scale of individual eddies, and thus the time-varying rates of occurrences of various eddies. This enables the model to capture dynamical details that are flow specific based on the initial and boundary conditions and any local or distributed energy sources and sinks, such as surface tension, whose interaction with turbulent flow is the present focus.

The instantaneous time scale governing the sampling of a given eddy is obtained using the appropriate dimensional combination of the eddy size and a measure of kinetic energy based on the profiles $u_i(y,t)$ within the eddy spatial interval. This approach allows surface tension (and other such effects) to be incorporated by modifying the kinetic energy due to eddy-induced change of the total phase interface associated with the eddy. This modification is implemented by changing the profiles $u_i(y,t)$ within the eddy interval in a way that applies the prescribed kinetic-energy change while conserving the y-integrated momentum of all velocity components.

This procedure has two effects. First, it modifies the likelihood of eddy occurrence during a given time increment. For example, this likelihood is zero if the surface-tension effect requires a kinetic-energy reduction that exceeds the presently available kinetic energy within the eddy interval, indicating that the eddy is energetically forbidden. Second, if the eddy is implemented, the associated changes of the profiles $u_i(y,t)$ represent the surface-tension-induced flow modification. Thus, eddy events not only advect the phase index, resulting in an implied change of interface area, but they also capture the effect of the latter on the flow.

Periodic boundary conditions are applied in all directions (therefore for ODT, in the y direction, which is the only available direction). When fluid crosses a periodic boundary in the y direction, its phase index flips so that the periodicity does not cause the creation of artificial phase interfaces.

As shown in Appendix A, eddy events can increase but not decrease interface surface area. For the decaying HIT configuration considered here, this implies that the eventual restoration of interface planarity after the turbulent motions are fully dissipated cannot be captured by ODT. Therefore the present study focuses on the early development of surface area, which in any case is the regime of greatest interest from the DNS viewpoint.

Accordingly, the time duration of simulated realizations is short enough so that the physical interface never reaches the y boundaries during DNS runs. Reported results for all ODT cases are ensemble averages of 2000 simulated realizations. Due to run-to-run statistical variability, the physical interface reaches a y boundary during a few of these realizations. Then the phase indices are changed as needed to prevent the interface from crossing the boundary and thus appearing unphysically near the opposite boundary due to the periodic boundary conditions. Owing to the rarity of this situation, the impact of this modification on the statistical outputs that are reported is negligible.

B. Direct numerical simulation

The DNS data is generated using a full three-dimensional incompressible Navier-Stokes flow solver[19,20]. Each phase is transported using an unsplit geometric semi-Lagrangian volume of fluid (VOF) method[21], with the curvature calculated through a mesh decoupled height function[22] and the pressure jump due to surface tension imposed using the ghost fluid method[23].

IV. VALIDATION OF THE ODT REPRESENTATION OF HIT

To simulate HIT, the ODT velocity profile is initialized with a low-wavenumber narrowband velocity profile. Periodic boundary conditions are imposed. u_{rms} is initially high enough so that Re_{λ_g} is much greater than the target value. As a result, ODT relaxes to a state that corresponds to freely decaying HIT when this target value is reached. A planar phase interface is then inserted, followed by further time advancement. The instant of interface insertion is designated as time $t = 0$, and the time coordinate is scaled in all plotted results by the large-eddy turnover time $\tau = k/\epsilon$ evaluated at $t = 0$.

ODT model parameters were set by comparison to the infinite-We_{λ_g} DNS case, for which the flow continues to behave as decaying HIT after $t = 0$ because the interface is dynamically passive for this case. Parameter setting is based only on the flow properties for this case, so interface evolution for this case, as well as for finite-We_{λ_g} cases, is a model prediction that is shown in Section V.

On this basis, the ODT model parameters defined in Appendix A 2 are chosen to be $C = 5.2$ and $Z = 10$. C scales the overall eddy rate, and therefore the turbulence decay rate, while Z scales the viscous suppression

of eddy occurrences, mainly at small scales, and therefore primarily affects the Kolmogorov scale. Importantly, the ODT treatment of viscous processes captures key features of the viscous-inertial balance such as the correct Re_{λ_g} dependence of the wavenumber (k) range of the inertial cascade.

The influence of Z is thus seen in the extent of the inertial range for given Re_{λ_g} prior to the high-wavenumber roll-off of the velocity spectrum into the dissipative wavenumber range. The comparison of ODT and DNS spectra is shown in Fig. 1.
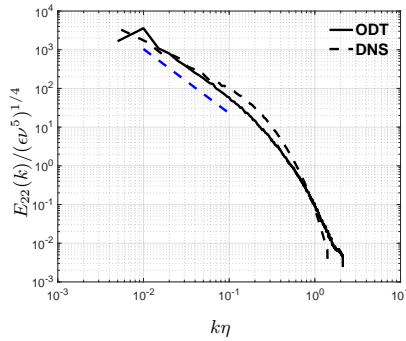

FIG. 1: For homogeneous decaying turbulence at $Re_\lambda = 155$, normalized DNS and ODT one-dimensional spectra of transverse velocity fluctuations $E_{22}(k)/(\epsilon\nu^5)^{1/4}$ (black lines); $(k\eta)^{-5/3}$ (dashed blue line).

In ODT, the distinction between the spectral properties of longitudinal and transverse velocity components is not captured because these velocities do not directly advect fluid in ODT and are not subject to the solenoidal condition that creates the distinction between longitudinal and transverse velocity in physical turbulence. (Though the solenoidal condition has no meaning in ODT, the 1D analogs of this and other conservation properties are obeyed by ODT.) Therefore the ODT one-dimensional velocity spectra $E_{jj}(k)$ are the model analogs of the transverse velocity spectrum $E_{22}(k)$ for all j. This spectrum, normalized by $(\epsilon\eta^5)^{1/4}$, is shown in figure 1, exhibits the $k^{-5/3}$ inertial-range scaling. As explained previously,[16] this scaling is an outcome reflecting ODT conservation properties and multiplicative (and therefore self-similar) scale reduction by triplet maps, rather than a behavior that is hard-wired into the model.

Because ODT and DNS are compared in Fig. 1 at the same value of Re_{λ_g} and Z has been tuned to match the k range of the DNS inertial cascade, the degree of consistency that is seen in the figure is expected. A noteworthy feature is that the ODT inertial range is in better conformance to $k^{-5/3}$ scaling than is the DNS spectrum. It is known that higher Re_{λ_g} is needed to see close con-

formance of DNS spectra with this scaling. (The chosen Re_{λ_g} for this study reflects affordability constraints resulting from the algorithmic complexity of interface tracking.) ODT does not reproduce this gradual approach to $k^{-5/3}$ scaling with increasing Re_{λ_g} because it is formulated on the basis of similarity principles that are inherently high-Re_{λ_g} properties.
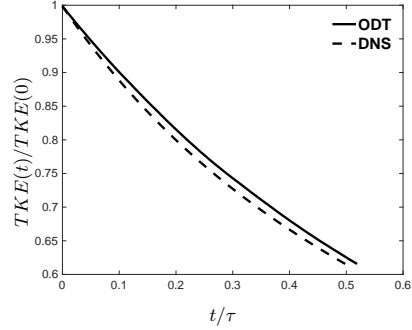

FIG. 2: Turbulent kinetic energy evolution for homogeneous decaying turbulence

Figure 2 shows the evolution of turbulent kinetic energy in both ODT and DNS simulations of decaying HIT. The good agreement of ODT with the DNS turbulence decay was obtained by tuning C to match the DNS energy dissipation at $t = 0$. Many of the statistical comparisons that follow are based on the flow states at $t/\tau = 0.5$.

V. COMPARISON OF DNS AND ODT INTERFACE STATISTICS

A. Cases and data-reduction procedure

Interface structure at $t/\tau = 0.5$ (i.e., after the initially flat interface has deformed for half a large-eddy turnover time) produced by individual DNS and ODT realizations for cases 1 - 4 are shown in Fig. 3. Case 1 in Fig. 3 corresponds to $We_{\lambda_g} = \infty$ ($\sigma = 0$), for which the interface is dynamically passive. It is apparent that the large-scale variations of the interface are similar for each case, while smaller interfacial features are increasingly lost as We_{λ_g} decreases to 1.36.

As indicated in Fig. 3, the ODT line orientation (y direction) is normal to the initial interface where the dashed line at $y = 0$ shows the initial interface location and the phases are distinguished by colors. Since ODT is a 1D model, the interface measure that it provides is the number of phase boundaries along the line at a given instant, where those boundaries are the model analog of intersections of a y-oriented line of sight with a notional interfacial surface separating the two phases. The latter

(a) $We_{\lambda_g} = \infty$

(b) $We_{\lambda_g} = 21.06$

(c) $We_{\lambda_g} = 8.47$
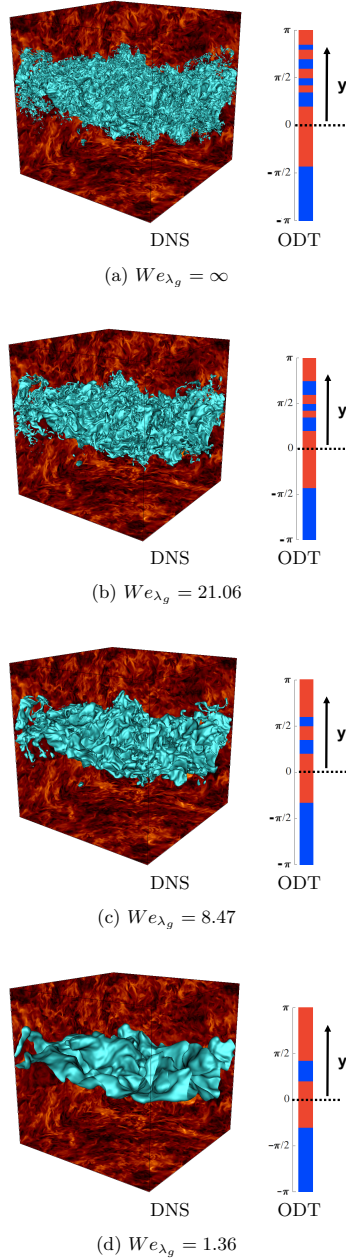

(d) $We_{\lambda_g} = 1.36$

FIG. 3: Interface configuration for the DNS and ODT at time $t/\tau = 0.5$. Distinct phases on ODT line are represented by different colors.

TABLE II: Mean number of interfaces in DNS and ODT simulations at at time 0.5τ

Case	ODT	DNS
$We_{\lambda_g} = \infty$	9	10
$We_{\lambda_g} = 21.06$	4	6
$We_{\lambda_g} = 8.47$	3	5
$We_{\lambda_g} = 1.36$	1.6	3

information is therefore extracted from the DNS simulations for comparison to the statistics provided by ODT. This involves data collection along lines (y direction) normal to the initial interface (x-z plane), which provides statistics along 512×512 lines where each is analogous in terms of data analysis to an ODT domain. Though the number of such DNS lines greatly exceeds the number of ODT realizations (2000) for each case, this does not necessarily imply greater statistical precision of the DNS results because the flow states along neighboring DNS lines are highly correlated but ODT realizations are statistically independent. Because phase index labeling is arbitrary, all statistical quantities are symmetric in y with respect to $y = 0$, so data for positive and negative y are combined and plotted over the y range $[0, \pi]$.

B. Number of interfaces

In what follows, the term interface refers to one intersection of a y-oriented line of sight with the notional (in ODT) or actual (in DNS) interfacial surface. On this basis, the ensemble average value of the total number of interfaces along the line of sight at $t = 0.5\tau$ for cases 1 - 4 is shown in Table II.

As noted in section IV, only flow-field information is used to set ODT parameters, and ODT interface results are predicted accordingly. (In Appendix A 3 it is explained that conversion from kinetic energy to surface-tension energy resulting from surface-area increase introduces no additional free parameters for finite We_{λ_g} because both energy forms are uniquely defined in ODT, albeit through simplifying assumptions.) The agreement with DNS in Table II is good for $We_{\lambda_g} = \infty$, with increasing under-prediction as We_{λ_g} decreases.

The $We_{\lambda_g} = \infty$ result indicates that, in the absence of surface tension, ODT provides a quantitative representation of material-surface increase, which is important not only for the present application but also for other applications involving advected surfaces, such as the propagation of flames and other reacting fronts. This agreement is dependent on the choice of the parameter C, which scales the overall eddy rate and therefore the characteristic time for exponential increase of the number of interfaces. Specifically, the agreement indicates that the value of C that gives the correct energy dissipation rate is also accurate with regard to interface development. This is not an *a priori* known property of the model formu-

lation, and accordingly lends significant support to the present model application.

In this context, less accurate prediction for finite We_{λ_g} can be attributed in part to the ODT treatment of the abovementioned energy conversion. One assumption in that treatment is especially inaccurate at low values of We_{λ_g}. Surface-tension energy change is the product of σ and the surface-area change. ODT time advances surface intersections with a line of sight, from which surface-area change must be inferred. As noted in Appendix A 3, this is done by assuming that the phase boundary is an isotropic random surface, consistent with the small-scale structure of high-Re_{λ_g} turbulence. However, Fig. 3 indicates increasing anisotropy with decreasing We_{λ_g} for these moderate-Re_{λ_g} cases.

The prefactor 2 in Eq. (A9) follows directly from the assumption that the phase boundary is an isotropic random surface. If instead it is a collection of planes normal to the y direction, each therefore corresponding to one point of intersection with the ODT domain, then the relation $\alpha = 2n$ in section A 3 becomes instead $\alpha = n$, which eliminates the factor of 2 in Eq. (A9). Figure 3.d suggests that the phase boundary is more plausibly idealized as primarily normal to the y direction at low We_{λ_g} than as isotropic, so Eq. (A9) potentially overstates the energy penalty for interface creation by as much as a factor of two. It is likewise plausible that this could result in half as much interface creation as a more accurate assumption about interface orientation, so this alone might explain why Table II indicates that ODT underestimates the number interfaces by almost a factor of 2 for $We_{\lambda_g} = 1.36$. Though an improvement might be achieved by using a more accurate case-specific prefactor in Eq. (A9), such information is not available *a priori* when ODT is used for prediction, and the intent here is to test its predictive capability rather than to do case-specific parameter fitting. At higher We_{λ_g} and Re_{λ_g} values of practical interest, isotropy should be a reasonably accurate assumption.

Figure 3 also indicates that the surfaces are smoother at lower We_{λ_g}, implying that the resistance of the surfaces to wrinkling by small eddies might suppress nearby eddy motions, much as a turbulent boundary layer becomes increasingly laminar as the wall is approached. Then the creation of surface overhangs, which is required to produce multiple intersections with a y-directed line of sight, might occur largely due to non-vortical shearing motions applied to locally tilted surface elements. ODT contains no representation of non-vortical motion, so it does not capture this mechanism and therefore would not reproduce the full extent of interface generation for conditions under which this mechanism is important.

To put these observations in context, the present comparisons are constrained by the limited parameter space that is accessible using DNS, which does not include the high-Re_{λ_g} regime that ODT is designed to represent most accurately. Additionally, order-unity errors are substantial in the context of point predictions, but

ODT comparisons to jet breakup, which likewise show errors of this magnitude, capture trends extending over orders of magnitude in Reynolds and Weber number, in which situation the order-one point-prediction errors are inconsequential[15]. In this context, the contributions of the present study are twofold: the simple flow configuration allows a simpler, less empirical ODT formulation than in[15] to be used, and detailed statistics that DNS can provide allow comparison of structural features of the flow as well as global properties such as the data in Table II. These structural features are explored next.

C. Interface number density

The interface number density, shown in Fig. 4, is obtained by taking the y derivative of the total number of interfaces between y and $-y$ and dividing the result by $2y$. Integration of the number density over $[0, \pi]$ gives the ensemble average value of the total number of interfaces on one side of the initial interface, which is half of the number of interfaces on the whole domain $[-\pi, \pi]$, where the latter is the quantity shown in Table II. This procedure yields the unshifted profiles in Fig. 4, which shows that the ODT profiles are substantially narrower than the DNS profiles.

The DNS images in Fig. 3 suggest that the surface is subject to large-scale displacements in the y direction superimposed on smaller-scale vortically induced displacements. Large-scale displacements are enabled by the periodic boundary conditions, which in principle allow non-vortical streaming motions in the positive and negative y direction.

Adopting the hypothesis that such motions, which ODT cannot capture, contribute to the greater broadening of the DNS profiles relative to the ODT profiles, the data is re-processed to eliminate the possible effects of this mechanism. The number of interfaces along a line of sight at a given instant must be negative because the pure-phase regions beyond the mixed-phase zone have opposite phase, so there must be an odd number of phase flips along any trajectory that extends through the mixed-phase zone. Then there is one 'median' interface such that it has an equal number of interfaces on either side of its location. The displacement of the median interface relative to $y = 0$ is deemed to be a measure of the displacement of the mixed-phase zone due to large-scale y-oriented motions. Therefore each instantaneous state along the line of sight is shifted so that the median interface is relocated to $y = 0$, as illustrated in Fig. 5, and this modified data ensemble is then used to obtain 'shifted' interface number-density profiles. The median interface is excluded from this data reduction because its displacement to $y = 0$ implies infinite number density at $y = 0$ (a δ-function spike) that reflects data conditioning rather than a physical effect.

ODT interfaces are not subject to non-vortical displacements so the ODT profiles in Fig. 4 that are based

on shifted data are not much different from those that are based unshifted data, but the effect of the shifts on the DNS profiles is pronounced and brings them into closer conformance to the ODT results. Full agreement of ODT and DNS profiles is impossible because of the differences between the areas under each pair curves that is implied by the results in Table II. Given this unavoidable discrepancy, the agreement of the shapes of the profiles is noteworthy, especially ODT and DNS the low-y plateau-cliff structure that is seen only for $We_{\lambda_g} = 1.36$. Notwithstanding the question of the origin and nature of the large-scale displacements of the DNS interfaces, the agreement of profile shapes seen in the shifted results suggests that ODT is at least somewhat representative of the structure of the DNS mixed-phase zone in a Lagrangian sense, meaning in a reference frame in which the ODT and DNS mixed-phase zones roughly coincide. Accordingly, this Lagrangian interpretation of the present ODT formulation is adopted, so all results that follow are based on shifted data.

D. Same phase probability

Two-point statistics provide a different perspective on interface structure from the single-point information presented in section V C. Power spectra are applicable in homogeneous directions, but the phase index is statistically homogeneous only in x and z, while the ODT domain is oriented in the inhomogeneous direction y. Since the power spectrum of a zero-mean property p is the Fourier transform of its two-point covariance $R(y_1, y_2) = \langle p(y_1)p(y_2)\rangle$, the latter embodies the same information and can therefore be used. In homogeneous directions, the covariance depends only on $|y_1 - y_2|$, but otherwise it is irreducibly dependent on both arguments.

Taking p to be the phase index, with possible values ± 1, then $p(y_1)p(y_2)$ is $+1$ (-1) if the phases at the two locations are the same (different). This can be rewritten as $[1 + p(y_1)p(y_2)]/2$, which is 1 or 0 in the respective instances. then $S = (1+R)/2$ is the probability of finding the same phase at the two locations. Since this embodies the same information as R, the same phase probability $S(y_1, y_2)$ is used as a representative measure of the two-point structure of the interface.

This statistic has been extracted from simulation data, and it is found that the features of interest are largely captured by the results for $y_2 = -y_1$. Adopting this specialization, $S(y)$ is defined as the probability that the same phase index is found at locations y and $-y$ relative to a specified origin. Based on the results in Section V C, the origin is taken to be the location of the median interface along the line of sight. In Fig. 3a, the same phase probability is plotted as a function of the absolute distance Δy between y_1 and y_2, so the plotted function is $S(\Delta y/2)$.

Due to the coordinate shift, the median interface is located at the origin, so $S(0)$ is strictly speaking unde-
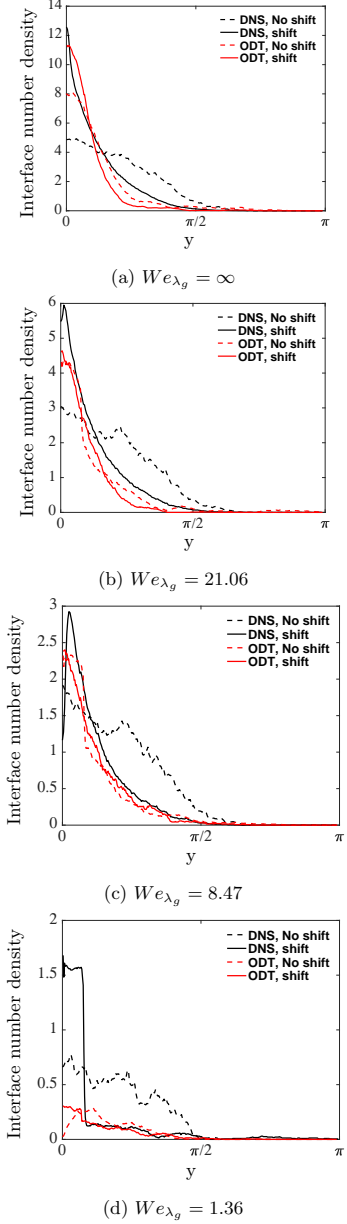

FIG. 4: The interface number density for both DNS and ODT at time $t/\tau = 0.5$.

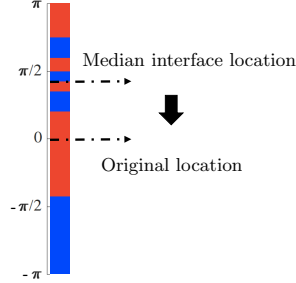fined, but because it reduces to a single-point statistic at

FIG. 5: Schematic of the shift of original to the location of the median interface.

$y = 0$, it is deemed to be unity. For a vanishingly small but nonzero argument, there is vanishing likelihood of more than one interface in $[-y, y]$, so $S(y)$ converges to zero in this limit and therefore, as defined, is discontinuous at $y = 0$ (which is immaterial because $S(0)$ is a non-informative quantity).

Results are presented for $t = 0.5\tau$ because it is a time when the mixed-phase zone occupies an order-one fraction of the computational domain but does not closely approach the domain boundaries. Accordingly, for values of the argument of S corresponding to locations near the boundaries, the phase indices remain at their initial values and therefore are never the same, giving $S = 0$, as seen in the plots.

The y location of the peak of S is a signature of the typical distance from the median interface to its nearest neighbor, thus identifying an interface-separation microscale. As expected, both DNS and ODT indicate that this microscale increases with decreasing We_{λ_g}. ODT predicts the location of the peak accurately except for the lowest We_{λ_g} value, for which both DNS and ODT indicate a broad peak, making the location of the peak inherently hard to predict.

A high peak value of S corresponds to low variability of the separation between adjacent interfaces, and vice versa. As We_{λ_g} decreases, there are fewer interfaces on the 1D domain, consist with higher variability of the separation between adjacent interfaces that is implied by the results. Interestingly, ODT over-predicts the peak value of S for all cases despite the fact that ODT consistently under-predicts the total number of interfaces, as shown in Table II. This indicates that the total number of interfaces is not the only property that determines the peak height.

Overall, the same phase probability is found to encode significant structural information, not all of which has been deciphered here. ODT is seen to capture the main We_{λ_g} dependences with reasonable quantitative accuracy in most cases.

(a) $We_{\lambda_g} = \infty$

(b) $We_{\lambda_g} = 21.06$

(c) $We_{\lambda_g} = 8.47$
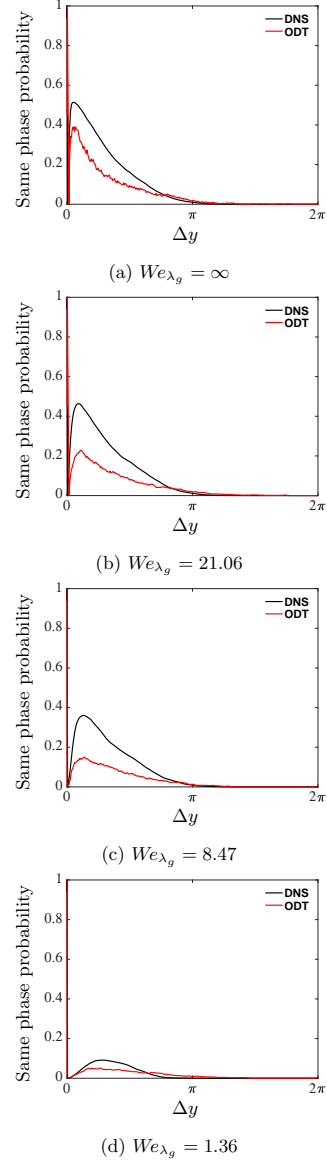

(d) $We_{\lambda_g} = 1.36$

FIG. 6: Same phase probability statistics for DNS and ODT at time $t/\tau = 0.5$. The origin is shifted to the location of the median interface.

VI. FLOW STATISTICS

A. Turbulent kinetic energy

Surface tension influences flow structure as well as interface evolution. For the interface initialization used in this study, interface evolution is inhomogeneous in the y direction even in the absence of surface tension. However, the flow field is homogeneous in that direction in the absence of surface tension, which is the basis of the ODT parameter assignment and validation for HIT in section IV.

For finite We_{λ_g}, surface tension acts as a kinetic-energy sink through the conversion of turbulent kinetic energy (TKE) into surface-tension energy due to the increase of the interface surface area. This sink is inhomogeneous in y, reflecting the spatial inhomogeneity of interface development. Therefore both the TKE and its budget are inhomogeneous in y. The former is examined next and the latter is examined in section VI B.

B. TKE budget

To examine the role played by surface-tension forces in TKE evolution, an energy budget for TKE, here denoted k, is formulated and evaluated. The TKE equation is

$$\underbrace{\frac{\partial k}{\partial t}}_{I} + \underbrace{u_j \frac{\partial k}{\partial x_j}}_{II} = \underbrace{\frac{1}{\rho}\frac{\partial}{\partial x_j}(pu_j)}_{III} + \underbrace{\frac{1}{\rho}\frac{\partial}{\partial x_j}(2\mu u_i S_{ij})}_{IV} - \underbrace{2\nu S_{ij}S_{ij}}_{V} + \underbrace{\rho u_i F_i}_{VI}, \tag{3}$$

where term I is the time rate-of-change, term II is the power of viscous forces, term III is the transport of q, term IV is the power of pressure forces, term V is the dissipation and term VI is the power delivered by interfacial forces F. Here, F is given by $F = \sigma\kappa\delta\vec{n}$.

Formulation of the ODT analogs of the budget terms in Eq. (3) is not straightforward due to the instantaneous eddy-induced displacements that represent advection in ODT. The equivalent ODT expressions for these terms have been derived for single-phase constant-property flow[24] and extended for application to buoyant stratified flow[25]. That extension introduce a gravitational potential energy source/sink akin to the present surface-tension source/sink, so the two extensions are conceptually analogous although the mathematical details are different. These details are not described except to note that they have been implemented numerically to produce the TKE budget results that are shown next.

VII. TIME EVOLUTION

To complement the detailed examination of spatial structure at $t = 0.5\tau$ that has been presented thus far, the time evolution some global properties of the flow are now examined. In this regard, the surface tension energy evolution in both ODT and DNS simulations is shown in Fig. 8.

VIII. SENSITIVITY TO MESH RESOLUTION

ODT is numerically implemented using a specially designed adaptive mesh that does not limit the resolution of the spacing of interfaces along the line of sight. In contrast the DNS is implemented using a uniform grid size. The present study compares ODT predictions to DNS results, so a minimum resolution Δy was superimposed on the adaptive mesh algorithm to enforce the same resolution in ODT as in DNS. This was done by forcing adaptive-mesh cells to merge as needed so that no cell size in ODT simulation falls below the DNS cell size. Eddies are required to overlap a minimum number of ODT mesh cells, so this can cause suppression of eddies that might otherwise be implemented, although this does not happen if the lower bound on cell size is sufficiently small.

As seen in Fig. 3, the formation of interfacial corrugation is suppressed on length scales smaller than a reference length scale that is determined by surface tension. When an eddy of size l with characteristic velocity u' will stop overturning the interface when surface tension on that scale balances inertia, i.e., when the Weber number $We = \rho u'^2 l/\sigma \sim 1$. The limiting length scale $l_\sigma \sim \sigma/\rho u'^2$ emerges from this simple balance as a function of u'. According to Kolmogorov[26], the expression for the characteristic velocity u' will depend on where the critical length scale falls within the universal equilibrium range. The two expressions for the critical length scale in the dissipation range and in the inertial subrange become $l_\sigma \sim (\sigma\nu/(\rho\epsilon))^{1/3}$ and $l_\sigma \sim (\sigma^3/(\rho^3\epsilon^2))^{1/5}$, respectively. As showed the resolution used in DNS simulation should be fine enough to resolve the the critical length scale l_σ. $We_{\lambda_g} = 21$ found as the highest Weber number that can be simulated by DNS without refining

(a) $We_{\lambda_g} = 21.06$

(b) $We_{\lambda_g} = 8.47$
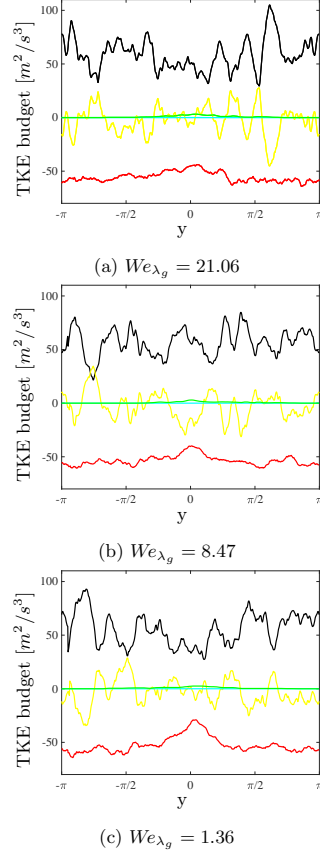

(c) $We_{\lambda_g} = 1.36$

FIG. 7: TKE budget terms: tke rate (——), dissipation
(——), surface tension (——), advective transport
(——), viscous transport (——)

its mesh. As figure 9shows the DNS mesh resolution was
fine enough to capture the number of interfaces. On the
other hand simulating higher weber numbers needs much
refinement of the DNS resolution.

IX.   ODT RESULTS FOR HIGHER We_{λ_g} AND Re_{λ_g}

A practical feature of the ODT surface-tension formu-
lation is that it might be useful as a subgrid closure for
large-eddy simulation of turbulence that includes, e.g.,
an under-resolved volume-of-fluids (VOF) treatment of
phase-interface evolution. This requires the model to be
run at We_{λ_g} and Re_{λ_g} values corresponding to the VOF
cell Weber and Reynolds numbers. To identify the ODT
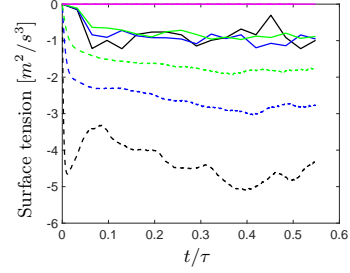resolution requirements for these conditions, $We_{\lambda_g} = 100$

FIG. 8: Surface tension energy evolution.
Case 1 : ODT, DNS (——), Case 2 : ODT (——), DNS
(- - -), Case 3 : ODT (——), DNS (- - -), Case 4: ODT
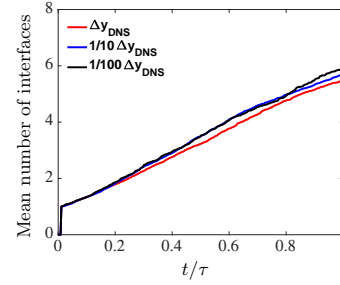(——), DNS (- - -)

FIG. 9: Mean number of interfaces predicted by ODT
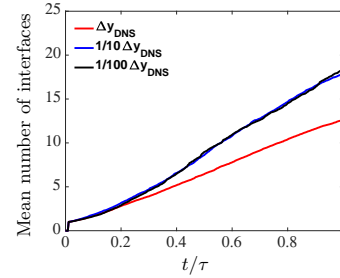at $We_{\lambda_g} = 21.06$ and $Re_{\lambda_g} = 155$.

FIG. 10: Mean number of interfaces predicted by ODT
at $We_{\lambda_g} = 100$ and $Re_{\lambda_g} = 155$.

and $Re_{\lambda_g}500$ are chosen as representative values.

Before showing results for this case, results for $We_{\lambda_g} =$
100 and $Re_{\lambda_g} = 155$ are examined in order to assess the
resolution required for higher We_{λ_g} based on Re_{λ_g} value
used thus far. As in section VIII, Δy_{DNS} for the re-
ported DNS cases is used as a reference resolution. The
ODT results shown in Fig. 10 indicate that a resolution
of $0.1\Delta y_{DNS}$ is sufficient with respect to the most im-

portant global property, while the choice Δy_{DNS} gives increasingly inaccurate results as the flow evolves. Reduction of DNS resolution below the latter value becomes very costly. The contrast between Figs. 9 and 10 indicates why 21.06 is the largest We_{λ_g} value for which the DNS was run.

Turning now to $Re_{\lambda_g} = 500$, the first consideration is the ODT energy spectrum for the HIT ($We_{\lambda_g} = \infty$) case. As in section IV, the HIT simulation was initialized so that the flow state relaxed to HIT structure before reaching the target value of Re_{λ_g}, which in this case is 500. The spectra obtained for various mesh resolutions are shown in Fig. 11. It is seen that a resolution of $0.1\Delta y_{DNS}$ is sufficient to resolve the spectrum. However, Fig. 12 indicates that higher resolution is needed to capture all the interfaces, showing that the interface microscale is smaller than η for this case as well as for the case shown in Fig. 10.

Figure 11 shows the one-dimensional energy spectrum at the inserting interface location for different mesh resolutions to find the mesh convergence.
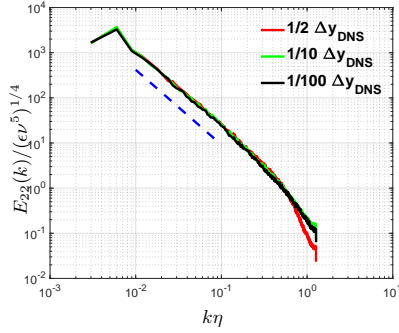

FIG. 11: For homogeneous decaying turbulence at $Re_{\lambda_g} = 500$, normalized ODT one-dimensional spectra of transverse velocity fluctuations $E_{22}(k)/(\epsilon\eta^5)^{1/4}$. $E_{22}(k)/(\epsilon\nu^5)^{1/4}$ (solid lines); $(k\eta)^{-5/3}$ (dashed blue line).

The interface microscale is thus seen to drive the cost of the simulation for conditions relevant to subgrid closure, requiring a scale range up to five orders of magnitude. ODT simulations under these conditions is too costly to operate as a fully coupled closure model in each VOF mesh cell, but it is feasible to run such ODT cases offline in order to build a look-up table that can be used for VOF closure.
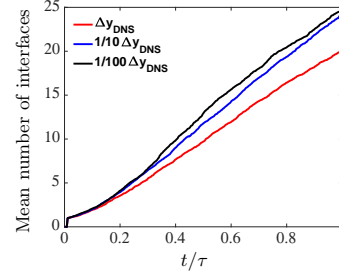

FIG. 12: Mean number of interfaces predicted by ODT at $We_{\lambda_g} = 100$ and $Re_{\lambda_g} = 500$.

X. DISCUSSION

In previous work, ODT was extended for application to jet breakup. That extension included several empirical treatments designed to capture particular features of that configuration. Here, a simpler configuration requiring minimal empiricism and parameter adjustment has been studied in order to focus on interpretation and validation of the fundamental ODT representation of the interaction between surface tension and fluid inertia. To simplify the interpretation of results, the two fluid phases are assumed to have the same density and viscosity, so for vanishing surface tension, the phase interface becomes dynamically passive and the chosen flow configuration reduces to decaying homogeneous isotropic turbulence (HIT).

ODT and DNS results have been compared for a range of Weber numbers. For $We_{\lambda_g} = \infty$, the interface is a passive material surface whose time development is itself useful validation information that is used to demonstrate that ODT simulation of HIT captures key features of material surfaces advected by turbulence. As We_{λ_g} is reduced, the accuracy of the ODT predictions decreases somewhat, reflecting the additional model simplifications associated with the treatment of surface-tension effects. A particular assumption identified as a likely error source is expected to be increasingly accurate with increasing We_{λ_g} and Re_{λ_g}, which is the regime of greatest practical interest. Even in the DNS-accessible regime that is more challenging in this regard, the present formulation captures more structural detail than any existing reduced model of surface-tension effects in turbulence, including both the spatial structure of the interface and the flow response to surface-tension effects (albeit through an energy-based rather than a momentum-based representation of that response).

ODT mesh resolution studies show that ODT mesh resolution requirements are quantitatively consistent with those of DNS. In the broader parameter space that is accessible only using ODT, it is shown that practical applications, even in the context of VOF subgrid closure, are so demanding in terms of the required scale range of

the simulation that ODT could be used for such closure only by off-line pre-tabulation, although a fully coupled closure could be feasible if ODT were under-resolved and thereby provided a scale-range extension without achieving full resolution.

Appendix A: One-Dimensional Turbulence

1. Time-advancement processes

ODT is a stochastic model simulating the evolution of turbulent flow along a notional line of sight through a three-dimensional flow. The flow state along that line of sight is treated as a closed system though physically it is an open system. This allows conservation laws to be enforced consistently, but not in the precise manner of 3D flow.

Time advancement of the present ODT formulation is expressed schematically as

$$\frac{\partial u_i}{\partial t} - \nu \frac{\partial^2 u_i}{\partial y^2} = Eddies, \qquad (A1)$$

where ν is the kinematic viscosity and the indices $i = 1$, 2, 3 denote the streamwise, lateral and spanwise velocity components, respectively, corresponding to the spatial coordinates (x, y, z). This equation formally represents the two processes that can change the value of u_i at a given location y and time t.

The left hand side represents viscous time advancement, which can be supplemented by body forcing and other case-specific processes. *Eddies* denotes a model that idealizes the advective effect of 3D eddies, which are represented by instantaneous maps applied to property profiles, supplemented by energy redistribution among velocity components. Surface tension does not appear in Eq. (A1) because its role in the model is to influence the occurrence and implementation of individual eddies.

Accordingly, turbulent advection is modeled in ODT by a stochastic sequence of events. These events represent the impact of turbulent eddies on property fields (velocity and any scalars that might be included) along the one-dimensional domain. During each eddy event, an instantaneous map termed the 'triplet map,' representing the effect of a turbulent eddy on the flow, is applied to all property fields. It occurs within the spatial interval $[y_0, y_0 + l]$, where y_0 represents the eddy location on the ODT line and l is the eddy size. A triplet map shrinks each property profile within $[y_0, y_0 + l]$, to one-third of its original length, inserts three identical compressed copies into the eddy range side by side so as to fill the range, and reverses the middle copy to ensure the continuity of each profile. The map mimics the eddy-induced folding effect and increase of property gradients. Formally, the

new velocity profiles after a map are given by

$$\hat{u}_i(y, t) = u_i(f(y), t), \qquad (A2)$$

here conveniently expressed in terms of the inverse map

$$f(y) = y_0 + \begin{cases} 3(y - y_0), & \text{if } y_0 \leq y \leq y_0 + \frac{1}{3}l, \\ 2l - 3(y - y_0), & \text{if } y_0 + \frac{1}{3}l \leq y \leq y_0 + \frac{2}{3}l, \\ 3(y - y_0) - 2l, & \text{if } y_0 + \frac{2}{3}l \leq y \leq y_0 + l, \\ y - y_0, & \text{otherwise,} \end{cases}$$
$$(A3)$$

which is single-valued. (The forward map is multi-valued.)

The triplet map is measure preserving, which implies that all integral properties of the flow field, such as mass, momentum, kinetic energy, and total linear measure of each fluid phase, are identical before and after applying the map. Various cases, such as buoyant stratified flow, involve sources and sinks of kinetic energy due to equal-and-opposite changes of one or more other forms of energy. Even in the simplest cases, viscosity converts kinetic energy into thermal energy. The resulting dissipation of kinetic energy is captured by Eq. (A1). Energy-conversion mechanisms other than viscous dissipation are incorporated by introducing an additional operation during the eddy event. The implementation of this operation to account for surface-tension changes is described.

In the present formulation, the triplet map can increase the number of phase interfaces within the eddy interval, as illustrated in section A 3, resulting in an increase ΔE_σ of surface-tension energy that must be balanced by an equal-and-opposite decrease of kinetic energy ΔE_{kin}, such that the total eddy-induced energy change $\Delta E = \Delta E_{kin} + \Delta E_\sigma$ is zero.

Accordingly, the formal statement of the eddy-induced flow change in Eq. (A2) is generalized to

$$\hat{u}_i(y, t) = u_i(f(y), t) + c_i K(y) + b_i J(y). \qquad (A4)$$

Here, $K(y) \equiv y - f(y)$ is the map-induced displacement of the fluid parcel that is mapped to location y and $J(y) \equiv |K(y)|$.

The six coefficients b_i and c_i are evaluated by enforcing the prescribed kinetic-energy change based on the surface-tension energy change E_σ, which is zero if the eddy interval contains only one phase. Momentum conservation in each direction i implies three more constraints. The two additional needed constraints are obtained by modeling the eddy-induced redistribution of kinetic energy among the velocity components. In accordance with return-to-isotropy phenomenology, these additional constraints impose a degree of equalization of the component kinetic energies.

Eddy events displace fluid elements and thus constitute a Lagrangian representation of turbulent advection. The corresponding Eulerian interpretation in terms of Eq. (A1) is that each event corresponds to an instantaneous change of properties at given y, so *Eddies* is a

sum of delta functions in time with weights that each represent the event-induced change of u_i at location y at the time of occurrence of a given event. This interpretation defines a formal representation of ODT time advancement in terms of Eq. (A1), but the Lagrangian fluid-displacement picture is more intuitive and closer to the numerical implementation of the model.

2. Eddy selection

ODT samples eddy events from an event rate distribution that depends on the instantaneous flow state and therefore evolves with the flow. Thus, there is no predetermined frequency of occurrence of eddy events collectively nor of a particular eddy type corresponding to a given location y_0 and size l.

The mean number of events during a time increment dt for eddies located within the interval $[y_0, y_0 + dy]$ in the size range $[l, l+dl]$ is denoted $\lambda(y_0, l; t) \, dy_0 \, dl \, dt$. The relation

$$\lambda(y_0, l; t) = C/(l^2 \tau(y_0, l; t)).\qquad(\text{A5})$$

defines an eddy time scale τ and an adjustable parameter C that scales the overall eddy frequency, where the argument t appearing on both sides of the equation indicates that both λ and τ vary with time for given values of y_0 and l because τ depends on the time-varying instantaneous flow state in the manner described next. (With this understanding, the arguments of τ are henceforth suppressed.) The dimensions of the event rate distribution λ are (length$^2\times$ time)$^{-1}$. To find the eddy time scale τ, the square of the implied eddy velocity l/τ is modeled as

$$(l/\tau)^2 \sim E_{final} - Z(\nu^2/l^2),\qquad(\text{A6})$$

where the first term, which is dependent on the instantaneous flow state, is specified by Eq. (A10) in section A 3 and the second term involving the parameter Z suppresses unphysically small eddies. The coefficient implied by the proportionality is absorbed into C.

In practice it would be computationally unaffordable to reconstruct the event rate distribution every time an eddy event or an advancement of Eq. (A1) takes place. Therefore eddy events are sampled using an equivalent Monte-Carlo numerical procedure called thinning.[27]

3. Multiphase eddy implementation in ODT

If the eddy range contains one or more phase interfaces, then E_σ must be evaluated in order to incorporate the surface-tension effect on eddy implementation as described in section A 1. The procedure is motivated by Fig. 13.a, which shows the initial state of within an eddy that contains a phase interface. For discussion purposes, the phases are termed liquid and gas though they have

FIG. 13: Multiphase eddy treatment in ODT. (a) The size-l spatial interval between the thick solid lines is selected for eddy implementation. It is a multiphase eddy containing both liquid (L) and gas (G) separated by one phase interface (thick dashed line), corresponding to interface number density $n = 1/l$ within the eddy interval. (b) A triplet map is implemented here as a permutation of the cells of a uniform spatial discretization of the 1D domain, illustrated by the reordering of cell indices within the eddy. Now there are three phase interfaces, corresponding to $n = 3/l$ and thus $\delta = 2/l$.

the same densities and viscosities in this study. This eddy is energetically allowed only if there is sufficient kinetic energy available to supply the surface-tension energy needed to create the amount of new interface resulting from map implementation. Modeling is needed in order to specify the surface-tension energy change.

Namely, the ODT analog of the volumetric density $\sigma\alpha$ of surface-tension energy, where σ is the surface-tension energy per unit area and α is the surface area per unit volume, must be identified, corresponding to the energy density

$$E_\sigma = \sigma\alpha/\rho \qquad(\text{A7})$$

per unit mass. The meaning and evaluation of α in ODT are considered.

Since an interface in ODT is represented by an isolated point on a line, geometric interpretation is required in order to obtain the area increase implied by, e.g., the triplet map illustrated in Fig. 13. A plausible assumption for highly turbulent cases involving wrinkled interfaces is that the interface is a statistically homogeneous isotropic random surface. For such a surface, the number density n of interface intersections along a line of sight corresponds to an interface area per unit volume $\alpha = 2n$.[28] This assumption is not precisely accurate for cases of interest, but it is convenient to adopt it as a universal assumption rather than to attempt a case-by-case treatment. On this basis,

$$E_\sigma = 2n\sigma/\rho,\qquad(\text{A8})$$

where in this context, n denotes interface number density within the eddy interval, i.e. the number interfaces in the interval divided by l.

In Fig. 13.a, $n = 1/l$ initially. Triplet mapping of a phase interface within an eddy produces three such interfaces. This is shown in Fig. 13.b and is interpreted as a tripling of interfacial area. The eddy-induced increase δ of the number density of interfaces due to triplet

mapping is thus $2/l$ for this eddy. Based on the relation $\alpha = 2n$, the interfacial area increase per unit volume is 2δ. Multiplication by the surface tension σ gives the surface tension potential energy per unit volume that is stored in the newly created interfaces. This implies the surface tension energy change per unit mass

$$\Delta E_\sigma = 2\sigma\delta/\rho. \tag{A9}$$

This explanation corrects a previous[15] erroneous discussion of these points, but the final result, Eq. (A9), is unchanged.

Conservation of total energy requires an equal and opposite change of the final kinetic energy. Here this implies

$$E_{final} = E_{kin} - \Delta E_\sigma, \tag{A10}$$

where E_{kin} and E_{final} are the available kinetic energy per unit mass before and after the change, respectively. Here, available means the maximum amount extractable by adding weighted J and K kernels to the instantaneous velocity profiles as shown in Eq. (A4). The change is implemented by similarly modifying the velocity profiles using weighted J and K kernels, but in this instance constraining the weighting coefficients b_i and c_i so as to extract the energy ΔE_σ from the flow field within the eddy interval.

[1] M. Linne, "Imaging in the optically dense regions of a spray: A review of developing techniques," Progress in Energy and Combustion Science **39**, 403–440 (2013).
[2] O. Desjardins, J. McCaslin, M. Owkes, and P. Brady, "Direct numerical and large-eddy simulation of primary atomization in complex geometries," Atomization and Sprays **23**, 1001–1048 (2013).
[3] M. Herrmann, "Detailed numerical simulations of the primary atomization of a turbulent liquid jet in crossflow," Journal of Engineering for Gas Turbines and Power **132**, 061506 (2010).
[4] T. Ménard, S. Tanguy, and A. Berlemont, "Coupling level set/vof/ghost fluid methods: Validation and application to 3d simulation of the primary break-up of a liquid jet," International Journal of Multiphase Flow **33**, 510–524 (2007).
[5] M. Gorokhovski and M. Herrmann, "Modeling primary atomization," Annu. Rev. Fluid Mech. **40**, 343–366 (2008).
[6] T. Lebas, Romain andf Menard, P. Beau, A. Berlemont, and F.-X. Demoulin, "Numerical simulation of primary break-up and atomization: DNS and modelling study," International Journal of Multiphase Flow **35**, 247–260 (2009).
[7] K. Sallam, Z. Dai, and G. Faeth, "Liquid breakup at the surface of turbulent round liquid jets in still gases," International Journal of Multiphase Flow **28**, 427–449 (2002).
[8] F. Ben Rayana, A. Cartellier, and E. Hopfinger, "Assisted atomization of a liquid layer: investigation of the parameters affecting the mean drop size prediction,(paper iclass06-190)," CD Proc. ICLASS (2006).
[9] P. Marmottant and E. Villermaux, "On spray formation," Journal of fluid mechanics **498**, 73–111 (2004).
[10] C. Dumouchel, "On the experimental investigation on primary atomization of liquid streams," Experiments in fluids **45**, 371–422 (2008).
[11] Z. Li and F. A. Jaberi, "Turbulence-interface interactions in a two-fluid homogeneous flow," Physics of Fluids **21**, 095102 (2009).
[12] P. Trontin, S. Vincent, J. Estivalezes, and J. Caltagirone, "Direct numerical simulation of a freely decaying turbulent interfacial flow," International Journal of Multiphase Flow **36**, 891–907 (2010).
[13] J. McCaslin and O. Desjardins, "Theoretical and computational modeling of turbulence/interface interactions," in Proceedings of the Summer Program (2014) p. 79.
[14] J. McCaslin, "Development and application of numerical methods for interfacial dynamics in turbulent liquid-gas flows," (2015).
[15] A. Movaghar, M. Linne, M. Oevermann, F. Meiselbach, H. Schmidt, and A. R. Kerstein, "Numerical investigation of turbulent-jet primary breakup using one-dimensional turbulence," International Journal of Multiphase Flow **89**, 241–254 (2017).
[16] A. R. Kerstein, "One-dimensional turbulence: Model formulation and application to homogeneous turbulence, shear flows, and buoyant stratified flows," Journal of Fluid Mechanics **392**, 277–334 (1999).
[17] W. T. Ashurst and A. R. Kerstein, "One-dimensional turbulence: Variable-density formulation and application to mixing layers," Physics of Fluids **17**, 025107 (2005).
[18] A. Movaghar, M. Linne, M. Herrmann, A. Kerstein, and M. Oevermann, "Modeling and numerical study of primary breakup under diesel conditions," International Journal of Multiphase Flow **98**, 110–119 (2018).
[19] O. Desjardins, G. Blanquart, G. Balarac, and H. Pitsch, "High order conservative finite difference scheme for variable density low Mach number turbulent flows," Journal of Computational Physics **227**, 7125–7159 (2008).
[20] O. Desjardins, J. McCaslin, M. Owkes, and P. Brady, "Direct Numerical and Large-Eddy Simulation of Primary Atomization in Complex Geometries," Atomization and Sprays **23**, 1001–1048 (2013).
[21] M. Owkes and O. Desjardins, "A computational framework for conservative, three-dimensional, un-split, geometric transport with application to the volume-of-fluid (VOF) method," Journal of Computational Physics **270**, 587–612 (2014).
[22] M. Owkes and O. Desjardins, "A Mesh-decoupled Height Function Method for Computing Interface Curvature," Journal of Computational Physics **281** (2015).
[23] R. Fedkiw, T. Aslam, B. Merriman, and S. Osher, "A non-oscillatory Eulerian approach to interfaces in multimaterial flows (the ghost fluid method)," J. Comput. Phys. **152**, 457–492 (1999).
[24] A. R. Kerstein, W. T. Ashurst, S. Wunsch, and V. Nilsen, "One-dimensional turbulence: vector formulation and application to free shear flows," Journal of Fluid Mechanics **447**, 85–109 (2001).
[25] A. R. Kerstein and S. Wunsch, "Simulation of a stably stratified atmospheric boundary layer using one-dimensional turbulence," Boundary-layer meteorology **118**, 325–356 (2006).
[26] A. Kolmogorov, "On the breakage of drops in a turbulent flow," Doklady Akademii Nauk SSSR **66**, 825828 (1949).
[27] S. M. Ross, Stochastic Processes, 2nd ed. (John Wiley & Sons New York, 1996).
[28] S. N. Chiu, D. Stoyan, W. S. Kendall, and J. Mecke, Stochastic geometry and its applications (John Wiley & Sons, 2013).

PAPER VI

A Subgrid-Scale Model for Large-Eddy Simulation of Liquid/Gas Interfaces Based on One-Dimensional Turbulence

A Subgrid-Scale Model for Large-Eddy Simulation of Liquid/Gas Interfaces Based on One-Dimensional Turbulence

Amirreza Movaghar [1], Robert Chiodi [2], Michael Oevermann [1]
Olivier Desjardins [2], Alan Kerstein [3]

Abstract. The interface/turbulence interaction between two fluids in a turbulent environment has an important role in many technical processes, e.g. primary liquid atomization in combustion devices. Primary atomization has a significant role in spray formation and its characteristics. The resulting dynamics typically span 4-6 orders of magnitude in length scales, making detailed numerical simulations exceedingly expensive. This motivates the need for modeling approaches based on spatial filtering such as large-eddy simulation (LES). In this paper, a new approach based on One-Dimensional turbulence (ODT) is presented to describe the subgrid interface dynamics. ODT is a stochastic model simulating turbulent flow evolution along a notional one-dimensional line of sight by applying instantaneous maps that represent the effects of individual turbulent eddies on property fields. It provides affordable high resolution of interface creation and property gradients within each phase, which are key for capturing the local behavior as well as overall trends. ODT has previously been shown to reproduce the main features of an experimentally determined regime diagram for primary jet breakup. Here a new approach called VODT is presented which produces a size-conditioned as well as a total time rate of generation of droplets for given flow conditions at an interface. At the LES level, the total droplet generation from VODT is interpreted as a rate of mass conversion of LES-resolved liquid into unresolved droplets. Preliminary results of applying VODT to a cell with a planar-shear-layer are discussed at the end of the paper.

Keywords: Turbulence, Atomization, Large-Eddy Simulation, One-Dimensional Turbulence

1 Introduction

The interaction between turbulence and interfaces of immiscible fluids is seen in many engineering applications, e.g., primary atomization in combustion devices. The atomization process plays a significant role in combustion performance, including efficiency

---

[1]Department of Mechanics, Chalmers University of Technology, Gothenburg, Sweden, movaghar@chalmers.se

[2]Sibley School of Mechanical and Aerospace Engineering, Cornell University, Ithaca, USA, rmc298@cornell.edu

[3]Cosultant, 72 Lomitas Road, Danville, CA, USA, alan.kerstein@gmail.com

and emissions. Despite its importance, a detailed description of primary atomization has remained elusive, due in part to insufficient understanding of how interfaces modulate the surrounding flow field and undergo breakup. Many attempts have been made to describe interfacial instabilities using linear stability analysis, however, these only provide a very limited picture of interfacial dynamics, especially in turbulence and complex geometries. Because of this, there remains a need to understand and model the interactions between two immiscible fluids in a turbulent environment.

Predictive simulations with high spatial and temporal resolution, i.e., Direct Numerical Simulations (DNS), offer an alternative way to study liquid-gas interface dynamics during primary breakup. But despite the significant benefits provided by DNS, the large computational cost precludes their use in many flows of engineering interest. Therefore, there is a need for appropriate interface dynamics models lower the computational cost of predicting the atomization process. While requiring phycsial models for the small unresolved scales of the flow, Large-Eddy Simulation (LES) has shown to be a useful tool that can provide much more flexibility on resolution coarser than DNS by introducing a spatial filter into the governing equations and resolving only the scales larger than the filter width [3]. However, the LES sub-filter models typically neglect the contribution of the surface tension term and are based on a cascade process hypothesis that may be questionable in the context of surface tension-driven atomization. This leads the need for a new LES subgrid interface dynamics model.

A One-Dimensional Turbulence (ODT) model is considered here as an affordable model for simulating large Reynolds and Weber number flow configurations. ODT is a stochastic model simulating turbulent flow evolution along a notional one-dimensional line of sight by applying instantaneous maps that represent the effects of individual turbulent eddies on the flow properties. ODT has recently been used by the authors [6] to reproduce the main features of an experimentally determined regime diagram for primary jet breakup.

ODT can be used both as a stand alone tool and as a sub-grid model for LES or RANS. This creates a possibility to use ODT as a subgrid resolution model in LES simulations to describe/model subgrid interface dynamics. This approach is described in detail in the following sections.

2 Governing equations

The flows investigated in this study are governed by the incompressible Navier-Stokes equations for immiscible two-phase flow. The momentum equation is given by

$$\frac{\partial \rho u}{\partial t} + u \cdot \nabla \rho u = -\nabla p + \nabla \cdot [\mu (\nabla u + \nabla^T u)] + \sigma \gamma \delta (x - x_\Gamma) n, \tag{1}$$

where u is the velocity, ρ the density, p the pressure, and μ is the dynamic viscosity. The last term in Eq. 1 is the singular surface tension force where γ denotes the curvature of the interface, δ is the Dirac delta function, x_Γ is the point on the interface Γ closest to the point x and n is the interface normal vector.

To compute the phase interface, in addition, a transport equation for the liquid volume fraction α in a computational cell is solved

$$\frac{\partial \alpha}{\partial t} + \nabla \cdot (u\alpha) = 0. \tag{2}$$

The interface unit vector n and the interface curvature γ can be theoretically expressed in terms of the liquid volume fraction as

$$n = \frac{\nabla \alpha}{|\nabla \alpha|}, \quad \gamma = \nabla \cdot n. \tag{3}$$

Following the continuum surface force approach [2] the surface tension force in Eq. 1 is modelled as

$$\sigma \gamma \delta(x - x_\Gamma) n = \sigma \gamma \nabla \alpha. \tag{4}$$

Using LES to simulate the flow field, the spatial filtering is applied to Eq. 1. In LES, the large scale structures are captured directly, whereas the small scale structures are filtered out. Applying any spatial filtering to Eq. 1, new terms appear, these are called sub-grid-scale (SGS) terms. LES is based on Kolmogorov's hypothesis: the large scale structures are dependent on the specific flow situation, whereas the behaviour of the small scale structures is isotropic and geometry independent, i.e. universal. If the scales that are filtered out are small enough to be considered as universal, the SGS terms can be closed by a model, e.g the Smagorinsky model. However, these models typically neglect the contribution of the sub-filter surface tension term and are based on a cascade process hypothesis that may be questionable in the presence of an interface.

In particular, LES does not see interface wrinkles below its resolution scale, so the LES-resolved interface is much smoother and has less total surface area than the true interface. Therefore it doesn't fully account for the true total amount of stored surface-tension area. As Fig 1 illustrates, when the Weber number is high enough there are some scales of interface wrinkling that are not resolved by the LES and cause droplet generation. The following sections describe how ODT can be used to model these unresolved scales.

3 One-Dimensional turbulence (ODT)

The ODT model of Kerstein used in this study is briefly described in this section. For a fully detailed description we refer to Kerstein et al. [4], Ashurst et al. [1], and its extension to modelling primary breakup by Movaghar et al. [6].

ODT is a stochastic model of turbulent flows that solves the unsteady one-dimensional transport equations for mass, momentum, and optionally other scalars such as species mass fractions and energy. The advantages of a turbulence model formulated as a one-dimensional unsteady stochastic simulation are twofold. First, a one-dimensional formulation enables affordable simulation of high Reynolds number turbulence over the full range of dynamically relevant length scales, resolving the interactions between turbulent advection and microphysical processes such as viscous dissipation, or as in this study, the interaction with a fluid interface. Second, this approach reproduces diverse
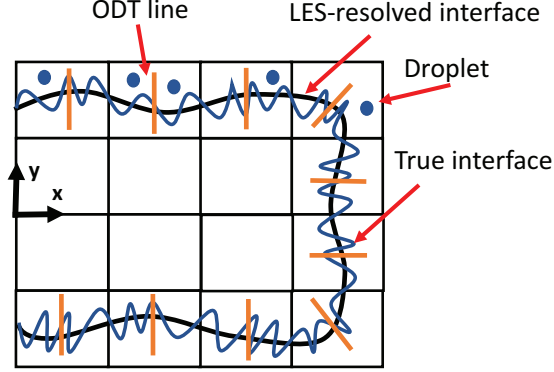
Fig. 1. Using ODT as a sub-filter model for LES

flow behaviors and permits high resolution of property profiles in the direction of the most significant gradients (parametrized by the spatial coordinate y in this study).

In contrast to common approaches based on the Navier-Stokes equations, ODT uses a set of mechanisms modeling the physical effects phenomenologically on a 1D line of sight through the domain. The fields defined on the one-dimensional domain evolve by two mechanisms: molecular diffusion and a stochastic process representing advection. The stochastic process consists of a sequence of events, each of which involves an instantaneous transformation of the velocity fields and the additional property profiles. During the time interval between each event and its successor, molecular diffusion occurs, governed by the equation

$$\partial u_i(y,t)/\partial t = \nu \partial^2 u_i(y,t)/\partial y^2. \tag{5}$$

Here u_i with $i \in 1,2,3$ are the three velocity components, with molecular transport coefficient ν (viscosity).

The eddy events representing advection may be interpreted as the model analog of individual turbulent eddies. In ODT, an eddy of size l is represented by an instantaneous map acting on each property field within an interval $[y_0, y_0 + l]$ on the line. The mathematical formulation of the map should satisfy measure preservation and continuity of mapped profiles. The new velocity field after the map event is given by,

$$\hat{u}_i(y,t) = u_i(f(y),t) \tag{6}$$

where the inverse of the triplet map is specified by

$$f(y) = y_0 + \begin{cases} 3(y - y_0), & \text{if } y_0 \leq y \leq y_0 + (1/3)l, \\ 2l - 3(y - y_0), & \text{if } y_0 + (1/3)l \leq y \leq y_0 + (2/3)l, \\ 3(y - y_0) - 2l, & \text{if } y_0 + (2/3)l \leq y \leq y_0 + l, \\ y - y_0, & \text{otherwise} \end{cases} \tag{7}$$

If the eddy range $[y_0, y_0 + l]$ contains no phase interfaces, then it is a single-phase eddy whose implementation is the same as in previous ODT formulations. If instead the eddy range contains an interface then it is a multiphase eddy requiring the domain-integrated energy conservation. This requires that the change of kinetic energy after the eddy event, ΔE_{kin} is equal and opposite to any surface-tension potential-energy change, ΔE_σ caused by triplet mapping of phase interfaces.

For this purpose, the kernel functions $c_i K(y)$ and $b_i J(y)$ are added to the u_i profile created formerly by triplet mapping. On this basis equation 6 is rewritten as

$$u_i(y) \rightarrow u_i(f(y)) + b_i J(y) + c_i K(y) \tag{8}$$

and

$$\rho(y) \rightarrow \rho(f(y)), \tag{9}$$

where $f(y)$ is the inverse of the triplet map, $K = y - f(y)$, $J = |K|$, and b_i and c_i are assigned based on physical modeling. The requirement $\int K(y)dy = 0$ enforces momentum conservation.

ODT samples eddy events from an instantaneous distribution that evolves with the flow. These events are individually parameterized by position y_0 and size l.
The number of events during a time increment dt for eddies located $[y_0, y_0 + dy]$ in the size range $[l, l + dl]$ is denoted $\lambda(y_0, l; t)dy_0 dl dt$, where the event rate density λ is defined as

$$\lambda(y_0, l; t) = C/(l^2 \tau(y_0, l; t)). \tag{10}$$

with dimensions of $events/(location \times size \times time)$. The adjustable parameter C scales the overall eddy frequency and τ is the eddy time scale. To find this eddy time scale, the square of the velocity implied by l and τ is modeled as

$$(l/\tau)^2 \sim E_{final} - Z(\nu^2/l^2). \tag{11}$$

On the right hand side, the first term is the final value of the available kinetic energy, denoted E_{kin} in the absence of surface-tension effects, $E_{final} = E_{kin} - \Delta E_\sigma$ and the second term involving the parameter Z suppresses unphysically small eddies, such as those smaller than the Kolmogorov scale. Following [6], ΔE_σ is formulated as

$$\Delta E_\sigma = -\frac{4\sigma}{\rho_{eddy} l}. \tag{12}$$

Because ΔE_σ and the last term in Eq. 11 are both negative, the right-hand side of that equation can be negative but the left-hand side must be positive. This is an indication that the selected eddy is energetically forbidden, corresponding to $\lambda = 0$ for such eddies.

4 Virtual ODT for LES/VOF closure

As described, ODT can be used as a stand alone computation tool. This creates a possibility to use ODT to compute a subgrid breakup table. As shown in Fig. 1 it is assumed

that the ODT closure of LES/VOF can be formulated on an ODT domain locally normal to a given interface element in every interface LES cell. For generality the interface is allowed here to be at any location $y = I$ on the ODT domain where I is the interface location. ODT produces a size-conditioned as well as a total time rate of generation of droplets at a given VOF interface. At the LES level, the total droplet generation is interpreted as a rate $\dot{M}$ of mass conversion of LES-resolved liquid into unresolved droplets that are then deemed to reside in the gas phase. Accordingly, for an interface element whithin a LES cell, droplet generation causes recession of the interface at a speed $\dot{M}/(A\rho_l)$ inserted as a source term into Eq. 2 and updates the LES governing equations. A reduced formulation of ODT, called virtual ODT (VODT), that is suitable for economical closure in this manner is introduced next.

As discussed earlier, ODT contains two main mechanisms, viscous time advancement and eddy events. For the tabulation purposes, we suppose there is no viscous advancement but only eddy sampling. Nevertheless the accepted eddies are not implemented and just their statistics are collected. Because the VODT state is not time advanced, the only effect of eddy events is droplet generation and the implied recession of the liquid surface. Therefore, eddies entirely contained in one phase have no effect, leaving only multiphase (hence droplet-forming) eddies to be considered. By not implementing the eddies, the eddy rate distribution is stationary. Thus the initial rate distribution is used to evaluate the rate of production of a droplet of any size. The effect of surface tension (and hence the *We* dependence), which does not appear in Eq. 5, is brought into the formulation through the physical modeling that specifies the eddy rate distribution.

A VODT droplet-forming eddy ranges from some location $y_0 < I$ to a location $y_0 + l > I$, which implies $l > I - y_0$ where . Based on the triplet-map definition, the eddy transfers 2/3 of the liquid interval $[y_0, I]$ to the droplet, while the rest remains in liquid form as defined in VODT. The implied surface recession is then $\Delta y = \frac{2}{3}(I - y_0)$, corresponding to the LES-level volume conversion $\Delta V = A_s \Delta y$ where A_s is the surface area of VOF interface element.

Δy is the only available length scale from which the droplet diameter D can be inferred, so $D = B\Delta y$ is assumed, where B is a tunable parameter. Then the ODT droplet is deemed to represent N physical droplets, where $N = \Delta V / \left(\frac{\pi}{6}D^3\right)$ is based on assuming spherical droplets. Using $\Delta V = A_s D/B$, this gives $N = 6A_s/(\pi B D^2)$. N need not to be an integer because it is meaningful only in terms of droplet statistics.

At the LES scale, it is assumed that the droplet spectrum in the gas phase is represented by a histogram based on either linear or geometric sized bins. Uniform linear bins of size dD are assumed here for illustration, although the reasoning is more general. To complete the formulation of VODT outputs, the total generation rate $G(D)$ of droplets in the size range $[D, D + dD]$ is evaluated. To do this, the droplets number probability distribution, $g(D) = \frac{dG}{dD}$ per unit diameter increment is first evaluated. Based on the the results that follow, $g(D)$ can be integrated over dD intervals to obtain the binned generation rates $G(D)$.

The fixed VODT flow state is piecewise linear in u, where the slope discontinuity is determined by steady state momentum-flux balance at the phase interface, which is at

the domain midpoint. The domain size, velocity difference across the domain, surface tension, and the phase viscosities and densities define a particular case.

The ODT eddy rate distribution $\lambda(y_0, l)$, which has no t dependence, has been evaluated exactly in closed from as a function of y_0 and l for a specified VODT state. To evaluate $g(D)$, this distribution is integrated over its arguments subject to the constraint $D = B\Delta y = \frac{2}{3}B(I - y_0)$, re-expressed as $y_0 = I - \frac{3}{2}\frac{D}{B}$. Formally this involves insertion of $\delta(y_0 - I + \frac{3}{2}\frac{D}{B})$ into the integral over dy_0, and thus

$$g(D) = N(D) \int_{\frac{3}{2}\frac{D}{B}}^{h-I+\frac{3}{2}\frac{D}{B}} dl \int dy_0 \, \lambda(y_0, l) \delta(y_0 - I + \frac{3}{2}\frac{D}{B}) = \frac{6A_s}{\pi B D^2} \int_{\frac{3}{2}\frac{D}{B}}^{h-I+\frac{3}{2}\frac{D}{B}} dl \, \lambda(I - \frac{3}{2}\frac{D}{B}, l).$$

The moments of the drop number probability distribution are then defined by

$$G_i(D) = \int_{D_{min}}^{D_{max}} g(D) D^i dD.$$

G_0 is the total number of droplets generated per unit time, G_1 is the total sum of diameter of the droplets per unit time, πG_2 is the total surface area of the droplets per unit time and $\pi G_3/6$ is the total volume of the droplets per unit time.

5   Results and Conclusion

As discussed, for this simple application VODT reduces to an algebraic system that is economical enough for on-the-fly runtime implementation. This makes VODT a computationally affordable tool to study different atomization processes. Fig. 2 shows a normalized droplet atomization rate of interfacial breakup in different Reynolds and Weber numbers. The droplet generation rate, G_0, shows the total number of drops in time and is normalized by local shear $\Delta u/h$. As seen in the Fig. 2, for relatively low injection velocities the atomization rate is primarily governed by the liquid surface tension. In Fig. 2 the density and viscosity ratios are both equal to 1. By varying the liquid/gas density ratio and keeping the viscosity ratio constant, Fig. 3 is generated, showing the atomization rate. As shown, VODT can generate the entire droplet dependant moments of the generation rate, $G_i(D)$ e.g. total volume of the drops per unit time for any flow condition.

As discussed earlier the main scope of this paper is to propose VODT as a subgrid model for LES/VOF simulations. Like ODT, VODT has three adjustable parameters C, Z, B that need to be calibrated for this planar shear layer application.

A possible basis for this that does not require external input is to run LES/VOF/VODT at different LES resolutions for the same case. If VODT is a good closure, then these results should all predict the same flow development and droplet statistics. As resolution improves, some of the droplet generation seen at the VODT level at coarse LES resolution should become LES-resolved, with VODT still giving the same results as at lower LES resolution for droplets still not resolved. This approach is currently under study and outcomes will be a part of discussions in future publications.
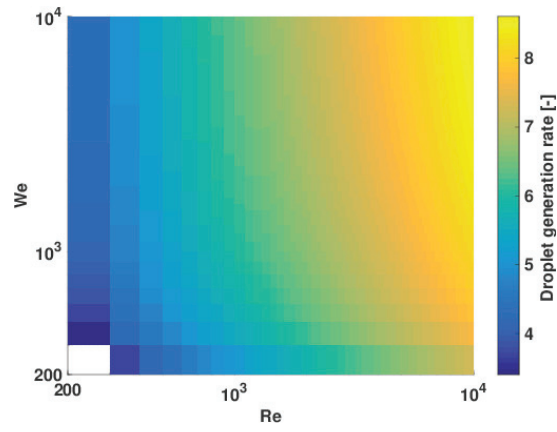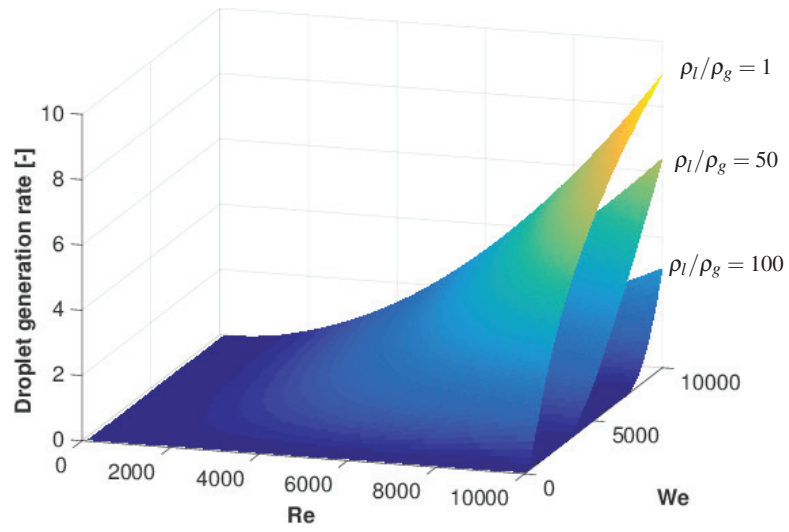
Fig. 2. Normalized droplet generation rate [-]

Fig. 3. Normalized droplet generation rate at $\rho_l/\rho_g = 1, 10, 100$ with $\mu_l/\mu_g = 100$

Acknowledgement

References

1. Ashurst, W. T., and Kerstein, A. R.: One-dimensional turbulence: Variable-density formulation and application to mixing layers. Physics of Fluids. 17, 025107 (2005).
2. Brackbill, J. U., Kothe, D. B., and Zemach, C.: A continuum method for modeling surface tension. Journal of Computational Physics. 100, 335-354 (1992).
3. Desjardins, O., McCaslin, J., Owkes, M., and Brady, P.: Direct numerical and large-eddy simulation of primary atomization in complex geometries. Atomization and Sprays. 23, 1001-1048 (2013).
4. Kerstein, A. R., Ashurst, W. T., Wunsch, S., and Nilsen, V.: One-dimensional turbulence: Vector formulation and application to free shear flows. Journal of Fluid Mechanics. 447, 85-109 (2001).
5. Movaghar, A., Linne, M., Oevermann, M., Meiselbach, F., Schmidt, H., and Kerstein, A. R.: Numerical investigation of turbulent-jet primary breakup using one-dimensional turbulence. International Journal of Multiphase Flow. 89, 241-254 (2017).
6. Movaghar, A., Linne, M., Herrmann, M., Kerstein, A. R., and Oevermann, M.: Modeling and numerical study of primary breakup under diesel conditions. International Journal of Multiphase Flow. 98, 110-119 (2018).